UC Berkeley
UC Berkeley Electronic Theses and Dissertations

Title

A Measurement of the proton-proton inelastic scattering cross-section at sqrt(s) =7 TeV with the ATLAS detector at the LHC

Permalink

https://escholarship.org/uc/item/4m34b24r

Author

Tompkins, Lauren Alexandra

Publication Date

2011

Peer reviewed|Thesis/dissertation

A Measurement of the proton-proton inelastic scattering cross-section at $\sqrt{s} = 7$ TeV with the ATLAS detector at the LHC

by

Lauren Alexandra Tompkins

A dissertation submitted in partial satisfaction of the

requirements for the degree of

Doctor of Philosophy

in

Physics

in the

Graduate Division

of the

University of California, Berkeley

Committee in charge:

Professor B. H. Heinemann, Chair
Professor Y. Kolomensky
Professor L. Blitz

Spring 2011

A Measurement of the proton-proton inelastic scattering cross-section at $\sqrt{s} = 7$ TeV with the ATLAS detector at the LHC

Abstract

A Measurement of the proton-proton inelastic scattering cross-section at $\sqrt{s} = 7$ TeV with the ATLAS detector at the LHC

by

Lauren Alexandra Tompkins

Doctor of Philosophy in Physics

University of California, Berkeley

Professor B. H. Heinemann, Chair

The first measurement of the inelastic cross-section for proton-proton collisions at a center of mass energy $\sqrt{s} = 7$ TeV using the ATLAS detector at the Large Hadron Collider is presented. From a dataset corresponding to an integrated luminosity of 20 μb^{-1}, events are selected by requiring activity in scintillation counters mounted in the forward region of the ATLAS detector. An inelastic cross-section of 60.1 ± 2.1 mb is measured for the subset of events visible to the scintillation counters. The uncertainty includes the statistical and systematic uncertainty on the measurement. The visible events satisfy $\xi > 5 \times 10^{-6}$, where $\xi = M_X^2/s$ is calculated from the invariant mass, M_X, of hadrons selected using the largest rapidity gap in the event. For diffractive events this corresponds to requiring at least one of the dissociation masses to be larger than 15.7 GeV. Using an extrapolation dependent on the model for the differential diffractive mass distribution, an inelastic cross-section of $69.1 \pm 2.4(\mathrm{exp}) \pm 6.9(\mathrm{extr})$ mb is determined, where (exp) indicates the experimental uncertainties and (extr) indicates the uncertainty due to the extrapolation from the limited ξ-range to the full inelastic cross-section.

To Dad,
for the tool bench,

and Mom,
for the secrets of math and broccoli.

ACKNOWLEDGMENTS

When I first joined the LBL ATLAS group as a wide-eyed young graduate student, I never dreamed that my dissertation research would involve measuring the inelastic proton-proton cross-section. Five years and one massive accelerator accident later, I feel fortunate to have been given an opportunity to *own* an LHC analysis in a way that would not have been possible with almost any other topic. I owe that opportunity to my adviser, Beate Heinemann. Throughout the past year she has been the trench commander on the front lines of this analysis with me. I have learned so much from her in this work and in the wide variety of other topics we have covered over the past four years. Along the way I have developed a deep respect and admiration for the way she does physics and the way she works with other people.

While Beate has been my primary mentor, I have also received much support and wisdom from past and present members of the LBL ATLAS group. This formidable group of physicists has given me better training than I could have gotten anywhere else. A few people deserve specific mention. Sven Vahsen was my guide when writing my first Athena code, and he taught me much during the cosmics analysis. Marjorie Shapiro has always been a willing mentor, providing valuable insight on whatever project I was working on. My dissertation is a small part of the work done by the ATLAS Soft QCD group. Analyzing the first LHC data was exciting, but the Min-Bias folks, who dove into the data with relish on day one, made it *fun* as well. The cross-section analysis was greatly improved by the guidance of its Editorial Board. In particular, the expertise of Emily Nurse, Paul Newman, and Halina Abramowicz, and the stewardship of Jon Butterworth and Kevin Einsweiller was crucial for navigating the muddled waters of soft interactions.

My work on ATLAS began in 2004 with the Orsay group in France. My thanks go to Daniel Fournier for sponsoring me as a completely unknown American student, Laurent Serin for giving me my first hardware experience, and Dirk Zerwas for advising me on my first full analysis. I would also like to thank my undergraduate adviser, Young-Kee Kim. Her dedication, enthusiasm and support made research an exciting and *wonderful* thing.

My higher education journey has encompassed much more than learning to do a physics analysis. Over a third of my life has been spent in the arms of the University of California, to which I am greatly indebted. No *place* has ever felt more like home. I owe a big thank-you to my friends from the cohort of 2005 and the wonderful people with whom they share

their lives. The ski weekends and Wednesday night dinners were a welcome respite from work. I have to thank Heather, without whom I would've never survived my stay at CERN. Max has been my solid, and oftentimes vocal, companion during the ups and downs of being an LHC grad student. I am so thankful to have spent the past few years sharing an office and a friendship with him.

My long friendship with Dana, Jasmin and Vidya has sustained me through the challenges of freshman problem sets and mid-twenties angst alike. Each of them is an inspiration in ways that I could never enumerate. My deepest thanks goes to Mom, Dad, Katie and Sean: I am *who* I am and *where* I am because of your love and encouragement. And lastly I want to thank Kyle. Through him I have learned what is truly important in life.

<div align="right">

# PREFACE

</div>

For the General Reader

On March 30th, 2010, the highest-energy man-made proton collisions to date occurred at the Large Hadron Collider (LHC) in Geneva, Switzerland, ushering in a new era of discovery for high-energy particle physics. The LHC is poised to answer some of the most fundamental questions of nature: what is the origin of mass? is our current understanding of elementary particle interactions a complete description of nature? and, possibly, what is the nature of dark matter? The work in this thesis concerns the first steps along the road to discovery. It aims for an understanding of the most abundant and inclusive of LHC processes, proton-proton inelastic collisions.

The LHC is a proton collision factory, churning out millions of collisions per second. It takes hydrogen atoms from a tank of gas, strips the atoms of their electrons, and accelerates the remaining protons to 99.999996% of the speed of light. The protons revolve around the LHC in two beams traveling in opposite directions, and are brought to collide at four points along the 27 km ring in a region no larger than a strand of hair. Each beam is divided into multiple bunches of 100 billion protons to maximize the probability that the protons will interact when the beams cross each other; even at those beam densities, only a few proton interactions occur per beam crossing.

Garden-variety proton-proton interactions happen 10 billion times more frequently than theorists predict interactions which produce the fabled Higgs boson should occur. Yet, the theorists cannot calculate from first principles how often protons interact with each other. By contrast, they can predict with relatively high accuracy how often a proton-proton interaction will yield a Higgs Boson. The reason that the rare Higgs production rate is easier to calculate than the total proton-proton interaction rate is because of *what* inside the proton is interacting. To produce a Higgs boson, which is a heavy particle, a large amount of energy is needed so very energetic parts of the proton must interact. However, only a small part of the proton carries significant energy, the rest is a teeming, low energy mess.Think of the proton as a ball of jello with a few BBs embedded inside of it. Most of

the time when two protons collide the jello makes a mess, but the BBs don't contact each other. However, on rare occasions a BB from one proton will hit one from the other proton head on and the result with be a clean interaction, like the collision of two billiard balls. Calculating the interaction of jello with jello is intractable, but calculating the interaction of two BBs is simple. Higgs boson production occurs in the rare "BB" collisions, the vast majority of LHC collisions, such as the one shown in Figure 1, are made of "jello".
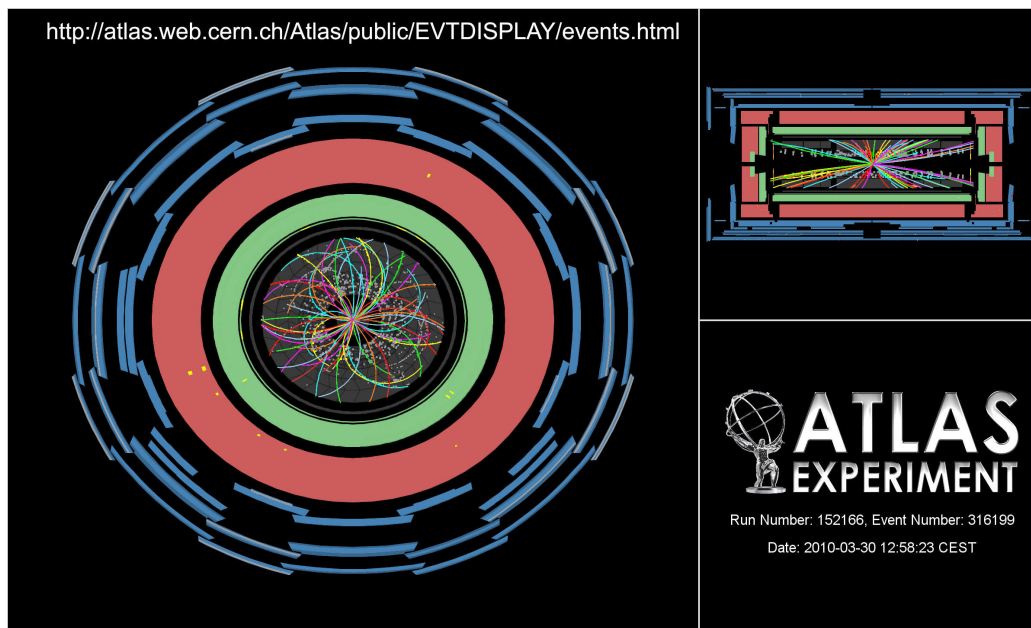
Figure. 1 A proton-proton collision event from the first day of 7 TeV collisions at the LHC. The outermost blue segments indicate the muon detectors. The pink and green regions indicate the hadronic and electromagnetic calorimeters, respectively. The grey shaded region shows the inner tracking detectors. The colored lines are the traces of charged particles, as determined from the energy deposits left in the detector by the particle, indicated by the grey dots. The left view is transverse to the beam direction, the upper right view is along the beam direction.

One of the most interesting features of proton-proton interactions is how the rate of interaction changes with different proton collision energies. How quickly the interaction rate increases sheds light on what mechanisms are involved in the interactions at different energies. Because the rate of proton interactions is so difficult to calculate, experimental measurements are critical to distinguishing which models of the interactions best describe nature. Measurements at past colliders mapped out the dependence of the interaction rate at low proton energies and found a slow dependence on the energy. Once data were taken at higher energies, the situation got murkier. For example, two experiments at the Fermilab accelerator in Batavia, Illinois, which has proton energies three and a half times lower than at the LHC, yielded discrepant results. At very high energies, cosmic ray data have been used to infer the proton-proton interaction rate. When cosmic ray protons bombard the

upper atmosphere they interact with atoms in the air. These interactions are measured by experiments, and are related to proton-proton interactions through approximate theoretical models. However, because these measurement rely on models and approximations, they have large uncertainties. Therefore, they provide little information on the high energy behavior of proton-proton interactions.

The measurement presented in this thesis uses the ATLAS detector at the LHC to measure the rate of proton-proton interactions at the highest energy man-made collisions in the world. Events are detected and counted using scintillator discs which sit 3.6 m from the center of ATLAS and have an inner radius of 14 cm and an outer radius of 88 cm from beam-pipe. The scintillators are made of a special plastic which emits light when traversed by a charged particle. The light signals that a proton-proton interaction has occurred.

(a)

(b)
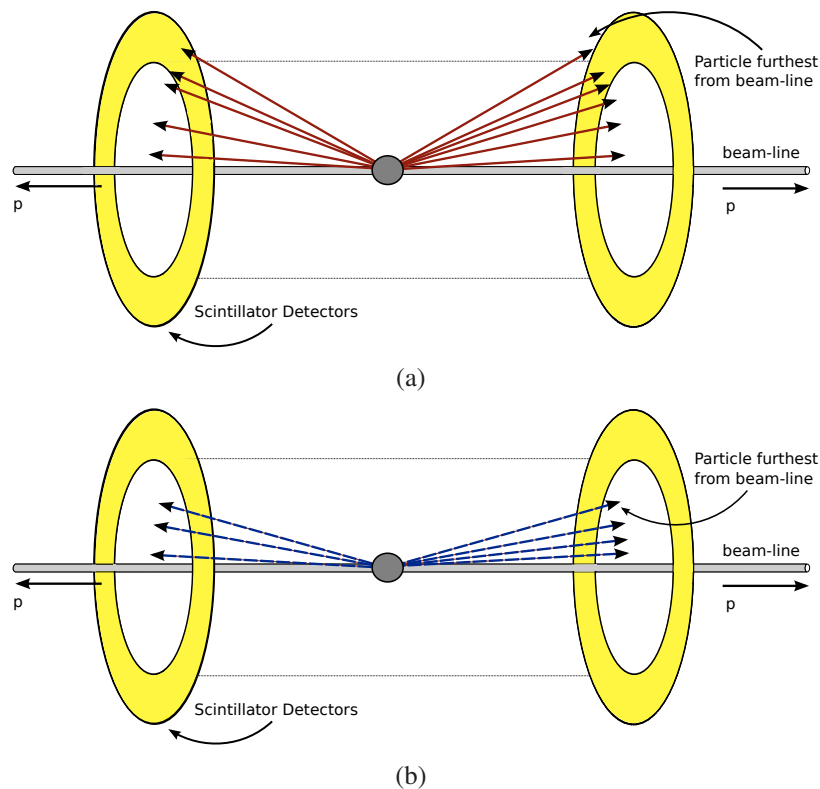
Figure. 2 Cartoon sketch of an event illustrating which events are visible to the detector. The yellow discs indicate the scintillator detectors, the red and blue dashed arrows represent particles created in a proton-proton interaction. In Figure (a) the event is detected because the particles intersect the scintillators. In Figure (b) it is not detected.

What distinguishes this measurement from measurements in the past is that it is restricted to only the subset of proton-proton interactions which the detector can observe. Most proton-proton interactions look like Figure 1. They are easily detectable because particles are produced in all directions. However, in some interactions the protons exchange

only a bit of energy and the new particles created in the interaction are emitted at small angles to the beam-line. Sometimes the new particles are so close to the beam-line that the detector cannot measure them. Figure 2 illustrates two events. In Figure P.2a the particles produced intersect the scintillator detectors and the event is observed. In Figure P2b the particles are too close to the beam-line and do not traverse the scintillators. Normally experiments use models of how often this happens to correct for these undetected events. The measurement in this thesis is defined as the rate of proton interactions in which the particle furthest from the beam line intersects the innermost edge of the detector. Therefore there is no large model-dependent correction for the undetected events. Because it is so well-defined, the measurement has very small uncertainties. In order to compare with past experiments and other models, this thesis also presents the interaction rate with a model-dependent correction for the undetected events.

The measurement presented in this thesis is highest energy direct measurement of the proton-proton interaction rate. The measurement does not show a dramatic rise of the interaction rate at LHC energies, indicating that no new mechanism is involved in the proton-proton interactions. Some models predict that at higher energies protons will interact through new channels not present at lower energies and that these additional channels will increase the interaction rate. The data suggest that this hypothesis is incorrect.

Contents

List of Figures

List of Tables

CHAPTER 1

Introduction

On March 30th, 2010, the highest-energy man-made proton collisions to date occurred at the Large Hadron Collider in Geneva, Switzerland, ushering in a new era of discovery for high-energy particle physics. The LHC is poised to answer some of the most fundamental questions of nature: what is the origin of mass? is the Standard Model a complete description of nature? and, possibly, what is the nature of dark matter? The work in this thesis concerns the first steps along the road to discovery. It aims for an understanding of the most abundant and inclusive of LHC processes, proton-proton inelastic collisions.

The physics of inclusive proton interactions is simultaneously the most basic and complex phenomenon at the LHC. Since the earliest days of hadron collider physics, total proton-proton cross-sections have been measured and puzzled over. Quantum chromodynamics (QCD), the theory of strong interactions, is currently unable to describe the inelastic cross-section, and therefore, myriad models are used to describe this high-energy, low momentum transfer phenomenon. Typically, proton inelastic interactions are divided into two categories: diffractive interactions, in which the final state protons or their dissociation products have no QCD color connection ($pp \rightarrow pX$, $pp \rightarrow XY$, $pp \rightarrow ppX$) and non-diffractive processes in which color flow is present ($pp \rightarrow X$). Non-diffractive events make up the bulk of the inelastic cross-section and are modeled reasonably well by tuned Monte Carlo generators. Diffractive events are poorly understood, and their understanding is critical to an understanding of the inelastic cross-section.

Existing data on the total (elastic + inelastic) proton-proton and proton-antiproton cross-sections are shown in Figure 1.1. The majority of the data are from measurements at colliders. The first measurements were made at fixed target experiments at the CERN Low Energy Antiproton Ring (LEAR), Synchro-Cyclotron (SC) and Proton Synchotron (PS) colliders. They were followed by colliding beams measurements at the Intersecting Storage Ring (ISR) and Super Proton Synchotron (SPS). Several TeVatron experiments measured the cross-section at a center-of-mass energy of 1.8 TeV. However, there is a long-standing 2.6σ discrepancy between the measurement of the CDF [2] experiment and of E710 and
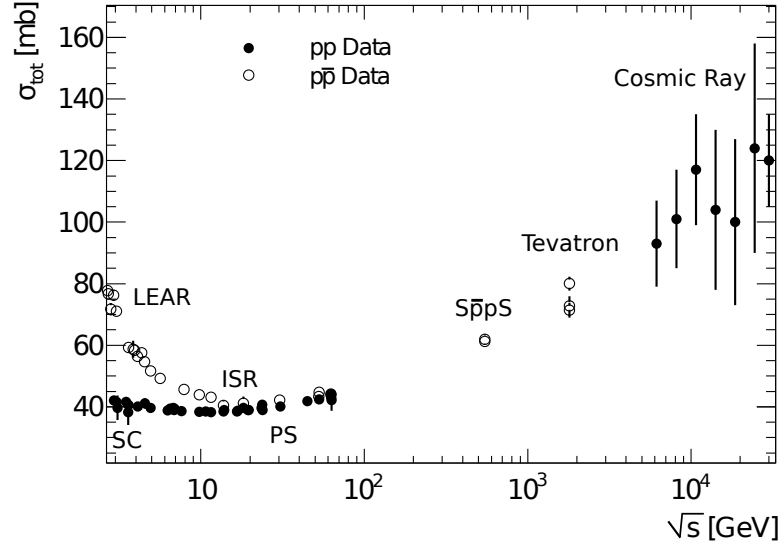
Figure 1.1. Proton-proton and proton-antiproton total cross-section as a function of $\sqrt{s}$. Data from [1]. The cosmic-ray measurements are of $\sigma_{\mathrm{p-air}}$ which is translated to σ_{pp} via Glauber theory.

E811 [3, 4] experiments[1].

Many of the collider-based data are obtained by measuring the forward elastic cross-section and using the optical theorem to obtain the total cross-section:

$$\sigma_{\mathrm{Tot}}^2 = \frac{16\pi}{1+\rho^2}\frac{1}{\mathcal{L}}\frac{\mathrm{d}N_{\mathrm{el}}}{\mathrm{d}t}\big|_{t=0} \tag{1.1}$$

where ρ is the ratio of the real to imaginary parts of the scattering amplitude, $\mathcal{L}$ is the luminosity and $\frac{\mathrm{d}N_{\mathrm{el}}}{\mathrm{d}t}\big|_{t=0}$ is the forward elastic scattering rate extrapolated to 0 momentum transfer. The optical theorem is discussed in detail in Appendix B. The CDF and E710/E811 experiments used a luminosity independent version of Equation 1.1 which required a measurement of the number of inelastic events as well as the elastic events. The difference in these two experiments has not been resolved.

The highest energy measurements in Figure 1.1 are from cosmic-ray experiments, which measure the proton-air cross-section, $\sigma_{\mathrm{p-air}}$, and use Glauber theory [5] to translate to $\sigma_{p-p}^{\mathrm{tot}}$ [6]. However, these extrapolations have large uncertainties and provide relatively little information on the high-energy behavior of the total cross-section. If both of the Tevatron measurements are considered, then the data on proton interactions are poor constraints on fits above $\sqrt{s} > 550$ GeV. Therefore, well-defined measurements of proton-proton interactions at the LHC will be important for testing models of hadronic scattering and of cosmic-ray air-showers.

---

[1]E811 was the successor to the E710 experiment. It used more sophisticated detectors and techniques.

The work in this thesis uses data collected with the ATLAS experiment on the second day of LHC collisions at a center-of-mass energy, $\sqrt{s}$, of 7 TeV to shed light on the subject. Simple, robust scintillator detectors, the Minimum Bias Trigger Scintillators (MBTS), are used to select inelastic interactions with high efficiency and minimal bias. The measurement is restricted to the acceptance of the scintillator detectors, which translates into a requirement on the invariant mass of the proton dissociation products, X, of $\frac{M_X^2}{s} > 5 \times 10^{-6}$ or equivalently, $M_X > 15.7$ GeV. Additionally, the dataset is used to constrain the relative contribution of diffractive processes for a variety of models. In order to compare with previous experiments and analytic predictions, the measurement is extrapolated to the full inelastic cross-section using Monte Carlo generators and analytic models. A summary of the results can be found in [7].

This thesis is structured as follows. First, a discussion of the theoretical and phenomenological underpinnings of proton-proton interactions is presented in Chapter 2. The inelastic cross-section measurement is outlined in Chapter 3. Descriptions of the LHC and the ATLAS experiment follow in Chapters 4 and 5, respectively. Chapter 6 explains the event reconstruction and Chapter 7 outlines the datasets and Monte Carlo simulation used in the analyses presented here. Chapter 8 details the detector performance and modeling relevant to this measurement. The backgrounds are presented in Chapter 9. Chapter 10 describes the determination of the luminosity via beam separation scans. Studies of the Monte Carlo modeling of diffractive event dynamics are presented in Chapter 11. Finally, the inelastic cross-section measurement is detailed in Chapter 12 and conclusions are drawn in Chapter 13.

CHAPTER 2

pp Interactions: Models and Monte Carlo Models

2.1 Overview and Historical Development

Proton-proton interactions play an important role in the narrative of modern particle physics. The first formulation of a theory of hadronic interactions was proposed by Yukawa in 1935 who suggested that the exchange of a 100 MeV particle, now called the pion, mediated the interactions between two hadrons [8]. A host of mesons and baryons were subsequently discovered, but the simple picture of exchange of these particles was unable to explain the existing experimental data on hadron-hadron interactions. In the late 1950s T. Regge solved the non-relativistic scattering equation and analytically continued the partial wave amplitudes of the solutions such that imaginary values of the angular momentum were possible [9]. The ensemble of the imaginary and real solutions to the equations were called a Regge trajectory. The real solutions described known mesons and baryons, and, once the imaginary solutions were included, the Regge trajectory could reproduce the dependence of the hadronic cross-section on the center-of-mass Mandelstam variable[1], s.

Yet, while Regge theory was adequate to explain the low energy scattering data, as the center-of-mass of experiments increased, it could not explain the dependence of the cross-section on higher s. In the 1960s, proton-proton scattering data showed the pp cross-section becoming constant. Motivated by these data, I. Pomeranchuk proved a theorem which, under certain assumptions, proved that the hadron-hadron and hadron-antihadron cross-sections would become asymptotically equal with increasing s [10]. This theorem necessitated the concept of the pomeranchukon or Pomeron, a Regge trajectory with the quantum numbers of the vacuum, which dominates scattering at high energies. A Regge description with a Pomeron trajectory was very successful at describing the experimental data on hadronic interactions. In particular, it was able to describe the *rise* of the cross-section at even higher s. Figure 1.1 shows the proton and antiproton cross-section measurements,

---

[1]The Mandelstam variables s, t, and u are described in Appendix A.

illustrating the rise of the cross-section as well as the equivalence of the proton-proton and proton-antiproton data at high $\sqrt{s}$.

In the late 1960s and early 1970s the theory of strong interactions entered a phase of rapid development with the introduction of the quark model and the formulation of QCD. QCD and quarks described well "hard interactions" in which there are large momentum transfers between the interacting particles. Preliminary attempts to integrate Regge theory and Pomeron trajectories into a QCD framework failed, and, while certain aspects of hadron scattering can be described by QCD, the theory is unable to explain many features of Regge phenomena, e.g. the dependence of the cross-section on s. The fundamental problem lies in the fact that strong coupling constant is large at low momentum transfer and consequently perturbation theory is not applicable.

Today, proton-proton interactions are understood to consist of three interaction types: *elastic* interactions in which no quantum numbers are exchanged between the initial and final state and there is no additional production of particles; *diffractive* events in which a Pomeron trajectory is exchanged and new particles are produced but no QCD color connection exists between the interacting protons, and *non-diffractive* (ND) events, the remainder of the inelastic interactions. Generally, the non-diffractive processes are described as interactions involving QCD color exhange. The diffractive interactions are subdivided into single- and double-diffractive dissociation (SD, DD) events in which one or both protons dissociate, respectively. These interactions are shown schematically in Figure 2.1. The events with Pomeron exchange typically are characterized by a large rapidity[2] gap between the proton systems due to the colorless exchange. In reality, this picture is a simplification of the rich and complex phenomena of hadron-hadron collisions, however it is a convenient description of the most salient features of the interactions.

This chapter takes a historical approach and begins by discussing Regge theory and Pomeron trajectories in Section 2.2. QCD and the parton model are reviewed in Section 2.3. Partonic descriptions of the Pomeron are described in Section 2.4. The chapter ends with a discussion of the current models of proton-proton interactions, starting with analytic models of cross-section in Section 2.5 and Monte Carlo models in Section 2.6.

2.2   Regge Theory and Pomeron Trajectories

Regge discovered that the non-relativistic scattering equation of a spherically-symmetric potential could be solved for non-integer, non-real values of angular momentum [9]. The singularities of the partial wave amplitudes of the solutions are a function of the Mandelstam variable for momentum transfer, t:

$$l = \alpha(t). \tag{2.1}$$

---

[2]The rapidity of a particle is defined as $\frac{1}{2}\ln\frac{E+|\mathbf{p}|c}{E-|\mathbf{p}|c}$, where E is the particle total energy and $|\mathbf{p}|$ is the magnitude of the four-momentum.
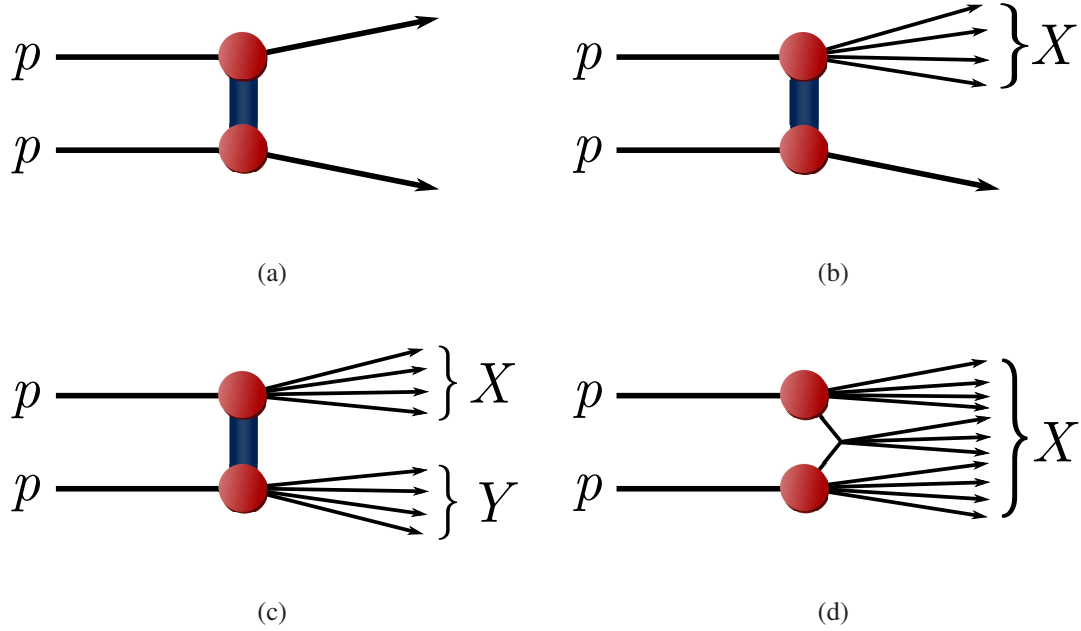
Figure 2.1. Sketches of proton-proton interaction types for elastic events (a), single-diffractive dissociation (b), double-diffractive dissociation (c), and non-diffractive dissociation (d). In these diagrams p indicates protons, the blue

Equation 2.1 defines the Regge trajectories. Each trajectory is associated with a family of particles with the same quantum numbers; the values of t for which $\alpha(t)$ is a non-negative integer correspond to the mass of physical particles. By including all of the known Regge trajectories, the scattering cross-section can be reproduced. The relation between l and t for particles with the same quantum numbers is given by

$$\alpha(t) = \alpha_0 + \alpha' t. \tag{2.2}$$

where α_0 is the Regge trajectory intercept and α' is the slope. Figure 2.2, a Chew-Frautschi plot, shows four Regge trajectories: that of the ρ, ω, f_2, and a_2 particles. The trajectories are degenerate, which did not necessarily have to happen.

As can be seen in the plot, the trajectory has a (nearly) universal slope and intercept, independent of the particle family from which it originates.

Each of the Regge trajectories contributes to the total cross-section with the following depedence on s:

$$\sigma^{ab}(s) \propto s^{\alpha(0)-1} \tag{2.3}$$

where σ^{ab} is the total interaction cross-section of particles a and b, and $\alpha(0)$ is the value of the Regge trajectory at $t = 0$. In Figure 2.2 $\alpha(0)$ is roughly 0.5, which indicates a cross-section decreasing with s. At $\sqrt{s}$ less than 10 GeV the observed total scattering
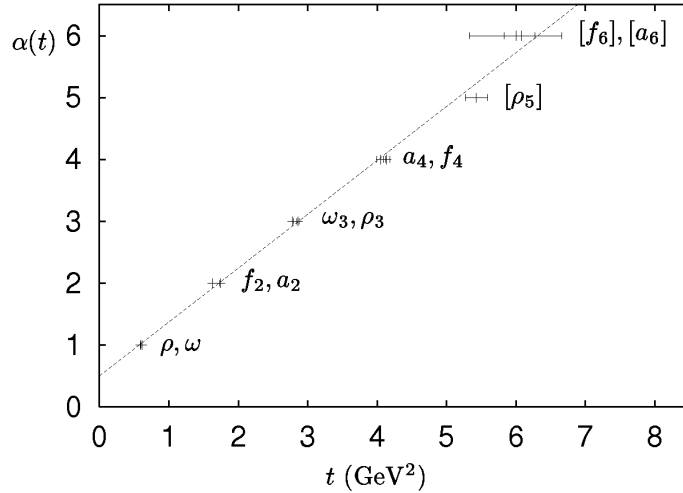
Figure 2.2. A Chew-Frautschi plot showing the relationship between mass and spin, or equivalently, the Regge trajectory for mesons. Reproduced with permission from [11].

cross-section for proton-proton and proton-antiproton interaction decreases with energy, as is predicted by the Regge trajectories. However, above 10 GeV the cross-section rises for both pp and $p\bar{p}$ scattering, as shown in Figure 1.1, which can not be accounted for by any known physical particles.

While Regge theory was developing, I. Pomeranchuk proved a theorem [10] stating that at sufficiently high center-of-mass energies, particle-particle interaction cross-sections become asymptotically equal to particle-antiparticle cross-sections. This statement was true under the assumptions that the cross-sections are asymptotically constant and that the ratio of the real to imaginary part of the forward scattering amplitude does not increase more rapidly than $\ln s$. Gribov introduced a Regge trajectory which assures this behavior [12]. This trajectory, which when summed is called the Pomeron, carries the quantum numbers of the vacuum and does not have any known particles corresponding to the integer spin values. In QCD terms, the Pomeron trajectory is thought to correspond to "glueballs", colorless multi-gluon objects [13]. Sections 2.4 and 2.5 further discuss attempts to reconcile Regge theory with QCD.

The addition of the Pomeron trajectory adds a term to the total cross-section formula:

$$\sigma^{ab}(s) \propto Y^{ab} s^{\eta} + X^{ab} s^{\epsilon}. \tag{2.4}$$

here $\eta = \alpha_{\mathbb{R}}(0) - 1$ refers to the Regge trajectory intercept corresponding to the ρ, ω, f_2, and a_2 particles and it is negative. The parameter $\epsilon = \alpha_{\mathbb{P}}(0) - 1$ refers to the Pomeron trajectory intercept and is positive. The coefficients ϵ and η are universal coefficients whereas Y^{ab} and X^{ab} depend on the interacting hadrons, a and b. The Pomeron trajectory is assumed

to behave the same as the ρ, ω, f_2, a_2 trajectory, therefore it is assumed that

$$\alpha_{\mathbb{P}}(t) = 1 + \epsilon + \alpha'_{\mathbb{P}}t. \tag{2.5}$$

Fits to existing data prefer values of

$$\eta = -0.45; \quad \epsilon = 0.081; \quad \alpha'_{\mathbb{P}} = 0.25 \text{ GeV}^{-2}. \tag{2.6}$$

The variable $\alpha'_{\mathbb{P}}$ is determined from fits [14] to small t data from the (ISR). Data from small t elastic scattering of pp (ISR) and $p\bar{p}$ (Tevatron) are shown in Figure 2.3 [15, 16]. The variables ϵ and η are determined from global fits to existing cross-section data [17, 18, 19].
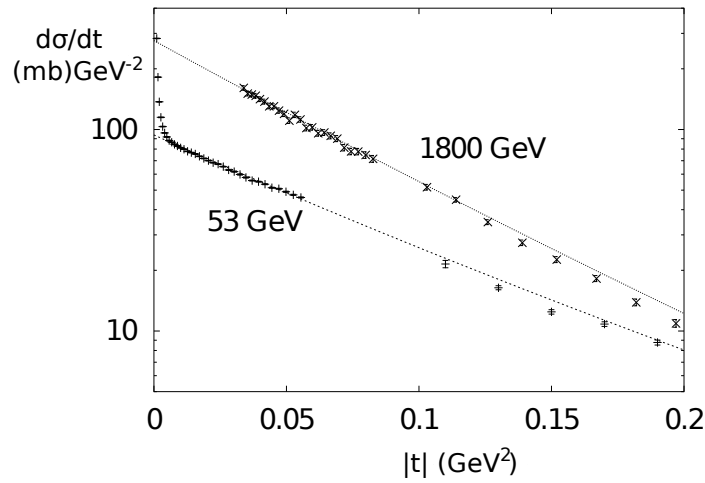
Figure 2.3. Elastic scattering data from pp 53 GeV [15] and $p\bar{p}$ 1800 GeV[16] with fits corresponding to $\alpha'_{\mathbb{P}} = 0.25 \text{ GeV}^{-2}$. Reproduced with permission from [11].

Equation 2.4 violates one of the few analytic constraints on hadron-hadron interactions: the Froissart-Martin bound [20, 21]. In 1961 Marcel Froissart proved, using general constraints of unitarity and analyticty[3], that the total cross-section could not rise faster than

$$\sigma^{tot}(s) \leq \ln^2\left(\frac{s}{s_0}\right). \tag{2.7}$$

where s_0 is some unknown scale. The theorem can be understood intuitively when considering the fact that the interaction cross-section of two particles is negligible beyond a certain impact parameter due to the time-energy uncertainty relation. Froissart showed that the impact parameter is determined by the natural log of the center-of-mass energy. The scattering cross-section cannot rise faster than the impact parameter squared, i.e. the cross-sectional area, and therefore the cross-section is bounded by $\ln^2(s)$.

Further discussion of cross-section models which modify the basic Regge theory to obey the Froissart bound are discussed in Section 2.5.

---

[3]Unitarity states the probabilities cannot exceed one, and analyticity means that functions cannot have discontinuous jumps in their values.

2.3   QCD and the Parton Model

While Regge theory developed as a viable model for hadronic interactions, a new theory pioneered by Gell-Mann and Zweig [22, 23] proposed an organizing principle for the multitudes of recently discovered hadrons. It began with Gell-Mann's eightfold way [22] which used the symmetry group SU(3)[4] to describe the masses and decays of the known hadrons. The success of the SU(3) description led Gell-Mann and Zweig to propose that hadrons were comprised of three fractionally charged fundamental particles, dubbed *quarks* by Gell-Mann. In symmetry group terms, these quarks form the *fundamental representation* of the SU(3) group. Today these particles are known as u, d and s quarks and the symmetry described by this approximate SU(3) theory is known as a "flavor symmetry" and is valid in the limit of equal mass quarks.

Flavor SU(3) was challenged, however, by the discovery of the Δ^{++} baryon, which had spin $+\frac{3}{2}$ and consisted solely of u quarks. Because quarks were believed to be spin $\frac{1}{2}$ fermions they could not simultaneously be in the same state as would be necessary to produce a $+\frac{3}{2}$ particle. To solve this violation of the Pauli exclusion principle, Han, Nambu and Greenberg proposed [24, 25] that the quarks had an additional SU(3) degree freedom, which is now called color. All quarks carried color charge and the hadrons were composed of combinations of which made the hadrons color singlets. The quark model had one problem: no quarks had ever been isolated in the laboratory and fractionally charged particles had never been observed. Therefore many, including Gell-Mann, believed quarks were only an abstract way of understanding nature.

Simultaneously, Feynman created the *parton model*, in which hadrons were composed to quasi-free point-like particles he called *partons* [26]. He developed the theory in response to results from the deep inelastic scattering experiments at the Stanford Linear Accelerator (SLAC), in which 20 GeV electron beams were scattered off of liquid hydrogen and liquid deuterium targets. These experiments were conceptually similar to the Rutherford scattering experiment in which the structure of the atom was determined. A Feynman diagram of the electron-proton interaction is shown in Figure 2.4. The electron emits a photon[5] with momentum four-vector q, which interacts with a parton carrying momentum fraction, x_p, of the proton. Measurements of the outgoing electron momentum translate into measurements of the charge distribution and in the proton, called structure functions. Higher order corrections give information about the gluon content of the proton.

At the same time as Feyman was developing the parton model, Bjorken postulated that the structure functionsmeasured in inelastic scattering depended only on the dimensionless ratio of the four-momentum transfer, q^2, to the electron energy loss [27]. This behavior, now called Bjorken scaling, is a consequence of a parton-like model, where the probe particle, in this case an electron, acts incoherently on the proton constituents. A more detailed discussion of deep-inelastic scattering experiments is given in Section 2.4. These

---

[4]SU(3) is the group of 3×3 matrices with unit determinant.

[5]More generally, it emits an electroweak boson.

measurements determined the *parton distribution functions* or PDFs which describe the momentum faction of the proton carried by its constituent quarks and gluons.
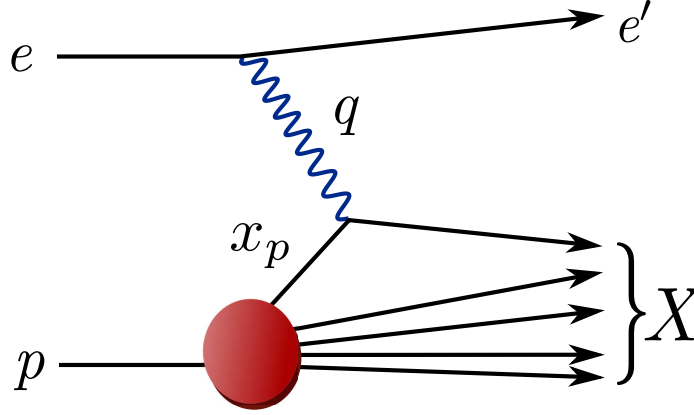
Figure 2.4. Feynman diagram of deep inelastic scattering. The electron interacts with a valence quark via a boson with four-vector q. The quark has a momentum fraction x_p of the proton and by measuring the scattered electron, x_p can be determined.

Once Gross, Wilczek and Polizter [28, 29] showed that SU(3) leads to asymptotically free gauge theories, i.e. the interactions between constituents becomes arbitrarily weak for asymptotically large energies, SU(3) QCD became a viable and accepted theory of strong interactions. In particular, asymptotic freedom allowed perturbation theory to be used in the calculation of QCD processes, and lead to the factorization theorem which states that the partonic scattering cross-section can be factorized from the PDFs [30, 31]. With factorization, cross-sections can be calculated via:

$$\sigma(P_1, P_2 \to X) = \sum_{i,j} \int \mathrm{d}x_1 \mathrm{d}x_2 f_i(x_1, Q^2) f_j(x_2, Q^2) \hat{\sigma}(i, j \to X; x_1 P_1, x_2 P_2, Q^2) \quad (2.8)$$

where $f_{i,j}$ are the parton distribution functions for partons i and j, x_1 and x_2 are the momentum fractions of parton i and j in proton 1 and 2, respectively, $\hat{\sigma}$ is the partonic cross-section for X to be produced and Q^2 is the momentum scale of the hard partonic interaction. Factorization is not explicitly proven for all cross-sections, but it is currently one of the most powerful tools for calculating cross-sections involving hadrons.

Asymptotic freedom and factorization are useful only in the large momentum transfer limit. They do not provide calculational tools for low momentum transfer hadron-hadron interactions. In fact, the opposite regime of arbitrarily low energy interactions gives rise to the phenomena of quark confinement. Because QCD interactions become arbitrarily strong at low energies, quarks and gluons cannot be observed individually, which is the principle of confinement. This statement is not rigorously proven but it is generally accepted.

In Equation 2.8, both the PDFs and $\hat{\sigma}$ depend on the QCD coupling constant, α_s. The statement that QCD interactions become strong or weak is another way of saying that α_s

becomes large or small. The coupling depends on the momentum transfer of the interaction, Q^2, by the following expression at leading order in perturbation theory:

$$\alpha_s(Q^2) = \frac{12\pi}{(33 - 2n_f)\ln\left(Q^2/\Lambda_{\text{QCD}}^2\right)} \tag{2.9}$$

where n_f is the number of quark flavors with masses less than Q^2, and Λ_{QCD} is extracted from fits to measurements of α_s. The scale Λ_{QCD} is considered to be the scale at which QCD is non-perturbative. It is roughly 200 MeV, the same scale as the pion mass or hadron size. For the majority of hadron-hadron scattering processes, Q^2 in Equation 2.8 is the momentum transfer between the protons. It is roughly Λ_{QCD} and, consequently, $\alpha_s \sim 1$. When the expansion parameter, in this case α_s, is $\gtrsim 1$, perturbation theory is not applicable. Because of these difficulties, QCD is unable to supply predictions for hadron-hadron cross-sections.

2.4 Partonic Descriptions of the Pomeron

Since QCD was established as the theory of strong interactions, attempts have been made to describe the Pomeron and Regge trajectory in terms of partons. The Pomeron trajectory has no known associated particles, unlike the Regge trajectory of the ρ, ω, f_2, and a_2. However, it can be described most simply as a two-gluon exchange process [32, 33, 34], with higher order corrections arising as a ladder of gluon exchange, as shown in Figure 2.5. Calculation of the Pomeron intercept, $\alpha(0)$, in this model [35] leads to a value of 1.0 which is in reasonable agreement with the measured value of 1.08.

(a)   (b)
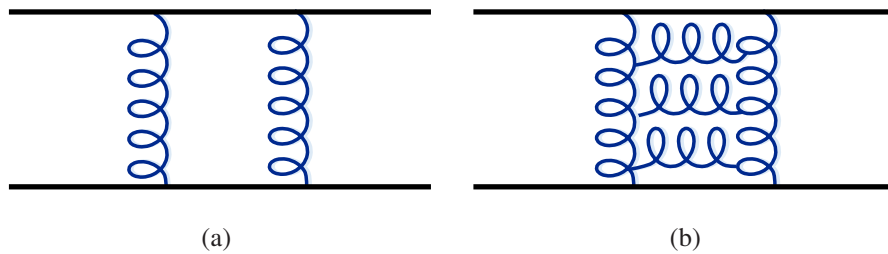
Figure 2.5. Feynman of two-gluon exchange between partons at leading order (a) and with a ladder of higher order gluon interactions (b).

High center-of-mass energy deep inelastic scattering experiments offer the opportunity to directly probe the partonic description of the Pomeron. The HERA collider at the DESY laboratory in Hamburg, Germany collides electrons and protons at a center of mass energy of 318 GeV with the primary goal of precise measurements of the proton DPFs. At the HERA experiments H1 and Zeus, events of the form $p + e \to e + X + p$ as well as $p + e \to$

$e + X + Y$ with a large rapidity gap between X and Y, were observed [36, 37, 38]. Both the intact proton and large rapidity gap are hallmarks of a diffractive interaction because both signal the exchange of a color-less object. These events were selected and analyzed to determine the *diffractive parton distribution functions* (DPDF).

Figure 2.6 shows an illustration of the $p + e \rightarrow e + X + p$, highlighting different factorization schemes. Figure 2.6(a) shows a case where the diagram can be factorized based on a hard scattering QCD collinear factorization theorem [39, 40]. This theorem states that for a fixed final state proton momentum the DPDF can be obtained. In this case the DPDF is dependent on the distribution of Pomerons in the proton, termed the *Pomeron flux*, and the momentum transfer in the interaction. The Figure shows the momentum transfer q of the probe particle, which interacts with a parton from a Pomeron with momentum fraction $x_{\mathbb{P}}$ of the proton with a Pomeron flux, $f_{\mathbb{P}/p}$. In this case the DPDF describing the probability to find a parton with momentum fraction x_p in the Pomeron is dependent on the Pomeron momentum fraction of the proton, $x_{\mathbb{P}}$. Figure 2.6(b) shows further factorization, which has been determined empirically, where the proton vertex factorizes as well. When this occurs, which the existing data suggest is applicable for low fractional proton losses, the shape of the DPDF is independent of the proton four-momentum. In other words, $x_{\mathbb{P}}$ is independent of p and x_p is independent of $x_{\mathbb{P}}$. In this regime diffraction can be described by the exchange of a Pomeron "parton" with universal parton densities [41]. The dependence of these DPDFs on x and q^2 can be determined using perturbative QCD as in the case of standard PDFs.
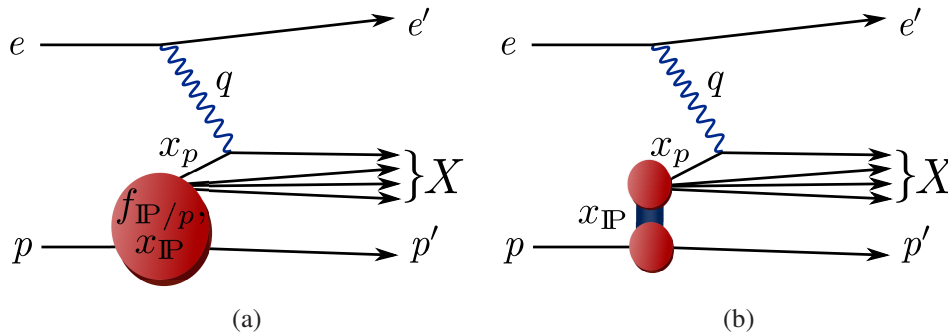
Figure 2.6. Illustration of $p + e \rightarrow e + X + p$. (a) shows the the point of QCD collinear factorization and (b) shows proton-vertex factorization.

The DPDFs determined at HERA fail badly at describing the Tevatron data on diffractive events [42], which would indicate their non-universality. However, reasonable agreement is achieved once multiple parton interactions are taken into account via a 'rapidity gap survival probability', i.e. the probability that the rapidity gap in the diffractive interaction is not spoiled by the non-diffractive interactions of other partons [42]. Due to the necessity of adding a rapidity gap survival probability, the DPDFs cannot be used to predict the hadron-

hadron cross-sections, however, they are useful in describing multi-particle production in diffractive events, as discussed in Section 2.6.

2.5 Analytic Cross-Section Models

2.5.1 Total Cross-Sections

The simplest model of the total cross-section is given by Equation 2.4, which includes a Regge and Pomeron contribution. However, as mentioned in Section 2.2, this equation violates the Froissart bound. Data from elastic scattering and total cross-section measurements can be fit well by the following function [1]

$$\sigma^{ab} = Z^{ab} + B \log^2(s/s_0) + Y_1^{ab}(s_1/s)^{\eta_1} - Y_2^{ab}(s_1/s)^{\eta_2} \tag{2.10}$$

where Z^{ab}, B, s_0, Y_1^{ab}, s_1, η_1, Y_2^{ab}, and η_2 are all parameters in the fit. The particles a and b are protons, photons, neutrons, pions, and kaons. Equation 2.10 is the **standard parametrization**. These terms are well-motivated, with $Z^{ab} + B \log^2(s/s_0)$ deriving from double and triple Pomeron exchange, and $Y_1^{ab}(s_1/s)^{\eta_1} - Y_2^{ab}(s_1/s)^{\eta_2}$ arising from the exchange of the a, ω, f, and a Regge trajectories. Equation 2.10 has the added benefit of explicitly obeying the Froissart bound. However, the equation has many free parameters, including several unknown scales (s_0, s_1), therefore it is useful to consider simpler models.

Donnachie and Landshoff argue [43] that Equation 2.4 with the interpretation of ϵ and η as effective values gives a reasonable and simple prediction for the dependence of the cross-section on s. They fit the pp and $p\bar{p}$ in the region $\sqrt{s} > 10$ GeV to 1.8 TeV and obtain

$$\sigma^{p\bar{p}} = 21.70s^{0.0808} + 98.39s^{-0.4525} \tag{2.11}$$
$$\sigma^{pp} = 21.70s^{0.0808} + 56.08s^{-0.4525} \tag{2.12}$$

The Pomeron term, $21.70s^{0.0808}$ is universal, while the a, ω, f, and a exchange term constant depends upon the initial state particles. The significant digits reflect the precision of the fits. They note this fit is dominated by the measurements at $\sqrt{s} < 100$ GeV therefore it is a success of the parametrization to fit the higher s data. The value of ϵ that they obtain does not correspond to a simple, single Pomeron pole. It is an effective intercept incorporating the effects of multiple Pomeron exchange.

The most common model for multiple Pomeron exchange uses the so-called *eikonal* representation[6]. The assumption is made that there are multiple Pomeron trajectories exchanged leading to a combined intercept of

$$\alpha_c(t) = \alpha_c(0) + \alpha_c' t. \tag{2.13}$$

---

[6]The following discussion follows [11].

In the case of two exchanges $\alpha_c(0)$ and α'_c are given by

$$\alpha_c(0) = \alpha_1(0) + \alpha_2(0) - 1 \tag{2.14}$$

$$\alpha'_c = \frac{\alpha'_1 \alpha'_2}{\alpha'_1 + \alpha'_2}. \tag{2.15}$$

This $\alpha_c(t)$ corresponds to a partial wave amplitude, A, of the solution of the Yukawa potential, which can be expressed in terms of the impact parameter $\mathbf{b}$ and s. This is the *eikonal representation*. The amplitude is then expressed as a Fourier transform back to momentum transfer space, and expanded in a Taylor series

$$A(s, -\mathbf{q}^2) = 2is \int d^2b \, e^{-i\mathbf{q} \cdot \mathbf{b}} \left(\chi - \frac{\chi^2}{2!} + \frac{\chi^3}{3!} \cdots - \frac{\chi^n}{n!} \cdots \right) \tag{2.16}$$

where the nth χ term corresponds to n Pomeron exchanges. Then, with a guess on the form of χ, or the *eikonal*, motivated by the exact expression for single Pomeron exchange, the optical theorem can be used to relate A at $t = 0$, the forward scattering cross-section, to σ^{tot}:

$$\sigma^{\text{tot}} \propto \log^2(s/s_0). \tag{2.17}$$

Donnachie and Landshoff argue [43] that the effect of the multiple Pomeron exchanges is weak because

- The same power of ϵ fits all available hadron-hadron and hadron-antihadron cross-sections.

- A single Pomeron contribution satisfies the *additive quark rule* [44] which states that

$$X^{ab} \propto n_a n_b \tag{2.18}$$

  where n_a and n_b are the number of valence quarks in a and b, respectively. It is observed that $X^{\pi p} : X^{pp} \approx 2 : 3$.

There are several additional models to mention:

- **Engel**: This model is implemented in the PHOJET Monte Carlo [45, 46], discussed in more detail in Section 2.6. It is based on the Dual Parton Model (see [47] for a review) which employs topological expansion to calculate interaction cross-sections [48]. Topological expansion tackles the non-perturbative nature of QCD by taking the large N limit, where N refers to either the number of colors or quark flavors in the theory, and using $1/N$ as the expansion parameter. The resulting diagrams are associated with various topologies (plane, cylinder, torus, etc.) which correspond directly to diagrams used in Reggeon Field Theory (RFT) [49]. Using RFT, the cross-sections for collisions of Pomerons with hadrons and Pomerons with Pomerons can be calculated. This description is valid in the regime where s is large compared to t. To
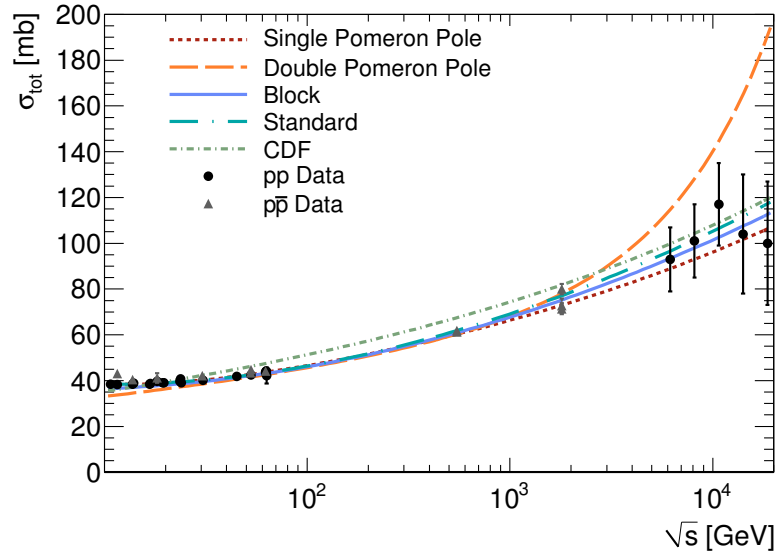
Figure 2.7. Proton-proton and proton-antiproton total cross-section as a function of $\sqrt{s}$ and fits. Single Pomeron Pole refers to the standard Donnachie and Landshoff parametrization, Double Pomeron Pole refers to the Donnachie and Landshoff model with the addition of a hard Pomeron. The Standard parametrization uses a multiPomeron exchange approach. The Block and CDF parametrization are explained in the text. Data from [1].

explain the rising cross-section and kinematic distributions, PHOJET uses an eikonalized hard and soft Pomeron with an explicit p_T cutoff between the two of approximately 3 GeV [50]. This description, with the explicit addition of Pomeron loops and triple Pomeron exchanges, automatically leads to a cross-section which obeys the Froissart bound.

- **Khoze, Martin and Ryskin**: This model [51] uses perturbative QCD in the high parton transverse momentum, k_t, region. BKFL [52, 53] evolution is used to evolve the parton densities, which orders the partons in terms of $\log \frac{1}{x}$ where x is Bjorken x. The BKFL approach gives a candidate for a Pomeron in terms of multiple gluon exchange. The model is then extended to the low k_T region where multiple Pomeron interactions are included using RFT. In this approach, the hard Pomeron contribution can be smoothly matched to the soft Pomeron contribution.

- **Block**: In [54] two models are used to fit existing total cross-sections which yield comparable results. The first is an eikonal fit inspired by QCD. In this model, the dominant eikonal term is given by a factorized eikonal

$$
\begin{aligned}
\chi(s,b) &= \xi_{qq}(s,b) + \xi_{qg}(s,b) + \xi_{gg}(s,b) & (2.19) \\
&= i[\sigma_{qq}(s)W(b;\mu_{qq}) + \sigma_{qg}(s)W(b;\sqrt{\mu_{qq}\mu_{gg}}) \\
&\quad + \sigma_{gg}(s)W(b;\mu_{gg})] & (2.20)
\end{aligned}
$$

where $\sigma_{ij}(s)$ are the partonic cross-sections for ij and $W(b; \mu_{ij})$ is the dipole form factor of the proton.

The second fit model uses real analytic amplitudes which require that the amplitudes used to calculate high-energy scattering cross-section are real functions which map smoothly onto low-energy amplitudes. This is a classic, model independent method [55]. It results in a cross-section of

$$\sigma_{pp} = B_1 + C_1 E^{-\nu_1} + B_2 ln^\gamma s - C_2 E^{-\nu_2} \tag{2.21}$$

where $B_{1(2)}$, $C_{1(2)}$, $\nu_{1(2)}$ and γ are fit parameters. The fits parameters are fixed by low-energy scattering data.

- **CDF parametrization**: This expression [56] is a refit of the simple single-Pomeron pole, using only the CDF measurement at 1.8 TeV and excluding the E710 measurement.

$$\sigma_{tot} = 24.36 \text{ mb} \cdot \left(\frac{s}{\text{GeV}^2}\right)^\epsilon$$

with $\epsilon = \alpha(0) - 1 = 0.0808$. This yields a cross section of $\sigma_{tot}(7 \text{ TeV}) = 101.9$ mb.

- **Donnachie and Landshoff Double Pomeron**: Donnachine and Landshoff revisited the possibility of a hard Pomeron after analyzing the HERA diffractive deep inelastic scattering data [57]. Their new parametrization [58], which gives similar results to the simple single pole, parametrizes the cross-section using both a soft and a hard Pomeron

$$\sigma_{tot} = 24.22 \text{ mb} \cdot \left(\frac{s}{\text{GeV}^2}\right)^{0.0667} + 0.0139 \text{ mb} \cdot \left(\frac{s}{\text{GeV}^2}\right)^{0.452}$$

This formulation yields a cross section of $\sigma_{tot}(7 \text{ TeV}) = 120.5$ mb. Although this model has two Pomeron poles, it does not account for multiple-Pomeron interactions.

Figure 2.7 shows a subset of the predictions compared with the existing total cross-section data. Most of the predictions only vary by 10% at LHC energies, however the Double Pomeron diverges with respect to the other models at high energy. It is inconsistent with the cosmic-ray data, but these data are model-dependent and have large errors so they are not used in the fit.

2.5.2 Inelastic and Diffractive Cross-sections

Most predictions of the inelastic cross-section from analytic models are obtained by applying the optical theorem to the total cross-section prediction to obtain the elastic cross-section and then calculating

$$\sigma_{\text{inel}} = \sigma_{\text{tot}} - \sigma_{\text{el}}. \tag{2.22}$$

Applying the optical theorem to the single Regge pole model yields the following elastic differential cross-section

$$\frac{\mathrm{d}\sigma^{el}}{\mathrm{d}t}(pp \to pp) = \frac{\sigma_{tot}^2(pp)}{16\pi} e^{2(b_0^{el} + \alpha'_{\mathbb{P}} \ln s)t}. \tag{2.23}$$

Using Mueller's generalization of the optical theorem [59], the single-diffractive dissociation cross-section can also be derived from the elastic cross-section

$$\frac{\mathrm{d}^2\sigma^{SD}}{\mathrm{d}t\mathrm{d}M^2}(pp \to Xp) \propto \frac{1}{M_X^2} \left(\frac{s}{M_X^2}\right)^{2(\alpha_{\mathbb{P}(0)}-1)} e^{2(b_0^{SD} + \alpha'_{\mathbb{P}} \ln \frac{s}{M^2})t} \tag{2.24}$$

where b_0^{SD} is the slope parameter describing the t-dependence of the cross-section and M is the invariant mass of the products of the dissociated proton, or *diffractive mass*. This equation is the standard Donnachie and Landshoff formulation of the differential diffractive cross-section and is the baseline for which most other models are compared to.

In the following the main features of the analytic models for the inelastic cross-section predictions used in this thesis are briefly described. Some models are used for their predictions of the inelastic cross-section, others for the differential diffractive event cross-section and some for both. The existing data and several of the models are shown in Figure 2.8.
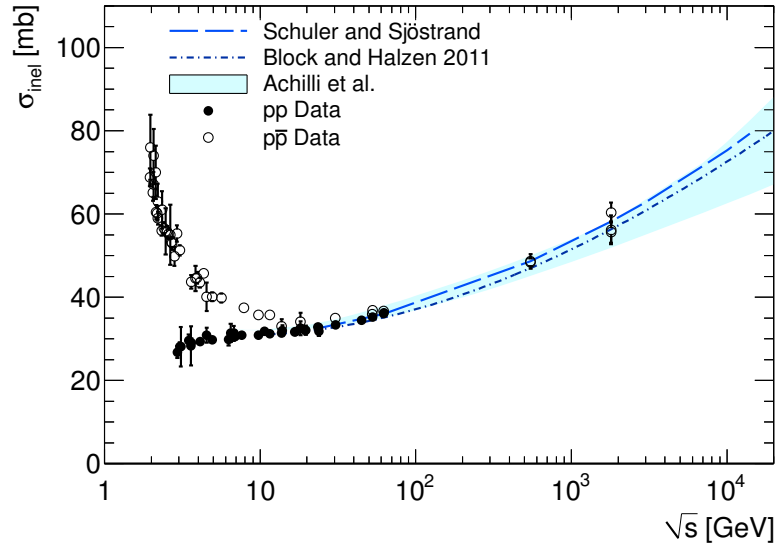
Figure 2.8. Proton-proton and proton-antiproton inelastic cross-section as a function of $\sqrt{s}$ and fits. Data from [1].

- **Schuler-Sjöstrand**: This model [60] directly uses Equation 2.4 as the total cross-section. The elastic cross-section is derived using the optical theorem. It begins with

Equation 2.24 but notes that it is only valid in a limited parameter space: $M_X^2 - m_p^2 < 0.15s$, where m_p is the mass of the proton. It is also limited to small values of t. In order to obtain a prediction of all t and M_X it introduces "fudge factors" to suppress production near the kinematic limits listed above. It also modifies the slope parameter for double-diffractive dissociation to keep it from becoming too small. In this approach the asymptotic behaviors of the diffractive cross-sections have the following energy dependence

$$\sigma_{SD} \quad \propto \quad \ln{(\ln s)} \qquad (2.25)$$
$$\sigma_{DD} \quad \propto \quad \ln s(\ln{(\ln s)}) \qquad (2.26)$$

- **Khoze, Martin and Ryskin**: The details of the total cross-section predictions for this model [51] are discussed in the previous subsection. The inelastic cross-section is obtained by the optical theorem. The differential diffractive cross-sections are calculated explicitly. In the intermediate diffractive mass range, the diffractive cross-section is similar to a standard Donnachie and Landshoff approach like in Equation 2.24. There is a suppression at low diffractive mass from the absorption of soft-k_t partons, which decreases the probability of dissociation. At high mass there is an increase of high-k_t partons, leading to an increase in the cross-section. This model is used for inelastic cross-section predictions.

- **Achilli** *et. al.*: This model [61] provides an explicit calculation of the inelastic cross-section. It is calculated on the assumption that hadron-hadron scattering arises from independently-distributed multiple-parton interactions. The inelastic cross-section is then dependent on the average number of collisions, $\bar{n}(b, s)$, which is calculated in an eikonalized model as a function of the impact parameter b and s. $\bar{n}$ is divided into a hard and soft component where the hard component is calculated in perturbative QCD, giving rise to *mini-jets*. The soft component is modeled in two different frameworks; one Regge-inspired, the other based on soft gluon k_t resummation. There is no separate differential diffractive event cross-section.

- **Berger and Streng**: This model [62, 63] is only used to give a prediction for the differential diffractive mass distribution. It uses a power law dependence of the cross-section on the diffractive mass, similar to the Donnachie and Landshoff model, with $\alpha(0) > 1$. Unlike the Donnachie and Landshoff model, the t-dependence of the differential cross-section is an exponential depending on M_X.

- **Bruni and Ingleman**: This model [64] is only used for a prediction of the differential diffractive mass spectra. It predicts a Pomeron with $\alpha(0) = 1$, leading to a strictly flat dependence of the cross-section on M_X^2, i.e. $\frac{d\sigma_{SD}}{dM_X^2} = \text{const.}$. The t-dependence of the cross-section is the sum of two exponential functions.

In this thesis the dimensionless unit $\xi = \frac{M_X^2}{s}$ is used to describe the differential diffractive cross-section. In the case of double-diffraction, ξ refers to the larger mass dissociation

system. Figure 2.9 shows the ξ distributions[7], normalized to unit area, for SD and DD events as predicted by the models listed above which have differential diffractive cross-sections. In addition, there are four variations of ϵ and α' in the Donnachie and Landshoff models. Although ϵ and α' are relatively well constrained by previous cross-section measurements, the large uncertainty in the diffractive event dynamics justifies varying them for the purposes of the acceptance calculations. Figures 2.9(a) and 2.9(b) show that the Engel and Schuler-Sjöstrand models predict higher average diffractive mass than the other models. The power-law based models with $\alpha(0) > 1$ are strongly peaked towards low diffractive mass. Figures 2.9(c) and 2.9(d) show that the variations in ϵ and α' have relatively little effect on the diffractive mass spectra relative to the variations with the other models.

2.6   Monte Carlo Models

By necessity, Monte Carlo models divide inelastic proton-proton interactions into three or four categories: non-diffractive events and two or three types of diffractive events. These classifications allow the generators to give predictions of exclusive quantities such as the final state particle multiplicities and momenta. The analysis presented in this thesis is sensitive to the dynamics of diffractive events, therefore predictions of the final state properties of these events is necessary.

Two Monte Carlo generators are used: PYTHIA and PHOJET [45, 46]. Additionally, two different versions of PYTHIA, 6.421 [65] and 8.135 [66], are considered. They use the same Schuler-Sjöstrand cross-section model for the diffractive processes, but differ in the fragmentation once a value of $M_{X(Y)}^2$ and t are chosen. The cross-sections implemented in PYTHIA and PHOJET for the individual processes are given in Table 2.1. It can be seen that there are significant differences in the diffractive contributions. PHOJET additionally includes central diffractive (CD) events where the protons do not dissociate but a central system of particles is created by the Pomeron interactions.

The PYTHIA generator models non-diffractive pp interactions by first calculating a partonic cross-section at leading order (2→2) in perturbation theory. The parton momentum are picked using the proton PDFs, as indicated in Equation 2.8. Then it uses parton showers to evolve the final state partons from the scale used in the partonic cross-section calculation to a low scale cut-off. The evolution models the radiation of gluons ($q \rightarrow qg$) and gluon splitting ($g \rightarrow gg$, $g \rightarrow q\bar{q}$) in the soft and collinear emission regime. This emission is also modeled in the initial state via the parton PDFs. Once the emission reaches the cut-off scale, which is a tunable parameter in the Monte Carlo generator, phenomenological models are used to form the partons into color singlet hadrons. PYTHIA uses the *Lund*

---

[7]For technical reasons, which are described in more detail in Chapter 3, the ξ values plotted in Figure 2.9 are calculated from the final state particles produced by a Monte Carlo model. The particle production for different Monte Carlo generators is discussed in detail in Section 2.6, but differences in the modeling of the particle production have little effect on the resulting ξ distributions.
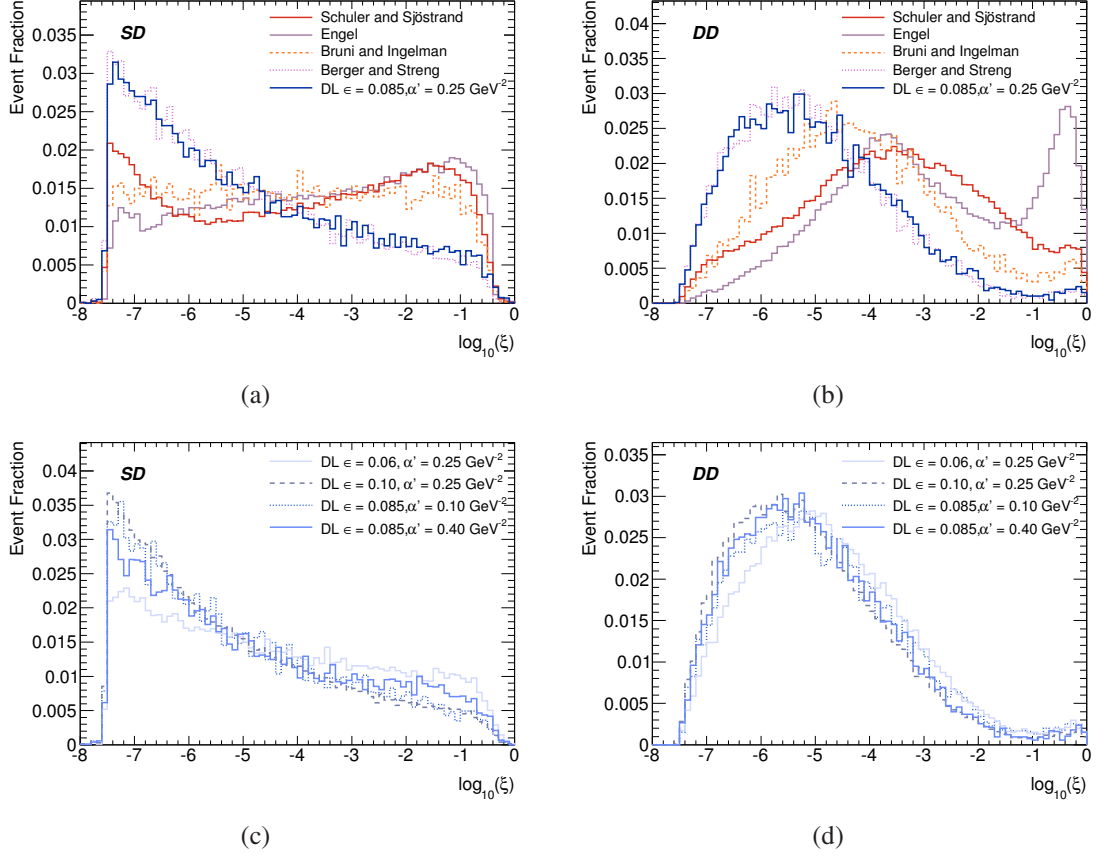
Figure 2.9. ξ distribution for SD (left) and DD (right) events at $\sqrt{s} = 7$ TeV comparing different ξ spectra as described in the text. (a) and (b) compare the distributions for the basic models used to assess the dependence of the cross-section of diffractive mass. (a) and (b) show variations of the Donnachie and Landshoff model when varying ϵ and α'.

string model [67], in which color flux tubes are stretched between quark and anti-quark pairs and are broken by the formation of a new $q\bar{q}$ pair; if the energy of the system is low enough mesons are formed, otherwise new flux tubes are stretched between the $q(\bar{q})$ from the old pair and the $\bar{q}(q)$ of the new pair. Diquarks and anti-diquark pairs can also be produced to form baryons. Once all of the partons have been combined into color singlets, fragmentation is finished.

PYTHIA uses QCD $2 \rightarrow 2$ processes to model non-diffractive interactions for both PYTHIA 8 and PYTHIA 6. The two generators differ in some of the treatment of the color connection between the initial and final states and in the tuning of the modeling parameters. For diffractive processes, fragmentation for a particular value of M and t are very different between the two.

- PYTHIA 6 only allows for "soft", i.e. non-perturbative, fragmentation of diffractive

Process	cross-section (mb)	
	PYTHIA	PHOJET
non-diffractive	48.5	61.6
single-diffractive dissociation	13.7	10.7
double-diffractive dissociation	9.3	3.9
central-diffractive dissociation	-	1.1
inelastic	71.5	77.3
	fractional contribution (%)	
f_D	32.2	20.3
f_{SD}	59.6	68.2

Table 2.1. Cross sections, f_D and f_{SD} values for PYTHIA and for PHOJET for $\sqrt{s} = 7$ TeV.

events. If the mass of the diffractive system is less than 1 GeV then it decays isotropically to a two-body system. If the mass is greater than 1 GeV, a valence quark or gluon is extracted from the proton. If a quark is extracted, a string is stretched between the quark and the remnant diquark. If a gluon is chosen, a string is stretched from the quark to the gluon and back to a diquark. The ratio of these two processes is a free parameter. In both cases, the string fragmentation proceeds as described above.

- PYTHIA 8 allows for both "soft" processes and "hard" perturbative process [68] in diffractive events. For diffractive masses less than 10 GeV the same string fragmentation is used as in PYTHIA 6. The probability for a perturbative description as a function of the diffractive mass M is given by

$$P_{\text{pert}} = 1 - \exp[(M - m_{\text{min}})/m_{\text{width}}] \qquad (2.27)$$

where m_{min} and m_{width} are free parameters. An *anzatz* for a leading order Pomeron DPDF set is used. The HERA DPDFs are not used because they are next-to-leading order which is inconsistent with the leading order PYTHIA calculations. The differential cross-section is given by

$$\frac{d\sigma(pp \rightarrow p + X)}{dx_{\mathbb{P}} dx_1 dx_2 d\hat{t}} = f_{\mathbb{P}/p}(x_{\mathbb{P}}, Q^2) \frac{d\sigma(p\mathbb{P} \rightarrow X)}{dx_1 dx_2 d\hat{t}} \qquad (2.28)$$

where $x_{\mathbb{P}}$ is the momentum fraction of the parton relative to the proton it interacted with

$$x_{\mathbb{P}} = \frac{E_{\text{Pom}}}{E_p}. \qquad (2.29)$$

$f_{\mathbb{P}/p}(x_{\mathbb{P}}, Q^2)$ is the Pomeron flux, essentially the probability for a proton to emit a Pomeron. $\frac{d\sigma(p\mathbb{P} \rightarrow X)}{dx_1 dx_2 d\hat{t}}$ is the Pomeron-proton differential cross-section and it is given by

$$\frac{d\sigma(p\mathbb{P} \rightarrow X)}{dx_1 dx_2 d\hat{t}} = f_{p_1/p}(x_1, Q^2) f_{p_1/\mathbb{P}}(x_2, Q^2) \frac{d\hat{\sigma}}{d\hat{t}} \qquad (2.30)$$

where $f_{p_1/p(\mathbb{P})}(x_{1(2)}, Q^2)$ is the proton (Pomeron) PDF for parton 1(2), with momentum fraction $x_{1(2)}$ of the proton (Pomeron) and $\frac{d\hat{\sigma}}{d\hat{t}}$ is the partonic cross-section for the two extracted partons. Figure 2.10 illustrates these quantities. In order to normalize the Pomeron flux, an effective Pomeron-proton cross-section, $\sigma_{\mathbb{P}p}$ is needed. It is a tunable parameter in the event generation which controls the number of multiple interactions in the event.
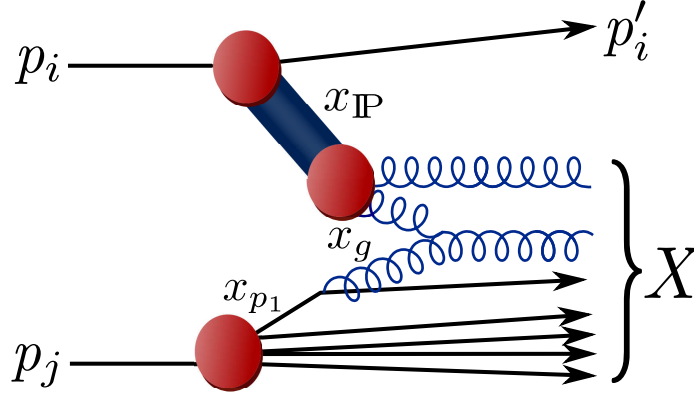
Figure 2.10. A single-diffractive dissociation event. $p_{i,j}$ are the momenta of the initial state protons. A Pomeron with momentum fraction $x_{\mathbb{P}}$ is extracted from p_i. A parton from p_j is extracted with momentum fraction x_{p_1} and interacts with a gluon from the Pomeron with a momentum fraction x_g of the Pomeron. X is the dissociation system and p'_i is the momentum of the scattered proton.

Once the parton interaction has been described, parton showering and fragmentation proceed as in the non-diffractive case.

The PHOJET model uses the Dual Parton Model, as mentioned in Section 2.5 for "soft" interactions and perturbative QCD for "hard" interactions. The two are separated by a momentum cut-off, $p_{\mathrm{T}}^{\mathrm{cut-off}}$. The perturbative treatment is similar to PYTHIA for non-diffractive events. The "soft" interactions are treated using Reggeon Field Theory. The number of soft and hard interactions in an event is given by

$$\sigma(n_s, n_h, s) = \int d^2B \frac{(2\chi_s)^{n_s}}{n_s!} \frac{(2\chi_h)^{n_h}}{n_h!} e^{-2(\chi_s+\chi_h)} \tag{2.31}$$

where the χ_s and χ_h eikonals are functions of s and B, the impact parameter representation of the soft and hard Pomeron. In RFT, the multiplicity of an event is obtained by using the optical theorem to "cut" the diagram associated with the Pomeron exchange. The cross-section for a particular number of cuts is given by the Gribov-Regge calculus [69]. In this formulation there are few free parameters and it naturally leads to "hard" interactions in diffractive events by the inclusion of the hard Pomeron.

Figures 2.11, 2.12, and 2.13 show the multiplicity, η distribution and p_T distributions of the three generators for each subprocess. It can be seen that for the non-diffractive processes, PYTHIA 6 has the highest peak multiplicity and hardest p_T spectrum of the three

generators. PHOJET has a distinctly lower average multiplicity and a relatively similar p_T spectrum to PYTHIA 8 for the non-diffractive events. Large differences between the generators are evident in the single-dissociation events. In the multiplicity plots, the PYTHIA generators have two distinct populations, although the PYTHIA 8 generator has a significantly higher multiplicity. PHOJET has a smooth distribution of multiplicities. PYTHIA 6 has approximately half as many particles per unit η. The momentum spectrum plots show a striking difference between PYTHIA 6 and the other two generators, which shows that the addition of a perturbative description of diffractive events drastically changes the event kinematics. The double-dissociation plots show many of the same trends as the single-dissociation plots. In particular the difference in the shape of the η distribution between the generators is notable.

(a)   (b)

(c)
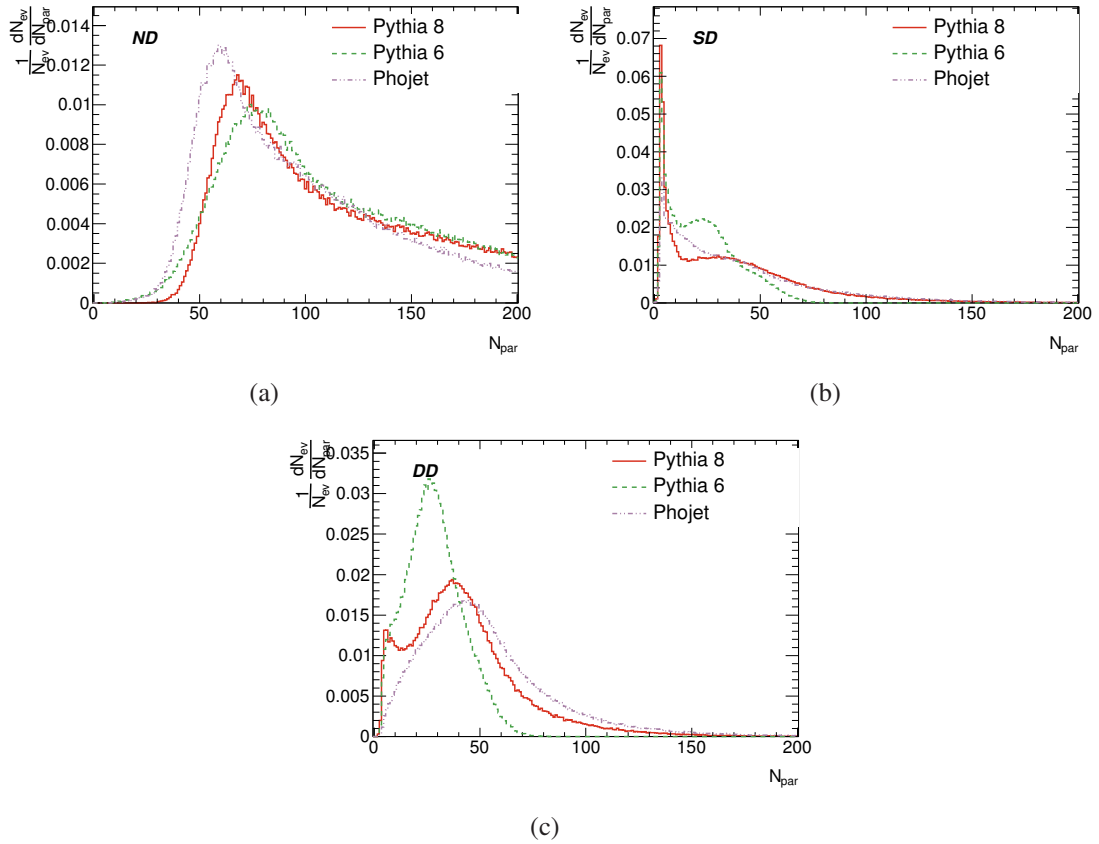
Figure 2.11. Number of particles with $p_T > 100$ MeV per event for for ND (a), SD (b), and DD (c) events comparing the PYTHIA 8, PYTHIA 6 and PHOJET generators at $\sqrt{s} = 7$ TeV.

It is worth mentioning that the modeling of the non-diffractive process has been studied in the context of measurements of charged particle multiplicities [70]. In these studies, tuned PYTHIA 6 Monte Carlo events were seen to give the best agreement with the data.
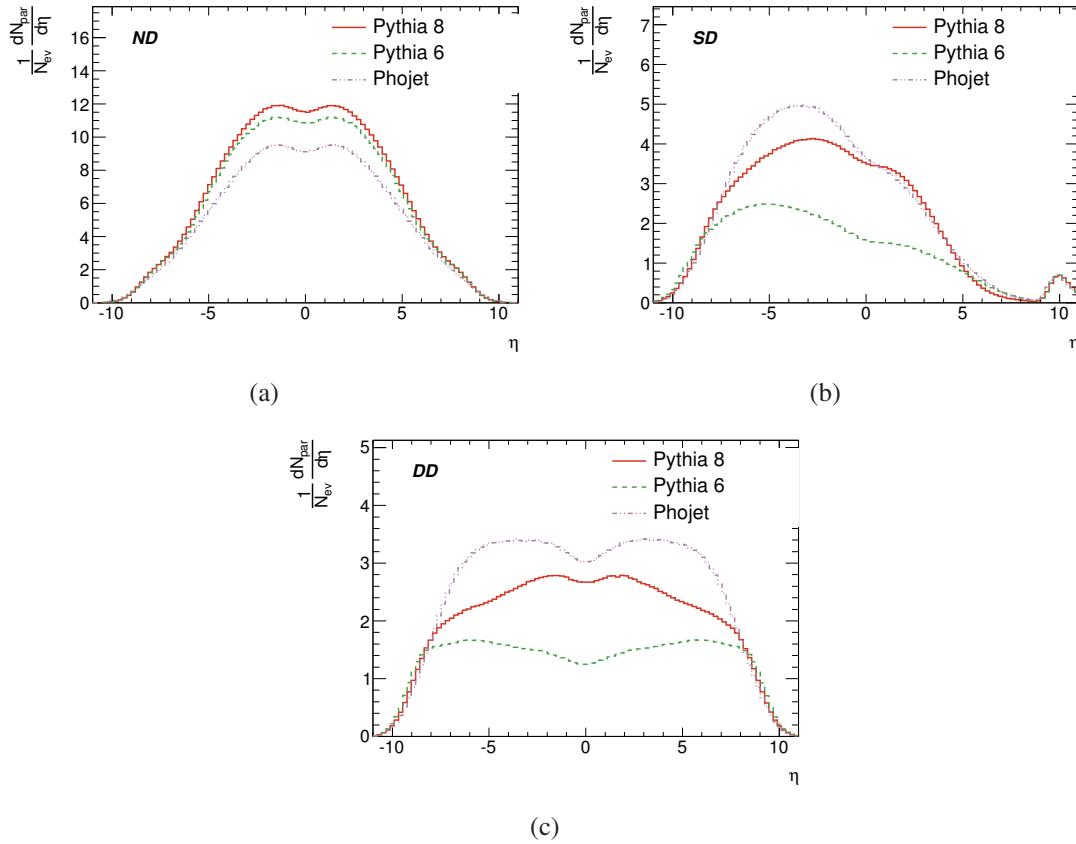
Figure 2.12. Inclusive η distributions for particles with $p_T > 100$ MeV for ND (a), SD (b), and DD (c) events comparing the PYTHIA 8, PYTHIA 6 and PHOJET generators at $\sqrt{s} = 7$ TeV. The η is defined such that the dissociated proton always has an η of $\tilde{1}0$.

PHOJET under-predicted the multiplicity and momentum spectra of the charged particles. Several alternative tunes of the PYTHIA 6 parameters have been made to describe minimum bias measurements at previous colliders. In this analysis the ATLAS collaboration MC09 tune [71] of PYTHIA6 is used but the tunes Perugia0 [72], DW [73], and variations the initial and final state radiation parameters were also studied. The difference between these various PYTHIA6 tunes were studied but are much smaller than those between the various generators.

(a)

(b)

(c)
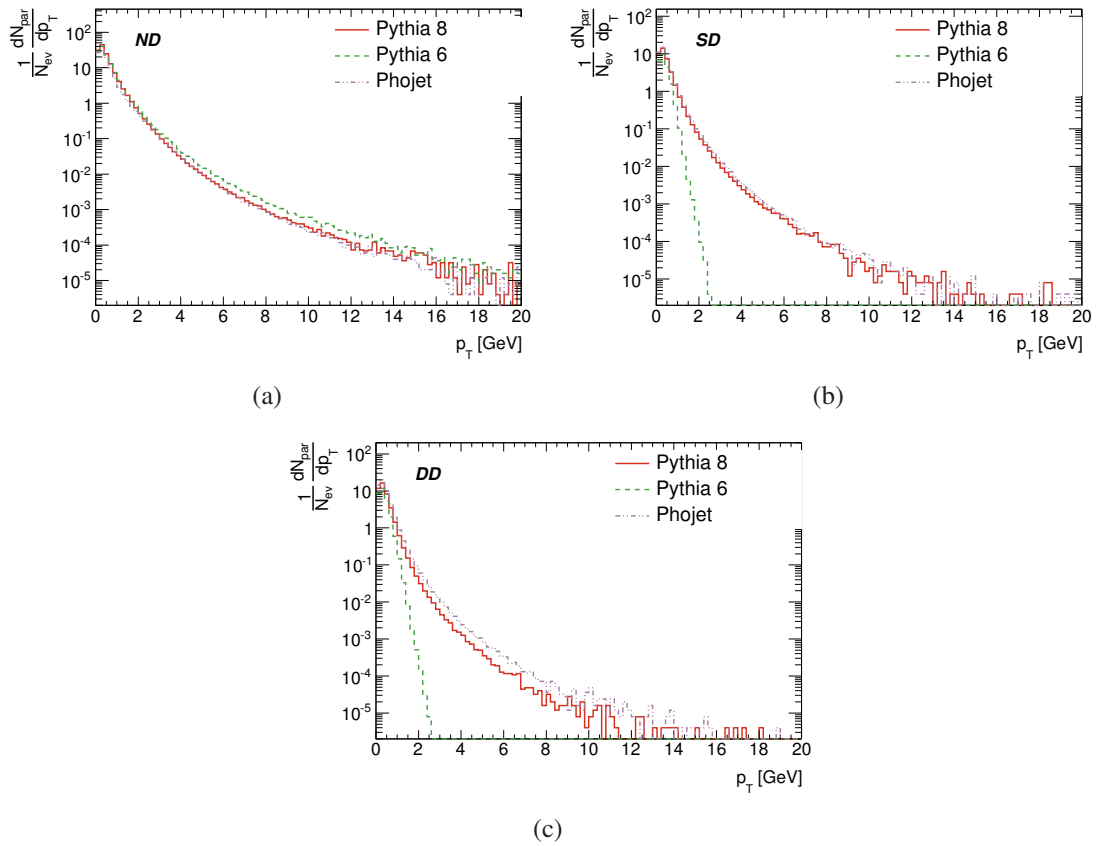
Figure 2.13. Inclusive p_T distributions for ND (a), SD (b), and DD (c) events comparing the PYTHIA 8, PYTHIA 6 and PHOJET generators at $\sqrt{s} = 7$ TeV.

<div align="right">

CHAPTER 3

</div>

Inelastic Cross-Section Measurement Overview

The general cross-section formula for the inelastic cross-section measurement is given by:

$$\sigma_{\text{inel}} = \frac{N - N_{\text{BG}}}{\epsilon \times A_{\text{inel}} \times \mathcal{L}} \tag{3.1}$$

where N is the number of observed events, N_{BG} is the number of background events, A_{inel} is the acceptance, ϵ is the efficiency to select an event in the acceptance and $\mathcal{L}$ is the luminosity. The particular event selection used in this analysis simply requires at least two of the 31 MBTS counters to collect a charge of at least 0.15 pC. Events satisfying this selection are collectively referred to as the *inclusive* sample.

As will be discussed in Chapter 10, the luminosity is measured using the beam scanning technique first proposed by Simon van der Meer [74]. The uncertainty is at present 3.4% [75]. The determination of the number of selected events and the background is straight-forward. However, the major challenge of the analysis is the determination of the acceptance A_{inel}.

A_{inel} can be decomposed into the individual contributions to the inelastic cross section as follows:

$$A_{\text{inel}} = \frac{A_{\text{incl}}^{\text{ND}}\sigma_{\text{ND}} + A_{\text{incl}}^{\text{SD}}\sigma_{\text{SD}} + A_{\text{incl}}^{\text{DD}}\sigma_{\text{DD}} + A_{\text{incl}}^{\text{CD}}\sigma_{\text{CD}}}{\sigma_{\text{inel}}} \tag{3.2}$$

$$= A_{\text{incl}}^{\text{ND}}\frac{\sigma_{\text{ND}}}{\sigma_{\text{inel}}} + A_{\text{incl}}^{\text{SD}}\frac{\sigma_{\text{SD}}}{\sigma_{\text{inel}}} + A_{\text{incl}}^{\text{DD}}\frac{\sigma_{\text{DD}}}{\sigma_{\text{inel}}} + A_{\text{incl}}^{\text{CD}}\frac{\sigma_{\text{CD}}}{\sigma_{\text{inel}}} \tag{3.3}$$

$$= A_{\text{incl}}^{\text{ND}}(1 - f_{\text{D}}) + f_{\text{D}}[A_{\text{incl}}^{\text{SD}}f_{\text{SD}} + A_{\text{incl}}^{\text{DD}}f_{\text{DD}} + A_{\text{incl}}^{\text{CD}}f_{\text{CD}}] \tag{3.4}$$

where

- $A_{\text{incl}}^{\text{ND}}$, $A_{\text{incl}}^{\text{SD}}$, $A_{\text{incl}}^{\text{DD}}$ and, in the case of PHOJET, $A_{\text{incl}}^{\text{CD}}$, are the acceptances of the event selection for the ND, SD, DD and CD processes.

- f_{D} is the fractional contribution of diffractive events to the inelastic cross-section: $f_{\mathrm{D}} = \frac{\sigma_{\mathrm{SD}}+\sigma_{\mathrm{DD}}+\sigma_{\mathrm{CD}}}{\sigma_{\mathrm{inel}}}$. PYTHIA predicts 32% for f_{SD} and PHOJET predicts 20%.

- f_{SD}, f_{DD} and f_{CD} are the fractional contribution of SD, DD and CD to the diffractive cross-section, e.g. $f_{\mathrm{SD}} = 1 - f_{\mathrm{DD}} - f_{\mathrm{CD}} = \frac{\sigma_{\mathrm{SD}}}{\sigma_{\mathrm{SD}}+\sigma_{\mathrm{DD}}+\sigma_{\mathrm{CD}}}$. PYTHIA predicts 60% for f_{SD} and PHOJET predicts 69%.

A priori, $A_{\mathrm{incl}}^{\mathrm{ND}}$, $A_{\mathrm{incl}}^{\mathrm{SD}}$, and $A_{\mathrm{incl}}^{\mathrm{DD}}$, as well as f_{D} and f_{SD} are unknown. Monte Carlo models give predictions for these values but they depend upon the underlying model assumed by each generator. In order to reduce the impact of these unknown quantities, the analysis takes two steps:

- First, the model dependence of the acceptance correction is limited by *quoting* the measurement for a restricted ξ-range. In Chapter 2 ξ was defined as being equal to $\frac{M^2}{s}$ where M was the invariant mass of the proton dissociation products. Because the detector has finite resolution and acceptance, we cannot measure M (equivalently ξ) directly, however the presence of an MBTS hit gives a lower limit on ξ. Therefore, ξ is calculated for only the Monte Carlo models, which give access to the four-vectors of all primary particles produced in an interaction. Primary particles are defined as particles with a lifetime $\tau > 0.3 \times 10^{-10}$s.

  In order to avoid ambiguities in assigning a final state particle to an initial proton system in the case of double diffractive dissociation, this measurement uses a modified diffractive mass. After ordering all primary particles in pseudorapidity, the largest pseudorapidity gap between adjacent particles is found. The mean pseudorapidity of the two particles which define the gap is used to assign all particles with greater pseudorapidity to one system and all particles with smaller pseudorapidity to the other. This variable will correspond to the true diffractive mass except for rare cases where the fluctuations in particle production produce a larger rapidity gap in the decay products of one system than between the two diffractive systems, which we term X and Y. The system with the largest mass is by definition X, and ξ is defined to be M_X^2/s. In the case of single-dissociation X is the system from the dissociated proton. In the case of double-dissociation, ξ is defined by the larger of the two dissociation systems. Figure 3.1 illustrates the definition.

  Because ξ is defined using final state particles, it is slightly dependent on the underlying fragmentation model of the generator with which it was calculated. PYTHIA 6 and PYTHIA 8 have very different fragmentation models, but, as can be seen in Figure 3.2, the differences lead to small discrepancies at high ξ.

  ξ is closely related to the η of the particle in a dissociation system which starts the rapidity gap. This value, η_{min}, is shown in Figure 3.3 for all three generators. It can be seen that in each case the dependence is linear with $\log \xi$ and that there is very little difference in the dependence between generators. The average $\eta - \xi$ relationship
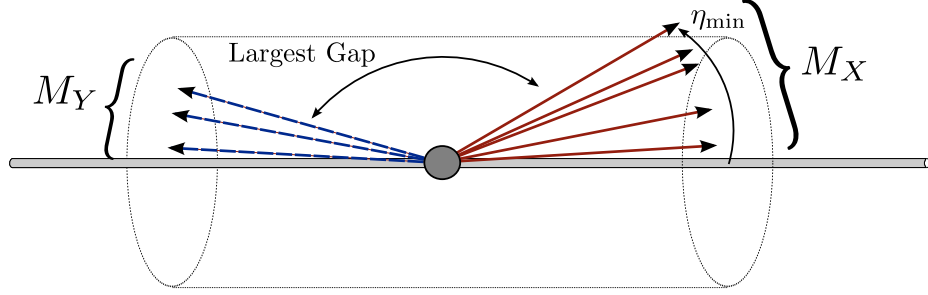
Figure 3.1. A schematic illustration of M_X, M_Y and $\eta_{\min}$ in a double-dissociation event. The blue dashed arrows indicate the smaller mass dissociation system, the solid red arrows indicate the higher mass system. The two systems are defined by the largest rapidity gap in the event.

(a)   (b)
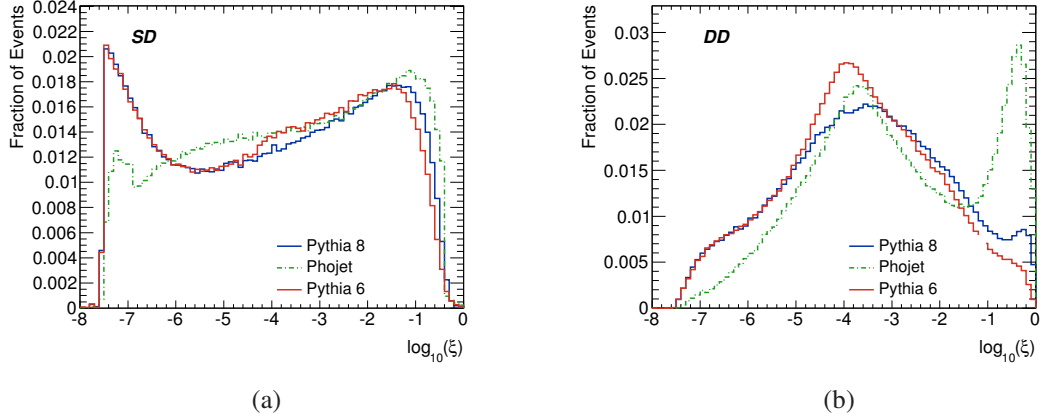
Figure 3.2. ξ distribution for SD (a) and DD (b) events at $\sqrt{s} = 7$ TeV comparing the three Monte Carlo generators. The difference in PYTHIA 6 and PYTHIA 8 is solely due to the difference in fragmentation between the two models.

is given by

$$\ln \xi = -\Delta\eta \tag{3.5}$$

where $\Delta\eta$ is the difference between $\eta_{\min}$ and η of the initial state proton system. Equation 3.5 arises because the dissociation systems are highly boosted along z, therefore the mass is related to the opening angle in θ. The maximum η-value of the MBTS coverage of 3.84 restricts the measurement to the kinematic range of $\xi > 5 \times 10^{-6}$.

- The second step the analysis takes to limit model-dependence is to use the data to constrain f_D by measuring the ratio of the number of events in a diffraction-enhanced to inclusive event sample. The diffraction-enhanced sample is obtained by creating a *single-sided* sample containing events with at least two hits on one side of the
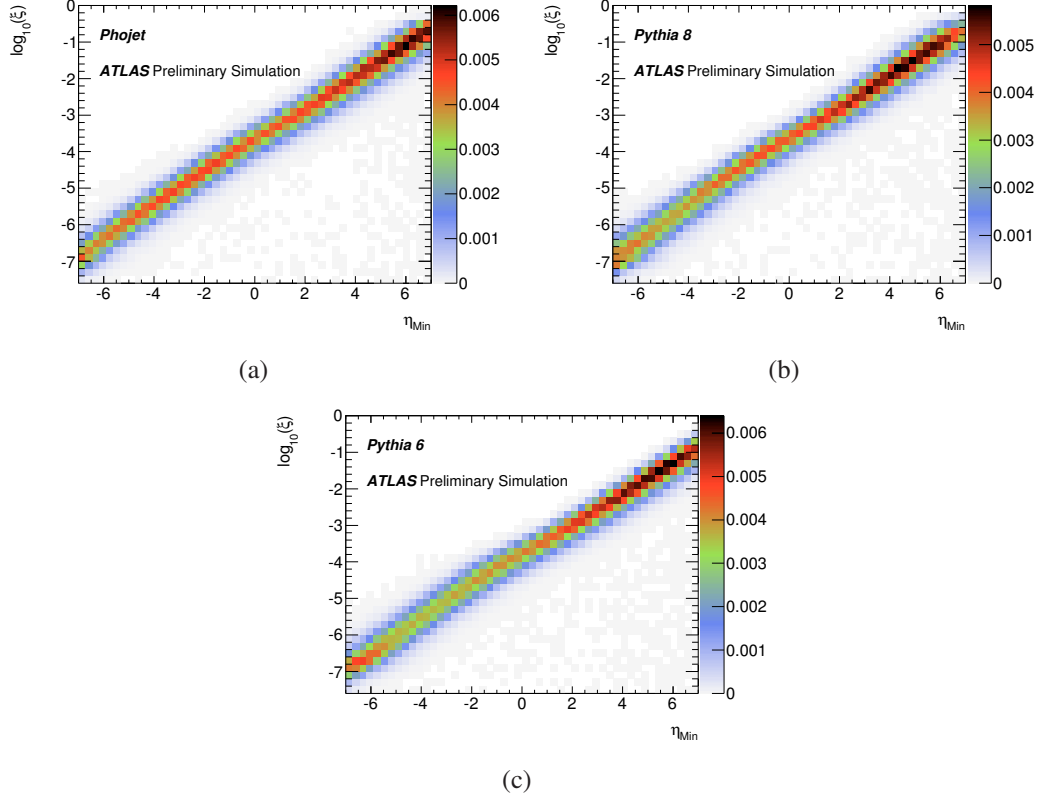
Figure 3.3. ξ versus the η of the particle which defines the rapidity gap between the intact proton and dissociation system in SD events(η_{Min}). PHOJET (a), PYTHIA8 (b) and PYTHIA6 (c) are shown.

MBTS in z and none on the other. This sample is expected to be dominated by SD events, and DD events in which only one of the two dissociation systems has $\xi > 5 \times 10^{-6}$. For example, PYTHIA predicts the fractional contribution of non-diffractive events to the single-sided sample to be 1%, while PHOJET predicts 8%. In the inclusive sample the non-diffractive process contributes about 74% and 80% for PYTHIA8 and PHOJET, respectively. The acceptances are presented in detail in Section 12.2. By taking the ratio of the *single-sided* to *inclusive* sample, and comparing the measured value to the MC predictions, the allowed values of f_{D} for each MC model are constrained. The ratio, R_{SS}, is given by

$$R_{\mathrm{SS}} = \frac{N_{\mathrm{SS}}}{N_{\mathrm{incl}}} \tag{3.6}$$

$$= \frac{A_{\mathrm{SS}}^{\mathrm{inel}} N_{\mathrm{inel}}}{A_{\mathrm{incl}}^{\mathrm{inel}} N_{\mathrm{inel}}} \tag{3.7}$$

$$= \frac{A_{\mathrm{SS}}^{\mathrm{inel}}}{A_{\mathrm{incl}}^{\mathrm{inel}}} \tag{3.8}$$

$$= \frac{A_{\text{SS}}^{\text{ND}} \frac{\sigma_{\text{ND}}}{\sigma_{\text{inel}}} + A_{\text{SS}}^{\text{SD}} \frac{\sigma_{\text{SD}}}{\sigma_{\text{inel}}} + A_{\text{SS}}^{\text{DD}} \frac{\sigma_{\text{DD}}}{\sigma_{\text{inel}}} + A_{\text{SS}}^{\text{CD}} \frac{\sigma_{\text{CD}}}{\sigma_{\text{inel}}}}{A_{\text{incl}}^{\text{ND}} \frac{\sigma_{\text{ND}}}{\sigma_{\text{inel}}} + A_{\text{incl}}^{\text{SD}} \frac{\sigma_{\text{SD}}}{\sigma_{\text{inel}}} + A_{\text{incl}}^{\text{DD}} \frac{\sigma_{\text{DD}}}{\sigma_{\text{inel}}} + A_{\text{incl}}^{\text{CD}} \frac{\sigma_{\text{CD}}}{\sigma_{\text{inel}}}} \tag{3.9}$$

$$= \frac{A_{\text{SS}}^{\text{ND}}(1 - f_{\text{D}}) + f_{\text{D}}[A_{\text{SS}}^{\text{SD}} f_{\text{SD}} + A_{\text{SS}}^{\text{DD}} f_{\text{DD}} + A_{\text{SS}}^{\text{CD}} f_{\text{CD}}]}{A_{\text{incl}}^{\text{ND}}(1 - f_{\text{D}}) + f_{\text{D}}[A_{\text{incl}}^{\text{SD}} f_{\text{SD}} + A_{\text{incl}}^{\text{DD}} f_{\text{DD}} + A_{\text{incl}}^{\text{CD}} f_{\text{CD}}]} \tag{3.10}$$

where the SS subscript indicates the single-sided event selection and the $incl$ indicate the inclusive event sample, as defined in Equation 3.2. To determine the relative contribution of diffractive events, the A terms are taken from the models, as well as f_{SD} and f_{CD}, and f_{D} is adjusted until the model prediction matches the measured value in data. Because the distinction between diffractive and non-diffractive events varies model-by-model, f_{D} is determined for each model separately.

Placing a cut on the diffractive mass modifies Equation 3.1 to

$$\sigma(\xi > 5 \times 10^{-6}) = \frac{(N - N_{\text{BG}})(1 - f_{\xi < 5 \times 10^{-6}})}{\epsilon_{\text{trig}} \times \epsilon_{\text{sel}} \times \mathcal{L}} \tag{3.11}$$

where $1 - f_{\xi < 5 \times 10^{-6}}$ corrects for the fraction of events in the inclusive sample which have $\xi < 5 \times 10^{-6}$, ϵ_{sel} is the event selection efficiency for events with $\xi > 5 \times 10^{-6}$, and ϵ_{trig} is the trigger efficiency with respect to the offline selection.

Using the tuned Monte Carlo simulation, ϵ_{sel} and $f_{\xi < 5 \times 10^{-6}}$ are taken directly from the MC and Equation 3.11 becomes

$$\sigma(\xi > 5 \times 10^{-6}) = \frac{(N - N_{\text{BG}})}{\epsilon_{\text{trig}} \times \mathcal{L}} \times C_{\text{MC}} \tag{3.12}$$

where

$$C_{\text{MC}} = \frac{1 - f_{\xi < 5 \times 10^{-6}}}{\epsilon_{\text{sel}}}. \tag{3.13}$$

C_{MC} is taken from Monte Carlo simulation (corrected for the MBTS efficiency measured in data), while the corrections for the trigger and backgrounds are determined from data. The Donnachie and Landshoff model with $\epsilon = 0.085$ and $\alpha' = 0.25 \text{ GeV}^{-2}$, henceforth referred to as the default model, is used to determine C_{MC} and a variety of other models, listed in Chapter 2.5, are used to determine any residual model uncertainty in these correction factors.

The measurement of $\sigma_{\text{inel}}(\xi > 5 \times 10^{-6})$ is presented in Chapter 12. It is additionally extrapolated to the full σ_{inel} using A_{inel} taken from the Donnachie and Landshoff model, with a large uncertainty due to the model dependence.

CHAPTER 4

The Large Hadron Collider

The Large Hadron Collider (LHC) [76] was first conceived in the early 1990s and approved in preliminary form by the CERN council in 1994 on the heels of the US Superconducting Super Collider (SSC) failure. The appeal of the LHC was tied to the fact that it was a bargain discovery machine; there was no need for a costly tunnel excavation because one of a suitable size already existed for the CERN electron-positron collider, LEP. This chapter reviews the motivation, design of the LHC and the running conditions from 2010.

4.1 Motivation

By the late 1980s, fundamental interactions of particles had revealed themselves to be relatively simple and elegant. Nearlly all known phenomena could be explained by SU(2)⊗U(1) electroweak theory and SU(3) QCD. The electroweak theory had once missing piece – a mechanism to break the symmetry and generate boson masses. The scale associated with the symmetry breaking was calculated to be a few 100 GeV and in the absence of a Higgs mechanism, in which a scalar field broke the symmetry, the weak interactions were calculated to be come strong and violate unitarity at approximately 1 TeV. And, while the fundamental particles had given no hint of substructure yet, if there were to be substructure it was calculated that it would appear at 10^{-17} cm or $\sim$1 TeV. Therefore, it was argued [77] that the next generation of collider needed to be in the multi-TeV scale, ideally with a center-of-mass energy of 10 to 50 TeV for a proton-(anti)proton collider. The SSC was proposed as a proton-antiproton collider with a $\sqrt{s}$ of 40 TeV but it would be relatively low luminosity. The LHC was put forward as a high luminosity machine at lower energy. 14 TeV was roughly what could be expected given realistic magnet field strengths and the diameter of the LEP tunnel. When the SSC was canceled in 1994, the LHC became the next energy frontier machine.

4.2 Design

The LHC is composed of over 1600 superconducting magnets arranged in a 26.7 km tunnel under France and Switzerland. The tunnel, which was built in the late 1980s for the Large Electron-Positron Collider (LEP), lies between 45m and 170m below the surface of the earth. The original design, which has been preserved for the LHC, divided the ring into eight arcs and eight straight sections to minimize energy loss from bremstralung by the original electron and positron beams. There are eight possible interaction points on the ring, four of which are in use for LHC experiments. ATLAS and CMS sit opposite each other on the ring and are the designated discovery experiments. LHCb and ALICE are "low" luminosity experiments investigating flavor physics and heavy ion collisions, respectively.

The LHC is designed to operate at a luminosity of 10^{34}s^{-1}cm^{-2} and a center of mass energy, $\sqrt{s}$, of 14 TeV. The machine is filled with *bunches* of protons with a minimum spacing of 25 ns. The revolution frequency of a bunch of protons is 11,245 Hz and there are roughly 3600 possible bunch slots in the machine. When the bunch-spacing is 75 ns or less, the beams are brought to collision at a *crossing angle* to reduce beam-beam interactions at points other than the nominal collision point.

On September 19th, 2009 the LHC had an accident which caused extensive damage to one sector of the ring and had significant implications for machine safety and beam energy [78]. It delayed the start of the LHC for a year and limited the center-of-mass energy to 7 TeV until improvements can be made to the machine. The incident is discussed further in Section 4.2.3. Full energy (14 TeV) will be achieved in 2014.

4.2.1 Accelerator Chain

The CERN accelerator complex, shown in Figure 4.1, begins with a bottle of hydrogen and ends with multi-TeV collisions. It uses a four accelerators to bring the protons from rest to 450 GeV, the injection energy of the beam into the LHC. All of the pre-accelerators were in use for physics programs at some point in CERN's 50+ year history.

To start, electrons are stripped from the hydrogen atoms and the remaining protons undergo the first stage of acceleration in the LINAC2, a linear accelerator commissioned in 1978 to produce 50 MeV protons for the Proton Synchrotron Booster. The Booster accelerates the protons to 1.4 GeV. It was built in 1972 and its RF system was recently upgraded to accommodate the needed bunch frequency of the LHC. Ultimately, it sets the bunch structure for the LHC because it is the first stage of bunched injection. The Booster delivers its protons at 324 ns spacing to the Proton Synchrotron (PS), which is CERN's first synchrotron. Constructed in 1959, it uses conventional electromagnets to accelerate protons to 26 GeV. The final stage in the chain is the Super Proton Synchrotron (SPS), a 450 GeV accelerator which was home to the W and Z bosons discoveries in the 1980s. The SPS is filled with 72 bunches at a time from the PS. It accelerates the protons to 450 GeV and sends up to 72 bunches at a time in the form of a *bunch-trains* into the LHC. Once all of the bunches are in the LHC the current is ramped in the magnets, until the beams are
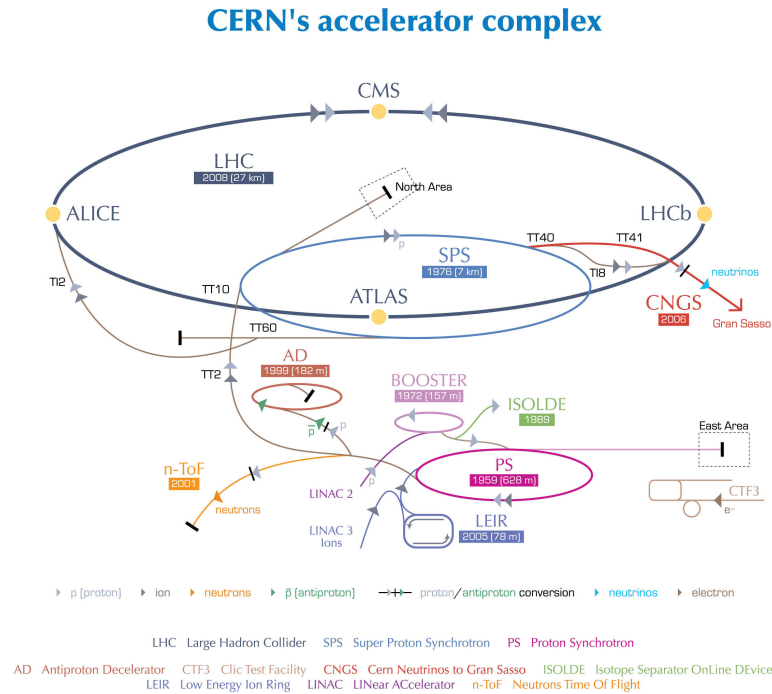
Figure 4.1. The CERN accelerator complex.[79]

at collision energy.

4.2.2 Magnets

The heart of the LHC is its enormous superconducting magnet system, consisting primarily of 15 m long dipole and quadrupole magnets. The dipole magnets are responsible for the bending of the beams, while quadrupole magnets provide focusing. Higher multipole corrector magnets are interspersed along the beamline. Acceleration is achieved through superconducting 400 MHz RF cavities.

The design of the magnets was driven by two factors, one physics based, the other construction constrained. To achieve the high luminosity needed to produce the rare processes the LHC intends to find, a proton anti-proton machine is not feasible due to the difficulty of accumulating a significant number of anti-protons. Proton beams cannot counter-circulate in the same vacuum chamber or beam-pipe as proton and anti-proton beams can, therefore separate magnetic fields and vacuum chambers are needed. However, the LEP tunnel is too narrow to fit two separate magnet systems, therefore a twin-bore design was adopted [80]. The LHC dipole design is shown in Figure 4.2. Two magnets and beam-pipes sit in the same cryostat and cold-mass which is cooled by superfluid helium to a temperature of

1.7K. The LHC constitutes the largest, coldest cryogenic system in the world.

The magnets are made of niobium titanium (NbTi) cables and have fields of up to 8 T at a current of nearly 12 kA. The total stored energy of the beams and current in the magnets is over 1 GJ which can be dangerous to the machine if it is relased in an uncontrolled way, such as through a quench. A quench occurs when the normally superconducting magnets loose their superconductivity, suddenly causing a large build up of resistance where the quench began. A quench protection system (QPS) based on monitoring changes in voltage between (nominally identical) magnets is in place to safegaurd the machine. When a quench is detected it usies heaters mounted on the magnet coils to raise the temperature and create an extended normally conducting zone along the length of the entire magnet and its neighbors. This process safely dissipates the energy in a large volume. In order to protect the machine and the detectors in the event of loss of control of the beam, a beam dump system is in place to extract the beam quickly and safely. It is triggered by beam conditions monitors at multiple points along the ring which look for an excess of interactions near the beamline. The beam can be extracted in O(100 μs).
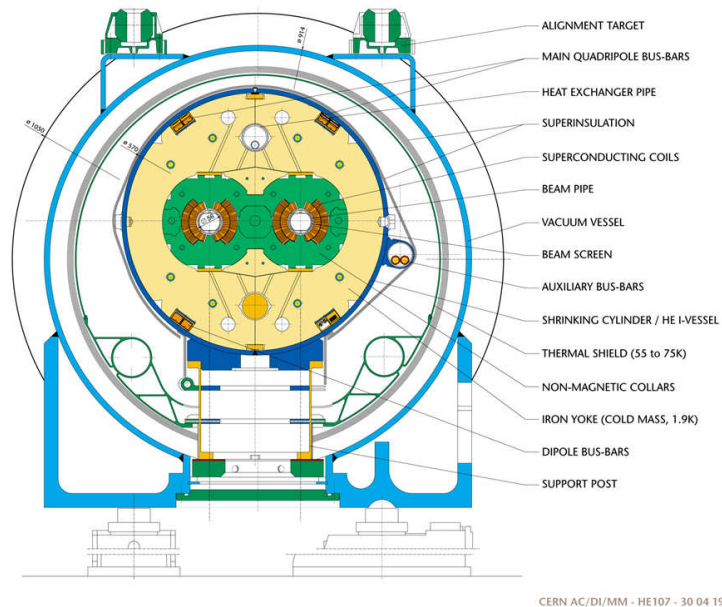
Figure 4.2. A cross section of the LHC dipole illustrating the twin-bore design.

Near the interaction regions, inner triplet magnets, which are a series of three quadrupole magnets with alternating gradients, bring the beams into collisions. The optics at the interaction region can be adjusted for different beam sizes and energies.

4.2.3 The September 19th Incident

Commissioning of the LHC began in the fall of 2008 with the establishment of single beam circulation at injection energy on September 10th. Shortly thereafter problem with a transformer suspended beam tests for several days. While the transformer was being replaced, experts performed powering tests in a section of the machine, Sector 3-4, to ramp the current in the magnets up to 9.3 kA, the current associated with 5 TeV beams. During the test a quench developed between two magnets in a region called a *bus bar splice*. An electrical arc occurred, which dissipated more the 4 MW in one second [78]. Part of the bus bar was vaporized and the helium enclosure was punctured, allowing the the superfluid helium to enter the cryostat vacuum insulation volume. The cyrostat subsequently punctured, leading to a rapid increase in the helium pressure. The pressure in the insulation volume rose as high as 0.8 MPa, ripping some of the 35 ton magnets from their support jacks and blowing off the door of the tunnel in that sector. In total, 755m of the tunnel was damaged. Reports after the incident [78] indicated that the initial arc was caused by poor soldering in the bus bar which failed. The QPS did not monitor the bus bars, which is why the quench developed undetected.

Recovery from this incident took over a year. In addition to replacing or refurbishing the damaged magnets, the QPS system was upgraded to include monitoring of the splices, more pressure release valves were installed and other potentially problematic bus bar splices were identified and fixed. However, it was determined [81] that until significant upgrade to the machine to fix more splices and further improve the machine protection systems, the machine energy would be limited. In January, 2011 it was decided [82] that the LHC would run at 7 TeV until the end of 2012, after which there would be a 1.5 year shutdown to make the improvements. In 2014 the LHC will come online at 14 TeV.

4.3 2010 Run Conditions

Because 2010 was largely a commissioning period, the LHC running conditions were significantly different than the design parameters discussed above. Due to machine safety concerns in the wake of the September 19th incident, the center-of-mass energy was limited to 7 TeV. The initial running period in March and April, which this thesis primarily concerns, saw instantaneous luminosities of 10^{27}cm^{-2}s^{-1}, while the peak luminosity, which was achieved in November, was 2.1×10^{32}cm^{-2}s^{-1}. Figure 4.3 shows the evolution of both the peak instantaneous and integrated luminosity over the 2010 7 TeV run period. Commissioning began with only one colliding bunch pair in ATLAS; in the fall the LHC was operating with bunch trains with 75 ns bunch spacing and a total of 368 colliding bunches. Table 4.1 compares the LHC machine parameters in the early 2010 7 TeV running, late 2010 running and nominal 14 TeV running. It is notable that the machine is already running at full bunch intensity. The increase to 10^{34} cm^{-2}s^{-1} will come from increasing the number of bunches in the machine and narrowing the bunch size. The bunch size is determined in

	Early 2010	Late 2010	Nominal
$\sqrt{s}$ [TeV]	7	7	14
n_b	1-2	348	2808
N_p	1.1×10^{10}	1.1×10^{11}	1.15×10^{11}
$\mathcal{L}[\text{cm}^{-2}\text{s}^{-1}]$	10^{28}	10^{32}	10^{34}
β^* [m]	11	3.5	0.6
Crossing angle [μrad]	0	200	285

Table 4.1. Comparison of the LHC machine conditions in early 2010, late 2010 and nominal design parameters. Early 2010 conditions were the same as for the run for the cross-section measurement. n_b is the number of colliding bunches in the machine, N_p is the number of protons per bunch or bunch intensity, and $\mathcal{L}$ is the average instantaneous luminosity. β^* is related to the amplitude function of the beam envelope at the interaction point. The crossing angle refers to the angle of the beams with respect to the nominal beamline at the collision point.

part by β^*, which determines the amplitude function of the beams at the interaction point. Initially beams collided head-on with no crossing angle at the interaction point, but once the bunch spacing became small with respect to the region that the two beams share the same beam-pipe, a crossing-angle was introduced to reduce beam-beam interactions.

(a)   (b)
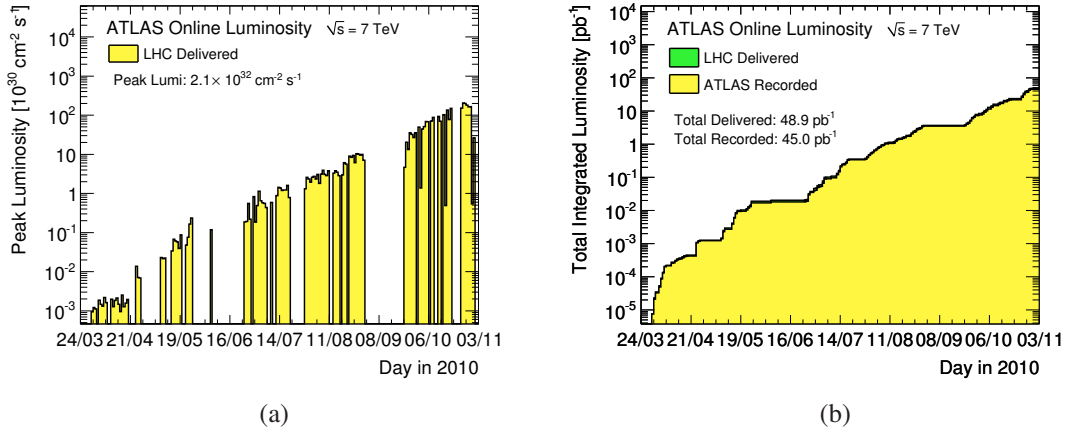
Figure 4.3. Peak luminosity by day (a) and total integrated luminosity by day (b) in 2010.

<div align="right">

CHAPTER 5

</div>

The ATLAS Detector

The ATLAS detector is one of four multi-purpose detectors at the LHC. It is a modern, hermetic collider detector built to measure final states elucidating the nature of electroweak symmetry breaking. The largest of the four experiments, ATLAS is defined by its signature muon spectrometer which consists of a large superconducting air-core toroid and precision tracking chambers. The spectrometer encases two layers of calorimeter, a lead and scintillator based hadronic calorimeter and a liquid argon electromagnetic calorimeter. Situated closest to the beam-pipe inside a 2T magnetic field is a three-part tracking detector using silicon pixel, silicon strip and transition radiation technologies. ATLAS, shown in Figure 5.1, uses a right-handed coordinate system with an origin at the nominal interaction point. It is oriented such that z is aligned along the beam-pipe, $+x$ points to the center of the LHC ring, and $+y$ is directed upwards. Cylindrical coordinates are used, with ϕ denoting the azimuthal angle in the transverse plane. Pseudorapidity, $\eta = -\ln\left(\tan\frac{\theta}{2}\right)$ where θ is the polar coordinate, is typically used as the angular coordinate with respect to the polar axis.

This chapter describes the sub-components of the ATLAS detector, beginning with the trigger and data acquisition system. Then, the active detector elements are described, starting with the inner tracking detector, followed by the calorimeter system, the muon spectrometer, and finally, the luminosity detectors.

5.1 Trigger and Data-Acquisition System

The ATLAS trigger and data acquisition system (TDAQ) is responsible for selecting and recording interesting events out of the nominal 40 MHz stream of inelastic interactions. A three-level staged approach is taken, with simple hardware based decisions at Level 1 to reduce the rate from O(MHz) to 75 kHz. A subset of the detector information is used to partially reconstruct the event at the Level 2 software based trigger which reduces the rate to 2.5 kHz. Lastly, the full detector information is used at Level 3 or the Event Filter (EF), which selects and writes events to storage at approximately 200 Hz. Collectively, Level 2
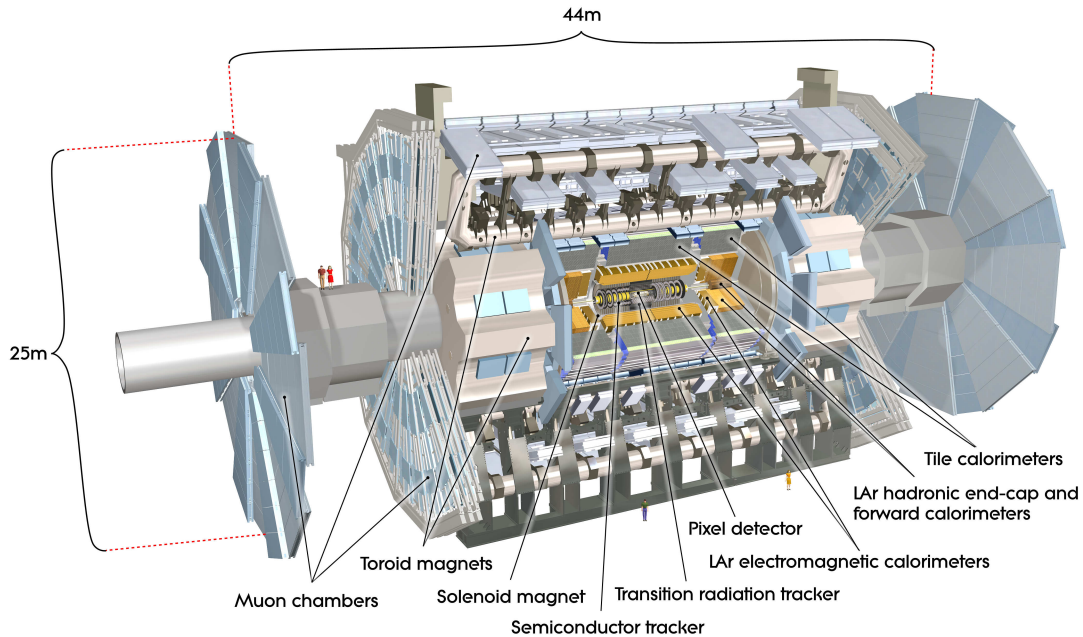
Figure 5.1. A diagram of the ATLAS detector indicating its sub-components [83].

and the EF are known as the High Level Trigger (HLT).

For the data used in this thesis, only the Level 1 trigger was used. The HLT was run in "pass-through mode" where the algorithms ran and recorded their decisions, but all events passing the Level 1 triggers were written to storage. At Level 1 algorithms implemented in the calorimeter trigger (L1Calo) hardware identify electron, photon, tau and jet-like objects and muon-like signatures are found in the muon trigger (MUCTP) hardware. At this point only information from the calorimeters, muon system and forward detectors is used. When a Level 1 object, is found a signal is sent to the workhorse of the Level 1 trigger, the Central Trigger Processor (CTP). The CTP collates the trigger signals from all of the parts of the detectors and forms multiplicities of objects. It additionally distributes the LHC clock, event number and bunch-crossing identifier to the data acquisition system.

Using a trigger menu, the CTP either selects an event or rejects it. Rejection can occur if a trigger menu item is not satisfied (e.g. the lowest muon threshold is not in the menu) or if an item is satisfied but it is *prescaled*. Prescaling limits the bandwidth of a particular trigger signature by only accepting every N^{th} event, where N is the prescale. In the meantime, the data acquisition system keeps the event information waiting for a trigger decision in buffers in the detector readout electronics.

If the event is selected, the CTP sends a signal to the L1Calo and MUCTP which retains information about the position of trigger objects, called regions-of-interest (ROI). A software farm partially builds the event using the data stored in buffer in the ROI and the Level 2 criteria are applied. If the Level 2 bit is passed then the data are taken off the

buffers for the entire detector and sent for full event building at the EF level. If an EF bit is set, then the data are written to storage.

5.2 The Inner Detector

The Inner Detector (ID) provides charged-particle tracking in a 2T solenoidal field up to $|\eta| < 2.5$. It is constrained by the following physics requirements:

- High quality momentum resolution for charged particles over a wide range of momenta.

- Excellent position resolution for primary vertex finding and secondary vertex identification.

In order to achieve these requirements the following additional design requirement are applied:

- Strong, uniform magnetic field - to make precise momentum measurements

- Minimal amount of material in the detector - to reduce multiple scattering and nuclear interactions

- Radiation hard technologies - to withstand the radiation dose sustained at close radii to the interaction point

- Low occupancy - to improve pattern recognition and detector performance in a high multiplicity environment

- Mechanical stability - to ensure that the detector alignment does not vary significantly with time.

ATLAS chose to satisfy these requirements using three technologies employed at different radii of the detector, each of which has a specific purpose. Closest to the beam-pipe at small radii is the three-layer Pixel detector, which provides the finest granularity measurements and is crucial for precise vertex finding. The intermediate layer of the ID consists of a four-layer silicon strip detector, which provides tracking through double-sided stereo-axial layers. This design allows for high-quality tracking at lower cost than silicon pixels. The outermost layer is a transition radiation tracker which uses thin tubes to provide, on average, 32 additional measurements per track as well as electron-pion separation through analysis of transition radiation. Figure 5.2 show the active elements of the barrel ($|\eta| \lesssim 1$). Carbon fiber support structures are used throughout the detector to provide stability at low material cost. Lastly, the detector is immersed in a 2T magnetic field generated by a thin, superconducting solenoid. The field axis is along the z direction. Table 5.1 summarizes the dimensions of each part of the Inner Detector system and 5.3 graphically illustrates them.
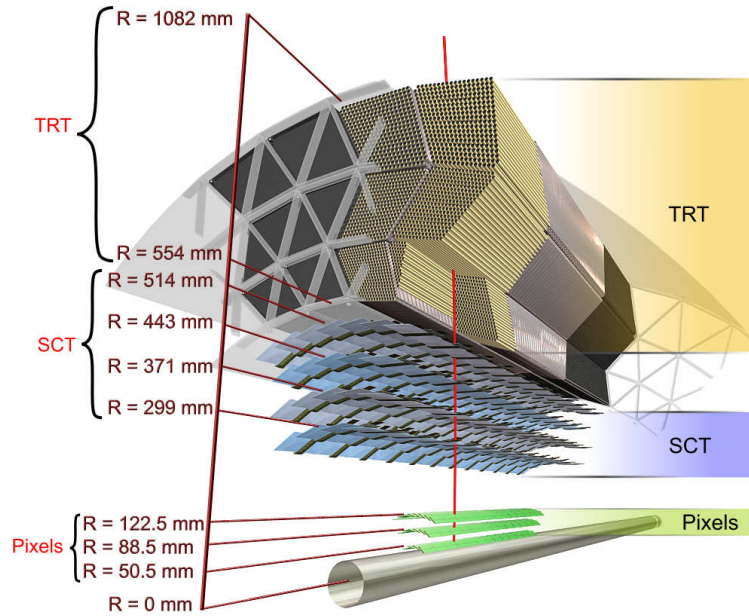
Figure 5.2. Cutaway of the ATLAS Inner Detector showing transverse barrel view. [83]

The material budget of the Inner Detector is shown in Figure 5.4 in both interaction lengths, λ, and radiation lengths, X_0. It can be seen that λ is dominated by the support structures for most of the η range, while X_0 is dominated by external services such as cooling and electrical connections. The amount of material is significant, totaling almost 1 λ and 2.5 X_0 at $|\eta|$ =1.5. The region which is most important for the work in this thesis is between $|\eta|$ of 2 and 4. It is dominated by pixel detector cabling, cooling, and other services.

5.2.1   Pixel Detector

The pixel detector is at the closest radius to the beam and therefore has the strictest requirements on radiation hardness, occupancy, and precision. All of these requirements are met, at least partially, by the use of a highly granular technology such as silicon pixels. The effects of radiation damage are mitigated by the small leakage current of pixels. The high granularity ensures low occupancy even at high charged particle multiplicities and translates into more precise measurements, improving track parameter resolution.

The detector consists of three barrel layers and two three-layer end-caps. Each layer is made of overlapping, identical silicon sensors mounted on *modules*, which are the building blocks of the pixel detector. In total, 1744 modules are used in the full detector. In the barrel, the modules have intrinsic resolutions of 10 μm in the plane transverse to the beamline and 115 μm in the longitudinal coordinate. In the end-caps, the precision coordinates are in the $z - \phi$ direction and there is lower accuracy in the r direction.

Detector		Radius (mm)			Length (mm)		
ID envelope		0	$< R <$	1150	0	$< |z| <$	3512
Beam-pipe		29	$< R <$	36			
Pixel Package		45.5	$< R <$	242	0	$< |z| <$	3092
	Barrel	50.5	$< R <$	122.5	0	$< |z| <$	400.5
	End-caps	88.8	$< R <$	149.6	495	$< |z| <$	650
SCT Package		255	$< R <$	610	0	$< |z| <$	2797
	Barrel	299	$< R <$	514	0	$< |z| <$	749
	End-caps	275	$< R <$	560	839	$< |z| <$	2735
TRT Package		554	$< R <$	1106	0	$< |z| <$	2744
	Barrel	563	$< R <$	1066	0	$< |z| <$	712
	End-caps	644	$< R <$	1004	848	$< |z| <$	2710

Table 5.1. Summary of the dimensions of the Inner Detector subdetectors, divided by detector package (including services and support structures) and active layers (Barrel and End-caps).

Figure 5.5(a) shows an exploded view of a pixel module. Front-end (FE) chips are bump-bonded to the silicon sensors. There are 16 FEs per module, each consisting of 2880 50 x 400 μm^2 pixels. Each pixel reads out the sensor charge and determines if it passes a threshold set by a comparator. The pixels are read-out in column pairs and the time-over-threshold (TOT) and hit timestamp are stored in a buffer until a trigger request signal is received. The TOT is proportional to the amount of charge deposited the the sensor and is used to improve the position resolution when a particle produces multiple pixels over threshold in a single layer.

The sensors, which constitute the active region of the pixel detector, are made of 250 μm thick oxygenated n-bulk silicon. A p-n junction is generated by n$^+$ implant bump-bonded to the FEs on one side of the sensor and p$^+$ implants on the other side. The depletion region is operated in reverse-bias. The implants are arranged in 144 columns and 328 rows; most pixels have a pitch of 400$\times$50 μm^2, however, there are some long pixels which have a 600$\times$50 μm^2 pitch. The intrinsic resolution of the sensors is 10 μm. For more information on the sensor design see [84].

The sensors are glued to a printed circuit board called the *flex-hybrid*. It contains the module control chip, which distributes the trigger and timing information, formats the data, and checks its integrity. It additionally sends data to the off-detector read-out system when a trigger request is received. More detail on the pixel electronics is found in [84].

5.2.2 Semi Conductor Tracker

The Semi Conductor Tracker (SCT) must meet nearly as stringent radiation dose and measurement precision requirements at the pixel detector, however, because it is further from the interaction point, the same occupancy constraints do not apply. In order to balance precision, radiation hardness and cost, a silicon micro-strip technology was chosen. The SCT consists of 15912 sensors arranged on 4088 modules which occupy four double-sided
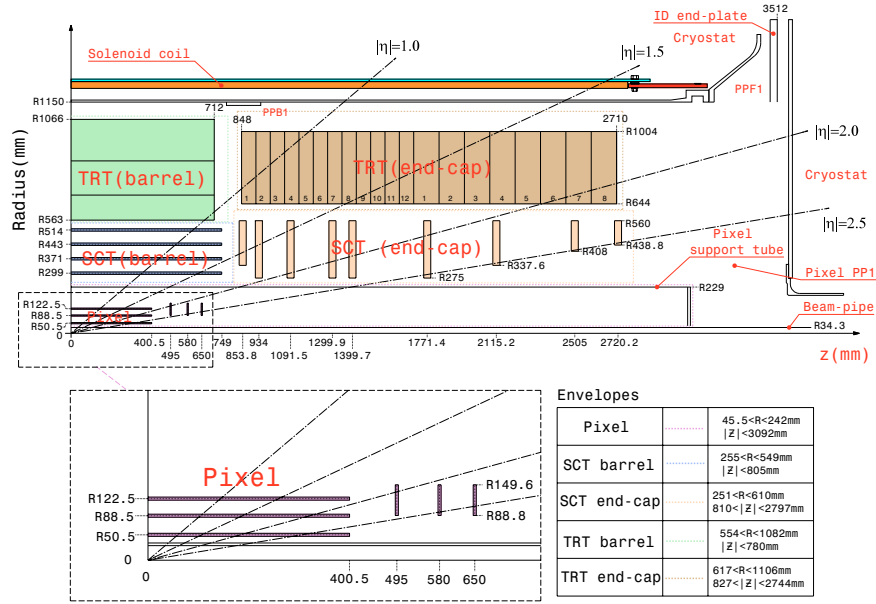
Figure 5.3. An $r - z$ view of a quarter of the Inner Detector, indicating the dimensions of each part of the detector. PP1,PPB1 and PPF1 indicate the patch panels for the Inner Detector services [83].

barrel layers and two nine-layer end-caps. In the barrel, the modules [85] are arranged in coaxial staves and the end-caps are perpendicular to the beam-line. A barrel module is shown in Figure 5.5(b).

The sensors are based on a standard p-n junction in oxygenated silicon with AC-coupled read-out strips. They are 6 cm long with a strip pitch of 80 μm. In the barrel, two sensors are daisy-chained together, creating a single 12 cm unit. Each module has two 12 cm sensor units glued to opposite sides of a base-board. The sensors are rotated at ± 20 mrad around the center of the module (40 mrad with respect to each other). This design results in 16 μm position resolution in the $r - \phi$ plane. The end-cap modules have a very similar design.

Unlike the pixel read-out, which contains the TOT analog information, the SCT features binary read-out. The hybrids consist of an integrated circuit with a pre-amplifier, signal shaper and a discriminator which determines whether or not the charge collected in a strip is over threshold. The hybrid also distributes the trigger and timing information as well as sends the compressed and serialized data to the off-detector read-out system. More detail on the SCT sensors and electronics is found in [85].

5.2.3 Transition Radiation Tracker

The Transition Radiation Tracker (TRT) is the outermost component of the Inner Detector and provides continuous tracking out to a radius of 1 m, improving the track resolution considerably at low cost. It additionally provides electron-pion separation. It is separated
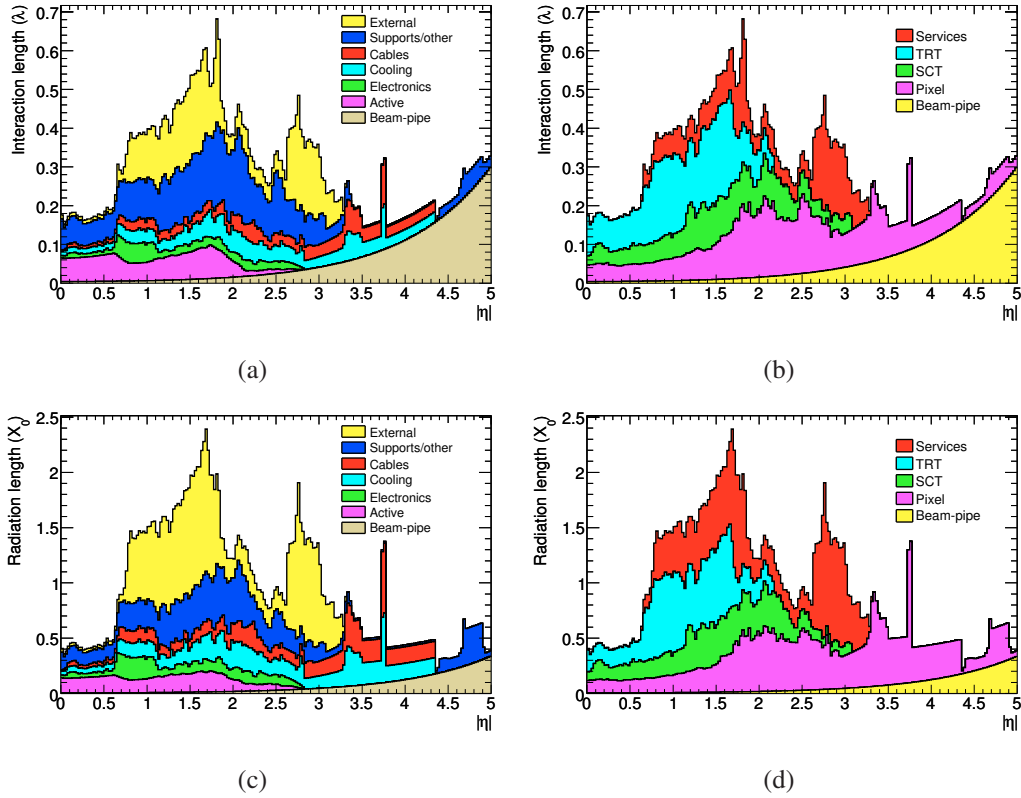
Figure 5.4. Material distributions at the exit of the ATLAS Inner Detector as a function of $|\eta|$. Shown in terms of interaction length (top) and radiation length (bottom) for both the detector subsystems(left) and the type of material(right). External refers to external services [83].

into a barrel ($|\eta| \lesssim 0.8$) and two end-caps ($1.0 \lesssim |\eta| \lesssim 1.9$) with a transition region in between. In the barrel region a particle will traverse at least 36 straws, and have a position measurement in the $R - \phi$ plane. In the end-caps a variable number of straws are crossed and the position measurement is in the $\phi - z$ plane.

The TRT is built out of straw tubes filled with a $Xe/CO_2/O_2$ gas mixture in a carbon fiber frame. A barrel module is shown in Figure 5.6. The 4 mm diameter tubes are made out of polyimide, with a thin layer of aluminium on one side and polyurethane on the other. In the center of each tube is a tungsten wire which is at ground with respect to the tubes which are at $\sim$-150V. Particles are tracked via ionizing radiation, and additional information is gained by transition radiation, which produces a much larger signal. The transition radiation is generated by polypropylene fibers in the barrel and polypropylene foils in the end-caps, which are interleaved with the straw tubes.

The TRT is read out at the end of each straw. The signal is amplified and shaped and then passed to two discriminators: one with a low threshold to detect minimum ionizing radiation and the other with a high threshold to detect transition radiation. The drift time
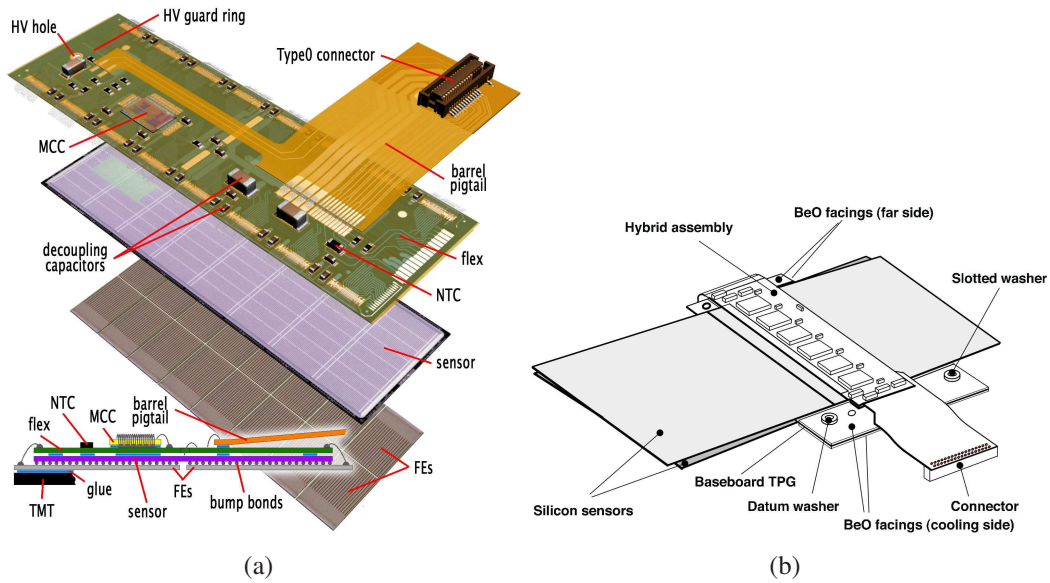
Figure 5.5. An exploded view of a barrel pixel module (b) and a SCT barrel module (b) [83].

of the signal is additionally measured, which improves the position resolution of the hit. More details on the TRT can be found in [86, 87].

5.3   The Calorimeters

The ATLAS calorimeter system is designed for precise measurements of particle energies over a wide dynamic range. It also needs to distinguish between electrons/photons and jets and contain hadronic showers for precise missing energy measurements. It is divided into an electromagnetic calorimeter, a central hadronic calorimeter, and two forward hadronic calorimeters. All the detectors except for the central hadronic calorimeter use liquid argon as the active material. The central hadronic calorimeter uses lower cost scintillator. In the following each of the three systems is described.

5.3.1   Liquid Argon Electromagnetic Calorimeters

The Liquid Argon electromagnetic calorimeter [88] is a non-compensating, ionization-based, sampling detector using lead passive material and liquid argon active material. It is divided into a barrel ($|\eta| < 1.5$) and two end-caps ($1.4 < |\eta| < 3.2$). Each region is housed in a separate cryostat, which thermally isolates the detector and keeps it at ≈ 88.5K with a temperature dispersion of less than 100 mK [89]. The precise temperature control is necessary because the liquid argon response varies with temperature.
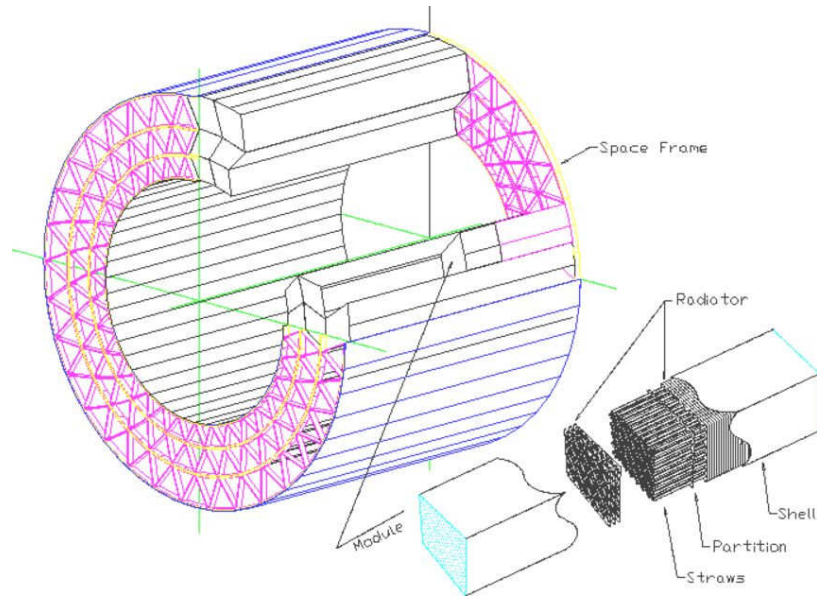
Figure 5.6. A schematic of barrel TRT module showing the straw and radiator structure. [83]

The calorimeter has an accordion-shaped geometry, shown in Figure 5.7, which provides full coverage in ϕ with no gaps. Each lead absorber is sandwiched between two sheets of stainless steel to provide structural support. In between absorber layers are copper electrodes [90] which are formed from three sheets of copper separated by a thin insulating layer of polyimide. The outer two layers are held at a high voltage with respect to the inner layer, which reads out the signal via capacitive coupling. The copper is etched into cells which define the granularity.

The detector has three levels of segmentation, which vary in η and radial depth. The innermost layer has the finest granularity and is designed for photon/pion separation and for precise η measurements of neutral particles. It has a depth of $6X_0$ and an η segmentation of $3.125{\times}10^{-3}$. The second layer varies from 6 to $24X_0$ and is designed to contain photon showers. It has an η segmentation of 0.025. The final layer is used to help measure high energy showers and separate between electromagnetic and hadronic showers. It has a depth of at least $2X_0$ everywhere and an η segmentation of 0.05.

The electrodes are read-out by front-end boards (FEBs) which are located at the cryostat feed-throughs. The FEBs amplify, shape and digitize the signal and then send it to the off-detector electronics. In parallel, amplified signals from multiple channels are summed for the Level 1 trigger.

The high granularity and variable segmentation allows for detailed shower shape analyses. In particular, there is good photon/pion separation and electron identification. The
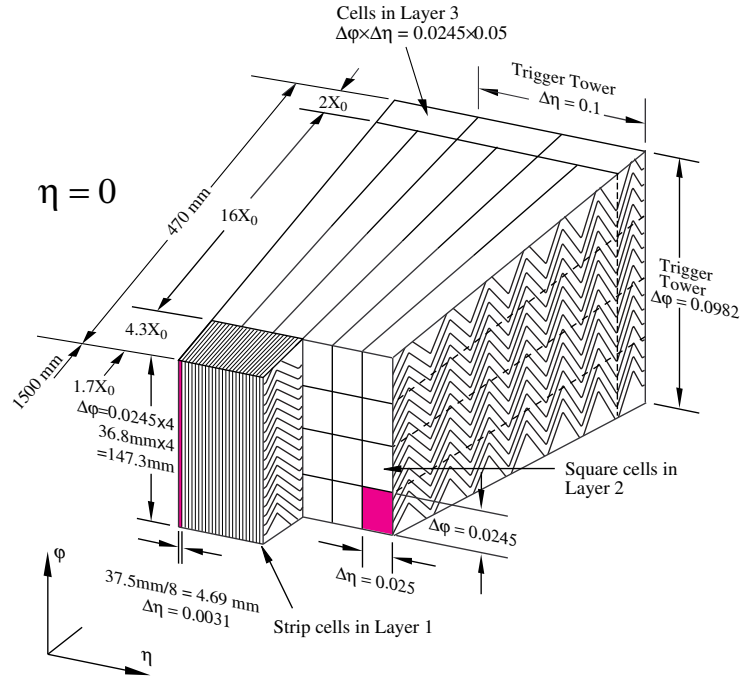
Figure 5.7. A diagram of an electromagnetic calorimeter segment. [83]

electromagnetic calorimeter is designed to have an energy resolution of

$$\frac{\sigma_E}{E} = \frac{10\%}{\sqrt{E}} \oplus 0.7\%$$

where E is the energy of the primary electromagnetic objects, e.g. electron or photon. This design goal gives precise measurements of not only electromagnetic objects but of jet energies as well [83]. Approximately two-thirds of the energy of a jet is lost in the electromagnetic calorimeter therefore the high precision of the electromagnetic calorimeter contributes to good jet energy resolution [91].

5.3.2 The Tile Hadronic Calorimeter

The Tile calorimeter is a non-compensating sampling calorimeter made of steel absorbers and plastic[1] scintillator active material. It consists of a barrel ($|\eta| < 1.0$) and two extended barrels ($1.0 < |\eta| < 1.7$) which surround the electromagnetic calorimeter. With a depth of $7.4\lambda_0$, it is designed to contain high energy hadronic showers at low cost. Additionally, the steel provides the flux return for the inner detector solenoid [92].

---

[1]Polystyrene doped with 1.5% PTP (p-terphenyl) and 0.044% POPOP($C_{24}H_{16}N_2O_2$) as the primary and secondary fluors, respectively.
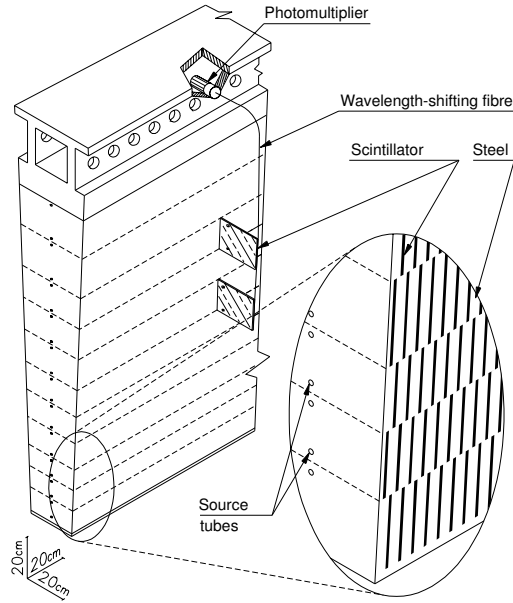
Figure 5.8. A diagram of a tile drawer. [83]

Each section of the detector is divided up into 64 modules in ϕ; a schematic of a module is shown in Figure 5.8. Scintillator tiles are inserted into a periodic structure of steel plates. Wavelength-shifting read-out fibers run along the tile edges to photomultiplier tubes (PMTs) which are at the top (largest R) of the module. The PMTs are housed in *drawers* along with the front-end electronics.

The front-end electronics for the Tile Calorimeter are bundled in the drawers with the PMTs, magnetic shielding and the 3-in-1 cards [93]. The 3-in-1 cards shape the PMT signal into a pulse with a 50 ns width and sum the signals of several cells for the Level 1 trigger. They also provide a calibration system using a cesium source. The shaped PMT pulse is sent to a 10-bit analog-to-digital converter (ADC) which samples the signal at the 25 ns bunch-crossing rate. The samples are then sent to the off-detector back-end electronics. The back-end electronics are common to all calorimeters and are described in Section 6.2.

The hadronic calorimeter is designed to have an energy resolution of

$$\frac{\sigma_E}{E} = \frac{50\%}{\sqrt{E}} \oplus 3\%$$

[83] and contain multi-TeV hadronic showers.

5.3.3 Forward Calorimeters

The ATLAS Forward Calorimeters consist of a copper and liquid-argon hadronic end-cap (HEC) calorimeter and a combination copper-tungsten and liquid-argon forward calorime-

ter (FCAL). The HEC covers $1.5 < |\eta| < 3.2$ and the FCAL covers $3.1 < |\eta| < 4.9$ and they are both housed in the same cyrostat as the electromagnetic endcap calorimeters. The arrangement of the calorimeters is shown in Figure 5.9(a). The design of these detectors differs from the previously mentioned calorimeters because they need to withstand the high flux of particles in the forward direction.

The HEC is conceptually similar to the liquid argon calorimeter described above. Scintillator would not withstand the radiation damage it would accrue at small radii to the beam-line, therefore liquid argon is used instead. The copper takes the place of the lead absorbers and the detector has a flat plate design, perpendicular to the beam-line, instead of the accordion structure.
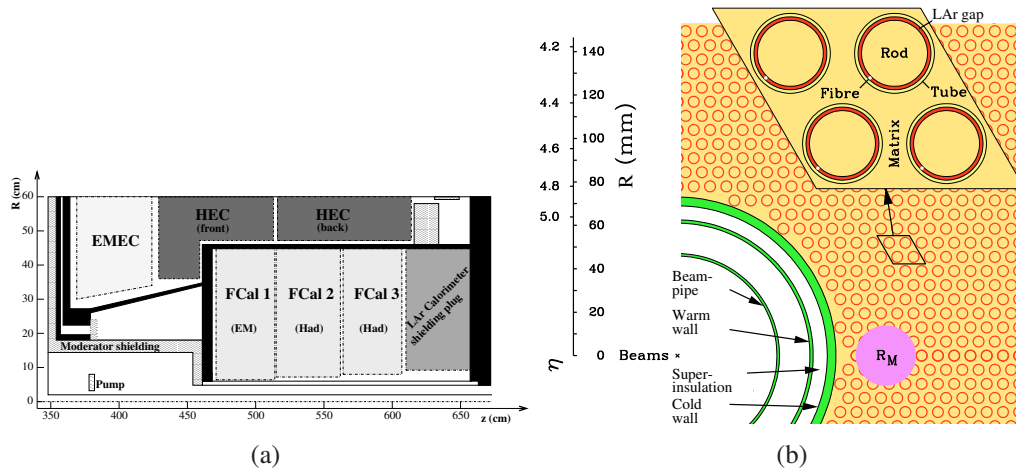
Figure 5.9. (a): Layout of the forward calorimeters. (b): cross-sectional sketch of the FCAL showing the electrode structure as well as the Molière radius, R_M [83].

The FCAL was designed to provide both electromagnetic and hadronic calorimetry in an intense radiation environment. The electrodes are formed of coaxial copper rods and tubes with a very small liquid argon gap in between for fast signal extraction. The gap is maintained by a radiation hard plastic wire wrapped around the tubes. The electrodes are held in a copper matrix in the first compartment and a tungsten matrix in the second and third compartments. The matrix is formed by drilling holes into the passive material plates. A cross-section of the FCAL is sketched in Figure 5.9(b).

5.4 The Muon Spectrometer

The ATLAS Muon System, shown in Figure 5.10, consists of several different tracking technologies arranged around a massive superconducting air-core toroid system. The toroid consists of a barrel and two end-caps providing 1 to 7.5 Tm in bending power. ATLAS chose an air-core design to minimize multiple scattering of the muons so that 10%

momentum resolution could be achieved at 1 TeV.
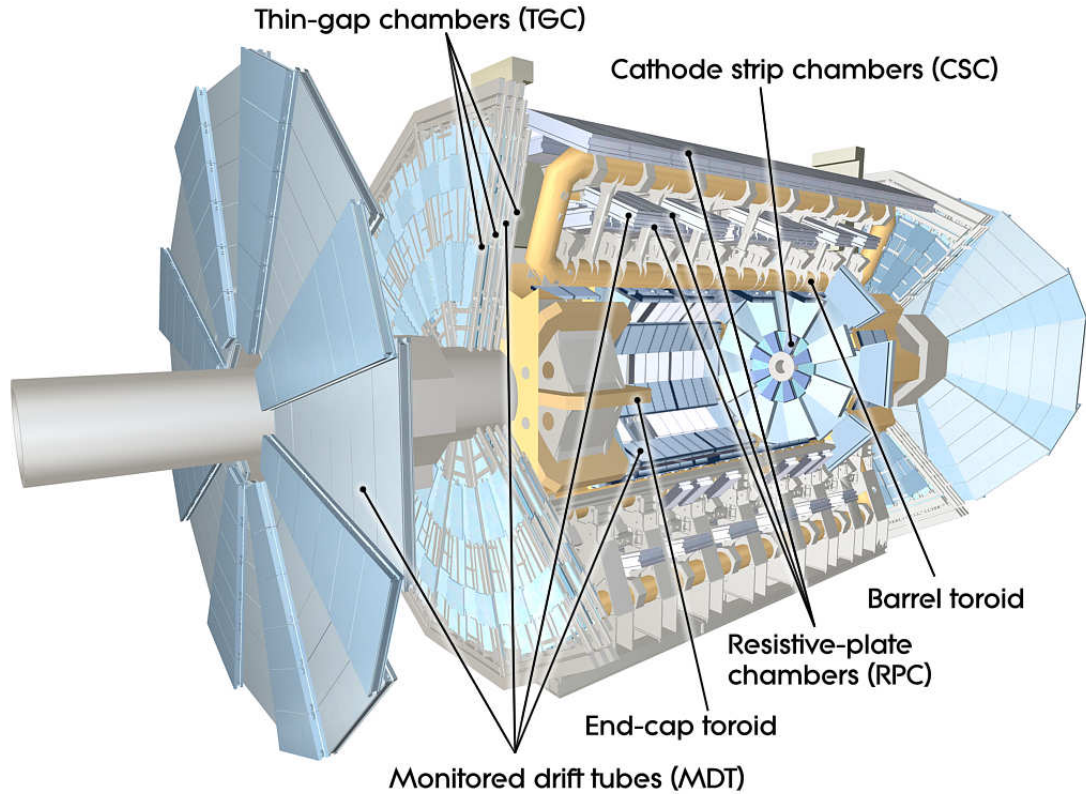
Figure 5.10. A cutaway view of the ATLAS muon system indicating the locations of the various tracking technologies. [83]

Four different tracking technologies are used. In the barrel, resistive plate chambers (RPCs) are used for triggering. They consist of parallel resistive plates separated by 2mm with a potential difference across them. Avalanches are triggered by particles ionizing the gas ($C_2H_2F_4$/Iso-C_4H_{10}/SF_6) in between the plates and are subsequently read-out. These provide a fast response so that triggering on muons can occur at Level 1. The trade-off is low position resolution: 10 mm in both z and ϕ. They are complimented by precision monitored drift tubes (MDTs) which are built out of pressurized tubes filled with Ar/CO_2 gas. Each tube has a coaxial tungsten wire that collects the ionizing charge. The timing of the signal is used to achieve a z position resolution of 35 μm. In the end-caps, thin gap chambers (TGCs), which are similar to multi-wire proportional chambers, take the place of the trigger chambers. Cathode strip chambers (CSCs) provide the precision measurements in the end-caps. CSCs are multi-wire proportional chambers with segmented cathodes to improve position resolution.

5.5   The Luminosity Detectors

ATLAS uses several detectors for luminosity measurements. In this section only the detectors relevant to this thesis are discussed.

5.5.1   Minimum Bias Trigger Scintillators

The Minimum Bias Trigger Scintillators (MBTS) are the primary detectors used in this measurement. They consist of 2 cm thick polystyrene scintillators behind a 3 cm boronated polyethylene moderator mounted 3.6 m from the interaction point on either side of the detector. Each side is divided into counters, consisting of an inner ($2.09 < |\eta| < 2.82$, 43 cm $< R <$ 88 cm) and outer($2.82 < |\eta| < 3.84$, 14 cm $< R <$ 43 cm) ring in η and eight sections in ϕ, leading to 16 possible measurements per side. In 2010 one of the inner counters on the C-side ($z < 0$) was dead, resulting in only 31 total possible measurements. Each counter is made of two pieces of scintillator glued down the middle. Wavelength shifting fibers embedded in a machined groove in each half of the scintillator and down the center of the detector collect the emitted light. The structure of the MBTS detector is shown in Figure 5.11(a). The wavelength shifting fibers are welded to normal optical fibers which transmit the signal to the Tile calorimeter PMTs and the readout proceeds exactly as for the tile calorimeter. The only difference is that the high gain output of the amplifier is sent to the trigger rather than the low gain, which is the default for tile calorimeter operation.

The MBTS is designed to provide simple and efficient triggering during early data taking. Each counter's Tile 3-in-1 card sends a trigger signal. On each side of the detector, the 16 signals are passed to an amplifier set to minimal gain. There are 2×16 outputs from the amplifier. One group of 16 is sent to a leading edge (LE) discriminator, the other is sent to a constant fraction discriminator (CFD). The LE output is then sent to the central trigger processor which determines how many MBTS counters were over threshold. It then sets the Level 1 trigger bits L1_MBTS_X and L1_MBTS_X_X, which indicates X MBTS counters were over threshold or X counters were over threshold on each side, respectively. The CFD is not currently used. Figure 5.11(b) shows the Level 1 trigger logic.

For the early part of the 2010 running period L1_MBTS_1 was the primary trigger. As will be shown in Chapter 8.2, it was highly efficient at selecting inelastic interactions. The MBTS scintillators are not radiation hard, and therefore they will yellow and become unusable sometime during the 2011-2012 run.

5.5.2   LUCID

LUCID (LUminosity measurement using Cerenkov Integrating Detector[2]) is ATLAS's primary luminosity detector. It is located 17 m from the interaction point and covers $5.5 < |\eta| < 5.9$. It functions as a relative luminosity detector, with the calibration for absolute

---

[2]Perhaps one of the worst reverse-engineered acronyms ever.

WLS fibers
4+4 / **4+4**

16 Plastic Scintillators

(a)

(b)
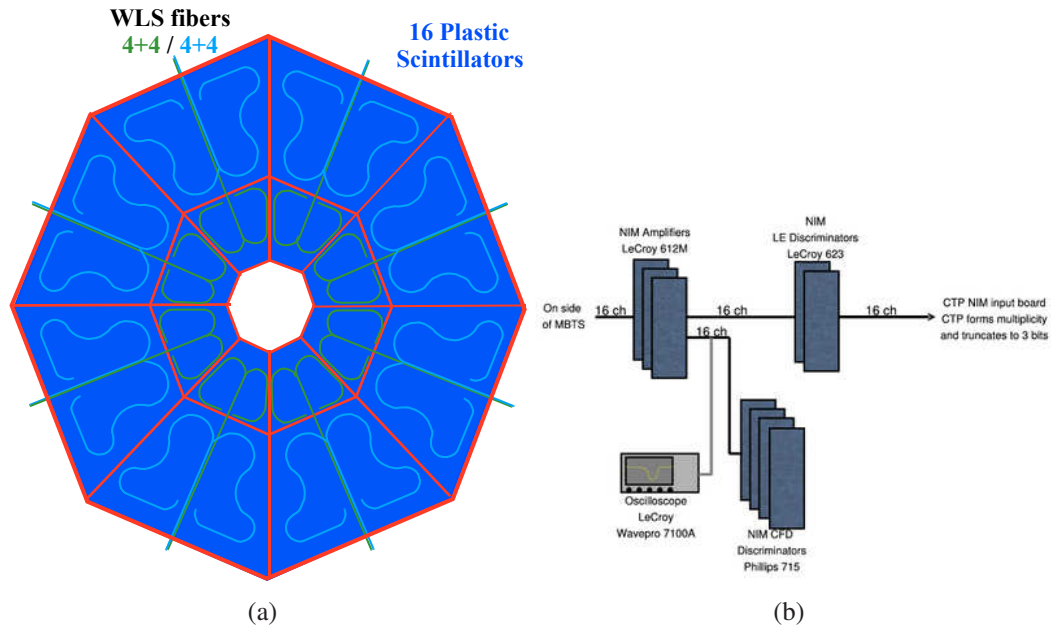
Figure 5.11. (a) The MBTS detector design showing the positions of the wavelength shifting fibers. (b) Schema of the MBTS trigger logic.

luminosity coming from machine parameters as described in Chapter 10 or measurements by the ALFA detector[3], once ALFA is operational.

LUCID consists of twenty 1.5 m in length, 15 mm in radius, highly-polished aluminum tubes filled with C_4F_{10}. Particles traversing a tube emit Cerenkov radiation which is reflected on average 3 times in the tube before it is read out by PMTs. The PMTs relay the signal to a constant fraction discriminator which has a preset threshold. The bunch-crossing-by-bunch-crossing luminosity is calculated on the read-out board by a Field Programmable Gate Array (FPGA). Every time a level-1 accept is recorded this information is sent to the ATLAS data acquisition system. This design is crucial for determining a luminosity independent of the ATLAS data acquisition system, which can suffer from dead-time.

Because LUCID is a very forward detector, it must contend with high occupancy and large radiation doses. At nominal LHC luminosities the PMTs will be replaced by quartz fibers coupled to the Cerenkov tubes by Winston cones, which will transmit the signal to shielded PMTs off-detector. Figure 5.12 shows a closeup of the connection between the tubes and PMTs, as well as the future coupling of the Winston cones to the quartz fibers.

---

[3]The ALFA detector is a far forward roman pot detector which will be used during special LHC runs to measure the forward elastic cross-section. It will simultaneously measure σ_{tot} and $\mathcal{L}$, from which the LUCID calibration will be derived.
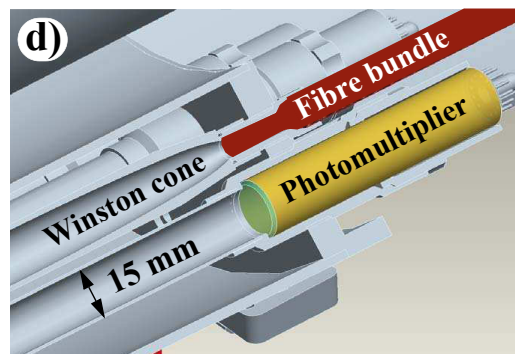
Figure 5.12. View of the coupling between the LUCID detector Cerenkov tubes and PMTs, as well as the future coupling via Winston cones to quartz readout fibers. [83].

<div align="right">

CHAPTER 6

</div>

Event Reconstruction

6.1 Track Reconstruction

This Chapter details elements of the ATLAS event reconstruction relevant to this thesis. Specifically, the track reconstruction and the calorimeter signal processing are described. This section concerns aspects of event reconstruction which relate to Inner Detector tracking. The ATLAS muon system also provides tracking but it is not discussed here.

6.1.1 Reconstruction Algorithms

Inner Detector reconstruction encompasses track, vertex and beam-spot reconstruction. The process begins with track reconstruction and concludes with primary vertex finding. Primary vertices are defined as the locations of proton-proton interactions, and there can be multiple primary vertices in an event if there are multiple proton interactions. The primary vertices are used to determine the luminous region, or beam-spot, roughly every two minutes during data-taking. Each of these steps is detailed below.

Track Reconstruction

The objective of charged particle tracking is to reconstruct a charged particle's trajectory from the energy it deposits in a detector. Because the detector is immersed in a magnetic field, the particle will take a helical path which will contain information about the particle's momentum vector. Any particle path can be represented by the following five parameters

$$d_0, z_0, \phi_0, \cot\theta, q/p_\mathrm{T} \tag{6.1}$$

modulo distortions due to energy loss and multiple scattering in the detector. The transverse impact parameter, d_0, is the distance of closest approach of the trajectory to the origin of the detector in the transverse $(x - y)$ plane. The point of closest approach is referred to as *perigee*. The longitudinal impact parameter, z_0, is the z coordinate of the trajectory at

perigee. ϕ_0 is the angle at perigee of the trajectory in the transverse plane. The polar angle, θ, is the angle with respect to the z axis made by the trajectory. The final parameter of the trajectory is the charged inverse of the particle's transverse momentum. It is given by the curvature of the track, $\rho = Bq/p_T$, where B is the magnetic field strength, q is the particle charge and p_T is its momentum in the transverse plane[1]. A sketch of the parameters in the transverse and longitudinal planes is shown in Figure 6.1. These parameters can also be expressed with respect to the point of closest approach to the interaction vertex (primary vertex), or the beam-spot, indicated by the superscript *"PV"* and *"BS"*, respectively.
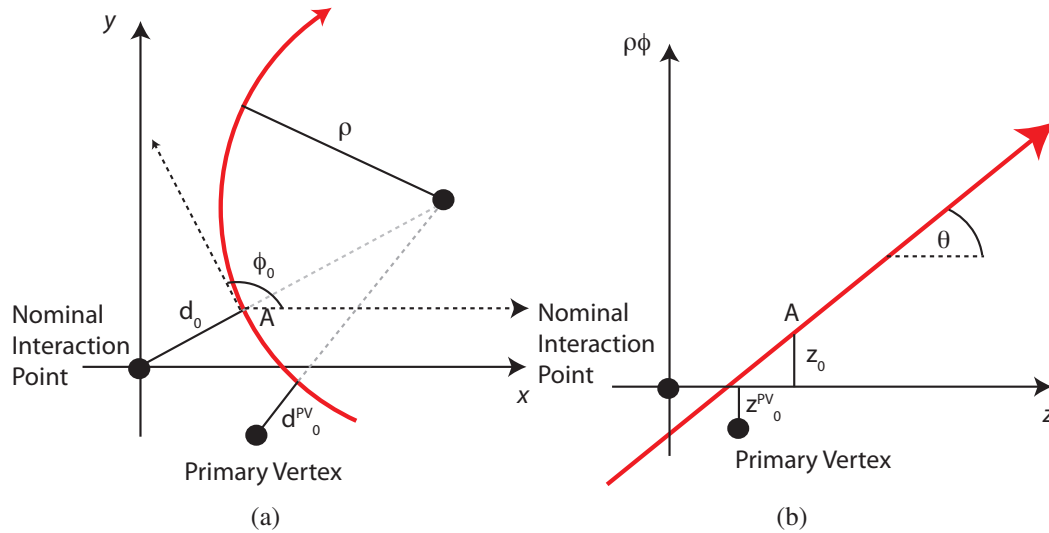
Figure 6.1. An illustration of track parameters in the transverse (a) and longitudinal (b) planes expressed with respect to the origin of the detector and the primary vertex.

The challenges of track reconstruction can be divided into two categories: track-finding and track-fitting. In the first, detector hits, .e.g. pixel clusters, SCT clusters, or TRT hits, are associated to form tracks. In the second, the hits are used to determine the parameters of the charged particle which created the track. The efficiency to find tracks is discussed in Section 6.1.2, and the parameter resolution is discussed in Section 6.1.3.

The ATLAS tracking suite is named New Tracking (NEWT) [94] and uses a modular, multi-stage approach to track reconstruction. A Kalman filter [95] is used as the primary track fitting algorithm. The tracking begins with an *inside-out* reconstruction algorithm which starts with hits in the silicon detectors. The inputs to track finding are *spacepoints*, consisting of:

- **Pixel clusters**, which are formed by clustering neighboring hits in the pixel detector. The local cluster position and radius of the pixel layer are used to determine a single three-dimensional point.

---

[1]Expressed in natural units assuming a uniform magnetic field.

- **Double-sided SCT clusters**, which are formed by clustering neighboring hit strips in the SCT detector. Clusters on opposing sides of each double-sided detector layer are then associated and the stereo position information is used to provide a single three-dimensional point.

TRT hits, which provide only two dimensional position information, are used in later parts of the reconstruction.

The first step of reconstruction creates track *seeds*, which are formed out of three space-points on separate layers. All possible combinations of hits from the first pixel layer to the first layer of the SCT are considered. Then the three measurement points are used to uniquely determine a circle which gives the seed parameters in the transverse plane, assuming a uniform magnetic field an neglecting multiple scattering. A cut on the p_T and d_0 of the seeds is applied to reject bad seeds and speed up the reconstruction. Next, the spacepoints are discarded and the algorithm uses the seed to define a road to search for hits. Practically this means that single-sided SCT clusters are used in addition to double-sided ones. It then proceeds to associate clusters to the track seeds. Each time a hit is associated, the fit is updated to include its information. A simplified model of the ATLAS detector geometry is used to predict each step of the filtering, taking into account the material crossed by the particle.

The hit association phase allows for hits to be shared by multiple tracks or creates *fake* tracks out of a random assortment of hits, resulting in a significant fraction of poor quality tracks. In order to clean up the found tracks, ambiguity solving [96] is used to select good quality tracks. First, the track is refit with a more sophisticated version of the ATLAS geometry to better estimate material effects. Second, the track is given a score, taking into account the χ^2/N_{dof} of the fit, the number and quality of hits from each subdetector and the number of holes[2] associated to the track. An iterative procedure is used to reduce the hit-sharing between tracks by assigning the shared hit to the track with the higher score and then refitting both tracks and re-evaluating their score. Once the ambiguity solving step is finished a quality cut is applied and only tracks passing a configurable threshold are kept. Lastly, the selected tracks are extrapolated to the TRT to define a road from which to attach TRT hits. Figure 6.2 illustrates the various steps of track finding. The track reconstruction process reconstructs tracks up to an $|\eta|$ of 2.5 and a p_T as low as 100 MeV.

After the inside-out tracking is run, the unassociated hits are used to do *outside-in* tracking, starting with the TRT. The outside-in tracking must be run last so that the possible combinations do not overwhelm the pattern recognition. TRT drift circles only give information in two directions: the $r - \phi$ plane in the barrel and $\phi - z$ plane in the endcaps. In the $r - \phi$ plane tracks with p_T of 500 MeV or greater are nearly straight lines over the length of the TRT detector and in the $\phi - z$ plane they are truly straight lines because the magnetic field does not produce any bending in that plane. A Hough transform [98] is used to reconstruct tracks. The transform works by mapping *each* hit in the $r - \phi$ ($\phi - z$) plane

---

[2]A hole is defined as an instance when a track is extrapolated through a detector layer but no hit is associated to it.
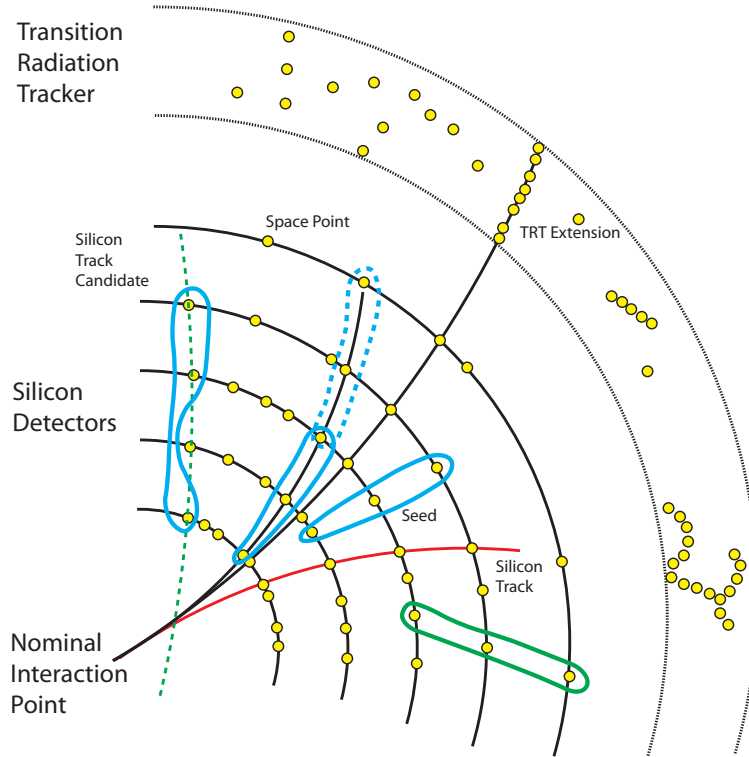
Figure 6.2. Schematic of the different stages of track reconstruction. Spacepoints are represented by the yellow dots and blue lines indicate track seeds. The dashed blue line is a seed which shares a single hit and the green line illustrates a seed which was rejected prior to hit association. The green dashed line indicates a track candidate which failed the impact parameter cuts. The red line represents a silicon-only track. The black line indicates a track including TRT hits. Figure reproduced from [97] with permission of the author.

into the space of straight lines intersecting the point, $\phi_0 - c_{T(z)}$, where $c_{T(z)}$ is $1/p_{T(z)}$:

$$c_{T(z)} = r(z) \cdot cos(\phi_0) + \phi \cdot sin(\phi_0) \tag{6.2}$$

If all hits arise from a single line, the lines in the $\phi_0 - c_{T(z)}$ plane will intersect at a single $\phi_0, c_{T(z)}$ value. Practically, the transform fills a histogram in several η bins for each event and the local maxima indicate the track segments.

Once a track segment is formed, it is used to define a road *into* the silicon detector. The algorithm searches for hits not already associated to an inside-out track. The same track fitting and scoring is performed as in the inside-out case, although with different criteria for the scoring. This track finding is powerful for finding electrons from photon conversions and other secondary particles from decays which are displaced a significant distance from the primary vertex.

Primary Vertex Reconstruction and Beam Spot Determination

After track-finding is completed, the tracks are used to find the primary event vertex. Immediately after the data is collected, a 36-hr calibration loop is run on a subset of the data in which the beam-spot is determined using primary vertices found without knowledge of the beam-spot. Then the bulk reconstruction is run and primary-vertex finding is rerun with the constraint of the beam-spot position. The following section describes how the primary-vertices are reconstructed.

The primary-vertex reconstruction [99] is divided into a finding and a fitting phase, as in the case of the track reconstruction.

The inputs to the primary vertex finding are tracks satisfying

- $p_T > 100$ MeV

- $|d_0| < 4$ mm

- $\sigma(d_0) < 5$ mm

- $\sigma(z_0) < 10$ mm

- $N_{SCT} \geq 4$ and $N_{SCT} + N_{pix} \geq 6$

where $\sigma(d_0)(\sigma(z_0))$ is the uncertainty on the $d_0(z_0)$ measurement. These cuts are used to reduce the fraction of tracks from secondary particles which are considered for the vertex finding.

An iterative vertex-finding algorithm is used. First, a vertex seed is determined by histograming the z_0 of all of the selected tracks. If the beam-spot has already been determined, the impact parameter with respect to the beam-spot, z_0^{BS}, is used. The seed position and nearby tracks are passed to an *adaptive vertex fitting* [100] algorithm which is χ^2 based. Tracks which are incompatible with the vertex are used to find additional primary vertices in the event. If the beam-spot has already been determined, the beamspot position is used as an additional constraint in the vertex fit. In the case of multiple primary vertices in an event, the vertex with the highest Σp_T^2 of the tracks in the event is the vertex associated with the hard interaction in the event. The vertex-finding efficiency was found to be over 90% efficient for events with at least two tracks with $p_T > 100$ MeV and fully efficient for events with at least six tracks with $p_T > 100$ MeV [70].

To determine the beam-spot, vertices with at least four tracks are considered. The position of the vertices are input to an unbinned maximum likelihood fit which extracts the beam-spot position in x,y, and z, as well as the width in each coordinate, and any tilt of the luminous region in the $x - z$ and $y - z$ planes. Typical sizes in the transverse planes were ≈ 0.05 mm and ≈ 40mm in the longitudinal plane in the early 2010 runs.

6.1.2 Tracking Efficiency

The charged particle tracking efficiency is dependent upon many factors such as the particle type, momentum and the amount of material a particle traverses. Muons, which have small interaction cross-sections in the 1 GeV to 1 TeV range, have very high tracking efficiency. Conversely, pions and protons interact strongly and therefore have lower tracking efficiency. The amount of material traversed by a particle determines the probability of having a nuclear interaction, which reduces the tracking efficiency. Electrons are even more difficult to reconstruct because bremstralung changes the momentum midflight. Lower momentum particles suffer from higher interaction rates and more multiple-scattering, making track-finding difficult. This section discusses the absolute tracking efficiency as well as studies of the relative efficiency of the silicon based tracking with respect to the TRT tracking.

Absolute Tracking Efficiency

The absolute tracking efficiency of all particle species can only be determined through Monte Carlo simulation studies. Generally the efficiency can be described by

$$\epsilon(\eta, p_\mathrm{T}, ...) = \frac{N_\mathrm{TrkMatch}(\eta, p_\mathrm{T}, ...)}{N_\mathrm{gen}(\eta, p_\mathrm{T}, ...)} \tag{6.3}$$

Where $N_\mathrm{gen}(\eta, p_\mathrm{T}, ...)$ is the number of generated charged particles as a function of the η, p_T, and any other variables, and $N_\mathrm{TrkMatch}(\eta, p_\mathrm{T}, ...)$ is the subset of those generated particles which are matched to a track. There are also *fake* tracks, which are reconstructed tracks not matched to any generated particles. The definition of a track match is dependent on the criteria used to do the matching. For example, generated particles can be matched to tracks by requiring that there be a track within a cone, $\Delta R = \sqrt{\Delta \eta^2 + \Delta \phi^2}$ of the generated particle at perigee. Alternatively, the Monte Carlo simulation information about which generated particles produced each hit on the track can be used to assign a probability that the track was created by a particular generated particle.

The following metric is used to assign the probability a track came from a specific particle:

$$prob. = \frac{10 \cdot N_\mathrm{pix}^\mathrm{gen} + 5 \cdot N_\mathrm{SCT}^\mathrm{gen} + N_\mathrm{TRT}^\mathrm{gen}}{10 \cdot N_\mathrm{pix}^\mathrm{rec} + 5 \cdot N_\mathrm{SCT}^\mathrm{rec} + N_\mathrm{TRT}^\mathrm{rec}} \tag{6.4}$$

where $N_\mathrm{det}^\mathrm{gen}$ is the subset of the hits on the reconstructed track, $N_\mathrm{det}^\mathrm{rec}$, which come from the generated particle. The pixel hits have a larger weight than the SCT hits because there are less than half as many pixel hits as SCT hits on track. The same reasoning applies to explain why the TRT hits have much lower weight. A single track can have matches to multiple generated particles. Therefore, a cutoff of $prob = 0.55$ is applied to determine whether a generated particle was matched to a track.

The efficiency is determined as a function of p_T and η, although the dependence on other variables was also examined. Figure 6.3 shows the tracking efficiency as a function of p_T and η, as determined in [70].

(a)   (b)
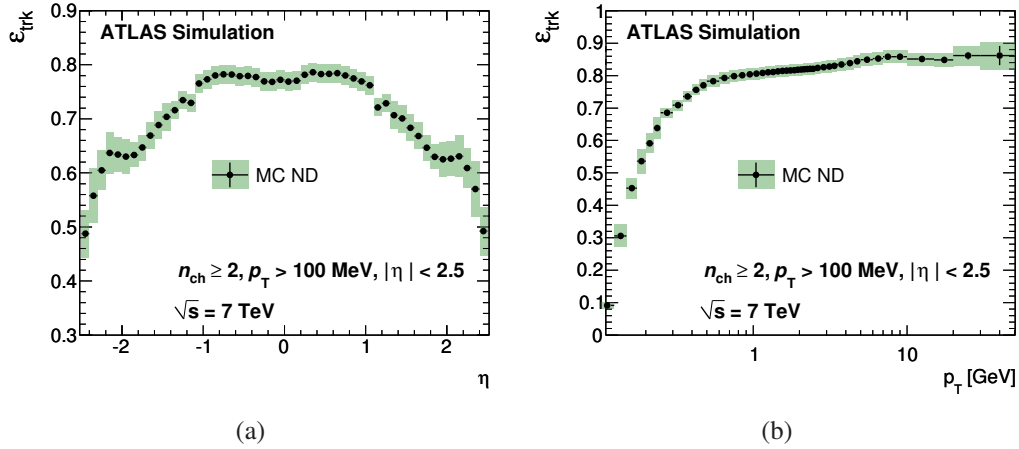
Figure 6.3. Tracking efficiency as a function of η (a) and p_T (b) determined with non-diffractive minimumbias Monte Carlo events [70].

In order to validate that the simulation accurately describes the tracking quantities and to give confidence that the efficiencies are correctly modeled, many distributions were studied. Figure 6.4 shows the average number of pixel and SCT hits on associated to a track as a function of η for tracks with $100 < p_T < 500$. This distribution is very sensitive to how well the Monte Carlo models the tracking in the data, and excellent agreement is found. However, in Section 11, track distributions for a diffraction-enhanced subset of events is examined and the agreement between data and MC simulation is worse than shown here.

Relative Silicon Tracking Efficiency

The absolute tracking efficiency used in early tracking analyses must come from the Monte Carlo simulation as methods for measuring the absolute efficiency require high statistics and are only applicable to specific particle species. However, constraints can be placed on the accuracy with which the simulation describes the tracking efficiency with data-driven techniques. This section describes a technique for measuring the silicon pattern recognition efficiency.

The combined tracks used for analysis are built from silicon track seeds. Therefore, it is important to understand the efficiency for the pattern recognition to create a silicon track, ϵ_{Si}. Standalone TRT tracking, in which tracks are formed with a pattern recognition algorithm which is independent from the inside-out tracking and uses no information from the silicon detectors, provides a suitable denominator to measure the silicon pattern recognition efficiency. In this study the standalone TRT Tracks are formed using an algorithm
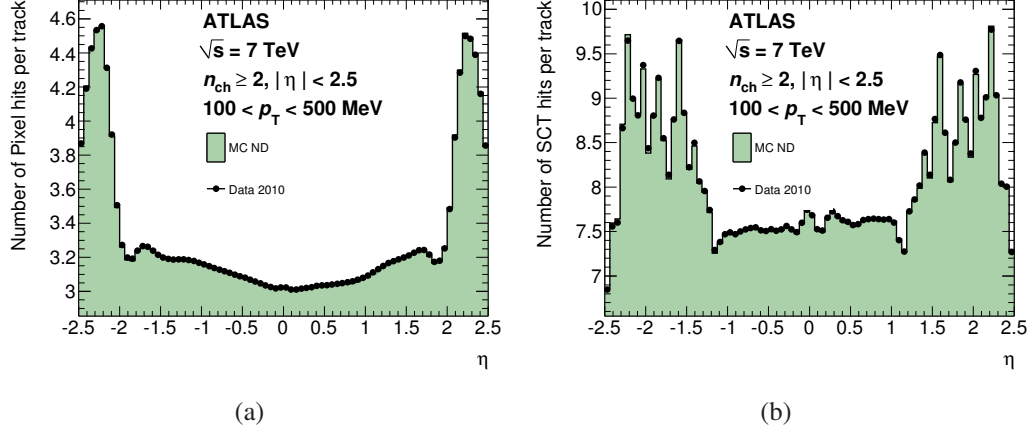
Figure 6.4. Average number of pixel (a) and SCT (b) hits as a function of η, comparing data and non-diffractive minimum-bias Monte Carlo events [70]. Only tracks with $100 < p_T < 500$ MeV are used.

developed for the combined test beam (CTB)[3] which has been modified to work in a collision environment. Unfortunately this algorithm only works in the TRT barrel. At the time of the first LHC collisions, the default Hough transform-based Standalone TRT tracking, which includes the endcaps, was not sufficiently robust to do this analysis.

Comparisons of the TRT and Silicon tracks cannot determine the absolute efficiency, but a relative efficiency, ϵ_{Si}^r, of the silicon tracking with respect to the TRT tracking can be examined by measuring the fraction of good quality TRT tracks for which a matching silicon track is found. The relative efficiency is defined as

$$\epsilon_{Si}^r = \frac{N_{Si+Trt}^{obs}}{N_{Trt}^{obs}} \tag{6.5}$$

$$\tag{6.6}$$

where N_{Trt} is the number of TRT tracks and N_{Si+Trt} is subset of TRT tracks matched to a silicon track. The definition can be expanded using the following equations:

$$\epsilon_{Si}^r = \frac{N_{Si+Trt}^{obs}}{N_{Trt}^{obs}} \tag{6.7}$$

$$\frac{N_{Si+Trt}^{obs}}{N_{Trt}^{obs}} = \frac{\epsilon_m \epsilon_{Trt} \epsilon_{Si} N}{\epsilon_{Trt} N + f_{Trt} N_{Trt}^{obs}} \tag{6.8}$$

$$\frac{N_{Si+Trt}^{obs}}{N_{Trt}^{obs}} = \frac{\epsilon_m^p \epsilon_{Trt}^p \epsilon_{Si}^p N^p + \epsilon_m^s \epsilon_{Trt}^s \epsilon_{Si}^s N^s}{\epsilon_{Trt}^p N^p + \epsilon_{Trt}^s N^s + f_{Trt} N_{Trt}^{obs}} \tag{6.9}$$

---

[3]The combined test beam refers to a period in 2004 when a slice of the Atlas detector was tested at a beamline at CERN.

where ϵ_m is the efficiency of the matching parameter, ϵ_{Trt} is the TRT tracking efficiency, N is the number of charged particles and f_{Trt} is the fake rate for TRT tracks. The efficiency for primaries and secondaries is denoted by the p or s superscript. Primaries are defined as tracks coming from from the primary vertex or prompt decays. Secondaries come from decays of long lived particles, nuclear interactions and electrons from photon conversions. The physics efficiency of interest is the primary efficiency, ϵ_{Si}^p, and consequently, cuts are used to limit the contribution from secondaries and fakes.

In the ideal case without secondaries and fakes, the relative efficiency would simplify to

$$\epsilon_{\mathrm{Si}}^r \;=\; \frac{N_{\mathrm{Si+Trt}}^{obs}}{N_{\mathrm{Trt}}^{obs}} \tag{6.10}$$

$$\;=\; \epsilon_m \epsilon_{\mathrm{Si}} \tag{6.11}$$

allowing a measurement of the "true" efficiency, up to the efficiency of the matching parameter. It will be shown that both ϵ_{Si}^r and the matching parameter distribution agree well within uncertainties between data and simulation, giving us confidence that the pattern recognition efficiency for silicon tracks, ϵ_{Si}, is described by the simulation.

This study requires that the TRT tracks are in the TRT barrel and have a $d_0 < 10$mm. The requirement on d_0 is looser than that typically used to select primary tracks to allow for the broader d_0 resolution of the TRT. No requirement is placed on the impact parameter in the z-direction because no measurement of this quantity is provided in the TRT barrel. In order to ensure that the tracks are well measured they are required to be formed from at least 20 TRT hits. No requirements are placed on the silicon tracks matched to the TRT tracks.

The difference in ϕ_0, the azimuthal angle expressed at perigee, between the TRT track and the closest silicon track is used as the matching parameter, $\delta\phi_{\mathrm{TRT-Si}}$. The $\delta\phi_{\mathrm{TRT-Si}}$ distributions for both data and simulation are shown in Figure 6.5. The data and MC agree well and it is notable that there is not a significant difference in the $\delta\phi_{\mathrm{TRT-Si}}$ distributions for the nominal geometry and a Monte Carlo sample with extra material in the detector description, indicating that the method is largely insensitive to the amount of material in the detector. The matching cut is chosen to be $\delta\phi_{\mathrm{TRT-Si}} < 0.04$ radians. The efficiency of this cut varies with momentum due to the change in resolution with momentum, but a fixed cut was chosen for simplicity.

Figure 6.6 and Figure 6.7 show the relative silicon tracking efficiency ϵ_{Si}^r for both data and simulation. In general, the data and the nominal MC agree well. When looking at the efficiency as a function of momentum, as in Figure 6.6, deviations between the data an MC are significantly less than 0.5%. The efficiency is lowest in the 0.5 GeV bin, at 86%. It reaches a plateau near 1 GeV at 96%. By dividing the MC into its primary and secondary contributions, it is apparent that the shape of the turn on curve is dictated by the secondary contribution. The primary contribution is nearly fully efficient by 0.6 GeV. The relative efficiency is lower for the secondaries partly due to the fact that the secondaries are significantly displaced from the primary vertex and often times do not leave enough hits to
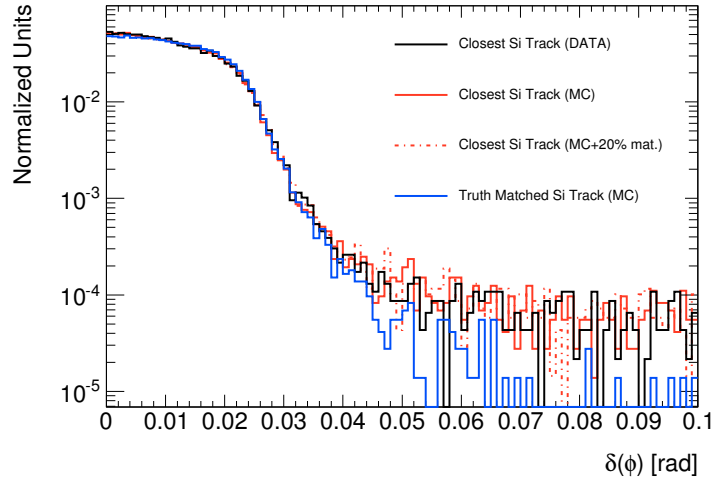
Figure 6.5. $\delta\phi$ between Standalone TRT track and closest Silicon (Resolved) track. The histogram for data (black line), for the default MC (red solid line), 20% extra material MC (red dashed line), and truth match MC track (blue line) are shown.

be reconstructed. Additionally, the matching is done using the perigee parameters which are inappropriate for secondaries since they do not originate from the primary vertex.

The efficiency as a function of d_0, shown in Fig. 6.7(a), is flat for a wide range of impact parameter values. Data and MC agree very well up to values of $\pm$ 12 mm, where the efficiency drops rapidly and the disagreement is up to a few percent. In the plateau region the total efficiency is approximately 97% for both data and MC.

Figure 6.7(b) shows the efficiency as a function of the other cut variable, the number of TRT hits on track N_{TRT}. Data and MC disagree up to a few percent for low values of N_{TRT} but in general agree very well. For very low numbers of TRT hits the relative efficiency is low. However, those TRT track are poorly measured and it is unsurprising that they don't match well to silicon tracks. As in the other distributions the primary efficiency is very high. The secondary efficiency continues to rise as a function of N_{TRT}, reaching a maximum value of 80% before the statistics become too poor to quote a number for the efficiency.

The systematic uncertainty, shown in Table 6.1, is divided into two components. The first is due to the level of data and MC agreement, and the second encompasses uncertainties in the method itself. The data-MC agreement systematic is taken as the raw difference between the data and MC and is found to be 0.1% for tracks with $p_{\mathrm{T}} < 1$ GeV and neglible for tracks with higher momentum. In order to obtain a systematic uncertainty on the method we vary the cuts on the denominator such as the d_0 cut and the number of TRT hits cut, as well as the $\delta\phi$ cut, and then take the spread in the difference in the ratio of data to MC multiplied by the efficiency in MC as the systematic. This definition captures how strongly the characterization of the agreement between data and Monte Carlo simulation
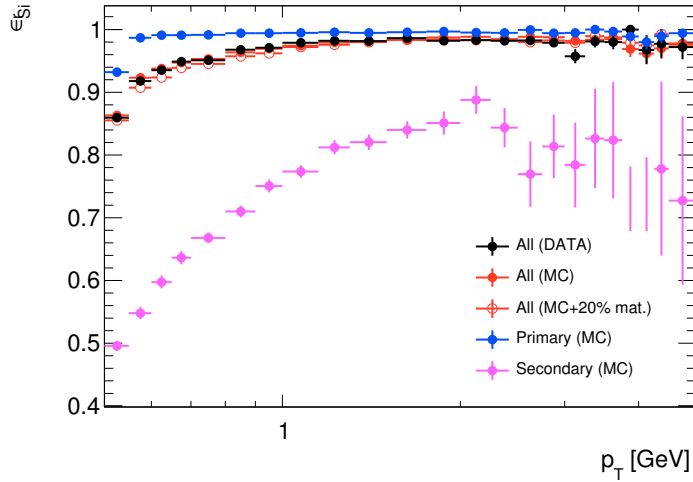
Figure 6.6. Relative efficiency of the Silicon tracking with respect to the TRT tracking as a function of the p_T of the TRT track. Data are in black, nominal Monte Carlo data are in red solid, and 20% extra material MC in red open circles. Additionally the MC efficiency was divided into primary(blue) and secondary(pink) contributions.

(a)   (b)
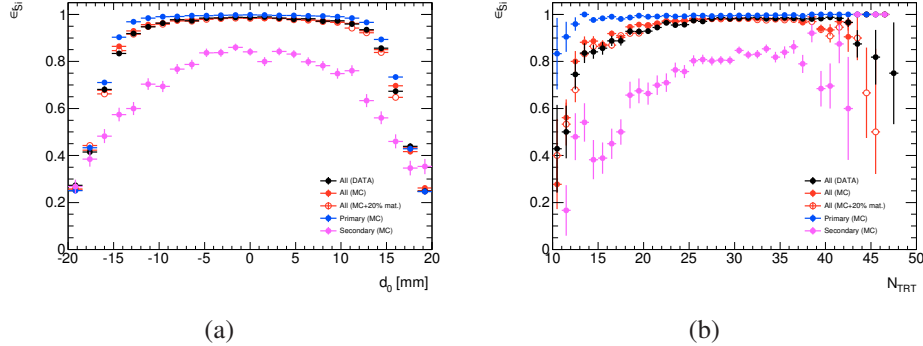
Figure 6.7. Relative efficiency of the Silicon tracking with respect to the TRT tracking for d_0 and N_{TRT}. Data are in black, nominal Monte Carlo data are in red solid, and 20% extra material MC in red open circles. Additional the MC efficiency was divided into primary(blue) and secondary(pink) contributions.

depends upon the specific tracks used to measure the efficiency and the defintion of a match. As is shown in the table, the variations in the cut values do not significantly effect the efficiency or the agreement between data and simulation and all variations are at the 0.5% level or less. In total we measure an uncertainty of a 0.73% on the tracks with 500 MeV $<$ p_T $<$1 GeV and 0.26% for tracks with p_T $>$1 GeV . The uncertainty is higher for the lower momentum range because the efficiency is changing rapidly in this region, allowing small discrepancies to have a greater weight than in the plateau region.

	$500 MeV < p_T < 1 GeV$			$p_T > 1 GeV$		
	Data(%)	MC(%)	Ratio	Data(%)	MC(%)	Ratio
default cuts	93.54±.08	93.64±.06	0.9989±.0011	97.79±.06	97.79 ±.05	1.0011±.08
sys. err.		.1%			<.01%	
$\delta\phi$ <.05 rad	94.22±.07	94.19±.06	1.0004±.001	98.08±.06	97.97±.04	1.0011±.007
<.03 rad	90.38±.09	90.09±.08	.9946±.0013	96.94±.07	96.94±.06	1.0000±.0009
$\delta\phi$ sys. err.		.40%			.01%	
d_0 < 5 mm	94.44±.10	94.46±.08	0.9998±0.0014	98.44±.07	98.23±.06	1.002±.0009
d_0 sys. err.		.08%			.1%	
N_{TRT} ≥ 18	93.39±.07	93.35±.06	.9985±.0011	97.81±.06	97.73±.05	1.0008±.0008
≥ 25	93.78±.08	93.73±.07	1.0005±.0011	98.10±.06	97.79±.05	1.0016±.0008
N_{TRT} sys. err.		.6%			.03%	
Total sys. err.		.73%			.26%	

Table 6.1. Summary of relative silicon efficiencies for data and simulation, as well as systematic uncertainties arising from discrepancies between data and simulation and dependence on the matching parameter ($\delta\phi$) and the denominator cuts(d_0, N_{TRT}). See text for further explanation.

Tracking Efficiency Systematic Uncertainties

The systematic uncertainties on the tracking efficiency arise from several sources which are listed below.

- **Material:** The ability of the Monte Carlo simulation to reproduce the true tracking efficiency crucially depends on the accuracy of the material modeling in the simulation. The agreement was studied using many methods. One method examined the reconstructed K_S^0 invariant mass from charged pion decays as a function of the position in the detector. A complimentary method looked at the length of tracks which is sensitive to the nuclear interaction modeling. Additional methods included looking at the width of hit residuals for low momentum tracks and looking at the efficiency for a track reconstructed with the pixel detector to be reconstructed in the SCT. The last method was particularly powerful for assessing the material budget in the forward regions of the detector. It was determined that the material is known to within 10% in the central region of the detector and up to 30% in the highest η regions of the tracker [70]. This leads to a $\pm 2 - 15$ % uncertainty on the tracking efficiency, depending on the η and p_T of the track.

- **Seed Resolution:** The tracking resolution effects the tracking efficiency at low momentum because mismeasured tracks with momentum greater than 100 MeV will either fall below the minimum track momentum cut of 100 MeV or tracks with lower momentum will migrate into the track sample. This leads to a $\pm 5\%$ uncertainty between 100 and 150 MeV.

- **Track Selection:** The agreement between data and MC on the track selection efficiency was determined by varying the track selection requirements and comparing the data and MC agreement. This leads to a flat $\pm 1\%$ uncertainty.

6.1.3   Track Resolution

The tracking resolution is a measure of how well the track reconstruction reproduces the parameters of the particle which created it. At low momenta, the track resolution is degraded by multiple-scattering. At high momenta, the resolution is driven by how well the detector is aligned.

Prior to first LHC collisions, the ATLAS inner detector took data with a cosmic ray trigger with the solenoid on and off. The solenoid-on data provided a unique opportunity to measure the tracking resolution *in-situ* with muons. The resolution was measured directly by splitting the tracks, which pass through both the top and bottom halves of the detector, into an upper and lower track. The difference of the measured track parameters of the upper and lower tracks were related to the tracking resolution via the following

$$\delta_v \quad = \quad v_{\text{up}} - v_{\text{low}} \tag{6.12}$$

$$\sigma(\delta_v) = \sqrt{\sigma^v_{\text{up}} + \sigma^v_{\text{low}}} \tag{6.13}$$

$$= \sqrt{2}\sigma_v \tag{6.14}$$

where v is the parameter of interest, such as p_{T}, d_0, etc. and $\sigma^v_{\text{up(low)}}$ is the track parameter resolution for the upper(lower) half-track. Equation 6.14 states that the width of the δ_v distribution is determined by the error on the upper and lower half-tracks and, assuming that the resolution is the same for both halves of the detector, gives the collision-like track resolution on v. Figure 6.8 sketches the procedure.
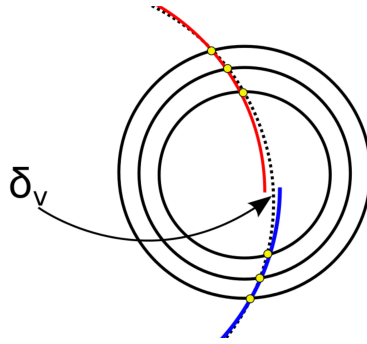
Figure 6.8. Toy example of half-tracks. The dashed black line indicates the particle trajectory. The yellow dots represent the hits created by the particle. The red (blue) line is the reconstructed track in the upper(lower) detector half. δ_v is the difference in the track parameter v at perigee.

Figure 6.9 shows the curvature ($\frac{q}{p}$) and transverse impact parameter (d_0) resolutions and biases as measured with the 2009 cosmic ray data [101]. In these plots tracks were required to have at least 2 pixel hits and 6 SCT hits and the full ID tracks were required to also have 25 TRT hits. Additionally they were required to have $|d_0| < 40$ mm in order to make the tracks as collision-like as possible without sacrificing too many statistics. These plots show that the inclusion of the TRT hits helps the momentum resolution considerably at high momenta. Additionally it shows momentum dependent curvature biases as well as a flat impact parameter bias, indicating that the alignment of the detector has weak misalignment modes. These plots were made with a preliminary alignment which has improved considerably since then.

With collision data the momentum resolution can be monitored using muon resonances such as the J/ψ and Υ mesons and the Z boson.

6.2 MBTS And Calorimeter Signal Reconstruction

The ATLAS calorimeters, while using a range of different technologies, have the same basic procedure for signal reconstruction: optimal filtering. The optimal filtering algorithm [103] used by ATLAS was first developed for liquid ionization calorimeters. However, it has been proven to accomodate scintillator based calorimters as well [104].
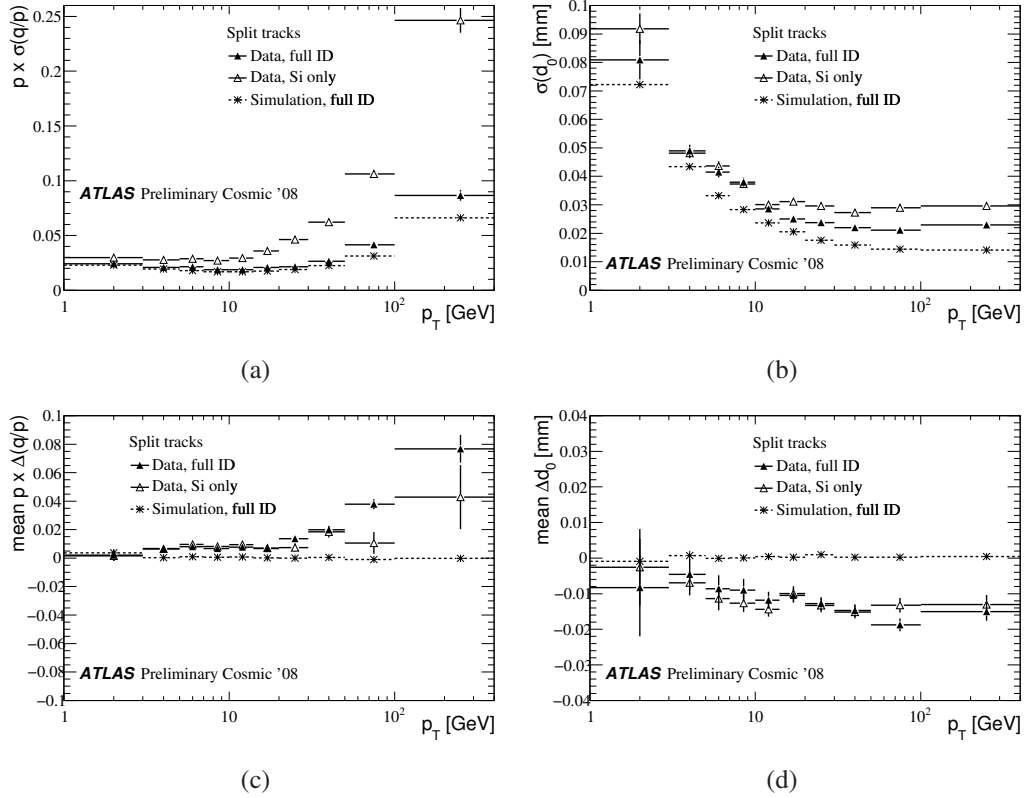
Figure 6.9. $\frac{q}{p}$ (a) and d_0 (b) resolution versus p_T. $\frac{q}{p}$ (c) and d_0 (d) resolution bias versus p_T. All plots using cosmic ray data collected in 2009 [102].

The Liquid Argon calorimeters and the Tile Calorimeter share the same basic back-end electronics to do the signal processing. The MBTS uses Tile PMTs and is fully integrated into the Tile read-out chain. Read-out drivers (RODs) on the back-end electronics board contain Digital Signal Processors (DSP) which recieve the samples of the detector signals from the front-end electronics. The shape of the signal and the number of samplings vary depending on the detector, but the procedure for fitting for the total charge or energy collected and time of arrival of the signal are the same. This fitting is done by the DSPs for the Level 2 triggering or in the offline reconstruction.

Each sample can be expressed in terms of the pulse shape function $g(t)$:

$$S_i = p + Ag(t_i + \tau) + n_i \tag{6.15}$$

where p is the pedestal, A is the amplitude of the signal, τ is the phase of the signal relative to the pulse shape function and n_i is the noise. If the pulse shape function and noise are known, then A, τ and p can be determined using a taylor expansion the above equa-

tion [104]:

$$A = \sum_{i=1}^{n} a_i S_i; \quad A\tau = \sum_{i=1}^{n} b_i S_i; \quad p = \sum_{i=1}^{n} c_i S_i \qquad (6.16)$$

where a_i, b_i, c_i are constants which are precalculated for each channel and stored on the ROD DSPs or in the offline reconstruction database. Knowing A and τ gives the charge deposited in the detector as well as the time of arrival of the signal. The fit results are then used for Level 2 trigger decisions. Figure 6.10 shows a toy model of a signal and samplings. The quality of the fit is also computed and is determined by

$$\chi^2 = \sum_{i=1}^{n} |(S_i - p) - A g_i| \qquad (6.17)$$

taking the absolute value is used online instead of squaring each term to reduce compuation time in the DSPs.

The optimal filtering procedure is performed again during the offline reconstruction, resulting in a more precise determination of the charge and time of the signal. Figure 6.11 shows the difference in the A- and C-side MBTS signal times for the offline and online algorithms in collision data [105]. Proton interactions from colliding beams have a Δt of 0, whereas beam-gas and beam-halo are at $\pm$ 25ns. The largest difference in the online and offline determinations are for the beam-gas and beam-halo events, which are significantly out-of-time. The peaks at $\pm$ 75ns in the offline are artificial. The differences in the background peak positions between the online and offline methods are due to biases in the online signal reconstruction.

The following sections detail the specifics of the Liquid Argon and Tile signals.

6.2.1   Liquid Argon Calorimeters

The Liquid Argon calorimeter signal consists of ionization charge collected by electrodes in the accordian structure. The signal has a very short rise-time and is followed by a linear decay, but it is shaped by the front end electronics into a bipolar distribution. The shaped signal as measured with cosmic rays is shown in Figure 6.12(a). The liquid argon signal is slow, lasting approximately 450 ns. Although sampling every 25 ns is possible, during normal data-taking only five samples are read-out.

6.2.2   Tile Calorimeter and the MBTS

The Tile Calorimeter signal output are scintillation pulses from PMTs which are shaped by the analog 3-in-1 card. Figure 6.12(b) shows the analog signal response after shaping in the high and low gain channels as determined from pion test beams. The shaping stretches the signals so that the samplings can be made at reasonable intervals. They are sampled
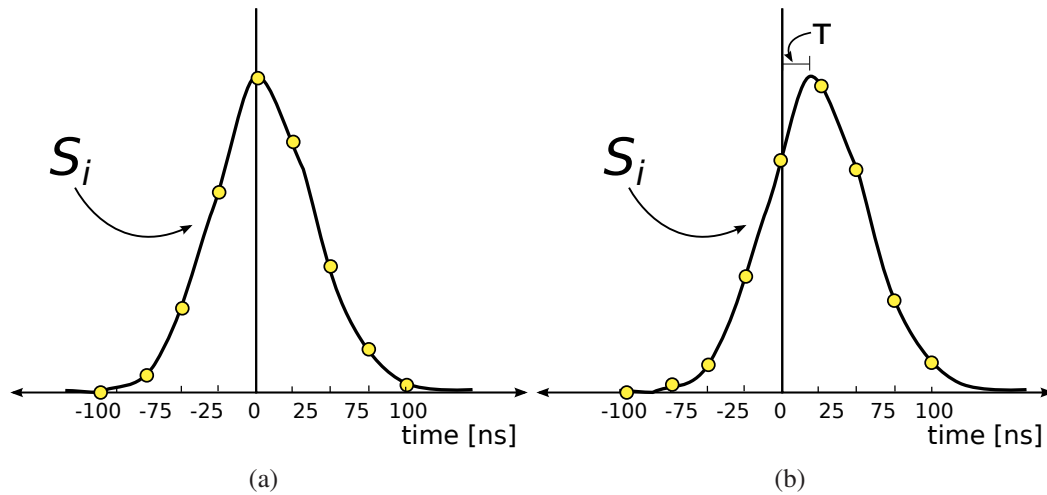
Figure 6.10. Toy representation of a PMT pulse in the black line, the yellow dots represent the sampling points. (a) represents an in-time pulse, (b) represents a pulse with phase τ.

seven times by the digitizer, as described in Section 5.3.2. The MBTS uses Tile PMTs and the full Tile readout chain. Therefore, the signals are very similar. Typical charges collected under the 2010 running conditions by the MBTS are 0.7 pC for a single particle. The MBTS offline performance is studied in detail in Chapter 8.
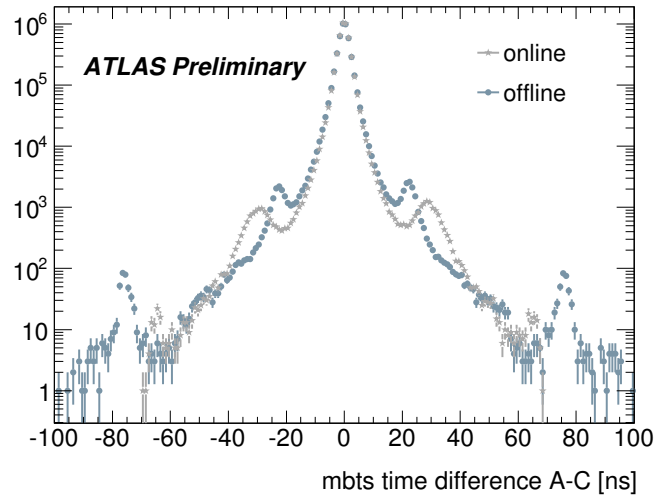
Figure 6.11. Difference in timing measurements between the A and C-sides of the MBTS for the online and offline algorithms in 7 TeV collision data. The differences in the background peak positions are due to biases in the online signal reconstruction [105].

(a)   (b)
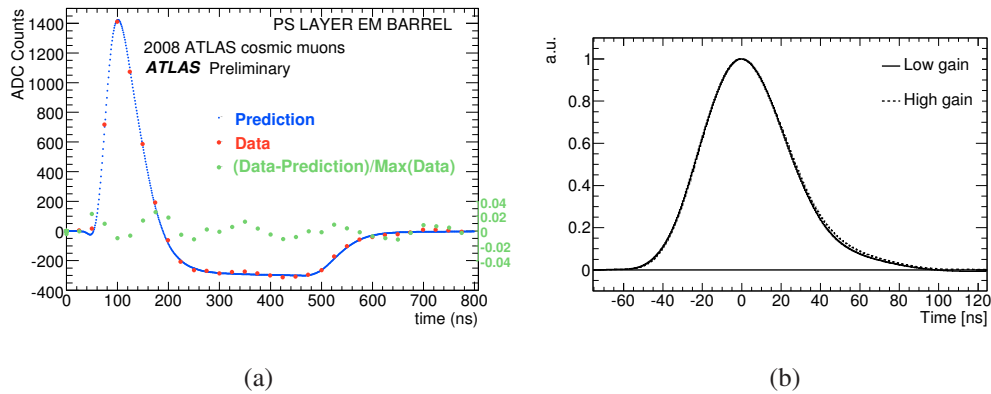
Figure 6.12. (a): Liquid argon pulse shape with the data (red points) and prediction(blue points) for cosmic ray muons. The green points indicate the fractional difference between the data and prediction. (b): Tile PMT signal shapes determined from pion testbeams for the low gain (solid line) and high gain (dashed line) channels [106].

CHAPTER 7

Collision and Monte Carlo Datasets

Nearly all of the work presented in this thesis used common datasets. This chapter describes both the collision data and the Monte Carlo data samples.

7.1 Data

The majority of the results presented here come from the second day of 7 TeV collisions: LHC fill 1013, ATLAS run 152221. This run consists of approximately 1.4 million events taken by the L1_MBTS_1 trigger described in Chapter 5.5.1. This trigger was run without a prescale and there were no requirements applied in addition to the single MBTS trigger hit. Two other runs are used for consistency checks: the first run at 7 TeV and a later run with a higher $\langle\mu\rangle$, the average number of proton interactions per crossing. The integrated and instantaneous luminosities as well as $\langle\mu\rangle$ are listed in Table 7.1 for each considered run.

These runs all have low $\langle\mu\rangle$. In the first two runs considered the effect of multiple interactions in a single crossing (pile-up) is negligible. In the third run, 154817, $\langle\mu\rangle$ is a non-negligible 0.1, and it is corrected for following the procedure outlined in Chapter 10.

All of the data were reconstructed with the same version of the reconstruction software and detector geometry[1]. The reconstruction algorithms used in this analysis are described

---

[1]The data were processed in the "May Reprocessing" using AtlasProduction-15.6.9.8, and the ATLAS-GEO-10-0-0 geometry tag.

LHC Fill	ATLAS Run	Peak $\mathcal{L}$ [10^{27} cm^{-2}s^{-1}]	Integrated $\mathcal{L}$[μb^{-1}]	$\langle\mu\rangle$
1005	152166	0.9	7.0	0.007
1013	152221	1.2	20.3	0.008
1089	154817	18.0	541.0	0.11

Table 7.1. Summary of the data used in this analysis. Shown is the LHC Fill number, the ATLAS run number, the peak and integrated luminosities and the average number of interactions per crossing, μ.

in Chapter 6.

7.2   Monte Carlo Models

Three primary Monte Carlo simulations are used: PYTHIA 6, PYTHIA 8 and PHOJET. The details of the physics modeling behind these generators is described in Chapter 2.6. Several million events were generated for each of the ND, SD, DD and CD (where applicable) processes for each generator. In this document *generator-*, *hadron-*, *particle-* and *truth*-level distributions refer to quantities calculated or determined from the four-vectors of particles produced by the Monte Carlo generators. The term *Fully simulated*-events refers to generated events which were passed through the detector simulation [107]. The detector simulation uses a description of the detector geometry and material implemented in Geant4 [108] to simulate the interactions of the generated particles with the detector. The events are then passed through the same software chain as the data. Because the beam-spot longitudinal width is different in the MC than in the data, the MC events are weighted to the data beam-spot distribution.

In addition to the three generators mentioned above, a fourth fully simulated sample is considered to understand the effect of variations in the detector simulation. To obtain the samples, generated events from the PYTHIA 6 sample were passed through the detector simulation with a different version of the detector geometry. The events were reconstructed with the default version of the geometry description, thereby mimicking the effects of having an inaccurate material description. The description used[2] has a 20% increase in the radiation length of the Pixel and SCT services. Figure 7.1 compares the total radiation length of the nominal geometry with the geometry used for the extra material sample and the "best guess" of the material distribution[3] which was determined after the samples were fully simulated.

When considering alternate models of the diffractive mass spectrum, PYTHIA 8 is used to generate events according to the alternate spectrum. Then, either the truth information from those events is used or the fully simulated PYTHIA 8 events are re-weighted to the truth spectrum. Table 7.2 lists the models considered for the cross-section measurement Unless otherwise indicated, the PYTHIA relative cross-sections are used to combine the SD, DD, and ND process for all models except PHOJET.

---

[2] ATLAS-GEO-10-00-04
[3] ATLAS-GEO-16-00-00
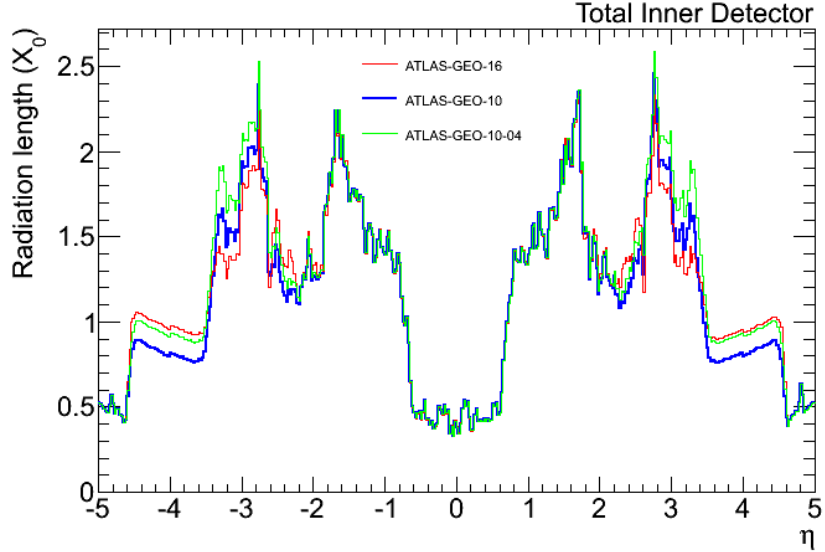
Figure 7.1. The material distribution in radiation lengths of the inner detector comparing the nominal geometry (Geo-10-00-00) with the geometry used for the extra material sample (Geo-10-00-04) and the "best guess" of the material distribution (Geo-16-00-00) which was determined after the samples were fully simulated.

Generator	Cross-section Model			Full Sim. ?
PHOJET	Engel			yes
PYTHIA 6	Schuler-Sjöstrand			yes
PYTHIA 8	Schuler-Sjöstrand			yes
	Donnachie and Landshoff	$\epsilon = 0.085$	$\alpha^{'} = 0.25\,\mathrm{GeV}^{-2}$	no
		$\epsilon = 0.06$	$\alpha^{'} = 0.25\,\mathrm{GeV}^{-2}$	no
		$\epsilon = 0.10$	$\alpha^{'} = 0.25\,\mathrm{GeV}^{-2}$	no
		$\epsilon = 0.085$	$\alpha^{'} = 0.10\,\mathrm{GeV}^{-2}$	no
		$\epsilon = 0.085$	$\alpha^{'} = 0.40\,\mathrm{GeV}^{-2}$	no
	Bruni and Ingelman			no
	Berger and Streng			no

Table 7.2. Summary of the models used in this analysis. The table indicates the generator was used for the modeling of exclusive properties, the cross-section model and whether or not fully simulated were available.

CHAPTER 8

MBTS Detector Response and Efficiency Measurements

The validity of the work presented in this thesis depends crucially on the understanding of the MBTS detectors. In particular, the determination of the agreement between the data and Monte Carlo simulation on the MBTS performance is one of the most critical experimental aspects of the work. Additionally, the simulation must accurately describe the material between the interaction point and the MBTS detector because it determines what fraction of the particles interact before reaching the MBTS. This chapter comprehensively examines the MBTS performance with a particular emphasis on the offline charge reconstruction and additionally constrains the agreement of the data and simulation on the material budget in the forward region of the detector. First, the offline noise profiles are determined. Next the trigger efficiency is determined. A data-driven approach to measuring the MBTS counter offline efficiency follows and the Monte Carlo simulation is tuned to reproduce the observed efficiency. Lastly, the agreement between the ability of the simulation to reproduce the material in the ATLAS detector in the MBTS acceptance is assessed.

8.1 Noise Profiles

The noise signal in the MBTS is generated by dark current in the PMTs as well as by intrinsic noise in the read out electronics which are shared with the Tile Calorimeter. It is typically well described by a double Gaussian centered at 0 pC. The noise was measured in the empty LHC bunches using events triggered by the zero bias trigger. The zero bias trigger randomly selects 25 ns window bunch-crossings with no LHC beam, therefore no particle signals, apart from exceedingly rare cosmic rays, are expected to contaminate this sample.

The noise distribution was plotted for each counter in Figure 8.1. All of the counters have similar noise profiles, and only a few counters have hits greater than $\pm$ 0.12 pC. Counters A5, A14 and C9 have slightly wider distributions. Counter A6 has one hit above
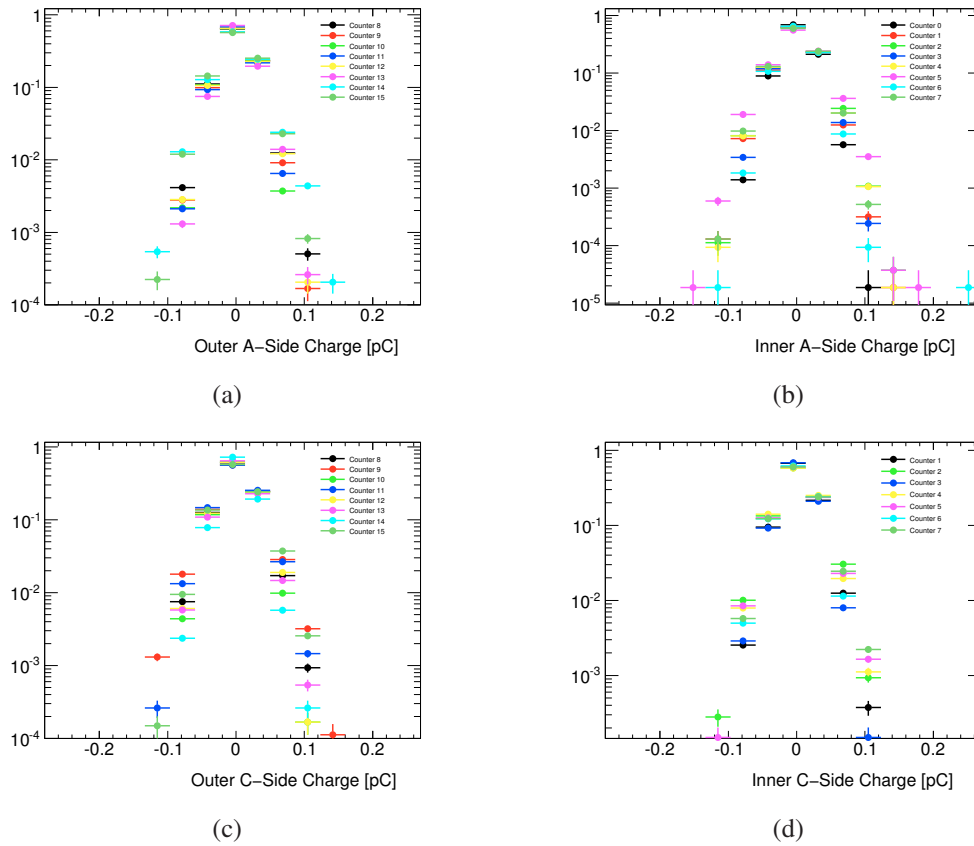
Figure 8.1. MBTS noise distribution measured in empty bunches for all counters on the A-side outer (a) and inner (b) ring and on the C-side outer (c) and inner (d) ring.

0.2 pC which could be from cosmic rays or "afterglow", a background described in Chapter 9. Overall, the noise is contained to less than 0.14 pC to the 10^{-4} level at the time this data was taken. The noise distribution is expected to widen as the counters accrue radiation damage. When fit with a double Gaussian, the typical model of the Tile Calorimeter read out electronics noise, the primary Gaussians have widths of 0.02 pC, while the secondary widths are generally slightly larger. However, the amplitudes of the second Gaussians are generally quite small, therefore a single Gaussian is an adequate description of the noise profile.

In the version of the detector simulation used for the Monte Carlo data processing in this document, the noise in the MBTS was artificially set to zero. Because new samples were unavailable at the time of this work, the noise was emulated in the simulation via an ad hoc smearing to all MBTS signals of a 0.02 pC width Gaussian centered at 0 pC.

8.2 Trigger Efficiency

The MBTS detector is primarily used by the ATLAS experiment for its highly efficient triggering on inelastic interactions. Its trigger capabilities are described in detail in Chapter 5.5.1.

In order to measure the trigger efficiency with respect to the offline event selection requirements, a reference trigger is used. The inelastic cross-section measurement counts the number of events with at least two offline MBTS hits, where a hit is defined as a counter with a charge greater that 0.15 pC. To measure the trigger efficiency with respect to that selection a purely random trigger is used as the reference. It randomly selects bunch-crossings when both beams are passing through ATLAS. Events from recorded by this trigger with at least two MBTS offline hits over threshold form the denominator of the efficiency measurement. The numerator is given by the subset of those event which also have the L1_MBTS_1 trigger bit set.
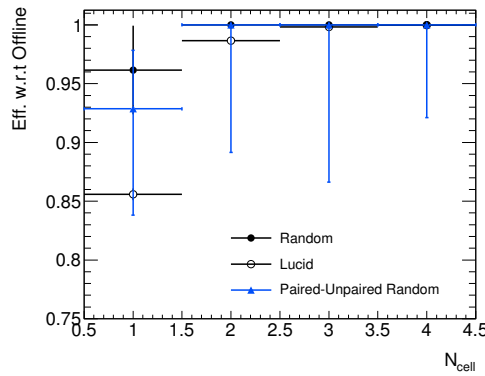
Figure 8.2. Trigger efficiency as a function of the number of MBTS cells with an offline charge of at least 0.15 pC. Shown are the efficiencies as determined using events triggered by the random trigger with (triangle) and without (closed circle) subtraction of unpaired bunches, and using events triggered by the LUCID trigger (open circle).

The effect of background was studied by subtracting events in the unpaired bunches passing a trigger which randomly selects bunch-crossings where a single beam is passing through ATLAS. No statistically significant effect was found. The trigger efficiency is measured to be $99.98^{+0.02}_{-0.12}\%$. A second reference trigger which requires at least one hit in the LUCID detector ($5.6 < |\eta| < 6.0$) is used to set the systematic uncertainty. It is sufficiently independent from the MBTS trigger because there is no overlap in η between the two detectors. This method yields an efficiency of 99.91%.

Figure 8.2 shows the efficiency as a function of the number of offline hits. Because of the low interaction rate of less than 0.01 interactions per crossing, the random trigger is inefficient at selecting inelastic interactions. For this reason, the trigger efficiency measurement is statistics limited.

In addition to the inelastic cross-section measurement, studies of tracks in a diffraction-enhanced minimum bias sample are also considered in this document. To measure the trigger efficiency in a sample with tracks, the efficiency of the L1_MBTS_1 trigger was studied as a function of the number of tracks in the event. For this measurement, the random trigger was used at Level 1 and additionally four pixel and four SCT spacepoints were

required at Level 2. This second requirement increased the efficiency to select inelastic interactions in the reference trigger. No requirement was made on the offline MBTS counters. In [109] the efficiency was measured as a function of the number of selected tracks with a p_T of 500 MeV or greater, and in [70] the efficiency was measured as a function of the number of selected tracks with a p_T of at least 100 MeV. The plots of the efficiency as a function of the number of tracks over threshold are shown in Figure 8.3. The impact parameter cuts of these tracks are with respect to the beam-spot, as indicated by the "BS" superscript.

(a)   (b)
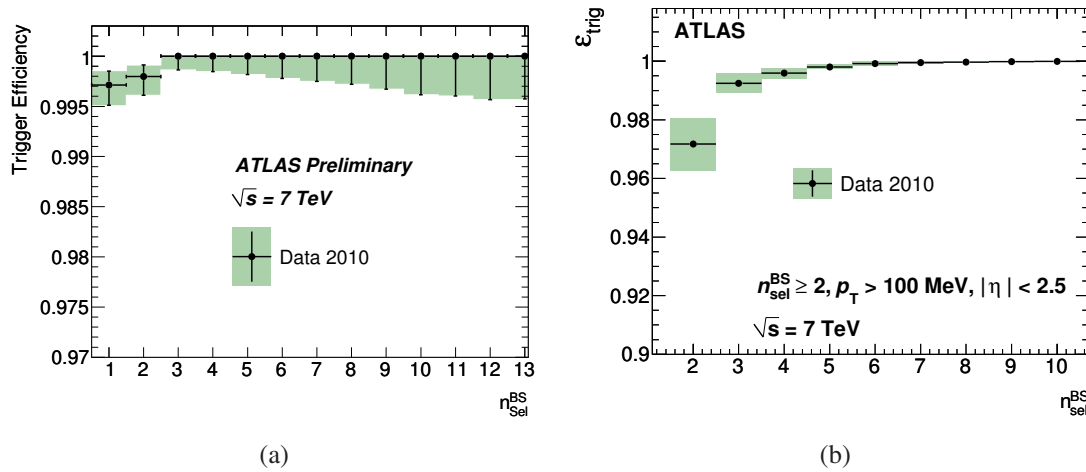
Figure 8.3. Trigger efficiency as a function of the number selected tracks with a p_T greater than 500 MeV (a) or 100 MeV (b). The green band indicates the systematic uncertainty due to the track selection and correlations between the reference trigger and the MBTS_1 trigger. [109, 70]

It is seen that the trigger efficiency is high, even for events with few, low momentum tracks.

8.3   Offline Efficiency Studies

The redundancy of the ATLAS detector can be used to investigate the MBTS counter efficiency in both data and Monte Carlo simulation. The basic premise of the studies presented in this section is to use measurements in other detectors which overlap with the MBTS acceptance to tag counters as having been traversed by a particle. For each tag the MBTS counter charge is plotted and evaluated to see if it passes the hit threshold. Specifically, tracks are used to probe the outer counters and calorimeter cells are used to probe the inner counters. Because the noise is negligible above 0.15pC, that value defines the signal threshold. This section first describes the track based studies and then the calorimeter based studies.

8.3.1 Efficiency Measurement with Tracks

The Inner Detector and the MBTS overlap in the region $2.09 < |\eta| < 2.5$, therefore the tracking can probe the performance of the outer counters in that region. Tracks with p_T of at least 100 MeV are extrapolated to the MBTS and used to select counters. Only those MBTS counters intersected by exactly one track are considered to reduce multiplicity dependence of the distributions. The dependence on particle multiplicity cannot be completely removed because there is no way to veto on particles in the region $2.5 < |\eta| < 2.8$, which is outside of the track reconstruction range. After the additional track veto the extrapolated track is further required to have a momentum of at least 200 MeV to reduce multiple scattering effects and it must have at least 7 SCT hits and 1 Pixel hit in order to select tracks which do not undergo nuclear interactions before exiting the Inner Detector. There is no requirement on TRT hits because the TRT only extends to $|\eta|$ of 2.0.
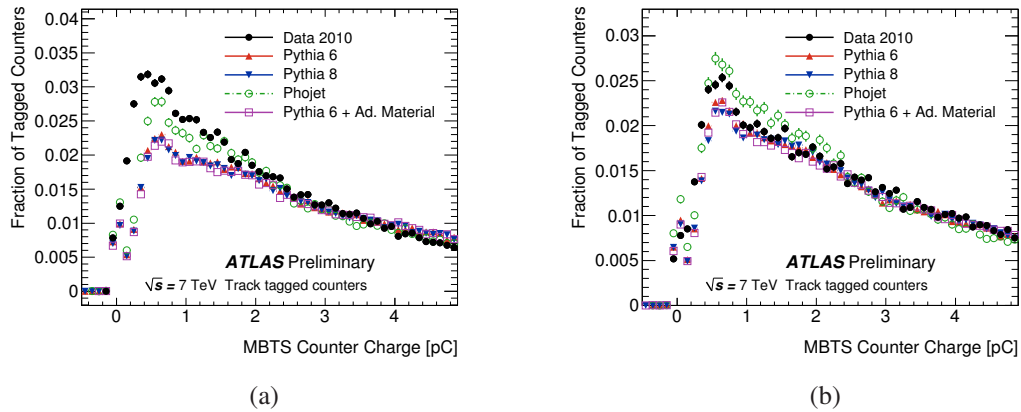
Figure 8.4. Typical counter charge distributions for MBTS counters tagged by tracks. (a) shows good agreement, while (b) shows poor agreement.

Figure 8.4 shows typical track-tagged counter charge distributions. These plots show a counter with good data and MC agreement and a counter with poor agreement. The variability is representative of the variations of the level of agreement between data and MC for all counters. It is evident that there is some physics dependence of the counter charge distribution by the difference between PHOJET and the PYTHIA based generators. PHOJET has a lower multiplicity than either of the PYTHIA generators therefore it is not surprising that it is peaked towards lower charge. But it should be noted that PYTHIA 8 has a higher multiplicity than PYTHIA 6 and there is little difference in those distributions. The data spectrum is softer and a larger fraction of the signal is contained in the 0.1pC to 0.5 pC range. The lower response can be attributed to an overall scale differences in the response between data and MC and to inefficiencies in the detector which are not modeled in the simulation. For example, it is known that the simulation does not model the loss of light collection efficiency at the edges of the detector. Another visible feature of the plot is

the small peak at 0 pC. It is primarily due to extrapolation error, i.e. cases where, due to measurement error, the particle which created the track did not actually intersect the tagged counter.

Using this distribution three quantities are defined: the fraction of tagged counters with a charge greater than 0.15 pC, termed the signal fraction (f_{sig}), the fraction of tagged counters with charge less than 0 pC, termed the zero fraction (f_{zero}), and the efficiency (ϵ) which is the number of tagged counters with charge greater than 0.15 pC divided by the total number of tagged counters less twice f_{zero}. The variable f_{zero} is the fraction of counters which record negative noise. Because the noise is symmetric about 0 pC, twice f_{zero} is the fraction counters recording noise hits. By subtracting twice f_{zero} from the denominator of ϵ, the contribution to the "inefficiency" from cases of extrapolation error is removed.

$$f_{\text{sig}} = \frac{N_{Q>0.15}}{N_{tot}} \tag{8.1}$$

$$f_{\text{zero}} = \frac{N_{Q<0.0}}{N_{tot}} \tag{8.2}$$

$$\epsilon = \frac{N_{Q>0.15}}{N_{tot} - 2.0 \cdot N_{Q<0.0}} \tag{8.3}$$

$$\tag{8.4}$$

Figure 8.5 shows these quantities for each counter on the A and C side of the detector. The PYTHIA MCs all have an f_{sig} of approximately 98%, while PHOJET is roughly 0.5% lower. This can be understood in the context of multiplicity. PHOJET has lower multiplicity, therefore in the case of extrapolation error, it is less likely that another charged particle traverses the counter in the region that the tracking does not cover (2.5< $|\eta|$ <2.8) and gives an appreciable signal. The data are 1 to 2% lower than the PYTHIA-based Monte Carlo simulation on average.

f_{zero} is consistent between the data and MC. There are differences of at most 0.4%, but the overall value agrees well, indicating that the extrapolation error is well modeled in the MC, as expected. The good agreement suggests that differences in f_{sig} between the data and the MC are due to inefficiencies in the counters. The plots of the efficiency support this claim. The PYTHIA-based MC have an average value of 99.4% whereas the data are closer to 98.5%. Table 8.1 shows f_{sig}, f_{zero} and ϵ averaged over all counters. The C-side has a slightly higher average efficiency than the A-side in the data.

The excellent angular resolution of the tracks can be used to map the MBTS response as a function of position in the counter. Figure 8.6 shows f_{sig}, as well as ϵ as a function of ϕ and η. The ϵ versus ϕ plots varies significantly from counter to counter and also within the counters. In several instances the efficiency of one half of a counter is substantially different than the other half. The discrepancy is likely due to differences in the light collection efficiency of the two pieces of scintillator which comprise each counter. In the f_{sig} plots both the data and MC exhibit distinct drops in between counters. These drops, which are

	f_{sig}	f_{zero}	ϵ
Data Side A	96.99 ± 0.05	1.32 ± 0.03	98.29 ± 0.04
Data Side C	97.37 ± 0.05	1.41 ± 0.04	98.76 ± 0.04
PYTHIA 6	98.07 ± 0.04	1.38 ± 0.04	99.44 ± 0.02
PYTHIA 8	98.15 ± 0.04	1.30 ± 0.03	99.45 ± 0.02
PHOJET	97.60 ± 0.08	1.71 ± 0.07	99.30 ± 0.04
Extra Material	98.12 ± 0.04	1.35 ± 0.04	99.46 ± 0.02

Table 8.1. Comparison of f_{sig}, f_{zero}, ϵ for data and Monte Carlo simulation for the outer counters as determined using track tagging.

largely due to extrapolation error, are more pronounced in the data. In the ϵ plots the MC no longer shows dips between counters, but the effect partially remains in the data. Near the counter edges the counter light collection efficiency decreases but the losses are not modeled in the MC, therefore the decrease in efficiency for the data but not the MC is expected. Additionally there are slight drops in the center of the counters which are present in the signal fraction in both the data and the MC which are largely absent in the efficiencies. This effect is not yet understood. There is little dependence of the efficiency versus η. The data fall off more rapidly at low η than in the MC which is likely due to light loss at the counter boundaries.

In order to achieve the same efficiencies in the MC as in the data, the MC threshold was raised until it achieved the data value, separately for each side. The results were consistent whether f_{sig} or ϵ was used. It was found that the A-side outer counter threshold needed to be increased to 0.28 pC and the C-side outer counter threshold needed to be raised to 0.26pC.

8.3.2 Efficiency Measurement with the Calorimeters

The calorimeters can be used in the same spirit as the track to probe the counter efficiency. The forward calorimeter (FCAL) spans $3.1 < |\eta| < 3.8$ while the electromagnetic end-cap (EMEC) covers $2.5 < |\eta| < 3.2$, allowing for studies of the inner counters and for consistency checks between the outer and inner counters. In this case, exactly one calorimeter cell above 1 GeV is required to tag a counter. This threshold was chosen to be above the noise of both the data and the MC.

Examples of counter charge distributions for counters tagged by FCAL and EMEC cells are shown in figure 8.7. Notably, the distributions from the FCAL tagged counters shows a significantly lower average charge than those tagged by the EMEC, indicating that the EMEC selects counters with higher multiplicity than the FCAL because its cell size is larger.

In both cases the peak at zero charge takes on greater importance than in the track tagged distributions due to the fact that the calorimeters detects neutral particles while the MBTS does not. The rate of neutrals, or equivalently, the size of the peak at 0 pC, is

	f_{sig}	f_{zero}	ϵ
Data side A	90.84 ± 0.07	7.02 ± 0.06	97.69 ± 0.04
Data side C	89.97 ± 0.07	7.38 ± 0.06	97.14 ± 0.04
Pythia6	90.05 ± 0.07	8.73 ± 0.06	98.66 ± 0.03
Pythia8	91.14 ± 0.06	7.69 ± 0.06	98.73 ± 0.03
Phojet	88.88 ± 0.13	9.74 ± 0.13	98.48 ± 0.05
Extra Material	90.91 ± 0.07	7.96 ± 0.06	98.78 ± 0.03

Table 8.2. Comparison of f_{sig}, f_{zero}, and ϵ for data and Monte Carlo simulation as determined by FCAL-tagging.

determined by both the particle multiplicity and the material between the interaction point and the MBTS detector. f_{zero} is examined in detail in Section 8.4.

Efficiencies determined with the FCAL

Figures 8.8 shows f_{sig}, f_{zero}, and ϵ for the FCAL tagged counters. The f_{sig} plots show variations of 3% among the Monte Carlo simulations and the data appear to agree with the Pythia 8 and the extra material Pythia 6 sample. f_{sig} increases with increasing multiplicity for the Monte Carlo simulations. Also, the extra material sample has a higher f_{sig} than the nominal Pythia 6 sample, indicating that the agreement of the data with the MCs does not lead to a trivial interpretation.

Figures 8.8(c) and 8.8(d) show the data to have a lower f_{zero} than any of the Monte Carlo simulations. The interpretation of these results are discussed in the context of the material description in Section 8.4.

Figures 8.8(e) and 8.8(f) show that the gross dependencies on multiplicity and material are removed in the ϵ plots. All of the Pythia based MCs have the same efficiency, approximately 98.7%, and Phojet has a slightly lower efficiency, at most 0.5% below Pythia. The data are 1 to 3% less efficient on average. One problematic counter is 4% lower than the Monte Carlo simulation.

Table 8.2 compares the average f_{sig}, f_{zero}, and ϵ of the Monte Carlo simulation and of the data on the A-side and C-side separately. There is no difference in the simulation averages between the A- and C-sides. In order to obtain the same average efficiencies in the MC as in data the A-side inner counter threshold must be increased to 0.32 pC and the C-side inner counter threshold must be increased to 0.38 pC.

Efficiencies determined with the EMEC

The EMEC is used as a cross check for both the track and FCAL based methods because it spans both the inner and outer counters. Its bias towards higher multiplicity makes it less sensitive to the efficiency of the counters, however it is still useful to confirm the general trends seen using the other detectors.

Figure 8.9 shows f_{sig}, f_{zero}, and ϵ for EMEC tagged counters. The counter by counter variations are the same as found with the track and FCAL analyses. In general these distributions show slightly better agreement of the data with the PYTHIA based simulation, but this can be attributed to the overall higher multiplicity of the sample.

8.4   Material

The amount of material between the interaction point and the MBTS detector plays a significant role in this analysis, primarily due to its effect on photon conversions. As explained in Section 8.3, greater amounts of material lead to higher rates of conversions, which in turn produces a higher charged particle multiplicity in the MBTS acceptance. The nominal simulation for the MC samples used in this analysis is known to have too little material in the Pixel services region as well as in other Inner Detector services. The extra material sample described in Chapter 7 is used for estimation of the material effects. It has a 20% increase in the pixel services radiation length. This is believed to be an underestimate for $2.2 < |\eta| < 2.8$, an overestimate for $2.8 < |\eta| < 3.3$ and is close to the experiment's best guess at the material budget for $|\eta| > 3.3$. In the region $|\eta| > 3.3$, where material effects are the most important for the acceptance, the extra material sample has a 15% increase in total radiation length over the nominal geometry.

In the central region of the detector, $|\eta| < 2.5$, the material distribution has been studied using conversion electrons and $K_s^0 \to \pi^+\pi^-$ decays, and is known to better than $\pm 5\%$ up to $|\eta| < 2.2$ and to $\pm 30\%$ for $2.2 < |\eta| < 2.5$ [70]. The large uncertainty in the forward region is due to lack of statistics as well as known mis-modeling in the geometry description in that region.

In the forward region of the detector, the material description is assessed using f_{zero}, which is sensitive to the fraction of converted photons. For two different descriptions of the material between the interaction point and MBTS detector, the description with more material will have less events with 0 pC, and consequently a lower f_{zero}, because photons, primarily from neutral pion decays, are more likely to undergo electron conversion. It is important to note that f_{zero} is also sensitive to the particle multiplicity. For a given detector description and two Monte Carlo simulations with different particle multiplicity, the simulation with higher multiplicity will see less events at 0 pC because it is more likely that a charged and neutral particle hit the detector at the same time, rather than just a neutral particle. Both of these effects (higher multiplicity, higher material) lower f_{zero}.

Figures 8.8(c) and 8.8(d) show f_{zero} as measured with the FCAL. PHOJET has the highest f_{zero} at nearly 0.1, followed by PYTHIA 6 at 0.09. The PYTHIA 6 extra material sample has an f_{zero} of roughly 10% less than that of the nominal sample. PYTHIA 8 samples has an f_{zero} of roughly 0.08. The data value is 0.07 which can be understood in the context of both the material and multiplicity. The minimum bias measurements [109, 70] indicate that PYTHIA 8 best reproduces the per-event normalization of the charged particle multiplicity distribution. Studies for those publications also suggest that the extra material sample is a

better description of the real material budget than the nominal sample in the forward region of the detector. Therefore it is expected that the data be approximately 0.01 lower than the PYTHIA 8 f_{zero} value, which is approximately observed. However, if a lower multiplicity, as predicted by PYTHIA 6, is assumed then 40% more material is needed in the forward region. The PHOJET Monte Carlo badly under-predicts the average charged particle multiplicity in inclusive events, therefore it is not used as a baseline from which to assess the material.
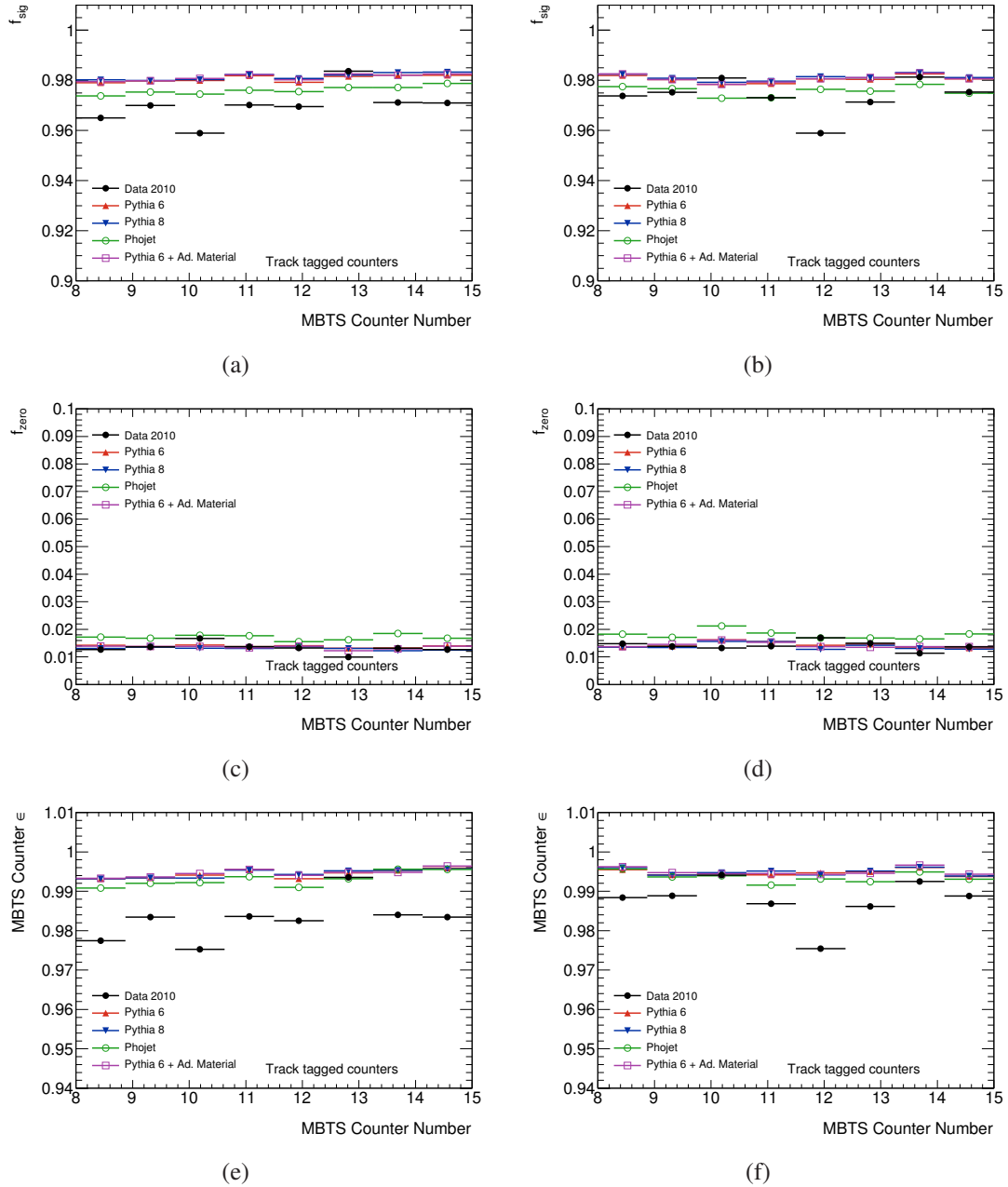
Figure 8.5. f_{sig} (a,b), f_{zero} (c,d), and ϵ (e,f) for the inner counters tagged by tracks. In all cases A side is on the left and the C side is on the right.
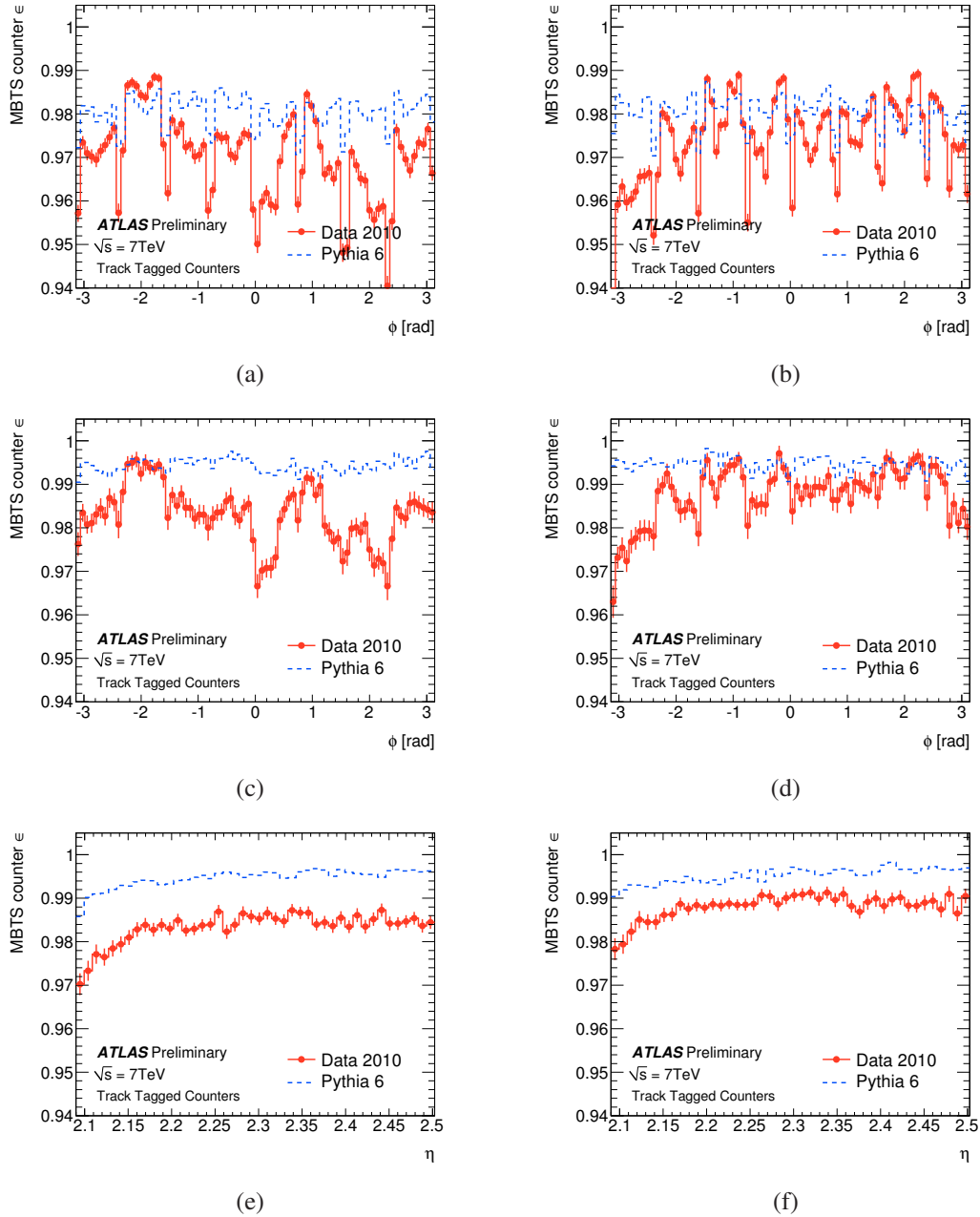
Figure 8.6. f_{sig} (a,b), ϵ versus ϕ (c,d) and ϵ versus η (e,f) determined with tracks of data compared with PYTHIA 6 Monte Carlo simulation. In all cases A side is on the left, C side is on the right.
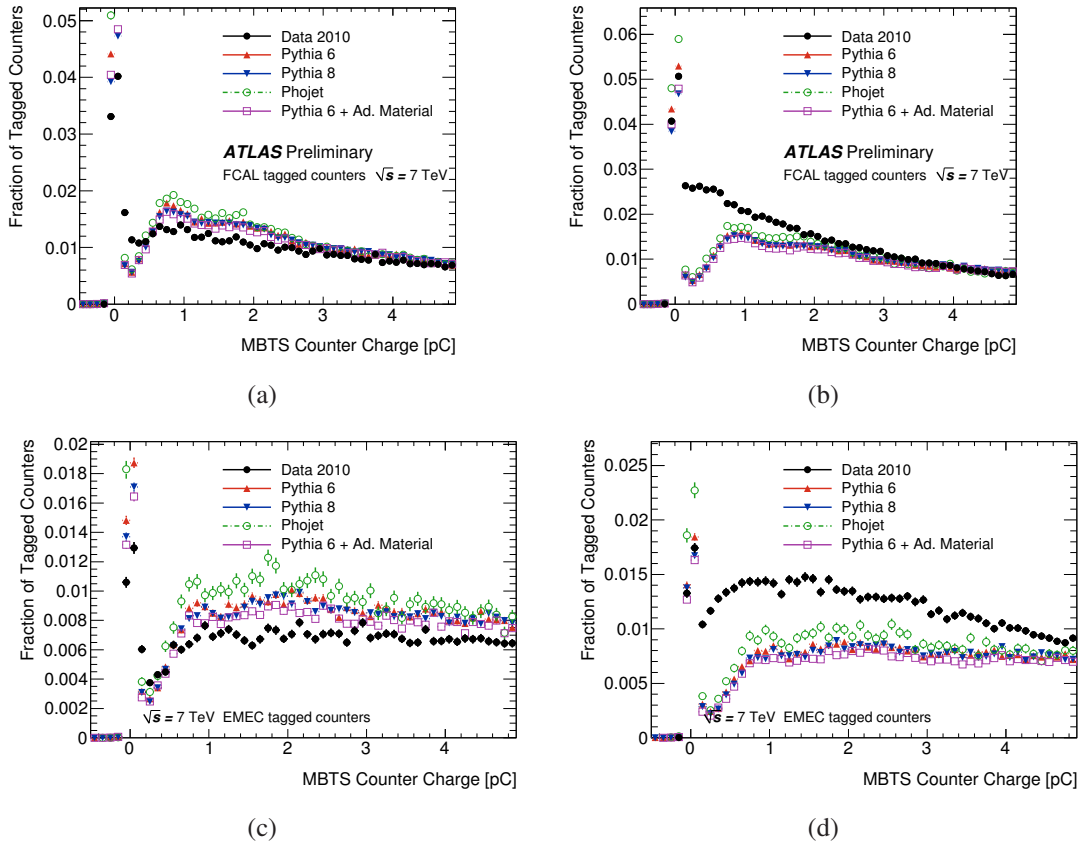
Figure 8.7. Typical counter charge distributions for MBTS counters tagged by calorimeter cells. FCAL tagged charged distributions for counter 7 on the A (left) and C (right) sides are on top, EMEC for the same counters are on bottom.
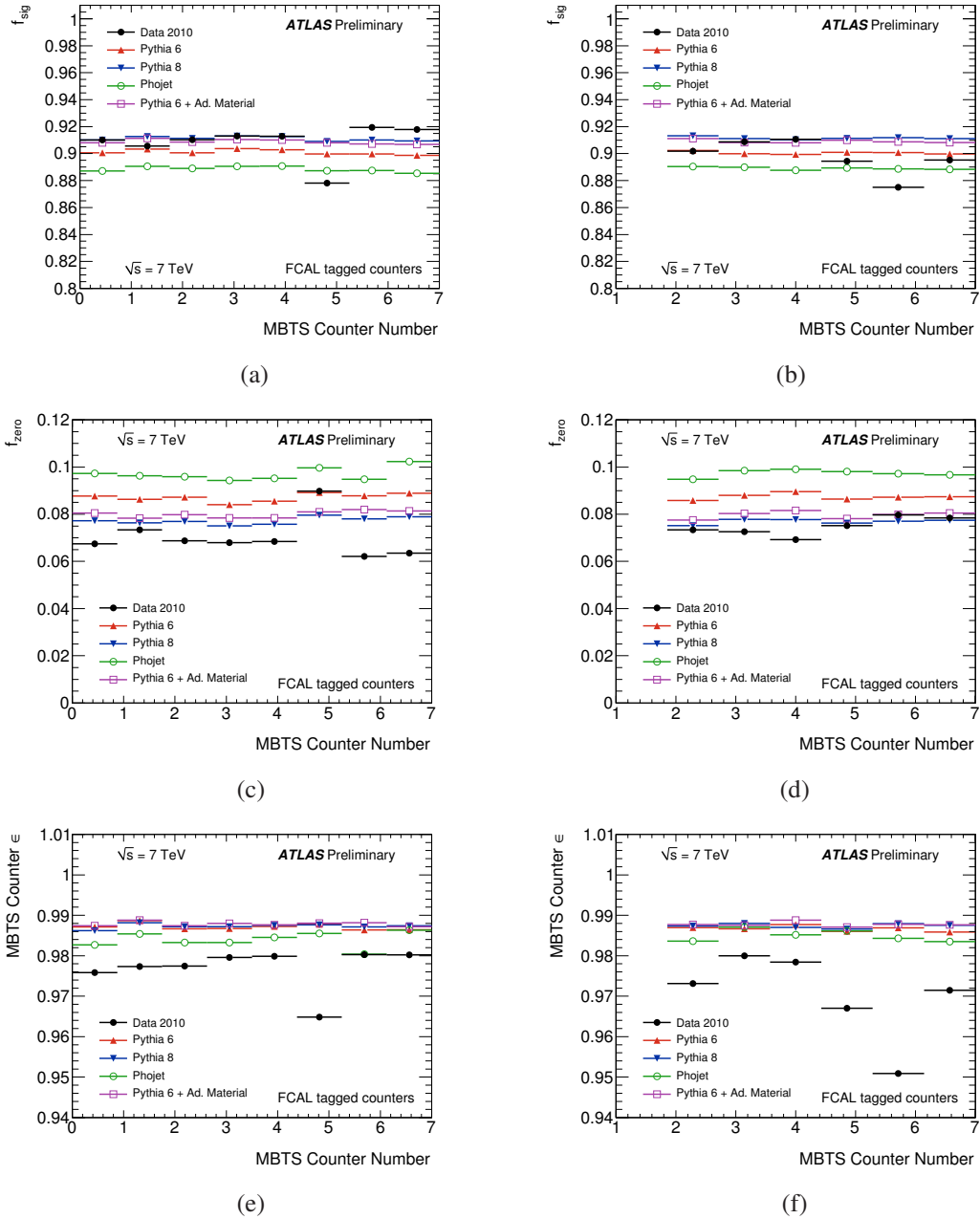
Figure 8.8. Top: f_{sig}, Middle: f_{zero}, Bottom: ϵ for the inner counters tagged by FCAL cells. In all cases A side is on the left, C side is on the right.
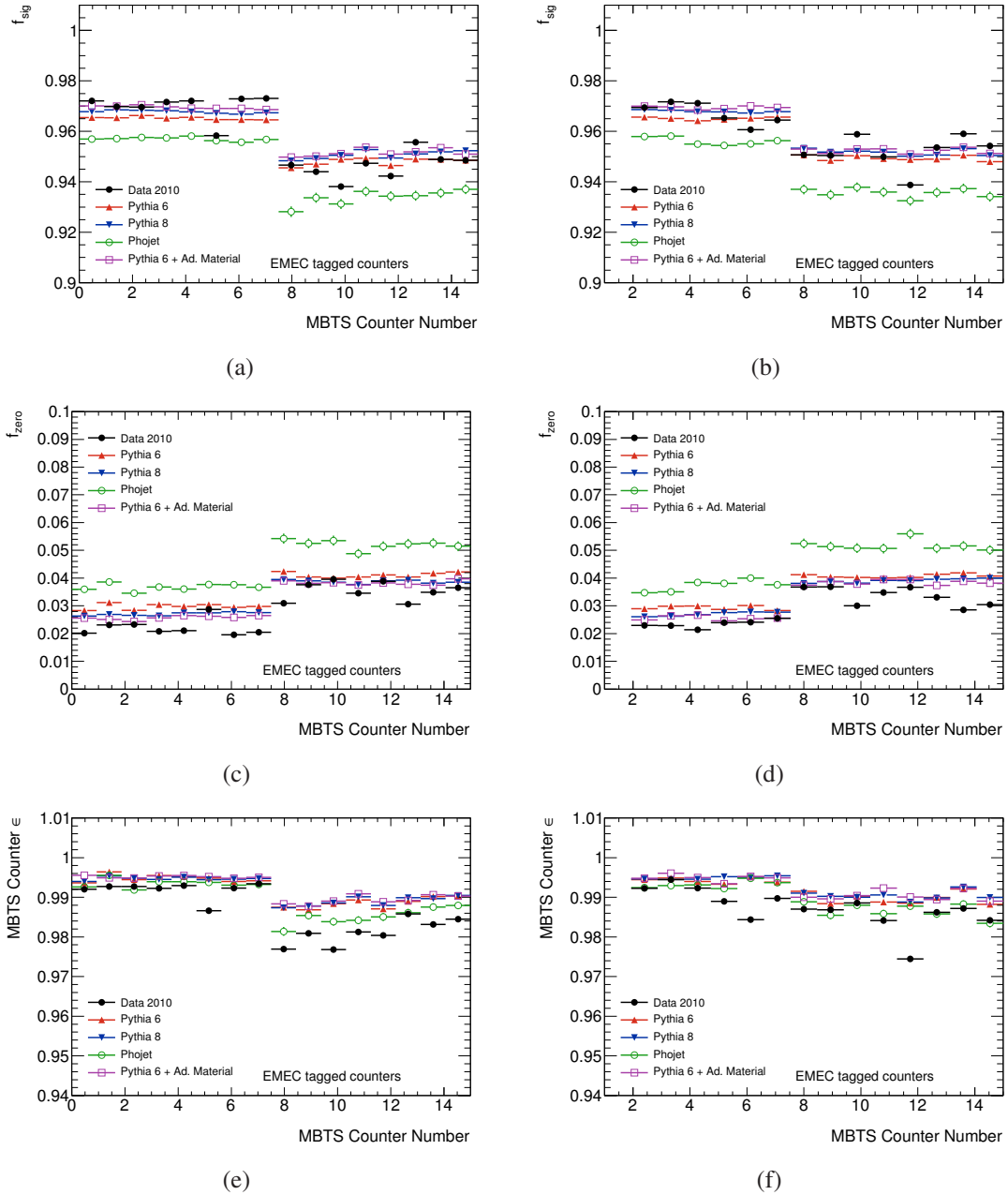
Figure 8.9. (a),(b): f_{sig}, (c),(d): f_{zero}, (e),(f): ϵ for the inner counters tagged by EMEC cells. In all cases A side is on the left, C side is on the right.

CHAPTER 9

Backgrounds

The measurements in this thesis aim to be as inclusive as possible, therefore there are no collision backgrounds that need to be modeled as would be the case in an exclusive measurement, e.g. jets faking electrons in a $Z \to e^+e^-$ measurement. All of the backgrounds considered here are considered "non-collision" backgrounds and are determined directly from the data. They fall into two categories: beam-related backgrounds and non beam-related backgrounds. The beam-related backgrounds include collisions of the beam with material upstream from the detector or gas in the beam-pipe, as well as the diffuse radiative background from the interactions of collision remnants with material in the detector called *afterglow*. Afterglow has two sources, *in-time* which affects the same bunch-crossing as when the collision occurred, and *out-of-time* where the afterglow was produced by a collision in a different bunch-crossing. Non beam-related backgrounds include noise and cosmic-rays. Each of these background sources is described in detail in this chapter.

9.1 Beam-Related Backgrounds

Beam-related backgrounds are generally determined from events recorded when only one beam was passing through ATLAS, termed unpaired bunches. This method is sufficient for determining the contributions beam-gas, beam-halo and out-of-time afterglow, but is inadequate for in-time afterglow. Therefore these two categories are treated separately below.

9.1.1 Beam-Gas, Beam-Halo, Out-of-time Afterglow

Beam-gas, beam-halo, and out-of-time afterglow make up the tradition beam-related backgrounds. Beam-gas refers to interactions of the beams with gas particles in the beam-pipe in the interaction region. The ATLAS vacuum is very clean and is able to be evacuated pressures of 10^{-11} mbar [110], therefore there are few beam-gas events. However, these events look very similar to diffractive collision events. Figure 9.1 shows the reconstructed

vertex position for a run prior to the first 7 TeV collisions when there was a single beam in the LHC. As it can be seen in the figure, the beam-gas vertex distribution is Gaussian in the x- and y-coordinates but is flat in the z-distribution. The statistics are poor because the quality of the ATLAS vacuum leads to few beam-gas events.
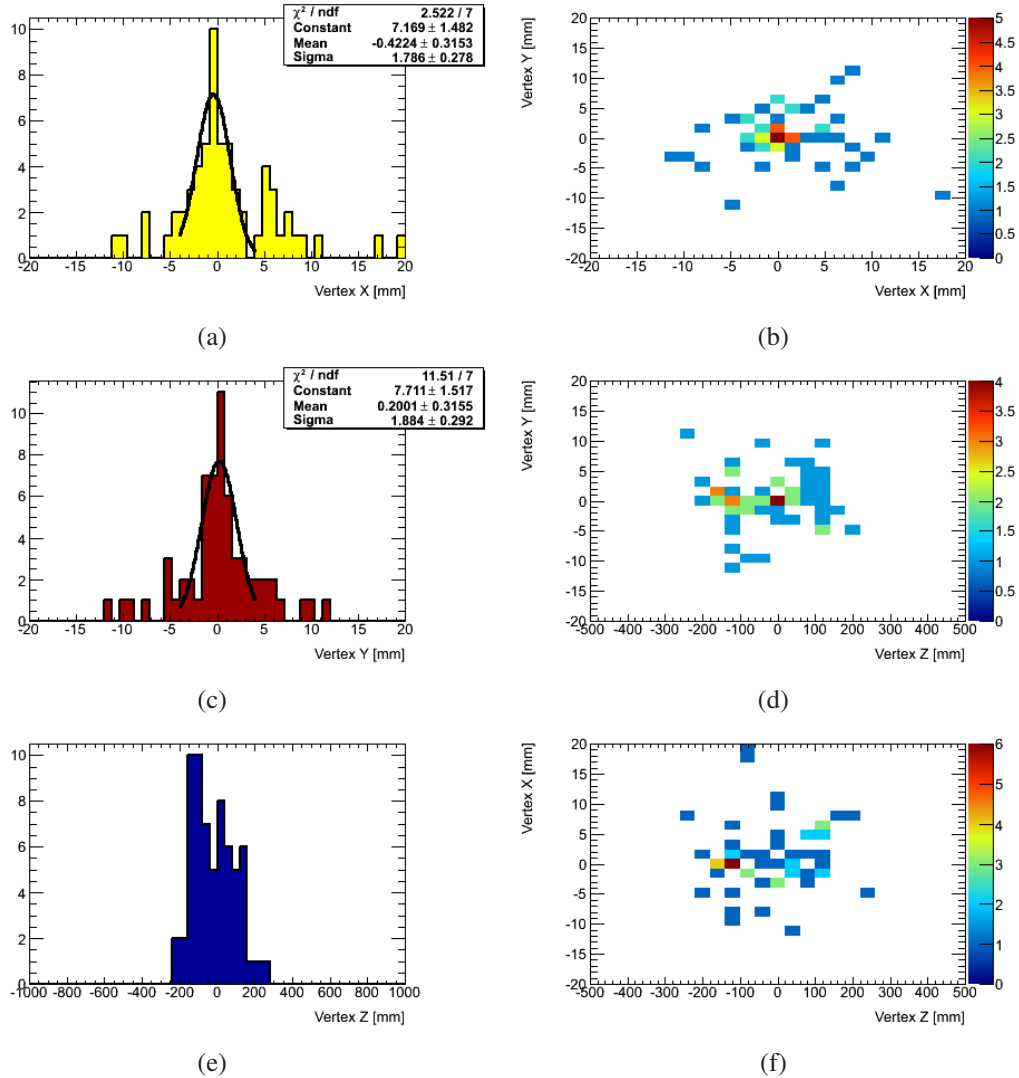
Figure 9.1. 1-D and 2-D vertex position distributions from beam-gas events in run 152164.

Beam-halo occurs when particles from the beam interact with material upstream from the detector, causing a "halo" of particles traversing with the beam, but at large enough radii to beam-line that they leave hits in the detector. They can be identified by looking at the difference in the time of hits between the A- and C-sides of the detector. Collision events have an average time difference of 0 ns while beam-halo events peak around ± 25 ns,

as was shown Figure 6.11.

Both beam-halo and beam-gas events produce hits in the MBTS detectors as well as tracks in the Inner Detector. As will be shown in Section 11.1.5, the track-based backgrounds are small and are significantly reduced once a track with p_T of 500 MeV is required.

Afterglow is a poorly understood background which is believed to be due to photons released by slow neutron capture. The neutrons are produced when collision products interact with the material in the detector. There is a time-constant associated with the background of 100s of μs [111], but in high luminosity fills it is still seen hours after the fill has ended. Figure 9.2(a) the rate of L1_MBTS_C triggers are plotted as a function of the bunch-crossing identifier (BCID) in run 152221. L1_MBTS_C consists of the OR of all individual MBTS counter triggers on the C-side of the detector. There was only one colliding bunch in ATLAS at BCID 1, which is seen as the large peak in the plot. However, an exponentially decaying trigger rate is seen for many BCIDs later which is due to the afterglow. The rate reaches a plateau value of approximately 0.5 Hz. This plateau is due to noise in the MBTS trigger system as well as long timescale afterglow.

(a)   (b)
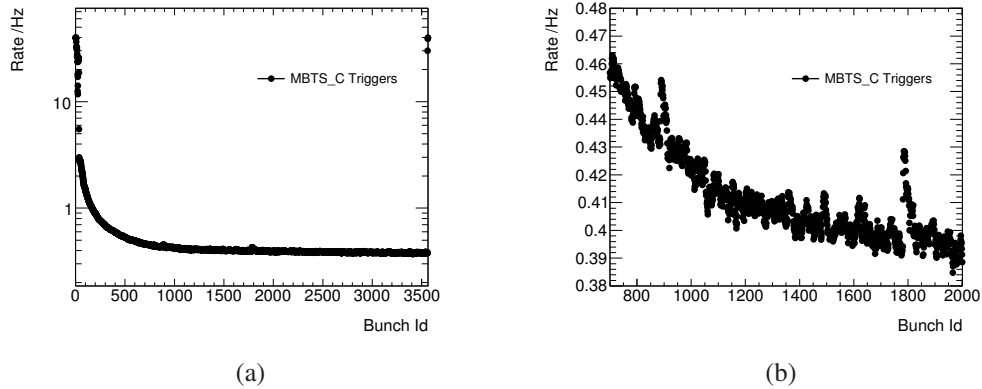
Figure 9.2. Rate of MBTS triggers on the C side of the detector as a function of BCID for run 152221. In this run the colliding bunch was at BCID=1, and unpaired bunches were present at BCID=892 (from beam 2) and BCID=1786 (from beam 1). The left plots shows all BCID on a log scale, the right zooms in on the unpaired bunches on a linear scale.

8

Run 152221 had two unpaired bunches traversing ATLAS at BCIDs 1786 (beam 1) and BCID 892 (beam 2). Figure 9.2(b) is a zoom of the BCID axis in this range. There are clear peaks of the unpaired bunches over the afterglow background. Therefore the unpaired bunches are used to estimate the background due to the beam-gas and beam-halo. Only beam 1 is used because it is less contaminated by afterglow than beam 2. The exact procedure used for the cross-section analysis is described in detail in Chapter 12.1. For this thesis, afterglow is a concern only for the MBTS detector.

9.1.2   In-time Afterglow

Figure 9.2(a) suggests that if there is no turn-on behavior, afterglow affects the bunch in which the collision occurs. This is termed in-time afterglow. The Geant4 simulation does not model this effect, therefore the data events could have additional MBTS hits not present in the simulated Monte Carlo events. In-time afterglow is hard to quantify, therefore a conservative approach is taken. The MBTS has fairly good individual hit time-resolution, therefore the fraction of late hits, e.g. hits inconsistent with the interaction time, can be estimated as the afterglow contribution.

Figure 9.3 shows the counter time distribution for events with exactly 1, 2 and 3 counters above threshold as well as with at least 20 counters above threshold. The $N_{counters} = 1$ plots clearly shows the out-of-time afterglow as the component which is flat in time. In the other plots the unpaired bunches show the beam halo and beam gas events which match well with features seen in the paired bunches. In the paired bunches the time distribution is asymmetric, showing a tail at positive times. It is assumed that this tail is attributed solely to afterglow and, after subtracting off the beam background contribution using the unpaired bunches, the fraction of hits in the high tail is calculated. The resulting fraction is termed the 'hit purity' and is calculated as

$$h.p.(N_{\text{counters}}) = 1 - \frac{N_{\text{counters}}(T > 0) - N_{\text{counters}}(T < 0)}{N_{\text{counters}}(\text{all } T)}.$$

For run 15221 a hit purity of 0.83 is measured for the $N_{counters} = 2$ and $N_{counters} = 3$ events. The $N_{counters} \geq 20$ events have a hit purity of 0.72, most likely due to the fact that higher multiplicity events will have higher rates of afterglow. The hit purity is a luminosity-dependent quantity and needs to be determined separately for each run.

9.2   Other Backgrounds

Other backgrounds include spurious hits due to noise as well as cosmic rays. The noise background can be measured using the BCIDs when there is no beam passing through ATLAS. As shown in Chapter 8.1, the noise is symmetric about 0 pC, therefore the noise can also be measured in the paired bunches by looking at the number of counters which have a charge less than -0.15 pC. Because the threshold is 7σ above the noise, there are no events recorded.

ATLAS sits 100 m under the earth's surface, therefore the low energy cosmic ray flux is significantly attenuated. During cosmic ray data taking the flux through the pixel detector was measured to be approximately 0.5 Hz. The MBTS horizontal cross-section is considerably smaller, therefore the flux is roughly two orders of magnitude smaller. In the runs considered there was only one colliding bunch, therefore only one 25ns window every 9 μs in which a trigger can be recorded. Therefore the cosmic-ray flux is negligible.

In any case, measuring the number of event passing in the unpaired bunches would also account for the noise and cosmic ray backgrounds, were they significant.
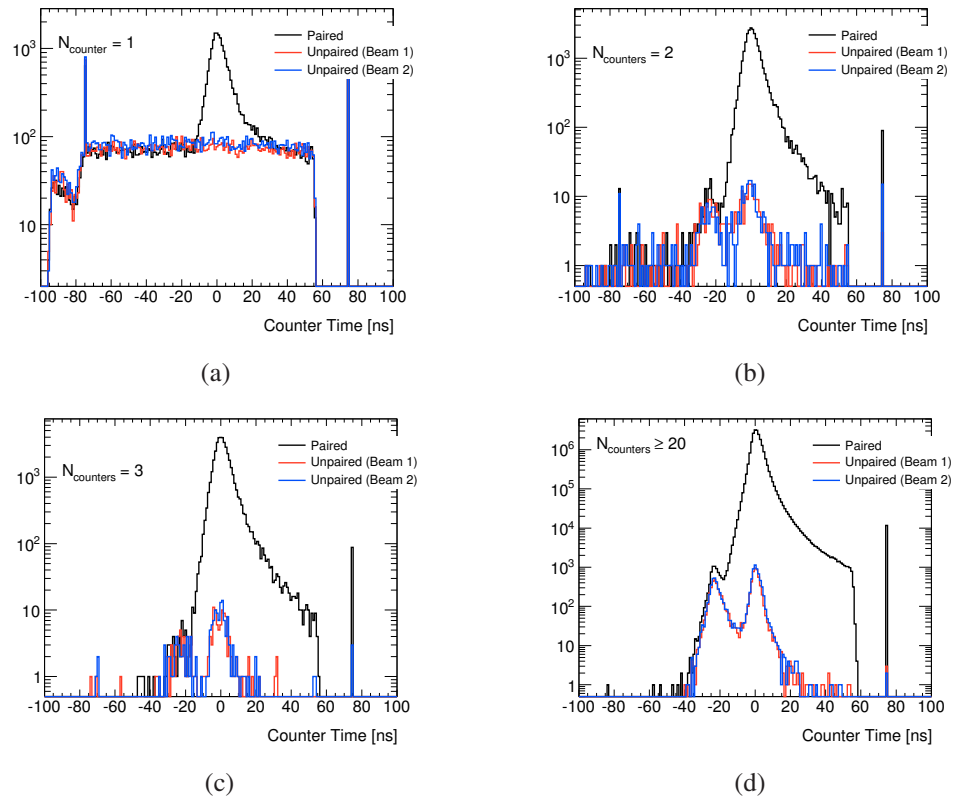
Figure 9.3. MBTS counter time distributions for events with 1,2,3 and ≥ 20 counters over threshold in run 15221. The colliding bunches are shown by the black histogram and the unpaired bunches in the blue and red histograms. In all histograms there is one entry per counter above threshold in the event.

<div align="right">CHAPTER 10</div>

Luminosity Determination

The determination of the delivered luminosity during the data-taking period used in this analysis provides the dominant experimental uncertainty. This chapter describes how the luminosity is measured and how its uncertainties are determined.

10.1 Introduction to Luminosity and Beam Separation Scans

Luminosity is a measure of the total possible interactions per unit area per unit of time produced by an accelerator [112]. It is the process-independent coefficient relating the cross-section to observed rate of events

$$\frac{dN}{dt} = \mathcal{L} \cdot \sigma. \tag{10.1}$$

Luminosity can be measured in several ways. If σ is well-known, either by previous measurements or by theoretical calculation, and if N can be determined to high accuracy, then $\mathcal{L}$ can be deduced by event-counting. However, the unruly nature of hadron collisions leads to large uncertainties on σ for all but relatively rare electro-weak processes such as W and Z production.

Luminosity can also be determined directly from beam parameters through the relationship

$$\mathcal{L} = \frac{N_1 N_2 f_r}{A_{\text{eff}}} \tag{10.2}$$

where N_1 and N_2 are the number of protons in beam 1 and beam 2, f_r is the beam revolution frequency and A_{eff} is the effective transverse area in which the two beams overlap [113]. The challenge in this method is to know accurately the number of protons per beam and the beam sizes, which determines A_{eff}. For a collider with n_b colliding bunches in the ring, Eqn. 10.2 becomes

$$\mathcal{L} = n_b f_r n_1 n_2 \int \rho_1(x, y) \rho_2(x, y) dx dy \tag{10.3}$$

where $n_{1,2}$ are the number of particles per bunch for beam 1 and 2, respectively and $\rho_{1,2}(x,y)$ is the particle density for each beam in the transverse plane [114]. When the beam densities are uncorrelated in x and y then Equation 10.3 becomes

$$\mathcal{L} = n_b f_r n_1 n_2 \int \rho_1(x)\rho_2(x)dx \int \rho_1(y)\rho_2(y)dy. \qquad (10.4)$$

$\int \rho_1(x)\rho_2(x)dx \int \rho_1(y)\rho_2(y)dy$ describes the beam-overlap or luminous region and is equivalent to $\frac{1}{A_{eff}}$ in Equation 10.3.

In 1968 Simon van der Meer introduced the concept of beam separation scans, now called van der Meer (vdM) scans, as a means of measuring the size of the luminous region, and consequently the luminosity, at CERN's Intersecting Storage Ring (ISR) [74].

He began with a variable defined by Darriulat and Rubbia [115], the effective beam height, which is sensitive to the overlap of the beams. It is defined as

$$b_{\text{eff}} = \frac{\int \rho_1(x)dx \int \rho_2(x)dx}{\int \rho_1(x)\rho_2(x)dx}. \qquad (10.5)$$

which is the charge of the two beams divided by the charge overlap integral. Because the density profiles can be expressed as a function of unit area times a constant normalization factor, this is equivalent to the inverse of the overlap fraction of the two beams.

Van der Meer proposed displacing the two beams in x (or y) and measuring the counting rate as a function of the displacement in order to measure b_{eff}. The counting rate, R, must be proportional to the overlap of the beams and the constant of proportionality, A, should be independent of the relative beam displacement. Therefore, the counting rate at displacement h in the x direction is given by

$$R_x(h) = A \int \rho_1(x)\rho_2(x-h)dx. \qquad (10.6)$$

Van der Meer defined a new variable b_{new} which is the area under the counting rate integral, divided by the counting rate at zero displacement. He showed that independently of the beam shape, this variable is equal to the effective beam height:

$$b_{\text{new}} = \frac{\int R_x(h)dh}{R_x(0)} \qquad (10.7)$$

$$= \frac{\int \left(\int A \cdot \rho_1(x)\rho_2(x-h)dx \right) dh}{A \cdot \int \rho_1(x)\rho_2(x)dx} \qquad (10.8)$$

$$= \frac{\int (\int \rho_1(x)\rho_2(x-h)dh)dx}{\int \rho_1(x)\rho_2(x)dx} \qquad (10.9)$$

$$= \frac{\int \rho_1(x)dx \int \rho_2(x)dx}{\int \rho_1(x)\rho_2(x)dx} \qquad (10.10)$$

$$= b_{\text{eff}}. \qquad (10.11)$$

$$\qquad (10.12)$$

Once the b_{eff} is known, $\int \rho_1(x)\rho_2(x)dx$ is easily determined:

$$\int \rho_1(x)\rho_2(x)dx \ = \ \frac{\int \rho_1(x)dx \int \rho_2(x)dx}{b_{\text{eff}}} \tag{10.13}$$

$$= \ \frac{n_1 n_2}{b_{\text{eff}}} \tag{10.14}$$

$$= \ \frac{n_1 n_2 R_x(0)}{\int R_x(h)dh}. \tag{10.15}$$

Before substituting for $\int \rho_1(x)\rho_2(x)dx$ in Equation 10.4 the variables $\Sigma_{x,y}$ are defined such that

$$\Sigma_{x,y} = \frac{1}{\sqrt{2\pi}} \frac{\int R_{x,y}(h)dh}{R_{x,y}(0)}. \tag{10.16}$$

Then Equation 10.4 can rewritten as

$$\mathcal{L} = \frac{n_b f_r n_1 n_2}{2\pi \Sigma_x \Sigma_y}. \tag{10.17}$$

$\mathcal{L}$ now corresponds to the peak instantaneous luminosity which was achieved at zero beam-displacement.

Knowing $\mathcal{L}$ at zero beam-displacement allows for a determination of σ for any given process:

$$\sigma_{\text{vis}} = \frac{dN_{\text{vis}}(h=0)}{dt} \frac{1}{\mathcal{L}_{h=0}}. \tag{10.18}$$

where σ_{vis} indicates the visible (i.e. detectable) cross-section for the process of interest. Therefore dedicated scans are performed to determine σ_{vis} for a variety of different processes and the resulting cross-sections are used in all other runs to determine the run-by-run luminosity. The run-by-run luminosity is measured in two-minute intervals, referred to as 'luminosity blocks'.

As will be discussed in Section 10.2, multiple interactions can occur in a single bunch-crossing. An alternative way of defining the luminosity is

$$\mathcal{L} = \frac{\mu_{\text{vis}} n_b f_r}{\sigma_{\text{vis}}}. \tag{10.19}$$

where μ_{vis} is the average number of visible interactions of the process of interest [111]. σ_{vis} and μ_{vis} are related to the total inelastic cross section by $\sigma_{\text{vis}} = \epsilon \sigma_{\text{inel}}$ and $\mu_{\text{vis}} = \epsilon \mu_{\text{inel}}$ where ϵ is the efficiency to detect an inelastic interaction.

10.2 Charged Particle Event Counting and Other Methods

The ATLAS experiment uses a number of different detectors and algorithms to determine the luminosity.

10.2.1 Luminosity Detectors

There is one dedicated luminosity detector, LUCID, which is described in detail in Section 5.5.2. Other detectors used for online luminosity measurements include the Zero Degree Calorimeter which sits at ± 140m from the interaction point and is sensitive to forward neutrons and photons, the MBTS, and diamond detectors close to the beam-pipe at $\pm$ 184 cm from the interaction point called beam conditions monitors. There are also several other detectors used in offline luminosity analyses, including timing information from the MBTS, timing information for the liquid Argon calorimeters, and charged particle tracks and primary vertices reconstructed in the Inner Detector. The charged particle track method will be discussed in detail in Section 10.2.3.

10.2.2 Luminosity Algorithms

Luminosity is currently determined in ATLAS using event counting, although hit counting in specific detectors is also possible. Most online luminosity detectors have two methods for counting events: OR and AND. OR event counting requires at least one hit in the detector. AND event counting requires a coincidence of hits in the detector on both sides of the interaction point. OR has a higher event rate but is more susceptible to backgrounds, while AND has extremely low background rates. However, the AND algorithm has a more complicated relationship between the number of observed events and $\mu_{\rm vis}$. Offline methods generally only have one method.

In all cases the luminosity is determined using Equation 10.19. The event counting is used to determine $\mu_{\rm vis}$ and $\sigma_{\rm vis}$ is taken from the vdM calibration. Because there can be more than one interaction per bunch-crossing, a relationship is needed between the number of observed events and $\mu_{\rm vis}$. There are two assumptions made to determine the relationship. First, it is assumed that the average number of interactions per crossing is Poisson distributed. Second, we assume that the probability for an interaction to be detected is independent of the presence of a second interaction in the event. This latter assumption is not strictly true for all of the methods, however it holds for our purposes.

With these two assumptions in hand, the Poisson probability for observing *no* event in a given bunch crossing for the OR algorithms is $P_0(\mu_{\rm vis}) = e^{-\mu_{\rm vis}}$. It follows that the probability of observing at least one event is

$$P_{OR}(\mu_{\rm vis}) \;=\; \frac{N_{OR}}{N_{BC}} \tag{10.20}$$
$$=\; 1 - P_0(\mu_{\rm vis}) \tag{10.21}$$
$$=\; 1 - e^{-\mu_{\rm vis}}. \tag{10.22}$$

It follows that

$$\mu_{\rm vis} = -\ln\left(1 - \frac{N_{OR}}{N_{BC}}\right). \tag{10.23}$$

where N_{OR} is the number of events and N_{BC} is the number of bunch-crossings. For an accelerator with n_b number of bunches and a revolution frequency of f_r, the number of events per second, n_{ev}^{corr}, is given by

$$n_{ev}^{corr} = -n_b f_r \cdot \ln\left(1 - \frac{n_{ev}}{n_b f_r}\right). \tag{10.24}$$

where n_{ev} is the number of observed events per second.

The case of AND algorithms is more complicated. The relationship between the number of events observed and μ_{vis} is not analytically invertible. Therefore, look-up tables are used to translate from observed events to μ_{vis}. The offline algorithms are all treated as OR algorithms. The ATLAS preferred method is the LUCID OR algorithm.

10.2.3   Charged Particle Event Counting

One of the offline methods used by ATLAS is charged particle event counting. It uses the number of events with at least one charged particle with $p_T > 500$ MeV and $|\eta| < 0.8$ to determine the luminosity. This phase space was chosen by the Rate Normalization Working Group [1] as a phase space accessible to the ALICE, ATLAS and CMS experiments to facilitate inter-experiment luminosity comparisons.

Practically, the charged particle event rate is determined by counting the number of events with at least one track in the designated phase space. The track is required to satisfy the following:

- be associated with a beam-constrained primary vertex with at least two tracks of $p_T > 150$ MeV.

- $|d_{\text{PV}}| < 1.5$ mm

- $|z_{\text{PV}} \sin\theta| < 1.5$ mm

- $N_{\text{Pix}} \leq 0$

- $N_{\text{SCT}} \geq 5$

where d_{PV} and z_{PV} are the transverse and longitudinal distances of closest approach to the primary vertex, respectively, and $N_{\text{Pix(SCT)}}$ are the number of Pixel(SCT) hits associated with the track. Additionally the event must have passed the L1_MBTS_1 trigger.

In order to obtain the number of events with at least one charged particle in the phase space from the number of events with at least one selected track, event loss due to trigger, vertex and tracking inefficiency must be corrected for. The corrections are done following

---

[1]A working group formed by the LHC Physics Center consisting of members of all four major LHC experiments and theorists.

the procedure outlined in [116]. Each event is given a weight, w_{ev}, to correct for the trigger and vertex inefficiencies:

$$w_{ev}(n_{\text{sel}}^{\text{BS}}) = \frac{1}{\epsilon_{\text{trig}}(n_{\text{sel}}^{\text{BS}})} \cdot \frac{1}{\epsilon_{\text{vtx}}(n_{\text{sel}}^{\text{BS}})} \qquad (10.25)$$

where $n_{\text{sel}}^{\text{BS}}$ is the number of tracks passing selection requirements when the impact parameter cuts are with respect to the beam-spot rather than the primary vertex. $\epsilon_{\text{trig}}(n_{\text{sel}}^{\text{BS}})$ and $\epsilon_{\text{vtx}}(n_{\text{sel}}^{\text{BS}})$ are measured in data and found to be high. ϵ_{trig} is nearly 100% for all multiplicities and ϵ_{vtx} is 95% for events with $n_{\text{sel}}^{\text{BS}} = 1$ and nearly 100% for all others. Both the trigger and vertex efficiency are 100% for $n_{\text{sel}}^{\text{BS}} \geq 4$.

To correct for loses due to tracking inefficiency, a Monte Carlo simulation-based Bayseian unfolding [117] is necessary. First, the ability of the simulation to reproduce the the tracking efficiency and the fraction of secondary particles passing the track selection is validated extensively as described in [118, 116] and in Section 6.1.2 of this thesis. Then, fully simulated minimum bias Monte Carlo events[2], including mixed ND, SD and DD components, are used determine the number of produced primary charged particles, n_{ch}, from the number of selected tracks, n_{sel}. The Monte Carlo events are used to populate a matrix, $M_{\text{ch,sel}}$ with n_{ch} as the row position and n_{sel} as the column position. $M_{\text{ch,sel}}$ is normalized such that the total event number does not change, except when $n_{\text{sel}} > n_{\text{ch}}$ which is rare. The matrix is applied to the n_{sel} distribution in data. The resulting n_{ch} distribution is used to reweight the $M_{\text{ch,sel}}$ and this procedure is repeated iteratively until the change between iterations was less than 1%. Once the n_{ch} distribution is obtained, each bin is corrected for event loss due to tracking inefficiency using the following factor

$$C(n_{\text{ch}}) = \frac{1}{1 - (1 - \langle \epsilon(n_{\text{ch}}) \rangle)^{n_{\text{ch}}}} \qquad (10.26)$$

where $< \epsilon(n_{\text{ch}}) >$ is the average tracking efficiency in the n_{ch} bin. In practice, this correction is only applied to the first six bins, after which it becomes negligibly small. To obtain the total number of events with at least one charged particle in the desired phase space, the corrected n_{ch} is integrated. The correction factor from the N_{trk} to N_{ch}, where N is the number of events, is found to be 1.039$\pm$0.017. The error includes systematic error on the tracking efficiency, vertex and trigger efficiencies and on the Monte Carlo-based correction procedure. The dominant uncertainty is due to the material knowledge uncertainty for the tracking efficiency. Figure 10.1 shows the n_{ch} distribution in a MC closure test.

When determining the charged particle event rate for a particular run, Equation 10.2.2 is used to determine the number of events per second on a lumiblock-by-lumiblock basis. The charged particle analysis uses the L1_MBTS_1 trigger which, when prescaled, accepts every s event, where s is the prescale. The error on the number of events passing the MBTS_1 trigger, $s \cdot n_{\text{MBTS\_1}}$, is the Poisson error on $s \cdot n_{\text{MBTS\_1}}$ modulo the rounding error on s. The rounding error is taken into account by adding $s/2$ to the event count and

---

[2]Pythia 6.421 with the ATLAS MC09 Monte Carlo tune was used.
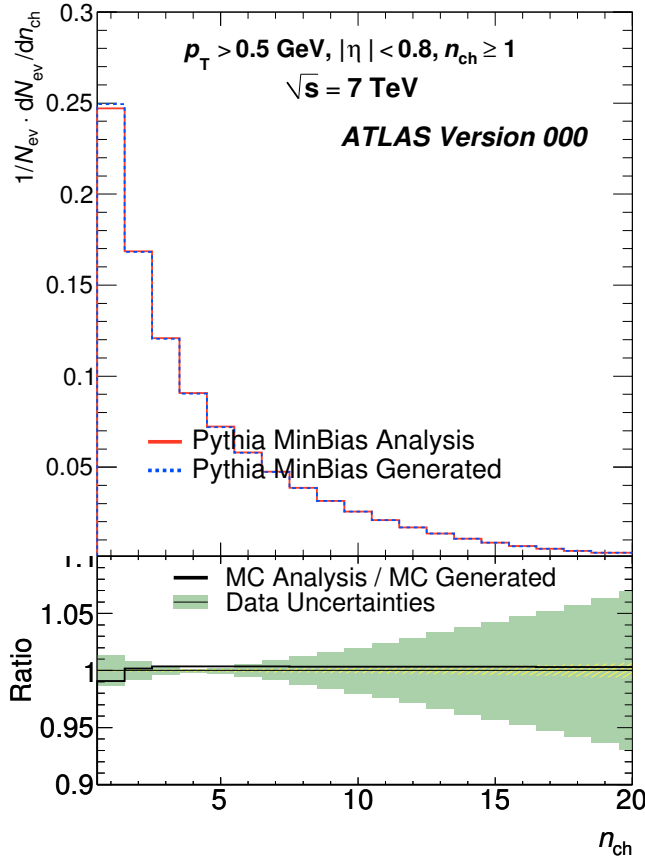
Figure 10.1. MC closure test of the correction procedure. The green band indicates the total systematic uncertainties on the measurement.

$s/\sqrt{12}$ to the statistical error. The number of selected events has the additional binomial uncertainty on the efficiency to select an event given the event passed the trigger. Therefore the total error on the number of recorded events is given by

$$\sigma(n_{\text{obs}}) = \sqrt{\epsilon \cdot n_{\text{MBTS\_1}} \cdot (1 - (1 - \frac{1}{s})\epsilon)} \oplus \frac{\epsilon \cdot s}{\sqrt{12}} \tag{10.27}$$

Once the μ-correction is applied the error on the corrected number of events is given by

$$\sigma(n_{ev}^{corr}) = s \cdot \sigma(n_{\text{obs}}) \cdot \frac{n_b f_r}{n_b f_r - n_{ev}} \tag{10.28}$$

Fig. 10.2 shows the resulting raw and corrected rates of events as a function of UTC time for LHC Fill 1089. The gaps in the run correspond to the second and third van der Meer scans and times when the ATLAS detector was not taking data.
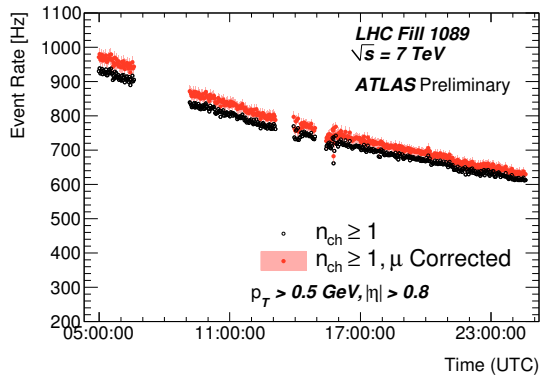
Figure 10.2. Rate of events in LHC Fill 1089 with at least one charged primary particle ($p_T > 0.5$ GeV/c, $|\eta| < 0.8$) versus UTC time corrected (red circles) and uncorrected (black circles) for multiple interactions.

10.3 Beam Separation Scan Analysis

10.3.1 Scan Descriptions

In 2010 there were five van der Meer scans performed for ATLAS. The first occurred on April 26th, the second and third on May 9th, and the fourth and fifth on October 1st. Table 10.1 gives parameters of each scan. [111] provides the full details of scans I through III, [75] details scans IV and V.

In scans I-III there was only one colliding bunch in ATLAS and the beam currents were relatively low. In scans IV and V there were 6 colliding bunches in ATLAS, which allowed for a bunch-by-bunch luminosity determination. Additionally, scans IV and V are the only scans with a crossing angle (200 μrad) and had a significantly higher average number of interactions per crossing than the previous scans.

For each scan the beams were centered at the nominal interaction point with a three point mini-scan in both the horizontal (x) and vertical (y) planes. The mini-scans were performed by using a closed orbit bump, in which the beams are displaced $\pm 1\sigma_b$ by disturbing the beam orbit using pairs of steering dipoles located on either size of the IP. σ_b is the nominal transverse beam size. Then the beams were displaced by $3\sigma_b$ in opposite directions and scanned through $\pm 3\sigma_b$, leading to a relative displacement of $\pm 6\sigma_b$. For scan I this was done first in x and then in y. For scans II and III the beams were taken from positive to negative nominal separation, followed by a hysteresis cycle where the full $\pm 6\sigma_b$ separation was run, followed by a scan from negative to positive nominal separation. This was done first in the x and then in the y direction. In all three of these scans, 27 steps were taken for scan direction. In IV and V x and y scans were performed sequentially as in Scan 1, and then repeated to test the reproducibility of the results. In this case, 25 steps were used. After each scan a re-centering of the beams was performed if necessary. After the last scan was performed, an x and y scan was performed with the beam offset by 1σ in the non-scanning direction to test coupling of the beams in x and y.

Figure 10.3 shows the scanning sequence for scans I, II, and III in the horizontal plane. Figure 10.4 shows the raw and μ-corrected track rates for the same scans. Only data taken

	vdM Scan I (April 26, 2010)	vdM Scan II, III (May 9, 2010)	vdM Scan IV, V (October 1, 2010)
LHC Fill Number	1059	1089	1386
Scan Directions	x,y	$x,,x,y,y$	x,y,x,y
N Steps per Plane	27	27	25
Δt per Step	30 s	30 s	20 s
n_b colliding	1	1	6
n_b total	2	2	19
N_p per bunch	$\sim 0.1 \cdot 10^{11}$	$\sim 0.2 \cdot 10^{11}$	$\sim 0.9 \cdot 10^{11}$
β-function at IP			
$\beta^\star$ (m)	~ 2	~ 2	~ 3.5
Transverse single beam size			
σ_b (μm)	~ 45	~ 45	~ 60
Crossing angle (μrad)	0	0	200
$\mathcal{L}$/bunch ($\mu b^{-1}/s$)	$4.5 \cdot 10^{-3}$	$1.8 \cdot 10^{-2}$	0.22
$\langle \mu \rangle$	0.03	0.11	1.3

Table 10.1. Summary of the main characteristics of the five *vdM* scans performed at the ATLAS interaction point. The values of $\mathcal{L}$/bunch and μ are given for zero beam separation.

during specific intervals-of-validity (IOV) were used in the scan analysis. The IOV correspond to the 30 s (scans I-III) or 20 s (scans IV and V) where the beams were not moving and considered stable.

(a)   (b)
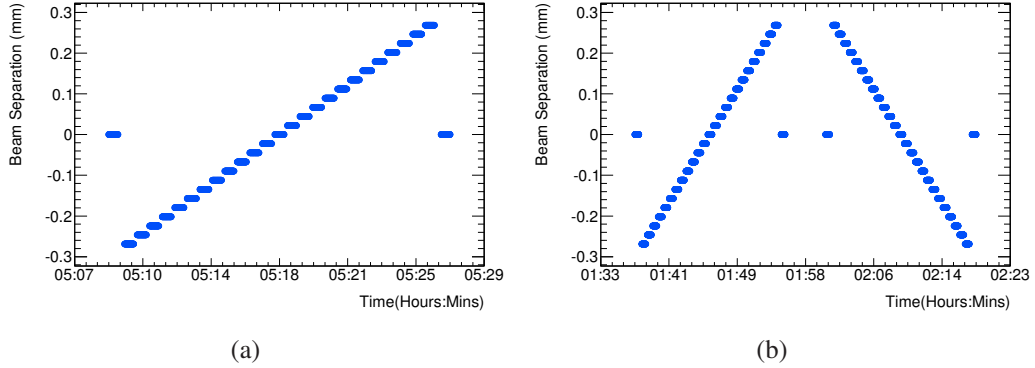
Figure 10.3.   Horizontal beam displacement versus local Geneva time for scan I (a) and scans II and III (b) [114].

(a)   (b)
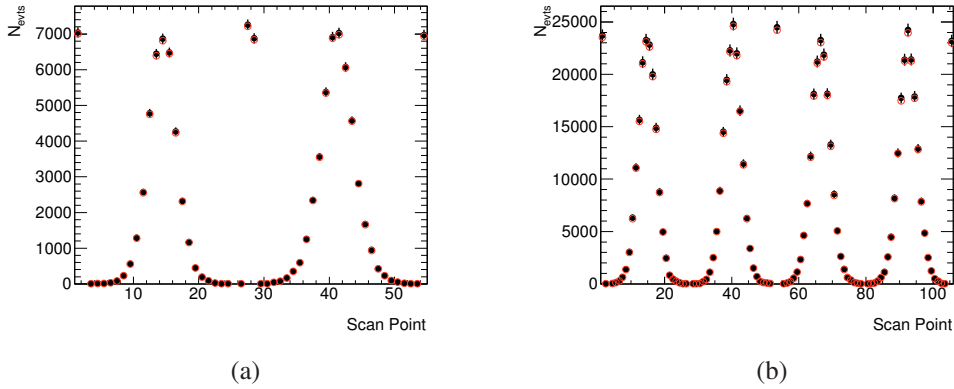
Figure 10.4. Rate of events with at least one track for vdM scan I (a) and Scans II and III (b) as a function of the scan point. The uncorrected data are in the red open circles, the μ-corrected data are the black points.

10.3.2   Fits for Beam Parameters

For each scan, the event rate was plotted as a function of the beam separation, and normalized to eliminate beam lifetime effects. The normalization at scan point p is given by

$$R(p) = \frac{(I_1 I_2)_{MAX}}{(I_1 I_2)(p)} R_{meas}^{corr}(p) \tag{10.29}$$

where $(I_1 I_2)_{MAX}$ is the maximum product of the beam currents measured during the scan, $(I_1 I_2)(p)$ is the measured product of the beam currents at scan point p and $R^{corr}_{meas}(p)$ is the μ-corrected measured event rate at p. R is called the *specific rate*.

For all algorithms and all scans, the data were fit well by a double Gaussian distribution. The specific rate as a function of the beam separation was fit to

$$R_x(x) = \frac{R_x(0)}{\sqrt{2\pi}} \left[\frac{f_a e^{-(x-x_0)^2/2\sigma_a^2}}{\sigma_a} + \frac{(1-f_a)e^{-(x-x_0)^2/2\sigma_b^2}}{\sigma_b} \right] \qquad (10.30)$$

and similarly for the y direction. Substituting this $R_x(x)$ into Equation **??** yields the following expression for Σ_x

$$\frac{1}{\Sigma_x} = \left[\frac{f_a}{\sigma_a} + \frac{1-f_a}{\sigma_b} \right]. \qquad (10.31)$$

Figure 10.5 shows the x and y fits for scans I, II, and II for the charged particle event counting method. Table 10.2 shows the fit results for the same method.

The charged particle method was not used for scans IV and V. Figure 10.6 shows fits by bunch group for the x scan in scan IV. The details of Scans IV and V fits are found in [75], what is presented here for the LUCID_OR algorithms summarizes the work contained therein.

For each scan the visible cross-section was computed by taking the average of the maximum specific rates in x and y and using the following formula

$$\sigma_{\text{vis}} = R^{MAX} \frac{2\pi \Sigma_x \Sigma_y}{n_b f_r (n_1 n_2)_{MAX}} \qquad (10.32)$$

where $(n_1 n_2)_{MAX}$ is the maximum product of the number or proton per bunch during the scan. Table 10.3 has the measured σ_{vis} and $\mathcal{L}_{spec}$ for the charged particle method. Averaging the scans yields a visible cross-section of

$$\sigma_{\text{vis}}^{\text{ch part}} = 42.7 \pm 0.2 \text{ mb}. \qquad (10.33)$$

The error is purely statistical.

For scans IV and V σ_{vis} was determined separately for each BCID and then averaged. Table 10.4 shows the measured σ_{vis} values for those scans with the LUCID_OR algorithm.

10.3.3   Uncertainties

Many sources of systematic uncertainty were considered in the vdM scan analysis. This section summarizes the uncertainty determination detailed in [75].

- **Beam Currents** The dominant uncertainty is the LHC beam current determination which is described in detail in [119, 120]. The integrated beam currents are measured

Scan	Mean X (μm)	Σ_X (μm)	Mean Y (μm)	Σ_Y (μm)	R_X^{MAX} (Hz)	R_Y^{MAX} (Hz)	$\frac{\chi_X^2}{DOF}$	$\frac{\chi_Y^2}{DOF}$
1	-1.67 ± 0.3	47.3 ± 0.3	-5.61 ± 0.35	56.1 ± 0.4	253.2 ± 1.6	249.3 ± 1.6	0.8	1.4
2	7.42 ± 0.34	58.5 ± 0.2	2.27 ± 0.36	62.3 ± 0.3	869.1 ± 4.2	841.2 ± 4.1	1.1	1.1
3	6.03 ± 0.33	59.3 ± 0.2	-0.32 ± 0.36	61.5 ± 0.3	869.6 ± 4.2	840.6 ± 4.1	1.1	0.9

Table 10.2. Results of the fit for the charged particle analyses. The mean of the convoluted beam width distribution is listed as mean position X and Y, Σ_x and Σ_y are the widths in the x and y directions, R_x^{MAX} and R_y^{MAX} are the maximum specific rates obtained during each scan, and $\frac{\chi_{X,Y}^2}{DOF}$ are the χ^2 probabilities divided by the number of degrees of freedom of the fit.

Scan Number	σ_{vis} mb	$\mathcal{L}_{spec}$ $(10^{29} \text{ cm}^{-2}\text{s}^{-1})$
1	42.61 ± 0.26	6.74 ± 0.05
2	42.84 ± 0.21	4.91 ± 0.02
3	42.93 ± 0.21	4.91 ± 0.03

Table 10.3. Measurement of the visible cross section and peak specific luminosity for each scan for the charged particle event counting method.

	LUCID_EventOR σ_{vis} (mb)	
BCID	Scan IV	Scan V
1	41.76 ± 0.07	41.68 ± 0.06
501	41.89 ± 0.07	41.63 ± 0.06
862	41.86 ± 0.06	41.76 ± 0.05
1451	41.78 ± 0.07	41.74 ± 0.06
1651	41.85 ± 0.07	41.71 ± 0.07
2301	41.87 ± 0.07	41.74 ± 0.06
Average	41.84 ± 0.03	41.71 ± 0.02
χ^2/DOF	0.61	0.66

Table 10.4. Measured σ_{vis} values for the LUCID_OR algorithm by BCID. Errors shown are statistical only. The χ^2/DOF is shown for the 5 degrees of freedom in the average value.

by DC current transformers (DCCT) and the bunch-by-bunch currents are determined with a relative measurement by the fast beam current transformers(FBCT). The absolute scale of the DCCT varies from fill to fill and has baseline drifts over the course of a fill. This leads to a 2.7% uncertainty which is uncorrelated between fills. Additional sources of current uncertainty arise from knowledge of the baseline offset as well as the bunch-to-bunch fraction. The uncertainties in these factors decrease with increasing bunch current, therefore the total beam current uncertainty is 5.6% for scan I, 4.4% for scans II and III, and 3.1% for scans IV and V.

- **Beam Centering** In order to achieve the true peak luminosity, the beams must be centered in the non-scanning plane. The uncertainty was determined by looking at the difference in the peak position at the beginning and end of the scans. For scans I through III this is a 2% uncertainty and for scans IV and V this is a 0.04% uncertainty.

- **Emittance Growth** The beam emittance grows over the course of the fill, changing the values of Σ_x and Σ_y. This should cancel with the corresponding decrease in R and therefore σ_{vis} should be unaffected. This is true for scans IV and V. For scans I through III, this effect is included in the 3% uncertainty due to non-reproducible effects.

- **Beam-position jitter** Jitter in the beam position within a given scan point was determined from the RMS of the beam position distribution within a scan point. This results in a 0.3% uncertainty for scans IV and V and the 2.7% uncertainty for non-reproducibility for scans I through III covers this effect.

- **Length Scale Calibration** The length scale calibration refers to the determination of the *true* beam separation at each point in the scan. Dedicated scans were run where the beams were displaced in the same direction and the beam-spot was determined at

each step. The uncertainty on scans I through III is 2% and is largely statistical. The 0.3% uncertainty found for scans IV and V is assumed to be uncorrelated between the scans.

- **Absolute Length Scale of ATLAS detector** Because the length scale is determined using the ATLAS detector, any systematic mismeasurements could lead to a bias in the length scale. This effect was studied using misaligned Monte Carlo simulation and found to be at most 0.3%.

- **Fit Model** A cubic spline fit was used in place of a Gaussian to determine the uncertainty due to the fit model. The difference in fit results was taken as a systematic uncertainty. This leads to a 1% uncertainty for scans I through III and 0.2% for scans IV and V.

- **Transverse Correlations** Correlations in the beam profiles between the x and y planes will modify the measured specific luminosity because the density profiles will no longer factorize. This leads to a 3% uncertainty on scan I, 2% on scans II and III, and a 0.9% uncertainty on scans IV and V.

- **μ-Dependence** Scans I, II and III were taken at low μ values, therefore the corrections were small, however a 2% uncertainty was applied based on the agreement between different algorithms for the value of μ. Scans IV and V had μ values from 0 to 1.3, therefore the agreement between algorithms over that μ range was used to set an uncertainty of 0.5%.

Table 12.8 summarizes the uncertainties and the level of correlation between scans of the given error source.

Scan Number	I	II–III	IV–V	
Fill Number	1059	1089	1386	
Bunch charge product	5.6%	4.4%	3.1%	Partially correlated
Beam centering	2%	2%	0.04%	Uncorrelated
Emittance growth and other non-reproducibility	3%	3%	0.5%	Uncorrelated
Beam-position jitter	–	–	0.3%	Uncorrelated
Length scale calibration	2%	2%	0.3%	Partially Correlated
Absolute ID length scale	0.3%	0.3%	0.3%	Correlated
Fit model	1%	1%	0.2%	Partially Correlated
Transverse correlations	3%	2%	0.9%	Partially Correlated
μ dependence	2%	2%	0.5%	Correlated
Total	7.8%	6.8%	3.4%	

Table 10.5. Relative systematic uncertainties on the determination of the visible cross section σ_{vis}.

10.3.4 Results

In order to combine the results from all five scans to determine the luminosity calibration the statistical and systematic uncertainties, as well as their correlations, were taken into account. The average value of the LUCID_OR σ_{vis} is $13.04 \pm 0.01 \pm 0.44$ mb. The χ^2 of the combination is 1.6. The combination is dominated by scans IV and V, collectively contributing 92% of the weight in the fit. The total fractional error is $\pm 3.4\%$.
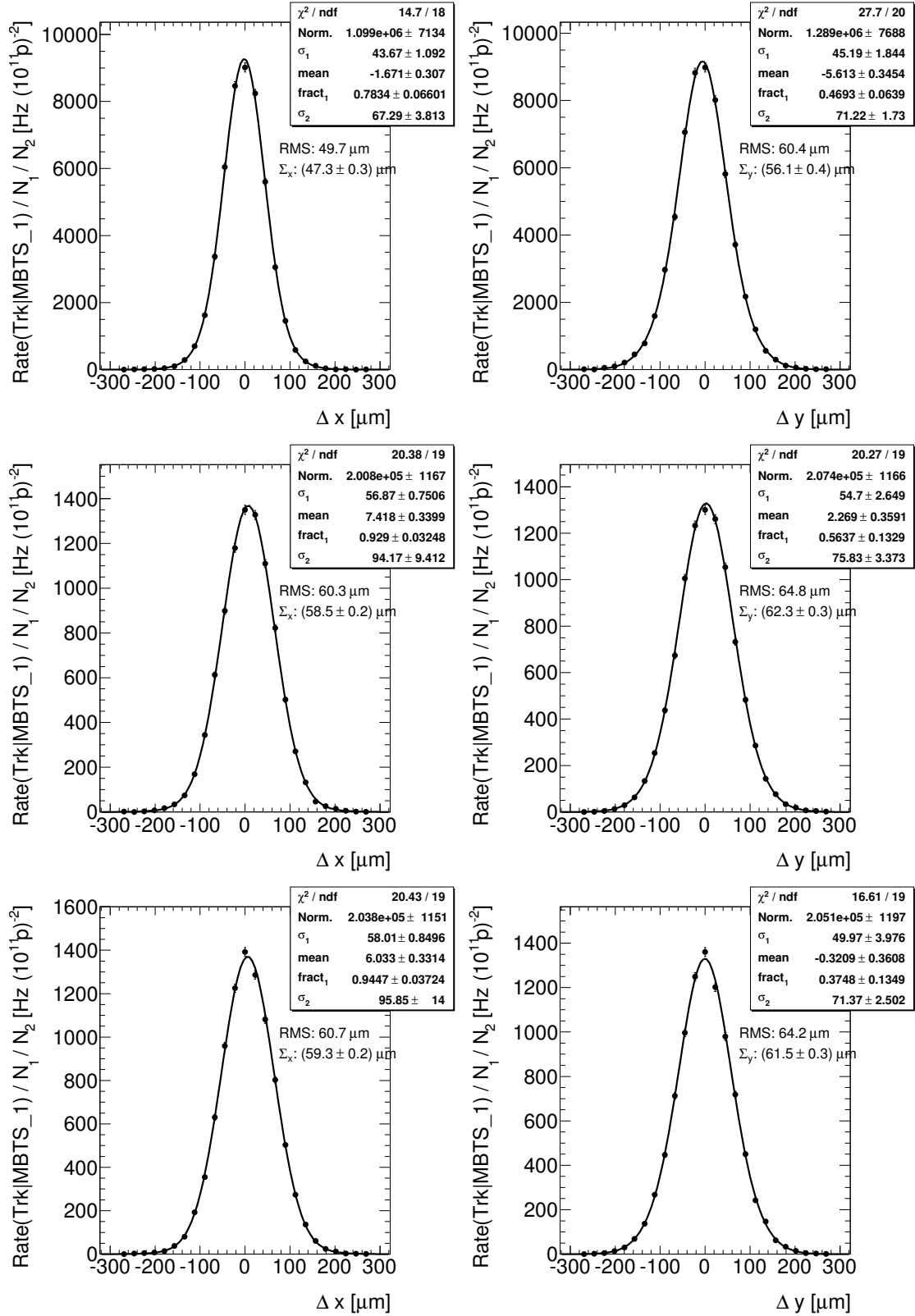
Figure 10.5. Fit results for the 1st (top), 2nd (middle) and 3rd (bottom) VdM scan using the charged particle event counting method.
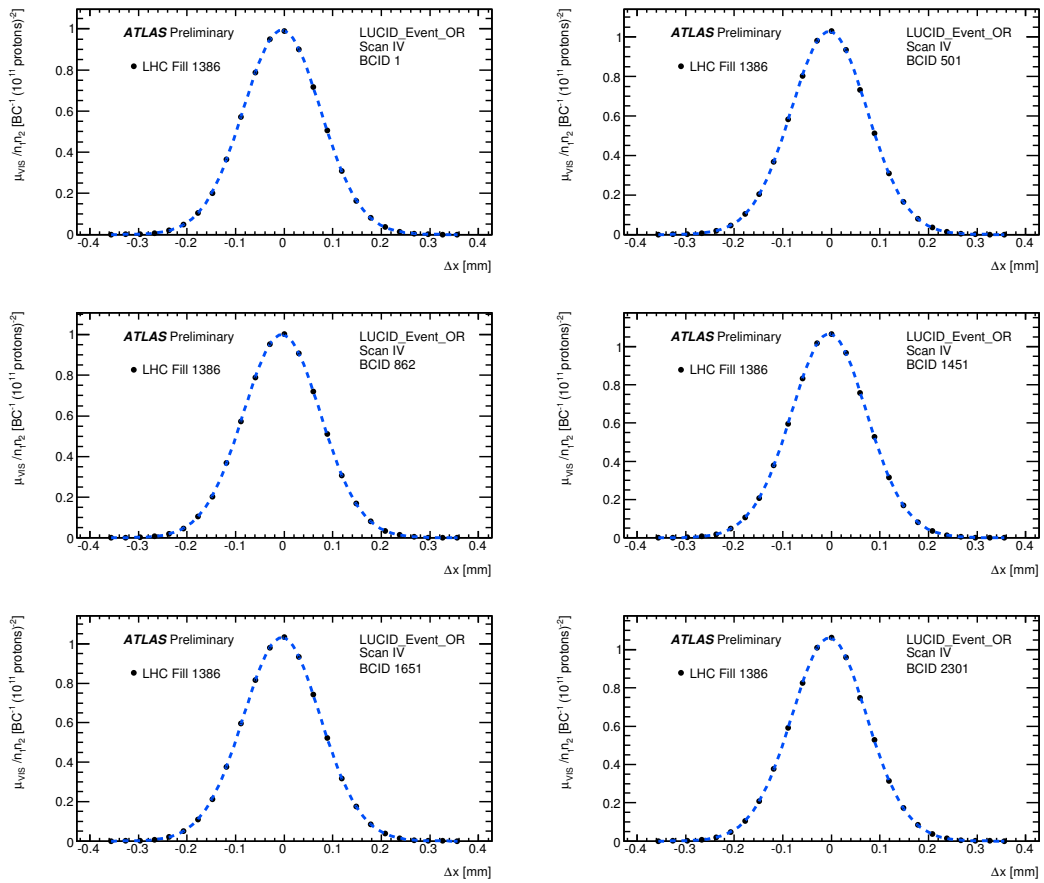
Figure 10.6. Fit results for the the LUCID_OR algorithm for six different bunch groups for Scan IV [75].

<div align="right">

CHAPTER 11

</div>

Comparisons of Monte Carlo Modeling of Diffractive Events

Before Monte Carlo models are used to assess the acceptance of the cross-section measurement, their ability to reproduce basic kinematic distributions of the data must be verified. Chapter 2 described the models Monte Carlo generators use to predict multiple particle production in non-diffractive and diffractive dissociation events. This chapter presents studies of the agreement between data and the Monte Carlo models on exclusive quantities in diffractive events. First, the ability of the Monte Carlo generators to reproduce charged particle distributions in a diffraction-enhanced sample is examined. This section largely summarizes work presented in [121]. Then, the data and Monte Carlo models are compared in the MBTS acceptance.

11.1   Track-based Studies

Distributions of charged particles are powerful tools for assessing data and Monte Carlo model agreement because they are sensitive to the properties of single particles. Reference [70] gives a comprehensive look at the properties of charged particles and events with at least two charged particles with $p_T > 100$ MeV and $|\eta| < 2.5$. This phase space is dominated by non-diffractive events. In order to tune the Monte Carlo parameters related to low momentum $2 \to 2$ scattering, charged particle multiplicity, pseudorapidity and momentum distributions are used. To minimize the effects of the uncertainty in diffractive modeling, diffractive-suppressed phase spaces are often used. Some experiments attempt to address this by removing the single-diffractive events from their datasets [122, 123, 124] while AT-LAS has published additional results in a high-multiplicity, high-momentum phase space where diffractive events are greatly suppressed [70].

In order to understand how well the generators model exclusive quantities in diffractive events, this section presents charged particle multiplicity, pseudorapidity and momentum distributions in a phase space which is dominated by diffractive dissocation events.

The events are selected by requiring that there be hits on only one of the two sides of the MBTS detector. As will be shown in Section 11.1.3, this selection results in a diffraction-dominated sample. Section 11.1.1 outlines the study. The datasets and event and track selection are described in Section 11.1.2. Section 11.1.4 discusses the agreement between data and the detector simulation for the tracking and MBTS detectors. Section 11.1.5 reviews the systematic uncertainties on the measurement, and Section 11.1.6 presents the comparisons.

11.1.1   Overview of Studies

A sample enhanced in diffractive events is created by selecting events where there is at least *one* MBTS hit on exactly one side of the detector (A- or C-side). Only one hit is required because the additional requirement of a track, which is detailed below, significantly reduces the backgrounds for events with just one hit over threshold. This selection essentially requires the presence of a forward rapidity gap in the event and therefore preferentially selects single-diffractive dissociation events and double-diffractive dissociation events in which the diffractive mass of one of the proton remnants is too small to be seen by the MBTS detectors[1].

This analysis further requires a track with a transverse momentum of at least 500 MeV and $|\eta| < 2.5$, similar to the selection in [109]. The details of the track selection are given in Section 11.1.2.

To investigate the event kinematics, the following distributions are plotted:

$$\frac{1}{N_{ev}}\frac{\mathrm{d}N_{trk}}{\mathrm{d}\eta}, \quad \frac{1}{N_{ev}}\frac{1}{2\pi p_T}\frac{\mathrm{d}^2 N_{trk}}{\mathrm{d}\eta \mathrm{d}p_T}, \quad \frac{1}{N_{ev}}\frac{\mathrm{d}N_{ev}}{\mathrm{d}n_{trk}}, \quad \frac{1}{N_{ev}}\frac{\mathrm{d}N_{trk}}{\mathrm{d}\Delta\eta} \tag{11.1}$$

where N_{ev} is the number of events with at least one track satisfying the single-sided MBTS requirements, p_T is the transverse momentum, η is the pseudorapidity of the track, n_{trk} is the number of selected tracks per event, and N_{trk} is the total number of selected tracks in the data sample. The variable $\Delta\eta$ is the absolute value of the difference in pseudorapidity between the edge of the MBTS detector that has no hit (η_{MBTS}) and the track, i.e. $\Delta\eta = |\eta_{MBTS} - \eta|$ where η_{MBTS} is $+2.08$ or -2.08 depending on which MBTS side did not have any hits. Tracks which enter this distribution cannot overlap in η with the MBTS acceptance of the side of the detecto which did not have any hits, i.e. $\eta > \eta_{MBTS}$ ($\eta < \eta_{MBTS}$) if $\eta_{MBTS} < 0$ ($\eta_{MBTS} > 0$).

Unlike the minimum bias analysis measurements cited above, these measurements are not corrected for detector effects. Corrections for tracking inefficiency and event loss to obtain charged particle level distributions are beyond the scope of this study. However, systematic uncertainties reflecting the agreement between data and detector simulation are

---

[1]In terms of $\xi = M_X^2/s$, ξ must be greater than 5×10^{-6} and less than 5×10^{-4}.In the case of double-diffraction the lower mass dissociation system must have a mass less than 5×10^{-6}. The $\xi-$acceptance is discussed in more detail in Chapter 12.

Run	$\mathcal{L}$ (μb^{-1})	N_{Ev}
152166	7.0	0.5M
152221	20.2	1.4M

Table 11.1. Luminosity and number of events recorded in the stream *physics_MinBias*.

presented. Therefore, the remaining differences between data and Monte Carlo events are attributed to differences in physics modeling.

11.1.2 Datasets and Event Selection

Data Sets and MC samples

The data used in this study come from the two ATLAS runs at $\sqrt{s} = 7$ TeV taken in late March and early April described in Chapter 7: 152166 and 152221. Only luminosity blocks where both the Inner Detector and the MBTS detector were functioning properly are considered. The integrated luminosity is approximately 27 μb^{-1}. Table 11.1 gives the luminosity and the number of events in the *physics_MinBias* stream, a data stream including all minimum bias triggers.

The Monte Carlo samples used are the same as those described in Chapter 7. Only the Schuler-Söjstrand SD and DD differential cross-section models are used for the PYTHIA 8 generators because this study is more sensetive to the charged particle kinematics than the diffractive mass distribution. The Monte Carlo events were weighted to approximately reproduce the longitudinal beamspot width observed in data. No reconstructed vertex is required for this event selection, therefore, an exact weighting cannot be performed.

Event and Track Selection

All events considered in the analysis must pass the L1_MBTS_1 trigger and have hits on only the A- or the C-side of the MBTS detector (but not both). In addition, at least one reconstructed track fulfilling the following requirements:

- $p_T > 500$ MeV
- $|\eta| < 2.5$
- $|d_0^{\mathrm{BS}}| < 1.5$ mm
- $|z_0| < 100$ mm
- $N_{\mathrm{Pix}} \geq 1$
- $N_{\mathrm{SCT}} \geq 6$

is required. This event selection does not require a primary vertex due to the relatively low vertex finding efficiency for the events of interest. Because they produce few central charged particles, many diffractive events do not have a reconstructed vertex.

Generator	A^{DD}_{1-trk}	A^{SD}_{1-trk}	A^{ND}_{1-trk}
Pythia 6	39.2%	37.0%	97.5%
Pythia 8	50.1%	55.6%	97.3%
Phojet	52.2%	63.7%	95.9%

Table 11.2.
Acceptances for events to have at least one track with $p_T > 500$ MeV and $|\eta| < 2.5$ for PYTHIA6, PYTHIA8 and PHOJET for double-diffractive (DD), single-diffractive (SD) and non-diffractive (ND) events.

Generator	DD		SD		ND	
	$A^{DD}_{incl-trk}$	A^{DD}_{ss-trk}	$A^{SD}_{incl-trk}$	A^{SD}_{ss-trk}	$A^{ND}_{incl-trk}$	A^{ND}_{ss-trk}
Pythia 6	97.23%	23.89%	97.67%	20.73%	99.9%	0.68%
Pythia 8	99.97%	26.97%	99.97%	22.93%	100.0%	0.13%
Phojet	97.89%	14.22%	97.80%	22.03%	100.0%	0.48%

Table 11.3. Acceptances for events with activity in either side of the MBTS, $A_{incl-trk}$, and on only one side of the MBTS, A_{ss-trk}, for events with at least one track with $p_T > 500$ MeV and $|\eta| < 2.5$ for Pythia 6, Pythia 8 and Phojet for double-diffractive (DD), single-diffractive (SD) and non-diffractive (ND) events.

11.1.3 Acceptance

The acceptances of the track requirement are give in Table 11.2 for the single-dissociation, double-dissociation, and non-diffractive events for the three MC programs. PYTHIA 8 and PHOJET both predict that 50% of DD events will have a track, while PYTHIA 6 predicts only 40%. Similarly, for SD events PYTHIA 6 predicts nearly 20% few events passing than PYTHIA 8 and 25% less than PHOJET. The gap between PYTHIA 6 and the other generators is due to is soft diffractive component. The generators predict between 95 and 97% of ND events pass the track cut.

Table 11.3 gives the acceptances of the MBTS hit requirement for double-diffractive, single-diffractive and non-diffractive events for PYTHIA6, PYTHIA8 and PHOJET. These acceptances are with respect to the track requirement. Both the inclusive (at least one hit in the MBTS detector) and single-sided (at least one hit on exactly one side of the detector) are shown for comparison purposes. The total acceptance is obtained by multiplying the numbers from Table 11.3 with those of Table 11.2.

It Table 11.3 the acceptances vary between 14% and 27% for the single-sided requirement for diffractive production, while for non-diffractive production the acceptances are less than 1% for all generators. For the inclusive requirement of any MBTS hit the acceptance is $> 97\%$ in all cases. The high acceptance value is expected because at least one central charged particle is ensured by the track requirement. Th generators predict similar acceptance values for the SD process but differ by nearly a factor two in the DD predictions.

11.1.4 Data and Simulation Response Agreement

Before determining the level of agreement between data and Monte Carlo models on underlying physics distributions, the degree to which the simulation reproduces the response of the detector and reconstruction must be assessed. The MBTS performance was extensively validated in Chapter 8. This section concentrates on the tracking performance for this event sample.

Chapter 6.1 and [109] already demonstrated that the data and Monte Carlo simulation agree well for inclusive minimum bias measurements. Because this study has a different event and track selection, it is necessary to check that the same level of agreement is found. Figure 11.1 shows a comparison of the transverse and longitudinal impact parameter distribution between data and PHOJET MC for the single-sided sample.
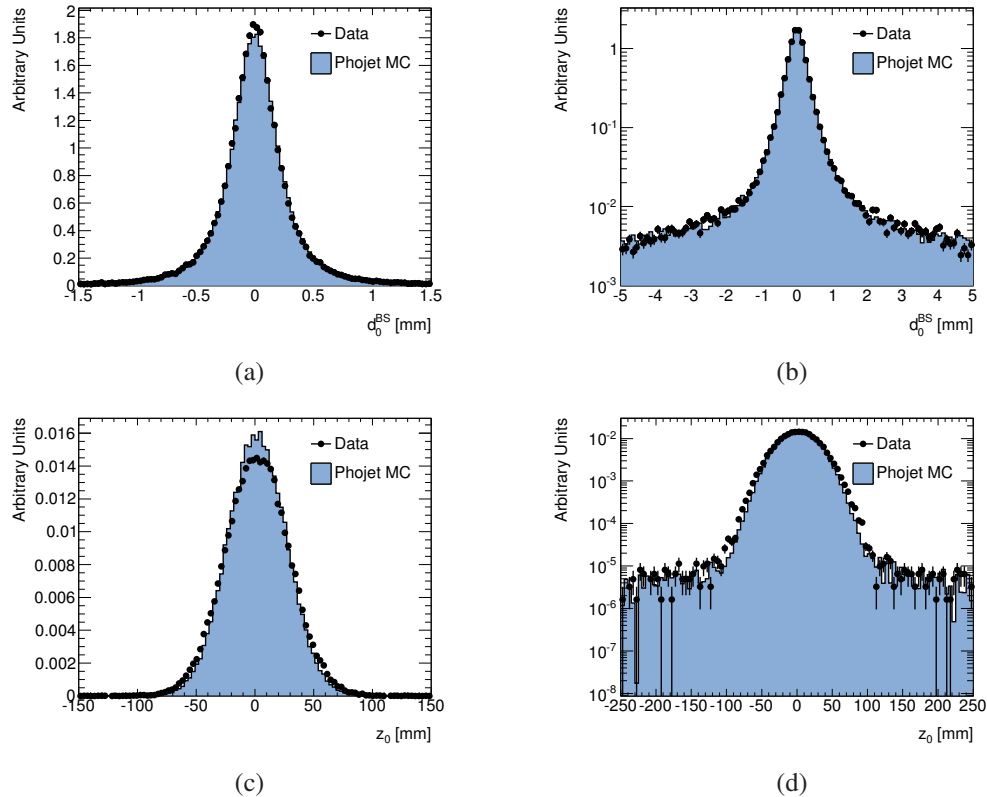
Figure 11.1. A comparison of transverse (a, b) and longitudinal (c, d) impact parameter distributions for events passing the single sided event selection. These distributions are shown applying all cuts apart from that on the quantity shown. The data (markers) are compared to PHOJET (histogram)

The agreement between data and simulation is fairly good for the transverse impact parameter distribution both in the core and the tails of the distribution. The data z_0 distribution is slightly broader than the simulation distribution, indicating that the re-weighting

does not work perfectly. However, the tail fraction ($|z_0| > 100$ mm) is in good agreement between data and MC.

Figure 11.2 shows the number of Pixel and SCT hits on track as well as the average number of Pixel and SCT hits versus η. The agreement between data and simulation is excellent. The data tracks have slightly fewer Pixel hits on average, the disagreement arising primarily from tracks in the forward region. The overall agreement of the average number of SCT hits on track is good. In the region $|\eta| > 1$ the average number of hits is varying strongly due to the structure of the SCT endcaps. This region is most sensitive to the longitudinal beamspot width, therefore differences between the data and MC simulation are expected.

(a)

(b)

(c)

(d)
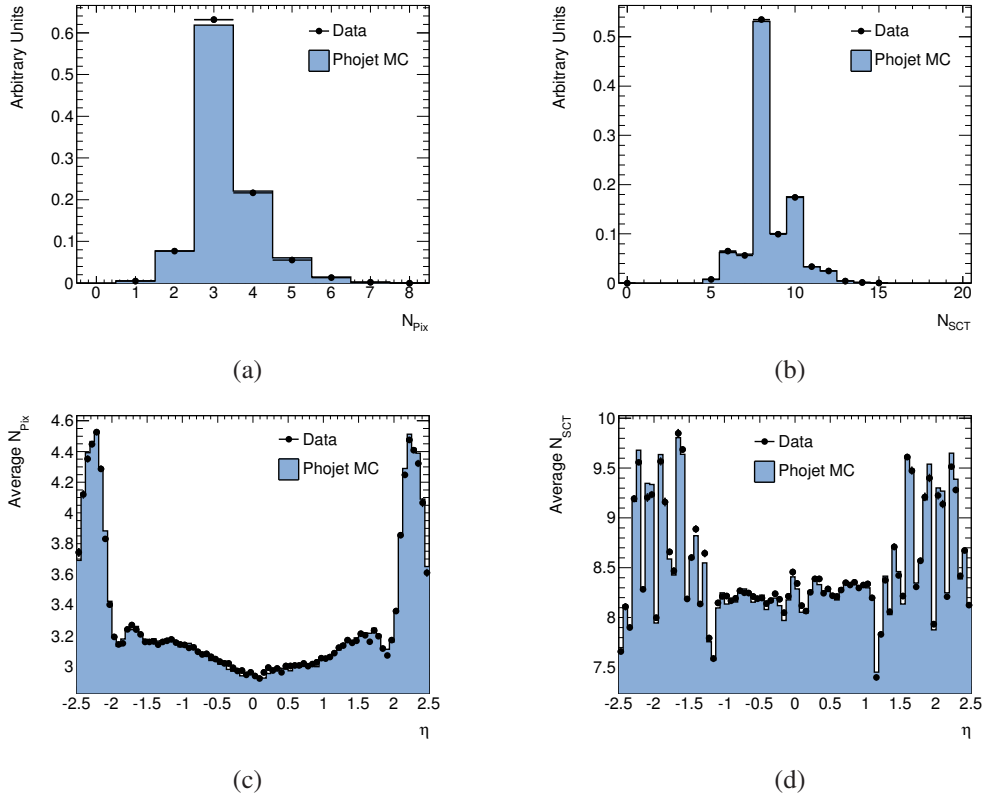
Figure 11.2. A comparison of silicon hit quantities for data (points) and PHOJET Monte Carlo. (a) and (b) show the number of Pixel and SCT hits on track, respectively. (c) and (d) show the average number of Pixel and SCT hits versus η.

11.1.5 Systematic Uncertainties

The systematic uncertainties in this measurement arise from three principle sources: beam backgrounds, the MC simulation of the MBTS performance and the MC simulation

of the tracking performance. Each subject is discussed in the following.

Beam Backgrounds

Beam backgrounds are described in Chapter 9. For this study the background is determined using the single, non-colliding (unpaired) bunches which traverse ATLAS. The two runs considered contain 41.5k MBTS triggered events in the unpaired bunches, 39.7k of which have activity on only one side of the MBTS. These numbers can be compared to the 1.4M MBTS triggered events in the paired bunches, 0.2M of which are single-sided. Once a track fulfilling all the selection cuts is required, there are 52 events passing the MBTS trigger in the unpaired bunches, 1 of which passes the single-sided selection. Loosening the track p_{T} requirement to 100 MeV yields 322 MBTS triggered events, 5 of which are single-sided. The colliding bunches have 1.2M MBTS triggered events with at least one 500 MeV track, with a subset of 5.3k single-sided events. Therefore it is concluded that the beam background represents less than 0.02% of the number of events selected in the colliding bunches and is neglected.

MBTS Response

The MBTS response systematic uncertainty was determined prior to the completion of the studies presented in Chapter 8. Therefore, a conservative method is used to assign the uncertainty. The threshold for the simulated events was kept at 0.15 pC and the data threshold was raised to 0.3 pC. Then, the analysis was repeated and the fractional difference in the resulting distributions (Equation 11.1.1) was taken as the uncertainty. It was assigned as a symmetric uncertainty, thereby covering the fact that the MC were more efficient than the data. The main result of the variation is to increase the number of ND events passing the cut. Intuitively the increase happens because ND events are most likely to have hits on both sides of the MBTS, and when the threshold is raised, hits can be lost, mimicking the single-sided selection. The data support this explanation: η distribution becomes more central and the p_T and n_{trk} spectra become harder due to the larger contamination from ND events.

Inaccuracies in the modeling of the material between the interaction point and the MBTS detectors were checked with the extra material PYTHIA 6 sample. Differences of less than 0.1% were found in the fraction of single-sided events, and therefore material effects were ignored in the MBTS response systematic uncertainties.

Tracking Performance

The performance of the Inner Detector tracking has been studied extensively in [109, 70]. This analysis applies the same track selection aside from the impact parameter cuts, which are with respect to the primary event vertex in [109, 70] instead of the beam spot as in this track selection. Because the difference is small and the distributions are well modeled by simulation, the tracking efficiency uncertainties are taken directly from Ref. [**?**].

Systematic Uncertainty	Systematic
Truth Primary Definition	$\pm 0.4\%$
Material	$\pm 3\%*$
Alignment	$\pm 1\%$
SCT Extension	$\pm 6\%\ (2.2 < |\eta| < 2.5)$ $\pm 4\%\ (1.6 < |\eta| < 2.2)$
Particle Composition	$\pm 0.2\%$
Resolution	$\pm 1\%\ (0.5 < p_{\mathrm{T}} < 0.6\ \mathrm{GeV})$

Table 11.4. The systematic uncertainties on the tracking efficiency used in [109]. All uncertainties are quoted relative to the track reconstruction efficiency except for the uncertainty due to the material which is absolute.

Chapter 6.1 summarizes the sources of systematic uncertainties on the tracking efficiency. Table 11.4 lists the systematic uncertainties relevant for this study.

The systematic uncertainty due to the tracking efficiency is assessed by varying a parametrized efficiency within the uncertainties and applying it to the Monte Carlo truth distributions. The fractional difference of the resulting distributions give the systematic uncertainty on the quantity of interest. The contribution of the tracking efficiency uncertainty to the uncertainty on the total number of events passing the single-sided selection cuts is 3%, whereas the uncertainty on the number of events passing the inclusive requirement is only 0.05%. This difference arises because the single-sided events are typically low multiplicity events. 90% of events have one or two tracks per event, leading tracking inefficiencies to translate directly into event losses. However, the impact of the event loss largely cancels out in the track distributions which are normalized by the total number of events passing the selection.

11.1.6 Comparisons

In data there are 52,801 events passing the single-sided selection out of 1,169,508 events passing the inclusive selection. Figures 11.3 and 11.4 show the track η, multiplicity and p_T distributions for events passing the single-sided MBTS requirement. The data are compared to the PYTHIA6, PYTHIA8 and PHOJET samples.

The η distribution in the data is rather flat. It is well modeled by PHOJET and PYTHIA8 in overall normalization while PYTHIA6 underestimates the data by about 15-20%.

The n_{trk} distribution is well modeled both by PYTHIA8 and PHOJET while the PYTHIA6 spectrum is much softer than the data until the high multiplicity region where the non-diffractive component dominates.

The track $\frac{1}{N_{ev}} \frac{1}{2\pi p_T} \frac{\mathrm{d}^2 N_{trk}}{\mathrm{d}\eta \mathrm{d}p_T}$ distribution predicted by PHOJET is in excellent agreement with the data over most of the p_T range. PYTHIA8 predicts a slightly softer spectrum than that observed in data. PYTHIA6 is much softer than the data between 1 and 3 GeV but agrees in the high p_T tail where the ND process dominates.

Fig. 11.5 shows $\frac{1}{N_{ev}} \frac{\mathrm{d}N_{trk}}{\mathrm{d}\Delta\eta}$. It is seen that the rate of tracks increases from 0.05 at $\Delta\eta = 0$
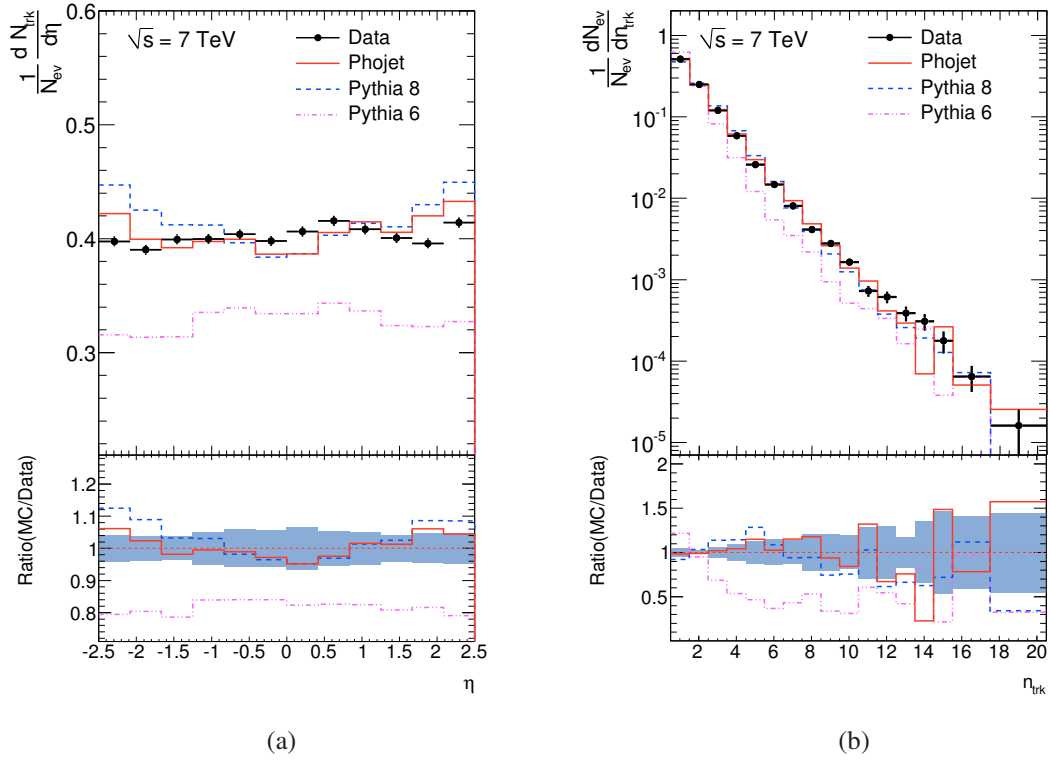
Figure 11.3. Distributions for the single-sided trigger requirement. Data are the black points, PHOJET is the solid red line, PYTHIA8 i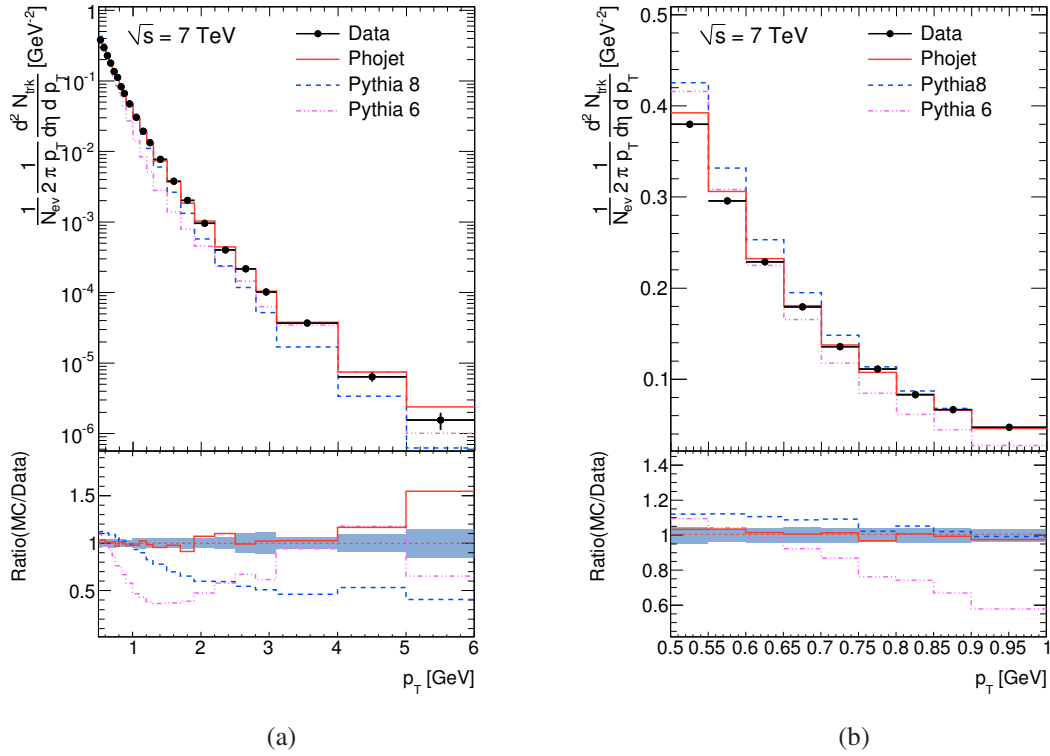s the blue dashed line and PYTHIA6 is the dash-dotted pink line. (a) shows $\frac{1}{N_{ev}}\frac{dN_{trk}}{d\eta}$ and (b) shows $\frac{1}{N_{ev}}\frac{dN_{ev}}{dn_{trk}}$. The bottom plots show the ratio of data to MC. In the ratio plot the blue band indicates the statistical and systematic errors.

to 0.8 at the highest $\Delta\eta$. At low $\Delta\eta$ all three generators describe the data well, but at high $\Delta\eta$, where the diffractive processes dominate, PYTHIA6 underestimates the rate of tracks. The systematic uncertainty at low $\Delta\eta$ is large as it is dominated by the ND component which is the most sensitive to the MBTS efficiency.

In order to understand the origin of the discrepancies between data and MC, it is useful to plot the distributions for each generator broken down into the SD, DD and ND sub-components. Figure 11.6 shows the eta distribution, Figure 11.7 shows the n_{trk}, Figure 11.8 shows the momentum spectrum and Figure 11.9 shows the $\Delta\eta$ distribution. The η and $\Delta\eta$ distributions best show the relative contributions from the different sub processes to the event sample. PHOJET favors single diffractive events whereas the PYTHIA models favor more equal contributions from both diffractive processes. PYTHIA 8 allows the smallest contribution from ND events, indicating a multi-particle production mechanism generating small rapidity gaps in between particles. In the track multiplicity and momentum spectrum plots PYTHIA 6 describes the tails of the distributions entirely with the ND components, whereas PYTHIA 8 and PHOJET have approximately equal contributions of all processes in
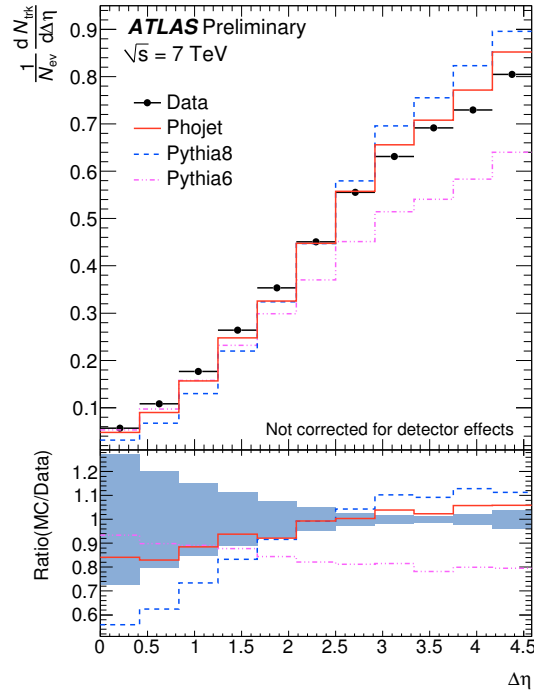
Figure 11.4. $\frac{1}{N_{ev}} \frac{1}{2\pi p_T} \frac{\mathrm{d}^2 N_{trk}}{\mathrm{d}\eta \mathrm{d}p_T}$ for the single sided trigger requirement. Data are the black points, PHOJET is the solid red line, PYTHIA 6 is the dash-dotted pink line and PYTHIA 8 is the blue dashed line. Shown is both the distribution as well as the ratio of data to MC. In the ratio plot the blue band indicates the statistical and systematic errors.

those regions. This difference is unsurprising given the lack of a hard component to diffraction in PYTHIA 6. Both PYTHIA 8 and PHOJET would do slightly better in describing the data if there was in increase in the ND component.

11.2 MBTS Multiplicity-based Studies

This section plots the MBTS multiplicity distribution, N_{counter}, for counters with charge above threshold and compares data to Monte Carlo simulation. The simulated events use the modified thresholds determined in Section 8.3 and the data uses the standard 0.15 pC threshold. The PYTHIA 6, PYTHIA 8 and PHOJET models are based on full simulation. The histograms for the other models presented are created by weighting the PYTHIA 8 full simulation events by the diffractive mass distribution to match the relevant model. As outlined in Chapter 3, the relative diffractive contribution, f_{D}, is set for each model to a value determined with the data. The details of this procedure are given in Chapter 12.2.2,

Figure 11.5. Distributions of $1/N_{ev}dN_{ev}/d\Delta\eta$ for the single sided trigger requirement. Data are the black points, PHOJET is the solid red line and PYTHIA8 is the blue dashed line, and PYTHIA6 the dash-dotted pink line. Shown is both the distribution as well as the ratio of MC to data. In the ratio plot the blue band indicates the quadratic sum of the statistical and systematic uncertainty.

but for clarity, the results are summarized here: f_D is 0.25 to 0.3, depending on the model.

The first comparison is of the inclusive counter distributions in Figure 11.10. The uncertainty band includes the uncertainty on the MBTS efficiency as well as the material as determined in Chapter 8.3. The efficiency uncertainty is determined by taking the difference between PYTHIA 8 with the tuned thresholds and the threshold which reproduces the most discrepant counter efficiency in data. The A- (C-) side inner counter thresholds were raised to 0.50 (0.60) pC. The A- (C-) side outer counter thresholds were changed to 0.18 (0.38) pC. The material uncertainty is taken as twice the difference in the distributions of PYTHIA 6 simulated with the nominal and extra material geometries. The factor of two comes from assuming that the difference between PYTHIA 6 and the data in the f_{zero} distribution is entirely due to extra material.

The Donnachie and Landshoff models match the data the most accurately in the inclusive samples. PHOJET shows the worst agreement. There are significant differences between PYTHIA 6 and PYTHIA 8 which are exclusively due to differences in fragmentation model of the diffractive components and tuning and color connection between the initial and final state in the ND component. No generator has high enough overall multiplicity,
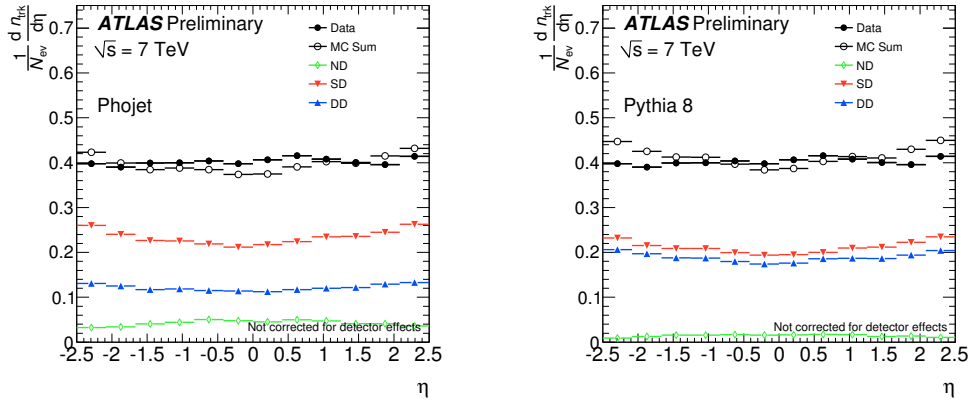
(a)

(b)
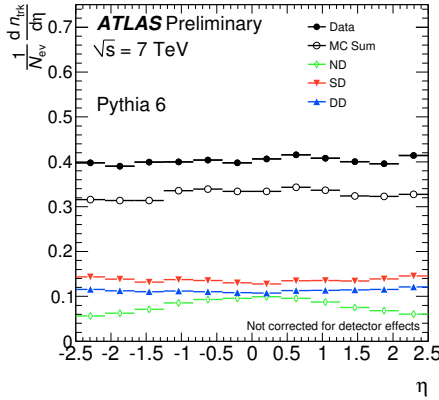
(c)

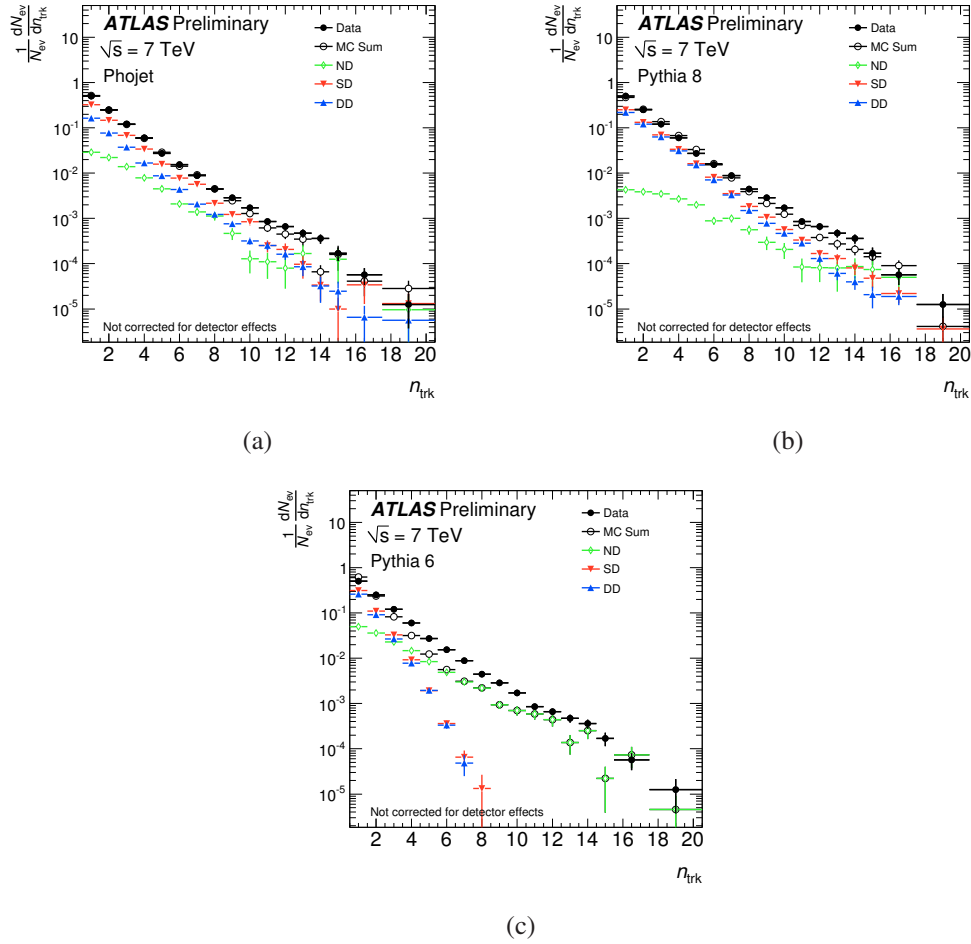**Figure 11.6.** $\frac{1}{N_{ev}}\frac{dn_{trk}}{d\eta}$ for the single sided trigger requirement. Data are shown in comparison with PHO-JET (a), PYTHIA8 (b) and PYTHIA6 (c). The non diffractive contribution is shown in green diamonds, the single diffractive in red triangles and the double diffractive is shown in blue inverted triangles. The data are the black points and the summed MC are the open black circles.

although the Donnachie and Landshoff models lie just outside the uncertainty band. In the low multiplicity region PYTHIA 6 over-estimates the event fraction while the other generators underestimate. Comparing the multiplicity in the inner and outer counters separately shows that the discrepancies are not confined to one particular η range.

The $N_{\text{counter}} = 1$ bin is not shown in any distribution because the background subtraction, described in detail in Chapter 9, does not work in this bin. In the unpaired bunches the majority of events with $N_{\text{counter}} = 1$ are from afterglow. Because the level of afterglow in the unpaired bunches is not the same in the paired bunches, the unpaired bunches do not accurately represent the background in the $N_{\text{counter}} = 1$ bin. The subtraction is valid for events with $N_{\text{counter}} > 1$ because these events are dominated by other background sources.

(a)

(b)

(c)

Figure 11.7. $\frac{1}{N_{ev}}\frac{dN_{ev}}{dn_{trk}}$ for the single sided trigger requirement. Data are shown in comparison with PHO-JET (a), PYTHIA8 (b) and PYTHIA6 (c). The non diffractive contribution is shown in green diamonds, the single diffractive in red triangles and the double diffractive is shown in blue inverted triangles. The data are the black points and the summed MC are the open black circles.

Figure 11.11 compares the counter multiplicity distributions in the single-sided event sample. In this sample PYTHIA 8 and PHOJET overestimate the event fraction at high multiplicity and underestimate it at low multiplicity, while PYTHIA 6 shows the opposite trend. The large difference between PYTHIA6 and PYTHIA8 is notable because the two have the same underlying diffractive mass distribution, indicating that the fragmentation contributes significantly to the multiplicity. Arguably, inner counter multiplicities show a broad distribution while the outer counters are peaked towards low values. The MC models are a poor match to the data for the inner counters but describe it better in the outer counters.
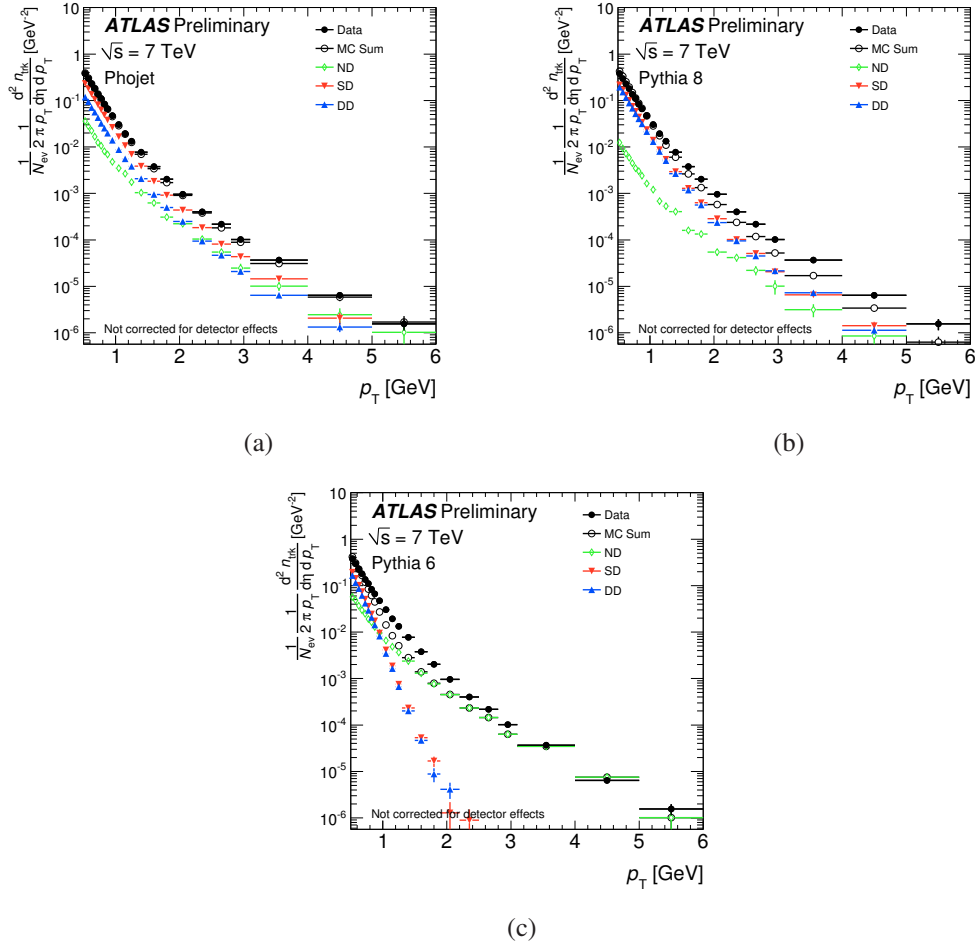
Figure 11.8. $\frac{1}{N_{ev}} \frac{1}{2\pi p_T} \frac{\mathrm{d}^2 n_{trk}}{\mathrm{d}\eta \mathrm{d}p_T}$ for the single sided trigger requirement. Data are shown in comparison with PHOJET (a), PYTHIA8 (b) and PYTHIA6 (c). The non diffractive contribution is shown in green diamonds, the single diffractive in red triangles and the double diffractive is shown in blue inverted triangles. The data are the black points and the summed MC are the open black circles.

11.3 Summary

The measurements of the properties of tracks in the diffractive-enhanced sample show the best agreement with the PHOJET Monte Carlo generator, which accurately reproduces the charged particle properties and the event level multiplicities. The PYTHIA 8 Monte Carlo generator reasonably reproduces the η-based distributions and the multiplicities but does not describe the p_T spectrum well. The MBTS multiplicity plots are best reproduced by PYTHIA 8 with a Donnachie and Landsoff parametrization. However, differences between PYTHIA 6 and PYTHIA 8 with the Schuler-Sjöstrand model show that the agreement in these variables depends strongly on the fragmentation model. When these results are
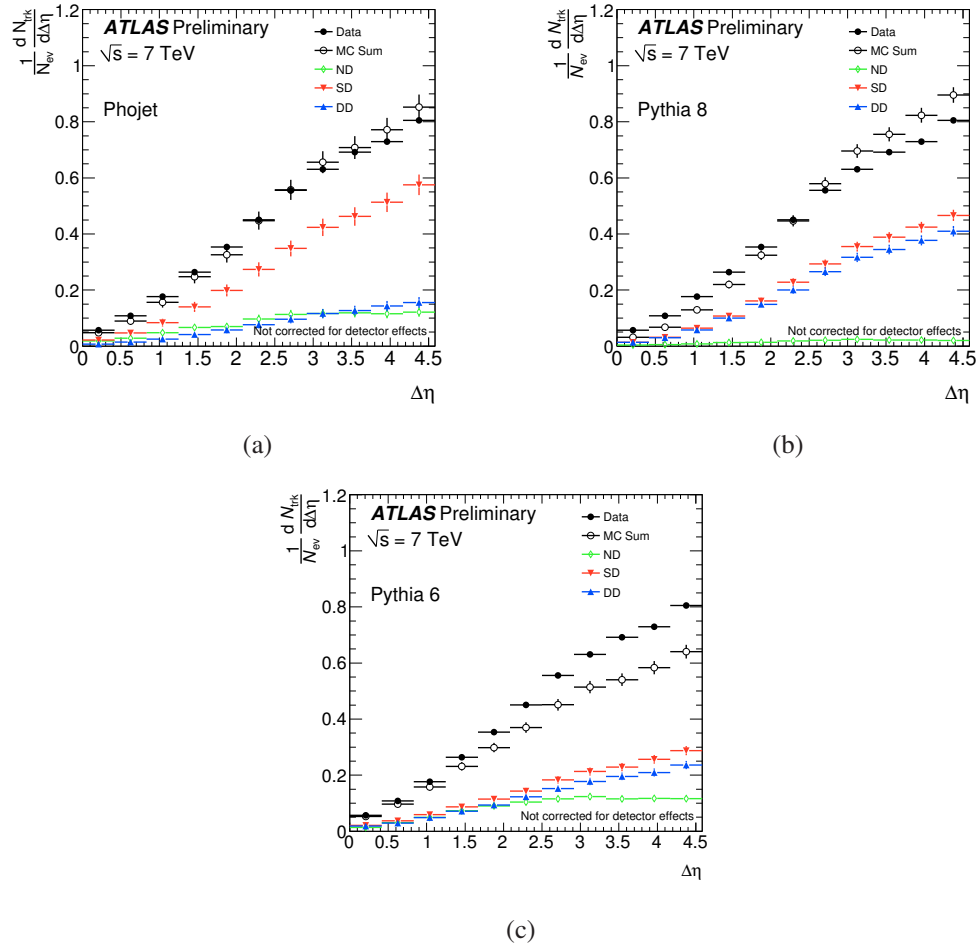
Figure 11.9. $\frac{1}{N_{ev}}\frac{dn_{trk}}{d\Delta\eta}$ for the single sided trigger requirement. Data are shown in comparison with PHO-JET (a), PYTHIA8 (b) and PYTHIA6 (c). The non diffractive contribution is shown in green diamonds, the single diffractive in red triangles and the double diffractive is shown in blue inverted triangles. The data are the black points and the summed MC are the open black circles.

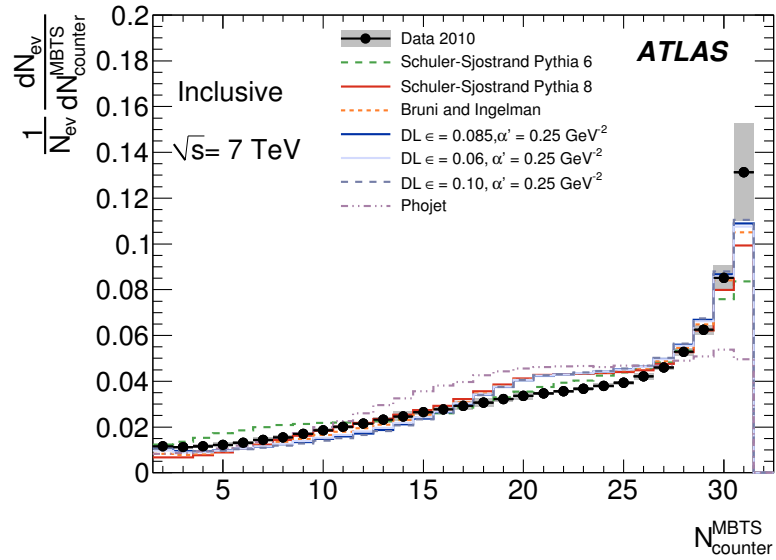taken with the results from minimum bias measurement [70], PYTHIA 8 with a Donnachie and Landshoff model emerges at the best overall description of inelastic interactions.
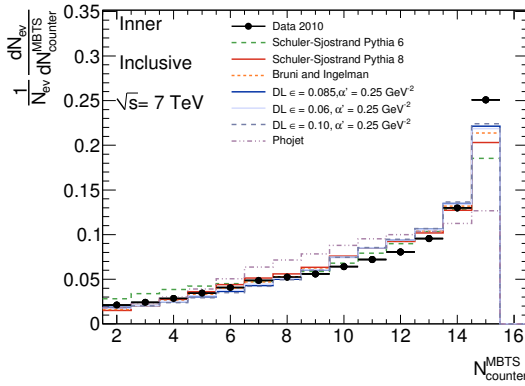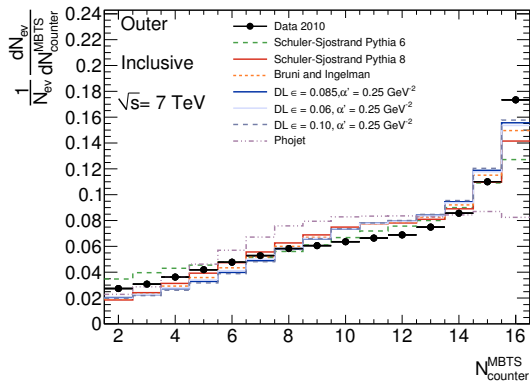
Figure 11.10. MBTS multiplicity comparing data and MC. (a) shows the inclusive hit distribution, (b) shows the inclusive inner counter hit multiplicities, and (c) shows the inclusive inner counter hit multiplicities . The band indicates the systematic uncertainty due to the MBTS response and material.
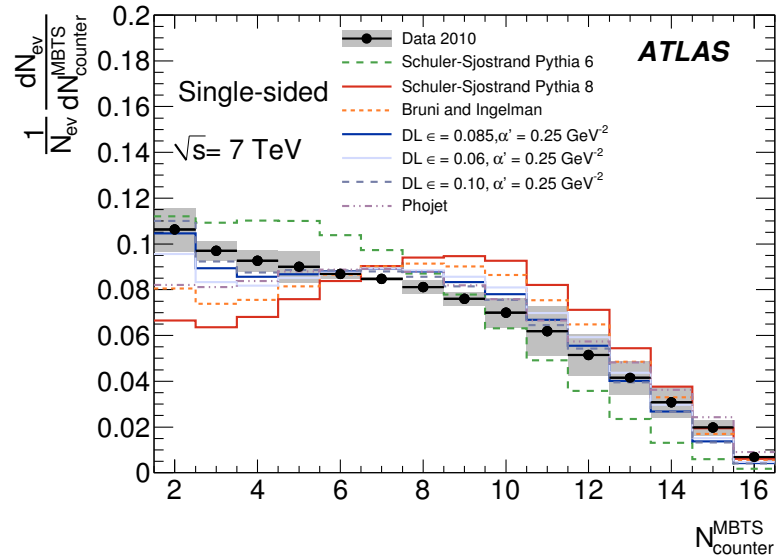
(a)
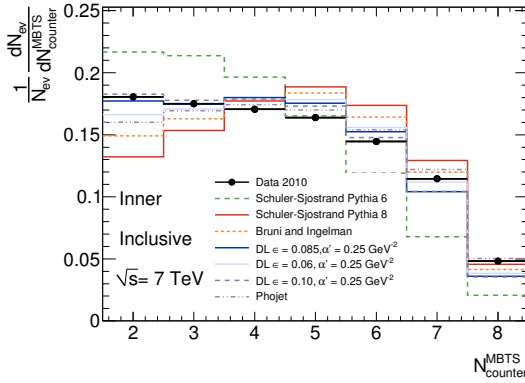
(b)
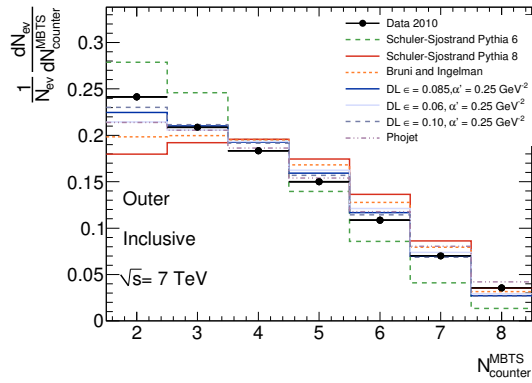
(c)

Figure 11.11. MBTS multiplicity comparing data and MC. (a) shows the single-sided hit distribution, (b) shows the inner counter hit multiplicities, and (c) shows the outer counter hit multiplicities for the single-sided events. The band indicates the systematic uncertainty due to the MBTS response and material.

<div align="right">

CHAPTER 12

</div>

Results

This chapter presents the results of the inelastic cross-section measurement using the inclusive sample defined in Chapter 3. The formula used to calculate the cross-section is given by Equation 3.12, reproduced here for convenience:

$$\sigma(\xi > 5 \times 10^{-6}) = \frac{(N - N_{\mathrm{BG}})}{\epsilon_{\mathrm{trig}} \times \mathcal{L}} \times C_{\mathrm{MC}}. \tag{12.1}$$

The measurement uses 1.2 million events, N, from run 152221, corresponding to an integrated luminosity, $\mathcal{L}$, of 20.25 μb. Chapter 7 describes the dataset in detail. The trigger efficiency, ϵ_{trig} , is measured to be $99.98^{+0.02}_{-0.12}\%$, as described in Chapter 8.2. While the backgrounds and MBTS performance are described in Chapters 9 and 8, those sections do not present the corresponding correction factors for the cross-section measurement. In the following sections the remaining factors necessary to calculate the inelastic cross-section are determined. In Section 12.1 the number of background events, N_{BG}, is calculated. The Monte Carlo simulation-based correction factor, C_{MC}, is presented in Section 12.2, which additionally details the determination of the relative contribution of diffractive events for each model. Section 12.3 reviews the systematic uncertainties and Section 12.4 presents the cross-section measurement.

12.1 Background Estimation

This measurement suffers from the primary backgrounds described in Chapter 9: beam-related backgrounds such as beam-gas, beam-halo and afterglow, and non-beam-related backgrounds such as noise and cosmic-rays. The measurement corrects for events which are purely background as inelastic interaction with low activity to migrate into the event sample because of additional hits supplied by afterglow.

Beam-gas and beam-halo events typically have multiple MBTS counters above threshold, whereas noise and out-of-time afterglow generally produce only one counter above threshold. These backgrounds are estimated as the sum of events passing the event selection in the unpaired bunches. In these runs, the same unprescaled trigger is used in the

	Intensity (10^9 p)	
	paired	unpaired
Beam 1	9.13	9.61
Beam 2	8.77	8.38

Table 12.1. Beam intensities in terms of protons per bunch for the paired and unpaired bunches in run 152221.

paired bunches and in the unpaired bunches. The out-of-time afterglow is overestimated using this method because the afterglow is correlated with the main collision event in the preceding paired bunches, as shown in Figure 9.2. Thus, the estimate of background from unpaired bunches will tend to be an overestimate of the true background contamination.

In order to reduce the effect of afterglow and noise, the event sample is restricted to events with at least two MBTS hits above threshold. This requirement cuts out the majority of out-of-time afterglow events which typically have only done counter above threshold. In principle, it also removes most of the noise-only events, but no events were found to have a charge less than -0.15 pC. Because the noise is symmetric about 0 pC, it is assumed that there are no events with noise hits greater than 0.15 pC in the event sample.

The background due to beam gas and beam-halo events is estimated from the unpaired bunches. Since the afterglow contribution is smaller for BCID=1786 (beam 1) than for BCID=892 (beam 2), only BCID 1786 is used for the background estimate. However, it must be corrected for the difference in currents between it and the other bunches. The correction proceeds as follows

$$N_{\text{BG}}^{\text{B1}} = N_{\text{unp}}^{\text{B1}} \times \frac{I_p^{\text{B1}}}{I_{\text{unp}}^{\text{B1}}} \tag{12.2}$$

$$N_{\text{BG}}^{\text{B2}} = N_{\text{unp}}^{\text{B1}} \times \frac{I_p^{\text{B1}}}{I_{\text{unp}}^{\text{B1}}} \times \frac{I_p^{\text{B2}}}{I_p^{\text{B1}}} \tag{12.3}$$

$$N_{\text{BG}} = N_{\text{unp}}^{\text{B1}} + N_{\text{unp}}^{\text{B2}} \tag{12.4}$$

$$= N_{\text{unp}}^{\text{B1}} \times \frac{I_p^{\text{B1}}}{I_{\text{unp}}^{\text{B1}}} \times \left(1 + \frac{I_p^{\text{B2}}}{I_p^{\text{B1}}}\right) \tag{12.5}$$

$$= 1.86 \times N_{\text{unp}}^{\text{B1}} \tag{12.6}$$

Here $N_{\text{BG}}^{\text{B1,2}}$ is the number of estimated background events in the paired bunches for Beam 1 or 2, $N_{\text{unp}}^{\text{B1}}$ is the measured number of events in the unpaired bunches for Beam 1 (BCID 1786), and $I_{\text{p,unp}}^{\text{B1,2}}$ is the current of the paired or unpaired bunches for Beam 1 or 2. The beam current values are taken from a database[1] and the beam intensities, which are derived from the currents, are listed in Table 12.1.

Table 12.2 shows the number of observed events in the paired bunches and the estimated background for the *single-sided* and *inclusive* event samples with different minimum MBTS counter requirements.

---

[1] The ATLAS conditions database folder `/TDAQ/OLC/LHC/LBDATA` in `COOL`.

Process	run 152221			
	N_{paired}	N_{BG}		
$N_{\text{counter}} \geq 1$				
single-sided	149518	23737	$\pm$	210
inclusive	1247851	24889	$\pm$	215
$N_{\text{counter}} \geq 2$				
single-sided	122490	422	$\pm$	28
inclusive	1220749	1574	$\pm$	54

Table 12.2. Number of events in the paired bunches (N_{paired}) and estimated background (N_{BG}) for the two runs we consider for all L1_MBTS_1 triggered events with at least one offline cell above threshold and the *single − sided* and the *inclusive* selection of at least two cells above threshold. The number of background events is based on the number of events in BCID 1786 and corrected for the difference in currents between Beam 1 and Beam 2 as defined in 12.2. The uncertainties are statistical only.

The inclusive sample contains 1.2 million events, 10% of which are single-sided. Fractionally, the beam background contributes 0.34% to the single-sided bunches and 0.13% to the full event sample. The single-sided events make up less than 30% of the background, indicating that it is mostly from beam-halo events, which produce hits on both sides of the detector. In contrast, when the event selection requirement is relaxed to only one counter above threshold, the background is dominantly single-sided and makes up 2% of the *inclusive* sample and 16% of the *single-sided* sample. This large background is the reason behind the requirement of at least 2 hits for the cross-section measurement.

Additionally, beam background events can overlap with collision events to increase the MBTS cell multiplicity. The overlap is a problem for the single-sided sample because it could cause a single-sided event to appear as a double-sided event. However, the luminosity of this run was low enough that there were only 0.007 events per crossing. There are roughly 2% as many events with $N_{\text{counter}} \geq 1$ in the unpaired bunches as in the paired bunches, leading to a beam background event every 0.0001 crossings. Therefore, an overlap occurs in 0.01% of the event sample, which is negligible.

Lastly, the contribution from in-time afterglow, which is not modeled in the Geant4 simulation, is estimated. Afterglow hits arising from collisions with less than 2 prompt MBTS hits could cause the events migrate into the event sample. As described in Chapter 9 the asymmetry of the time of the MBTS hits is used as an upper limit on the in-time afterglow contribution.

Binomial statistics are used to find the fraction of events with two real hits, f_{real}, as a function of the number of observed counters over threshold:

$$f_{\text{real}}(N) = \sum_{n=2}^{N} \binom{N}{n} h.p.(N)^n (1 - h.p.(N))^{N-n} \qquad (12.7)$$

$$f_{\text{real}}(2) = h.p.(2)^2 \qquad (12.8)$$

$$f_{\text{real}}(3) = h.p.(3)^3 + 3h.p.(3)^2(1 - h.p.(3)) \qquad (12.9)$$

where $N = N_{\text{counter}}$, the number of counters over threshold.

The hit purity of the $N_{\text{counter}} = 2$ and $N_{\text{counter}} = 3$ events was found to be 0.83. Therefore 67% of events with $N_{\text{counter}} = 2$ have two real hits and 92% of the events with $N_{\text{counter}} = 3$ have at least two real hits. $N_{\text{counter}} = 2$ and $N_{\text{counter}} = 3$ each make up approximately 1% of the event sample and therefore, 0.4% of events in the selected events sample have less than two real hits. In the single-sided sample, the $N_{\text{counter}} = 2$ and $N_{\text{counter}} = 3$ events each make up approximately 10% of the event sample. The afterglow is at most 3.6% of this sample.

An uncertainty of 100% is assumed on both the in-time afterglow and other beam-related background determinations. The resulting uncertainties are added in quadrature. This conservative estimate is due to the fact that the afterglow contribution is not well-understood but it is clear that it can only be overestimated using these methods. The uncertainties from other sources, such as the beam-current ratios, are small compared to the afterglow uncertainty.

12.2 Acceptance

This section discusses the acceptance of the event selection as determined with Monte Carlo models. First, the MBTS detector acceptance is discussed for the diffractive and non-diffractive sub-processes in Section 12.2.1. Then, the data are used to constrain the relative diffractive cross-sections in Section 12.2.2. A determination of ϵ_{sel} and $f_{\xi < 5 \times 10^{-6}}$ for the measurement range follows in Section 12.2.3. Finally, the extrapolation to $\xi > m_P^2/s$ is discussed in Section 12.2.4.

12.2.1 MBTS Acceptance

The MBTS acceptance for the inclusive and the single-sided selections are given in Table 12.3. The inclusive values are very high for the non-diffractive component for all generators, while it is as low as 43% for some of the diffractive contributions. The single-sided numbers show that the non-diffractive component is significantly suppressed for this selection: less than 1% of the ND events are selected. For the diffractive components ϵ_{sel} varies between 27 and 41%. The effect of variations in the Monte Carlo tuning was investigated using several different PYTHIA 6 tunes[2]. The differences between the tunings in the acceptance were smaller than the differences between the MC models, and therefore the tuning was not considered in further studies. This large variation in acceptance motivates the restriction of the measurement to a well-defined ξ-range. It also motivates constraining the relative diffractive contribution to the cross-section.

Figure 12.1 shows the efficiency of the MBTS selection (ϵ_{Sel}) as a function of ξ and η_{min}[3]. The efficiency agrees between the different generators to within 5% as a function

---

[2]Perugia0 and DW were used for all three subprocesses, and there were serveral other variations of inital and final state parameters for non-diffractive events only.

[3]η_{min} is defined in Chapter 3

Generator	Model	ND	SD	DD	CD
		Fraction of events passing the *inclusive* selection (%)			
PYTHIA 6	Schuler-Sjöstrand	99.90	67.96±0.07	82.14±0.05	-
PHOJET	Engel	99.96	74.80±0.06	90.82±0.04	88.20±0.05
PYTHIA 8	Schuler-Sjöstrand	100.00	68.69±0.07	83.19±0.05	-
PYTHIA 8	Bruni and Ingelman	100.00	68.11 ± 0.48	75.75± 0.44	-
PYTHIA 8	Berger and Streng	100.00	47.35 ± 0.51	55.40± 0.51	-
PYTHIA 8	DL $\epsilon = 0.085,\alpha' = 0.25$ GeV^{-2}	100.00	48.73 ± 0.51	56.10± 0.51	-
PYTHIA 8	DL $\epsilon = 0.06,\alpha' = 0.25$ GeV^{-2}	100.00	58.24 ± 0.50	62.60± 0.50	-
PYTHIA 8	DL $\epsilon = 0.10,\alpha' = 0.25$ GeV^{-2}	100.00	43.62 ± 0.51	51.67± 0.51	-
PYTHIA 8	DL $\epsilon = 0.085,\alpha' = 0.10$ GeV^{-2}	100.00	45.49 ± 0.51	57.39± 0.51	-
PYTHIA 8	DL $\epsilon = 0.085,\alpha' = 0.40$ GeV^{-2}	100.00	49.97 ± 0.51	54.67± 0.51	-
		Fraction of events passing the *single-sided* selection(%)			
PYTHIA 6	Schuler-Sjöstrand	0.99±0.01	26.65±0.06	31.68±0.07	-
PHOJET	Engel	0.69±0.01	30.85±0.07	23.16±0.06	46.62±0.07
PYTHIA 8	Schuler-Sjöstrand	0.16±0.01	27.98±0.06	34.34±0.07	-
PYTHIA 8	Bruni and Ingelman	0.16 ± 0.01	32.72 ± 0.48	41.14± 0.50	-
PYTHIA 8	Berger and Streng	0.16 ± 0.01	29.55 ± 0.47	35.69± 0.49	-
PYTHIA 8	DL $\epsilon = 0.085,\alpha' = 0.25$ GeV^{-2}	0.16 ± 0.01	28.73 ± 0.46	35.71± 0.49	-
PYTHIA 8	DL $\epsilon = 0.06,\alpha' = 0.25$ GeV^{-2}	0.16 ± 0.01	30.83 ± 0.47	38.72± 0.50	-
PYTHIA 8	DL $\epsilon = 0.10,\alpha' = 0.25$ GeV^{-2}	0.16 ± 0.01	27.87 ± 0.46	33.82± 0.48	-
PYTHIA 8	DL $\epsilon = 0.085,\alpha' = 0.10$ GeV^{-2}	0.16 ± 0.01	28.47 ± 0.46	35.60± 0.49	-
PYTHIA 8	DL $\epsilon = 0.085,\alpha' = 0.40$ GeV^{-2}	0.16 ± 0.01	28.31 ± 0.46	35.59± 0.49	-

Table 12.3. Acceptance of the inclusive and single-sided event selection for PYTHIA 6, PHOJET, PYTHIA 8 with the Schuler-Sjöstrand model and PYTHIA 8 re-weighted for other diffractive mass models. All these acceptances are given with respect to the full ξ-range.
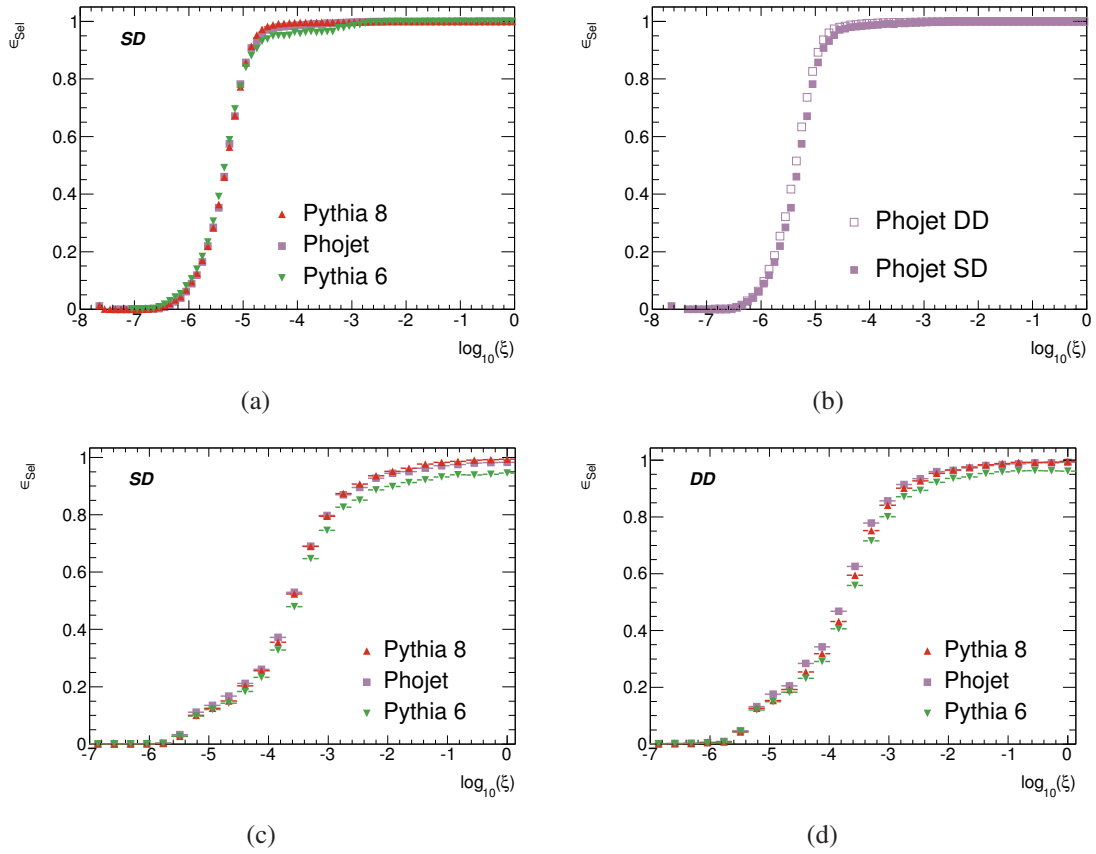
Figure 12.1. Efficiency of the inclusive MBTS selection as a function of $\log_{10}(\xi)$ for single-diffractive (a) comparing PYTHIA 6, PYTHIA 8, and PHOJET. A comparison of the efficiency between single- and double-dissociation (b) events for PHOJET. (c) and (d) show the same efficiency as a function of η_{min}. In the case of double-dissociation the higher mass system is plotted.

of ξ and η_{Min} for the SD processes, and to within 8% for the DD processes. The SD and DD efficiencies agree to within 8% as a function of ξ and 10% as a function of η_{Min}. At $\xi = 5 \times 10^{-6}$ the MBTS selection is 50% efficient. The large width of the efficiency turn on in η_{min} is due to the requirement of at least 2 MBTS hits over threshold, which effectively requires a second particle to also be within the acceptance.

Figure 12.2 shows the efficiency of the single-sided selection for single- and double-dissociation events as a function of the maximum diffractive mass in the event. While all of the generators have the same turn-on and turn-off in efficiency with diffractive mass, they achieve different plateau values. The higher multiplicity generators, PHOJET and PYTHIA 8 have similar behavior for the single-dissociation events, but differ for the double-dissociation events. The difference is likely due to the correlations between the two dissociation systems in these events.
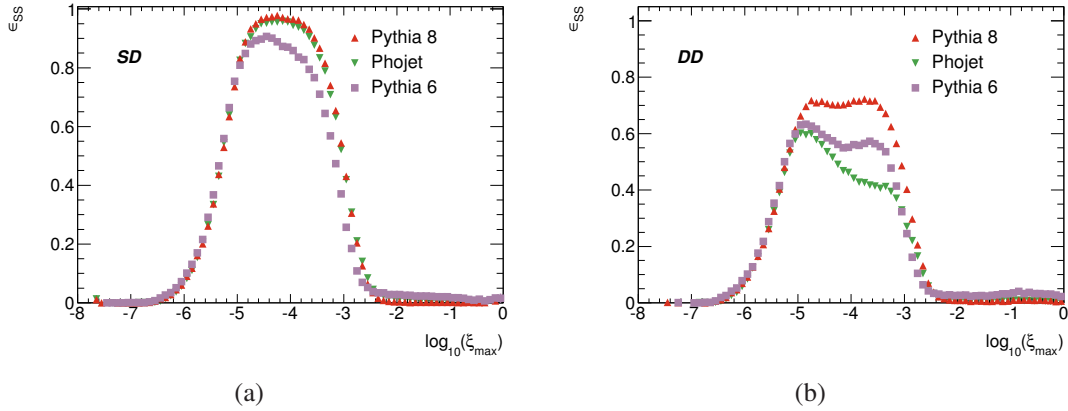
Figure 12.2. Efficiency of the single-sided MBTS selection as a function of $\log_{10}(\xi)$ for single-diffractive (a) and double-diffractive (b) events comparing PYTHIA 6 , PYTHIA 8 and PHOJET . In the case of double-dissociation the higher mass system is plotted.

12.2.2 Fractional Contribution of Diffractive Processes

As seen in Table 12.3, the single-sided selection strongly suppresses non-diffractive events. Consequently, the quantity f_D can be determined experimentally from R_{SS}, the fraction of events in the inclusive sample that have hits on only one side of the MBTS detector. The dependence of R_{SS} on f_D is outlined in Equation 3.10.

Table 12.4 lists the values obtained by the MC generators for R_{SS}.

$$R_{SS} = [10.02 \pm 0.03(\text{stat.})^{+0.07}_{-0.36}(\text{sys.})]\%$$

is measured for the inclusive sample in data. The systematic uncertainties on R_{SS} include the MBTS response, backgrounds, and the material effects, which are described in Chapters 8, 9 and 8.4, respectively.

Assuming the acceptance values from Table 12.3, R_{SS} is predicted as a function of the relative diffractive contributions (f_D and f_{SD}). For the models without full simulation, PYTHIA 8 events are re-weighted to match the ξ distribution described by each model. In Fig. 12.3 f_D is varied, keeping f_{SD} fixed at the value predicted by the relevant generator (see Table 2.1). It is seen that the preferred value for f_D varies between 25% and 30% depending on the model. Because the relative DD to SD contributions are also not well known, σ_{DD}/σ_{SD}, is also varied. Figure 12.4 shows the predictions assuming $\sigma_{DD}/\sigma_{SD} = 1$ and $\sigma_{DD}/\sigma_{SD} = 0$ as two extreme choices. [4].

The maximum and minimum allowed values of f_D are determined from the measured value of R_{SS} by taking the intersection of the MC predictions with the systematic error band of the data. The values are determined for each of the models separately and for the

---

[4]$\sigma_{DD}/\sigma_{SD} = 1$ is an extreme choice because for reasonable models of diffractive processes, the DD component does not exceed the SD component until $s \gg 100$ TeV [60].

Generator	Model	R_{SS} (%)
PYTHIA 6	Schuler-Sjöstrand	10.83 ± 0.01
PHOJET	Engel	6.85 ± 0.01
PYTHIA 8	Schuler-Sjöstrand	10.83 ± 0.01
PYTHIA 8	Bruni and Ingelman	12.94 ± 0.1
PYTHIA 8	Berger and Streng	12.39 ± 0.1
PYTHIA 8	DL $\epsilon = 0.085, \alpha' = 0.25\,\text{GeV}^{-2}$	12.16 ± 0.1
PYTHIA 8	DL $\epsilon = 0.02, \alpha' = 0.25\,\text{GeV}^{-2}$	12.56 ± 0.1
PYTHIA 8	DL $\epsilon = 0.15, \alpha' = 0.25\,\text{GeV}^{-2}$	9.98 ± 0.1
PYTHIA 8	DL $\epsilon = 0.085, \alpha' = 0.10\,\text{GeV}^{-2}$	12.15 ± 0.1
PYTHIA 8	DL $\epsilon = 0.085, \alpha' = 0.40\,\text{GeV}^{-2}$	12.04 ± 0.1

Table 12.4. Predicted values for R_{SS} at $\sqrt{s} = 7$ TeV for PYTHIA 6, PHOJET, PYTHIA 8 with the Schuler-Sjöstrand model and PYTHIA 8 re-weighted for other diffractive mass models.

variations of σ_{DD}/σ_{SD}. The results are listed in Table 12.5. The fitted f_D value is average of f_D^{min} and f_D^{max} for the default σ_{DD}/σ_{SD} and the error is the spread in allowed f_D values for $\frac{\sigma_{DD}}{\sigma_{SD}} = 1$ and $\frac{\sigma_{DD}}{\sigma_{SD}} = 0$. The central values range from 25% to 30% and the error is typically between 1% and 3%. It is interesting to note that although the exclusive particle properties of the PYTHIA 8 and PYTHIA 6 are very different, they prefer a very similar value of f_D. This similarity suggests that the R_{SS} measurement is primarily sensitive to the differential diffractive mass distribution rather than the diffractive event modeling.

12.2.3 ϵ_{sel} and $f_{\xi < 5 \times 10^{-6}}$

The kinematic range of the measurement is restricted by defining the acceptance with respect to a limited diffractive mass range, as described in Section 3.

Table 12.6 lists the fraction of events with $\xi > 5 \times 10^{-6}$ that pass the event selection (ϵ_{sel}) as well as $f_{\xi < 5 \times 10^{-6}}$, the fraction of events in the inclusive event sample that have $\xi < 5 \times 10^{-6}$. ϵ_{sel} is greater than 90% for all processes, generators and diffractive mass spectra. When the ND, SD, and DD components are combined with the value of f_D in Table 12.5 the inelastic efficiencies are between 98.5 and 99.5 %. $f_{\xi < 5 \times 10^{-6}}$ varies more significantly. It is as low as 1.2% and as high as 8.3% for the diffractive processes. It is consistent with 0 for the ND process. The large variations in $f_{\xi < 5 \times 10^{-6}}$ for the diffractive processes are attributed to differences in the diffractive mass spectra at low ξ. The total inelastic $f_{\xi < 5 \times 10^{-6}}$ varies between 0.3 and 1%.

12.2.4 Extrapolating to $\xi > m_p^2/s$

In order to extrapolate from $\sigma(\xi > 5 \times 10^{-6})$ to σ_{inel}, the fraction of the inelastic cross-section within the kinematic range of the measurement ($\xi > 5 \times 10^{-6}$) is determined for each model. Table 12.7 gives the fraction of events that fulfill the $\xi > 5 \times 10^{-6}$ cut for the individual processes, i.e. $\sigma(\xi > 5 \times 10^{-6})/\sigma_{inel}$. This fraction is nearly 100% for all

Generator	Model	default σ_DD/σ_SD		σ_DD/σ_SD		σ_DD/σ_SD = 0	σ_DD/σ_SD = 1	fitted f_{D}
		f_{D}^{max}	f_{D}^{min}	f_{D}^{max}	f_{D}^{min}	f_{D}^{min}	f_{D}^{max}	
PYTHIA 6	Schuler-Sjöstrand	28.6	29.9	31.0	31.4	28.3	29.6	$29.3^{+2.1}_{-0.9}$
PHOJET	Engel	28.7	29.9	26.7	27.9	30.7	32.0	$29.3^{+2.7}_{-2.7}$
PYTHIA 8	Schuler-Sjöstrand	29.0	30.2	31.2	32.4	28.6	29.8	$29.6^{+2.8}_{-2.6}$
PYTHIA 8	Bruni and Ingelman	24.5	25.5	26.7	27.8	24.1	25.1	$25.0^{+2.8}_{-0.9}$
PYTHIA 8	Berger and Streng	26.0	26.9	27.6	28.6	25.6	26.6	$26.4^{+2.2}_{-0.9}$
PYTHIA 8	DL $\epsilon = 0.085, \alpha' = 0.25 \,\mathrm{GeV}^{-2}$	26.4	27.4	28.4	29.4	25.9	26.9	$26.9^{+2.5}_{-1.0}$
PYTHIA 8	DL $\epsilon = 0.06, \alpha' = 0.25 \,\mathrm{GeV}^{-2}$	25.3	26.2	27.5	28.5	24.8	25.7	$25.7^{+2.8}_{-0.9}$
PYTHIA 8	DL $\epsilon = 0.10, \alpha' = 0.25 \,\mathrm{GeV}^{-2}$	27.1	28.0	28.8	29.7	26.7	27.6	$27.5^{+2.2}_{-0.8}$
PYTHIA 8	DL $\epsilon = 0.085, \alpha' = 0.10 \,\mathrm{GeV}^{-2}$	26.4	27.4	28.3	29.4	26.0	27.0	$26.9^{+2.5}_{-0.9}$
PYTHIA 8	DL $\epsilon = 0.085, \alpha' = 0.40 \,\mathrm{GeV}^{-2}$	26.6	27.6	28.8	29.9	26.1	27.1	$27.1^{+2.8}_{-1.0}$

Table 12.5. Minimum and maximum f_{D} values allowed by the R_{SS} measurement for the MC models for different assumptions on f_{SD} as derived from the inclusive R_{SS} measurement. The last column shows the fitted value of f_{D} for each generator and the uncertainty derived from the variations of f_{SD}.

Generator	Model	ND	SD	DD	CD	Inelastic
				ϵ_{sel}(%)		
PYTHIA 6	Schuler-Sjöstrand	99.93	95.14±0.06	95.37±0.03	-	98.81±0.03
PHOJET	Engel	99.97	95.98±0.05	97.65±0.02	92.00±0.04	99.28±0.03
PYTHIA 8	Schuler-Sjöstrand	100.00	96.69±0.05	96.84±0.03	-	99.22±0.03
PYTHIA 8	Bruni and Ingelman	100.00	95.70±0.24	94.54±0.25	-	99.06±0.17
PYTHIA 8	Berger and Streng	100.00	93.00±0.36	90.83±0.37	-	98.76±0.26
PYTHIA 8	DL $\epsilon = 0.085, \alpha' = 0.25\,\text{GeV}^{-2}$	100.00	93.43±0.34	91.16±0.37	-	98.77±0.25
PYTHIA 8	DL $\epsilon = 0.06, \alpha' = 0.25\,\text{GeV}^{-2}$	100.00	94.48±0.13	92.25±0.15	-	98.87±0.09
PYTHIA 8	DL $\epsilon = 0.10, \alpha' = 0.25\,\text{GeV}^{-2}$	100.00	92.44±0.17	90.49±0.18	-	98.71±0.12
PYTHIA 8	DL $\epsilon = 0.085, \alpha' = 0.10\,\text{GeV}^{-2}$	100.00	93.16±0.36	91.67±0.35	-	98.81±0.26
PYTHIA 8	DL $\epsilon = 0.085, \alpha' = 0.40\,\text{GeV}^{-2}$	100.00	93.69±0.33	90.82±0.38	-	98.76±0.25
				$f_{\xi<5\times10^{-6}}$(%)		
PYTHIA 6	Schuler-Sjöstrand	0.01	2.48±0.04	2.22±0.02	-	0.56±0.03
PHOJET	Engel	0.00	2.16±0.04	1.23±0.02	1.58±0.02	0.33±0.03
PYTHIA 8	Schuler-Sjöstrand	0.00	2.19±0.04	1.99±0.02	-	0.50±0.03
PYTHIA 8	Bruni and Ingelman	0.00	3.05±0.20	3.73±0.21	-	0.64±0.15
PYTHIA 8	Berger and Streng	0.00	5.42±0.32	7.62±0.35	-	0.98±0.24
PYTHIA 8	DL $\epsilon = 0.085, \alpha' = 0.25\,\text{GeV}^{-2}$	0.00	5.11±0.31	7.08±0.33	-	0.96±0.23
PYTHIA 8	DL $\epsilon = 0.06, \alpha' = 0.25\,\text{GeV}^{-2}$	0.00	3.91±0.11	6.01±0.13	-	0.83±0.08
PYTHIA 8	DL $\epsilon = 0.10, \alpha' = 0.25\,\text{GeV}^{-2}$	0.00	5.91±0.16	8.27±0.17	-	1.05±0.12
PYTHIA 8	DL $\epsilon = 0.085, \alpha' = 0.10\,\text{GeV}^{-2}$	0.00	6.02±0.34	6.79±0.32	-	1.00±0.25
PYTHIA 8	DL $\epsilon = 0.085, \alpha' = 0.40\,\text{GeV}^{-2}$	0.00	5.02±0.30	7.71±0.35	-	1.00±0.23

Table 12.6. Fraction of events with $\xi > 5 \times 10^{-6}$ passing the event selection(ϵ_{sel}), and fraction of the selected events with $\xi < 5 \times 10^{-6}$ ($f_{\xi<5\times10^{-6}}$) for all considered models. The *inelastic* values on the far right relate directly to the values in Equation 3.11 for ϵ_{sel} and $f_{\xi<5\times10^{-6}}$ with the relative diffractive cross-sections determined in 12.2.2. Errors less than 0.01% are not shown.
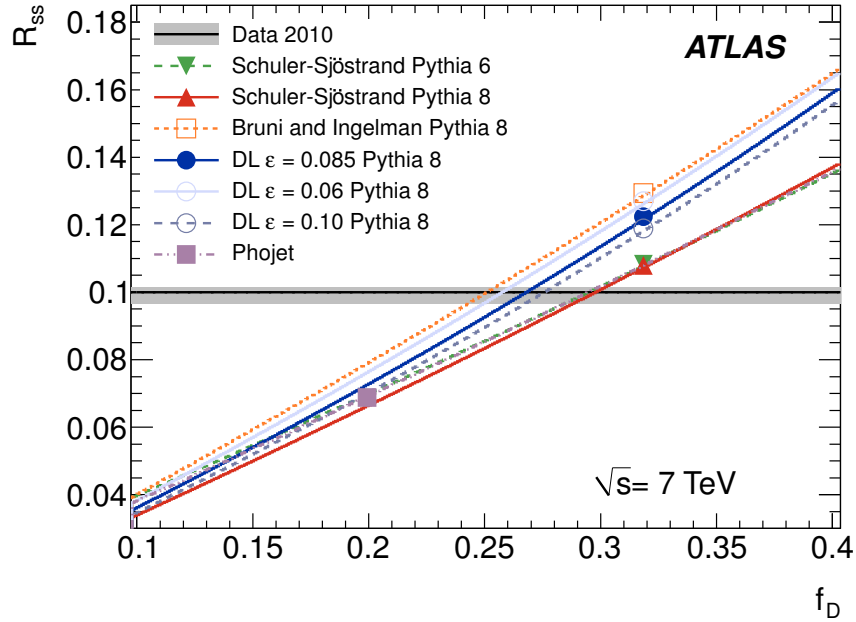
Figure 12.3. R_{SS} versus f_D. The data are shown as the line with systematic uncertainties (grey band). Also shown are the predictions as a function of f_D for a variety of models. For each model th point indicates the predicted value of R_{SS} for the default value of f_D. In this case the default value for f_{SD} is assumed for each sample, i.e. 59.6% for PYTHIA and additional models and 68.6% for PHOJET. For all models but PHOJET the σ_{CD} is taken to be 0.

models of the ND processes, whereas it varies between 44% and 76% for the SD events and between 53% and 92% for the DD events depending on the assumed ξ-dependence of the diffractive cross section. Additionally, there are predictions from M. Ryskin based on the work in [51] which predicts $\sigma(\xi > 5 \times 10^{-6})/\sigma_{inel} = 77 - 82\%$.

To perform the extrapolation of the cross-section measurement from the restricted ξ-range to the full range, the model by Donnachie and Landshoff with $\epsilon = 0.085$ and $\alpha' = 0.25 \text{ GeV}^{-2}$ is used because it gives the best description of the MBTS hit multiplicity for the single-sided sample (see Fig. 11.11). It predicts 87.2% acceptance for the ξ cut. The lowest acceptance value is obtained with the Ryskin model. The highest fraction is given by the Engel model, which predicts 95% of the cross-section to have $\xi > 5 \times 10^{-6}$. The full spread of the acceptance value is taken as a systematic uncertainty, leading to an extrapolation factor of 1.145 ± 0.115.

12.3 Systematic Uncertainties

The systematic errors on the total cross section measurement are summarized in Table 12.8. The following sources contribute to the total uncertainty:

Generator	Model	ND	SD	DD	CD	Inelastic
			Fraction of events with $\xi > 5 \times 10^{-6}$ (%)			
PYTHIA 6	Schuler-Sjöstrand	99.96	69.72±0.10	84.22±0.05	-	92.82±0.04
PHOJET	Engel	99.98	76.10±0.10	91.86±0.04	94.35±0.03	96.01±0.03
PYTHIA 8	Schuler-Sjöstrand	100.00	69.58±0.10	84.19±0.05	-	92.74±0.04
PYTHIA 8	Bruni and Ingelman	100.00	69.02±0.45	77.29±0.41	-	93.06±0.30
PYTHIA 8	Berger and Streng	100.00	48.17±0.49	56.54±0.48	-	87.21±0.33
PYTHIA 8	DL $\epsilon = 0.085, \alpha' = 0.25\,\text{GeV}^{-2}$	100.00	49.51±0.49	57.37±0.48	-	87.27±0.33
PYTHIA 8	DL $\epsilon = 0.06, \alpha' = 0.25\,\text{GeV}^{-2}$	100.00	59.25±0.21	63.96±0.21	-	90.02±0.12
PYTHIA 8	DL $\epsilon = 0.10, \alpha' = 0.25\,\text{GeV}^{-2}$	100.00	44.41±0.22	52.57±0.22	-	85.62±0.13
PYTHIA 8	DL $\epsilon = 0.085, \alpha' = 0.10\,\text{GeV}^{-2}$	100.00	45.91±0.49	58.54±0.48	-	86.82±0.33
PYTHIA 8	DL $\epsilon = 0.085, \alpha' = 0.40\,\text{GeV}^{-2}$	100.00	50.67±0.49	55.74±0.48	-	87.19±0.33

Table 12.7. Fraction of events with $\xi > 5 \times 10^{-6}$ for all considered models. The most right-hand column can be understood in terms of Equations 3.1 and 3.11 as $\sigma(\xi > 5 \times 10^{-6})/\sigma_{inel}$. The values for the relative diffractive cross-section determined in 12.2.2. When the error is not shown it is less than 0.01.
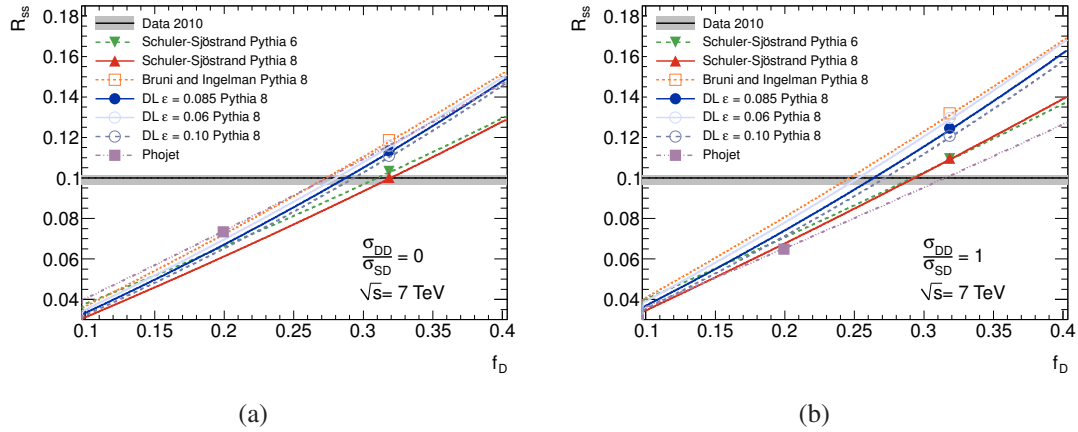
Figure 12.4. R_{SS} versus f_{D} with $\frac{\sigma_{\text{DD}}}{\sigma_{\text{SD}}} = 1$ (a) and $\frac{\sigma_{\text{DD}}}{\sigma_{\text{SD}}} = 0$ (b). The data are shown as the line with systematic uncertainties (grey band). Also shown are the predictions for a variety of models as function of an assumed value of f_{D}.

- **MBTS trigger efficiency**: The efficiency of the trigger requirement with respect to the offline requirement of two MBTS hits is studied in data as described in Chapter 8.2. The trigger efficiency is measured with randomly triggered events to be $99.98^{+0.02}_{-0.12}\%$. In order to set a systematic uncertainty, a trigger requiring at least one hit in the LUCID detector ($5.6 < |\eta| < 6.0$) is used to independently determine the efficiency. This method yields an efficiency of 99.91%. The difference between the LUCID based and random trigger based methods is taken as the uncertainty. Both methods agree within the statistical uncertainties and 0.07% is taken as the uncertainty.

- **MBTS response**: Chapter 8 showed that the data and MC simulation disagree in the shape of the signal charge distribution, leading to a lower average counter efficiency in the data. This effect is emulated in the MC by increasing the threshold to 0.28 pC (0.26 pC) on the A- (C-) side outer counters and 0.32 pC (0.38 pC) on the A- (C-) side inner counters. The systematic uncertainty associated with tuning the MBTS efficiency in the simulation is obtained by varying the MC thresholds until they match the efficiency of the counter in data which is furthest from the mean counter efficiency on each side and ring. The resulting thresholds are 0.50 (0.60) pC for the A- (C-) side inner counters and 0.18 (0.38) pC for the A- (C-) side outer counters. Changing the MC thresholds to these values results in a 0.09% variation on C_{MC} for PYTHIA6 and in smaller variations for the other models. Thus 0.1% is taken as the uncertainty due to the MBTS response.

- **Beam background determination**: As described in Chapter 9 and Section 12.1, the background contribution is estimated from the unpaired bunches and from the

asymmetry of the MBTS counter time measurement. Conservatively, 100% error is assumed on the beam background, leading to a 0.42% uncertainty on the cross section measurement.

- **Luminosity**: The uncertainty on the luminosity was described in detail in Chapter 10. The 3.4% uncertainty is dominated by the uncertainty on the measurement of the beam currents.

- **Acceptance**: The acceptance correction uncertainty is divided into several parts:

  - **Relative diffractive cross-section**: The value of f_D preferred by the data and its uncertainty is determined for each MC model as described in Section 12.2.2. The difference in C_{MC} obtained using the spread of the allowed f_D values (Table 12.5) is set as the systematic uncertainty. This variation leads to a symmetric 0.26% uncertainty on C_{MC} determined with the Donnachie and Landshoff $\epsilon = 0.085, \alpha\prime = 0.25$ GeV^{-2} parametrization.

  - **MC Multiplicity**: The dependence of the correction factor on the multiplicity of the diffractive system was determined by the taking the difference between C_{MC} determined with PYTHIA 8 and PYTHIA 6. These two models have the same cross-section model but quite different particle multiplicity distributions for diffractive events. The difference leads to a 0.36% uncertainty on C_{MC}.

  - **ξ-dependence** : The dependence on the input diffractive mass distribution is determined by comparing the value of C_{MC} for all models. The maximum difference between the Donnachie and Landshoff $\epsilon = 0.085$, $\alpha\prime = 0.25$ GeV^{-2} model with all other models is taken as the uncertainty. The largest difference comes from the PHOJET prediction and results in a 0.36% uncertainty on C_{MC}.

- **Material**: An excess in material with respect to the model used for simulation increases the MBTS multiplicity due to the increased rate of conversions as well as increased scattering. The effect of material is evaluated by taking twice the difference in C_{MC} of the PYTHIA 6 MC simulated with the nominal and extra material geometries as described in Section 8.4. This contributes 0.20% to the uncertainty on the cross-section measurement.

The CD process is only included in PHOJET. Including or not including this process in PHOJET makes a 0.01% difference to C_{MC} which is negligible compared to the systematic uncertainties listed above. Therefore, there is no additional uncertainty due to the CD contribution.

12.4 The Cross-section Measurement

The final result depends upon C_{MC}: the combination of ϵ_{Sel} and $f_{\xi<5\times10^{-6}}$. Using the calculated ϵ_{Sel} and $f_{\xi<5\times10^{-6}}$ values in Table 12.6 and the relative diffractive contribution,

Source	Uncertainty (%)
Trigger Efficiency	0.07
MBTS Response	0.09
Beam Background	0.42
f_D	0.26
MC Multiplicity	0.36
ξ-dependence	0.36
Material	0.20
Sub Total	0.75
Luminosity	3.40

Table 12.8. Sources of systematic uncertainty and their effect on the cross section measurement.

f_D as determined in section 12.2.2, C_{MC} is determined. Table 12.9 lists ϵ_{sel}, $f_{\xi<5\times10^{-6}}$ and C_{MC} for each model using the experimentally determined values of f_D which are also listed.

The PYTHIA 8-generated Donnachie and Landshoff model with $\epsilon = 0.085$, $\alpha' = 0.25$ GeV^{-2} is taken as the default MC, which gives $\epsilon_{sel} = 98.77\%$ and $f_{\xi<5\times10^{-6}} = 0.96\%$, leading to a correction factor of 1.0028. The observed number of events is 1,220,743, the number of background events, N_{BG}, is $1,574 \pm 1.01$, and the luminosity is $20.25 \pm 0.69 \ \mu$b^{-1}, resulting in a cross section of

$$\sigma(\xi > 5 \cdot 10^{-6}) = 60.33 \pm 0.05(\text{stat}) \pm 0.45(\text{syst}) \pm 2.05(\text{lumi}) \ \text{mb}.$$

where (stat), (sys), and (lumi) are the statistical, systematic and luminosity uncertainties, respectively.

Table 12.10 lists the predictions from Schuler Sjöstrand, PHOJET (Engel) and Ryskin *et. al.*, the only models for which a prediction of $\sigma(\xi > 5 \cdot 10^{-6})$ is available. Figure 12.5 graphically shows the results. Compared to the Schuler Sjöstrand (PHOJET) prediction of 66.4 mb (74.2 mb), the data value is 2.9σ (6.7σ) lower. The data are 1.9 to 4.1σ higher than the Ryskin *et. al.* prediction. The uncertainty is dominated by the uncertainty on the luminosity measurement. Runs 152166 and 154817 were additionally checked and the same cross-section was measured to within 0.8%. Runs 152166 and 152221 had very similar run conditions, but 154817 had non-negligible pile-up, and consequently, a higher afterglow bpackground. The consistency of the results shows the robustness of the measurement. This level of agreement (0.8%) is expected within the run-to-run luminosity uncertainties.

The measurement is extrapolated to the full inelastic cross-section assuming the ξ-dependence as given by the various models listed in Table 12.7. The model by Donnachie and Landshoff with $\epsilon = 0.085$, $\alpha' = 0.25$ GeV^{-2} is used, which gives a correction factor of 1.145 ± 0.115, as discussed in Section 12.2. Using this value an inelastic cross-section of

$$\sigma_{inel} = 69.1 \pm 2.4(\text{stat} + \text{syst} + \text{lumi}) \pm 6.9(\text{extr}) \ \text{mb}$$

is obtained where (extr) indicates the extrapolation uncertainty. Figure 12.5 shows the inelastic cross-section vs $\sqrt{s}$ and Table 12.10 compares the extrapolated to results to several predictions. Within the large uncertainty, the extrapolation agrees with the predictions from Schuler-Sjöstrand and most of the other analytic models. The only model in disagreement

Generator	Model	ϵ_{sel}	$f_{\xi<5\times10^{-6}}$	C_{MC}	f_{D}
PYTHIA 6	Schuler-Sjöstrand	0.9881 ± 0.0003	0.0056 ± 0.0003	1.0064	0.293
PHOJET	Engel	0.9928 ± 0.0003	0.0033 ± 0.0003	1.0040	0.293
PYTHIA 8	Schuler-Sjöstrand	0.9922 ± 0.0003	0.0050 ± 0.0003	1.0028	0.296
PYTHIA 8	Bruni and Ingelman	0.9906 ± 0.0017	0.0064 ± 0.0015	1.0030	0.251
PYTHIA 8	Berger and Streng	0.9876 ± 0.0026	0.0098 ± 0.0024	1.0026	0.264
PYTHIA 8	DL $\epsilon=0.085,\alpha'=0.25$ GeV^{-2}	0.9877 ± 0.0025	0.0096 ± 0.0023	1.0028	0.269
PYTHIA 8	DL $\epsilon=0.06,\alpha'=0.25$ GeV^{-2}	0.9887 ± 0.0009	0.0083 ± 0.0008	1.0031	0.257
PYTHIA 8	DL $\epsilon=0.10,\alpha'=0.25$ GeV^{-2}	0.9871 ± 0.0012	0.0105 ± 0.0012	1.0024	0.275
PYTHIA 8	DL $\epsilon=0.085,\alpha'=0.10$ GeV^{-2}	0.9881 ± 0.0026	0.0100 ± 0.0025	1.0020	0.269
PYTHIA 8	DL $\epsilon=0.085,\alpha'=0.40$ GeV^{-2}	0.9876 ± 0.0025	0.0100 ± 0.0023	1.0024	0.271

Table 12.9. $f_{\xi<5\times10^{-6}}$, ϵ_{sel}, f_{D} values, and cross section correction factor (C_{MC}) for the various models of inelastic interactions and diffractive cross-sections, using the fitted f_{D} value.

$\sigma(\xi > 5 \times 10^{-6})$ [mb]	
ATLAS Data 2010	$60.33 \pm 2.10(\text{exp.})$
Schuler and Sjöstrand	66.4
PHOJET	74.2
Ryskin *et al.*	$51.8 - 56.2$
$\sigma(\xi > m_p^2/s)$ [mb]	
ATLAS Data 2010	$69.4 \pm 2.4(\text{exp.}) \pm 6.9(\text{extr.})$
Schuler and Sjöstrand	71.5
PHOJET	77.3
Block and Halzen	69 ± 1.3
Ryskin *et al.*	$65.2 - 67.1$
Gotsman *et al.*	68
Achilli *et al.*	$60 - 75$

Table 12.10. Measurement and theoretical predictions of the inelastic cross-section for the restricted kinematic range, $\xi > 5 \times 10^{-6}$, and for the full kinematic range, $\xi > m_p^2/s$. The experimental uncertainty (exp.) includes the statistical, systematic and luminosity uncertainties. The extrapolation uncertainty (extr.) only applies to the full kinematic range and is listed separately.

is the Engel-based PHOJET. The agreement between the result and the Schuler-Sjöjstrand prediction improves in the extrapolation because the DL model is used for the extrapolation factor instead of the Schuler-Sjöjstrand correction factor.

It should be noted that because the primary measurement is mostly independent of the models, the extrapolation uncertainty can be reduced in the future when more data is available on diffractive cross-sections at low ξ. For example, preliminary results of large rapidity gap cross-sections up to $|\eta| < 4.9$ reported in [125] indicate that PHOJET normalized to a 30% relative diffractive contribution describes the data well. Future measurements with forward proton-tagging detectors[5] will greatly improve the knowledge of the single-diffractive cross-section at low ξ [126, 127].

---

[5]The ALFA detector, a far forward proton tagging detector, is scheduled to take data in late 2011.
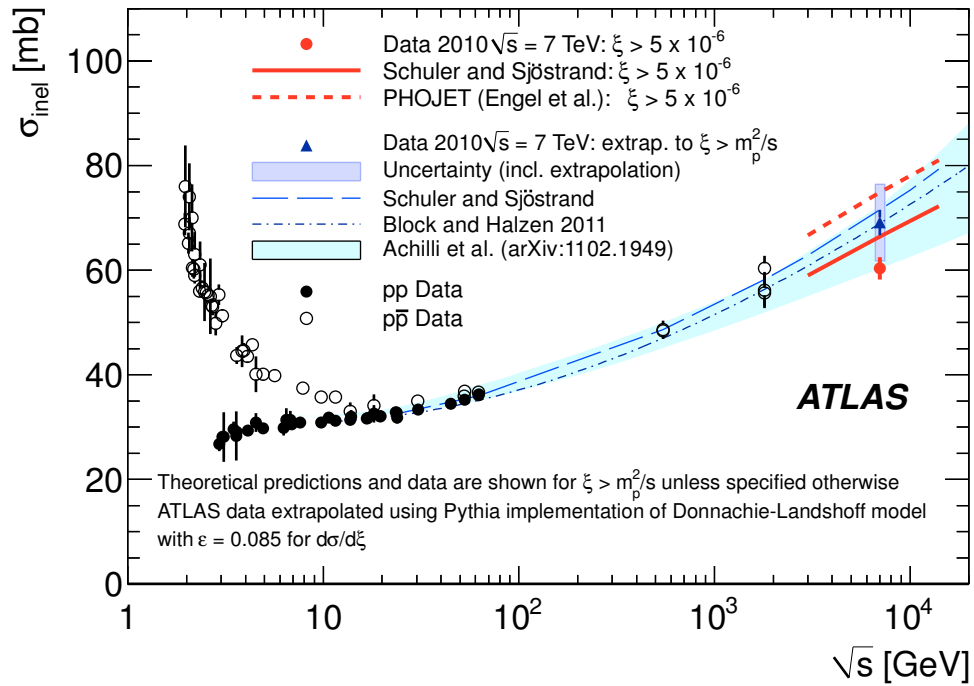
Figure 12.5. The inelastic cross-section versus $\sqrt{s}$. The ATLAS measurement for $\xi > 5 \times 10^{-6}$ is shown as the red filled circle and compared with the predictions of Schuler and Sjöstrand and PHOJET for the same phase space. Data (filled circles for pp data and unfilled circles for $p\bar{p}$ data) from several experiments are compared with the predictions of the pp inelastic cross-section from Schuler and Sjöstrand [60] (as used by PYTHIA), by Block and Halzen [128] and by Achilli *et al.* [61]. An extrapolation from the measured range of $\xi > 5 \times 10^{-6}$ to the full inelastic cross-section using the acceptance of $87 \pm 10\%$ is also shown (blue filled triangle). The experimental uncertainty is indicated by the error bar while the total (including the extrapolation uncertainty) is represented by the blue shaded area.

<div align="right">

CHAPTER 13

</div>

Conclusion

In summary, this thesis details the first measurement of the proton-proton inelastic cross-section at $\sqrt{s}$ =7 TeV. The cross-section is obtained by selecting approximately 1.2 million events with at least two hits in forward scintillator counters. The luminosity of the data sample was measured to be 20 μb^{-1} using a far-forward, Cherenkov light based, relative luminosity detector. The measurement is restricted to the acceptance of the scintillator detectors, $\xi > 5 \times 10^{-6}$, where $\xi = M_X^2/s$, the invariant mass of the largest proton dissociation system in the event. This phase space fully contains non-diffractive events and accepts over half of diffractive events. The details of the acceptance depend on the model of the diffractive cross-section. The events are corrected for the event selection efficiency, ϵ_{Sel}, and for the fraction of events in the selected sample which have $\xi < 5 \times 10^{-6}$, $f_{\xi < 5 \times 10^{-6}}$. In order to limit the model-dependence of the correction, the relative diffractive contribution is measured *in-situ* for each of the 10 models used to generate a correction factor. The total correction factor, including the ϵ_{trig}, ϵ_{sel} and $f_{\xi < 5 \times 10^{-6}}$, which was derived from a model with a single Pomeron pole with $\alpha(0) > 1$,is 0.03%.

The cross-section is measured to be

$$\sigma(\xi > 5 \times 10^{-6}) = 60.33 \pm 0.05(\text{stat}) \pm 0.45(\text{syst}) \pm 2.05(\text{lumi}) \text{ mb} \qquad (13.1)$$

where (stat), (sys), and (lumi) are the statistical, systematic and luminosity uncertainties, respectively. The systematic error of 0.75% is dominated by the model dependence of ϵ_{sel} and $f_{\xi < 5 \times 10^{-6}}$. The dominant experimental uncertainty is due to the luminosity measurement. It arises from the measurement of the beam currents during the van der Meer scans which determined the luminosity calibration factor. Comparisons to the models used by Monte Carlo generators show that the cross-section measured in the data is lower than predicted.

In order to compare to analytic models, the measured value of the cross-section is extrapolated to the total inelastic cross-section. The same model used to derive ϵ_{Sel} and $f_{\xi < 5 \times 10^{-6}}$is used to obtain the central value. The uncertainty on the extrapolation is assessed using a variety of other models. The factor used to correct the observed cross-section

is 1.145±0.115, resulting in an inelastic cross-section of

$$\sigma_{\mathrm{inel}} = 69.1 \pm 2.4(\mathrm{stat} + \mathrm{syst} + \mathrm{lumi}) \pm 6.9(\mathrm{extr}) \; \mathrm{mb}. \tag{13.2}$$

where (extr) is the uncertainty due to the extrapolation. This measurement agrees nicely with most predictions for the cross-section at 7 TeV, but it should be noted that without a better understanding of the differential diffractive cross-section at low ξ, the uncertainty on the measurement is large.

The results presented here, the highest energy direct measurement of the proton-proton inelastic cross-section, constitute a benchmark measurement for high-energy particle physics. The measurement of the inelastic cross-section for $\xi > 5 \times 10^{-6}$ is well-defined with small experimental errors and little model dependence. The extrapolation uncertainty is at present large, but will benefit in the future from improved knowledge of the diffractive cross-sections.

Bibliography

[1] **Particle Data Group** Collaboration, K. Nakamura *et al. J. Phys. G* **37** (2010) 385–401.

[2] **CDF** Collaboration *Phys. Rev. D* **50** no. 9, (Nov, 1994) 5550–5561.

[3] **E710** Collaboration, N. Amos *et al. Phys. Rev. Lett.* **68** (1992) .

[4] **E811** Collaboration, N. Amos *et al. Phys. Lett. B* **445** (1999) .

[5] R. J. Glauber and G. Matthiae *Nucl. Phys. B* **21** (1970) .

[6] T. K. Gaisser, U. P. Sukhatme, and G. B. Yodh, "Hadron cross sections at ultrahigh energies and unitarity bounds on diffraction," *Phys. Rev. D* **36** no. 5, (Sep, 1987) 1350–1357.

[7] **ATLAS** Collaboration, "Measurement of the Inelastic Proton-Proton Cross-Section at $\sqrt{s}$ =7 TeV with the ATLAS Detector," `arXiv:1104.0326 [hep-ex]`. Submitted to Nature Communications.

[8] H. Yukawa, "On the interaction of elementary particles," *Proc. Phys. Math. Soc. Jap.* **17** (1935) 48–57.

[9] T. Regge *Il Nuovo Cimento.* **14** (1959) .

[10] I. Y. Pomeranchuk *Soviet Physics: Journal of Experimental and Theoretical Physics* **7** (1958) .

[11] S. Donnachie, G. Dosch, P. Landshoff, and O. Nachtmann, *Pomeron Physics and QCD*. Cambridge University Press, 2002.

[12] V. N. Gribov *Soviet Physics: Journal of Experimental and Theoretical Physics* **41** (1961) .

[13] H. B. Meyer and M. J. Teper, "Glueballs and the pomeron," *Nuclear Physics B - Proceedings Supplements* **129-130** (2004) 200 – 202. Lattice 2003.

[14] G. Jaroskiewicz and P. Landshoff *Physical Review* **D10** (1985) .

[15] E. Nagy *et al. Nuclear Physics* **B150** (1979) .

[16] **E710** Collaboration, N. Amos *et al. Physics Letters* **B247** (1990) .

[17] J. R. Cudell, V. Ezhela, K. Kang, S. Lugovsky, and N. Tkachenko, "High-energy forward scattering and the pomeron: Simple pole versus unitarized models," *Phys. Rev. D* **61** no. 3, (Jan, 2000) 034019.

[18] P.D.Collins and F. Gault *Physical Review* **73B** (1978) .

[19] A. Donnachie and P. V. Landshoff, "Total cross sections," *Physics Letters B* **296** no. 1-2, (1992) 227 – 232.

[20] M. Froissart, "Asymptotic behavior and subtractions in the Mandelstam representation," *Phys. Rev.* **123** (1961) 1053–1057.

[21] A. Martin *Nuovo Cimento* **42** (1966) .

[22] M. Gell-Mann, "The Eightfold Way: A Theory of Strong Interaction Symmetry," tech. rep., DOE Technical Report, 1961.

[23] G. Zweig, "An SU3 Model for Strong Interaction Symmtery and its Breaking," Tech. Rep. CERN Report-8419, 1964.

[24] M. Y. Han and Y. Nambu, "Three-triplet model with double $su(3)$ symmetry," *Phys. Rev.* **139** no. 4B, (Aug, 1965) B1006–B1010.

[25] O. Greenberg, "Spin and unitary-spin independence in a paraquark model of baryons and mesons," *Phys. Rev. Lett.* **13** (1964) 598–602.

[26] R. P. Feynman, "Very high-energy collisions of hadrons," *Phys. Rev. Lett.* **23** no. 24, (1969) 1415–1417.

[27] J. D. Bjorken, "Asymptotic sum rules at infinite momentum," *Phys. Rev.* **179** no. 5, (Mar, 1969) 1547–1553.

[28] D. J. Gross and F. Wilczek, "Asymptotically free gauge theories.," *Phys. Rev. D* **8** no. 10, (Nov, 1973) 3633–3652.

[29] H. D. Politzer, "Reliable perturbative results for strong interactions?," *Phys. Rev. Lett.* **30** no. 26, (Jun, 1973) 1346–1349.

[30] J. C. Collins, D. E. Soper, and G. Sterman, "Factorization for one-loop corrections in the drell-yan process," *Nuclear Physics B* **223** no. 2, (1983) 381 – 421.

[31] J. C. Collins and D. E. Soper, "Back-to-back jets in qcd," *Nuclear Physics B* **193** no. 2, (1981) 381 – 443.

[32] F. Low *Phys. Rev.* **D12** (1975) .

[33] S. Nussinov *Phys. Rev. Lett.* **34** (1975) .

[34] J. Gunion and D. Soper *Phys. Rev.* **D15** (1977) .

[35] A. Donnachie and P. Landshoff *Phys. Lett.* **B296** (1992) .

[36] **H1** Collaboration, "First measurement of the deep-inelastic structure of proton diffraction," *Physics Letters B* **348** no. 3-4, (1995) 681 – 696.

[37] **H1** Collaboration, C. Adloff *et al.*, "Inclusive measurement of diffractive deep inelastic ep scattering," *Z. Phys.* **C76** (1997) 613–629, `arXiv:hep-ex/9708016`.

[38] **The Zeus** Collaboration, Chekanov *et al.*, "Measurement of the q and energy dependence of diffractive interactions at hera," *The European Physical Journal C - Particles and Fields* **25** (2002) 169–187.

[39] J. C. Collins, "Proof of factorization for diffractive hard scattering," *Phys. Rev. D* **57** no. 5, (Mar, 1998) 3051–3056.

[40] J. C. Collins, "Erratum: Proof of factorization for diffractive hard scattering [phys. rev. d 57, 3051 (1998)]," *Phys. Rev. D* **61** no. 1, (Nov, 1999) 019902.

[41] G. Ingelman and P. E. Schlein, "Jet structure in high mass diffractive scattering," *Physics Letters B* **152** no. 3-4, (1985) 256 – 260.

[42] P. Newman and F. Schilling, "Hera diffractive structure function data and parton distributions," in *Workshop on HERA and the LHC*. 2004-2005. `arXiv:hep-ex/0511.032v1 [hep-ex]`.

[43] A. Donnachie and P. V. Landshoff, "Total cross-sections," *Phys. Lett.* **B296** (1992) 227–232, `hep-ph/9209205`.

[44] P. Desgrolard, M. Giffon, E. Martynov, and E. Predazzi, "The additive quark model revisited: Hadron and photon induced cross-sections," *Eur. Phys. J.* **C9** (1999) 623–631, `arXiv:hep-ph/9811393`.

[45] R. Engel *Z. Phys.* **C66** (1995) 203–214.

[46] R. Engel and J. Ranft *Phys. Rev.* **D54** (1996) 4246–4262.

[47] A. Capella, U. Sukhatme, T. Tran, and C. Tan, "Dual parton model," *Physics Reports* **236** (1994) 225–329.

[48] R. Engel, F. W. Bopp, D. Pertermann, and J. Ranft, "Extrapolation of hadron cross sections to supercollider energies within the two-component dual parton model," *Phys. Rev. D* **46** no. 11, (Dec, 1992) 5192–5195.

[49] H. D. I. Abarbanel, J. D. Bronzan, R. L. Sugar, and A. R. White, "Reggeon field theory: Formulation and use," *Physics Reports* **21** no. 3, (1975) 119 – 182.

[50] F. W. Bopp, R. Engel, and J. Ranft, "Rapidity Gaps and the Phojet Monte Carlo," in *LAFEX International School of High Energy Physics*. 1998. `arXiv:hep-ph/9803437`.

[51] M. G. Ryskin, A. D. Martin, and V. A. Khoze, "High-energy strong interactions: from 'hard' to 'soft'," `arXiv:1102.2844 [hep-ph]`.

[52] E. Kuraev, L. Lipatov, and V. Fadin *Sov. Phys. JETP* **45** (1977) .

[53] Y. Y. Balitsky and V. Fadin *Sov. J. Nucl. Phys.* **28** (1978) .

[54] M. Block, "Hadronic forward scattering: Predictions for the large hadron collider and cosmic rays," *Physics Reports* **436** no. 3-6, (2006) 71 – 215.

[55] M. M. Block and R. N. Cahn, "High-Energy p anti-p and p p Forward Elastic Scattering and Total Cross-Sections," *Rev. Mod. Phys.* **57** (1985) 563.

[56] **CDF** Collaboration, F. Abe *et al. Phys. Rev. D* **50** (1994) .

[57] A. Donnachie and P. V. Landshoff, "New data and the hard pomeron," *Phys. Lett.* **B518** (2001) 63–71, `arXiv:hep-ph/0105088`.

[58] A. Donnachie and P. V. Landshoff, "Does the hard pomeron obey Regge factorization?," *Phys. Lett.* **B595** (2004) 393–399, `hep-ph/0402081`.

[59] A. M. Mueller, "$O(2, 1)$ analysis of single-particle spectra at high energy," *Phys. Rev. D* **2** no. 12, (Dec, 1970) 2963–2968.

[60] G. A. Schuler and T. Sjöstrand, "Hadronic diffractive cross sections and the rise of the total cross section," *Phys. Rev. D* **49** no. 5, (Mar, 1994) 2257–2267.

[61] A. Achilli *et al.*, "Total and inelastic cross-sections at LHC at CM energy of 7 TeV and beyond," `arXiv:1102.1949 [hep-ph]`.

[62] E. Berger, , *et al.*, "Diffractive hard scattering," *Nucl. Phys.* **B286** (1987) .

[63] K. Streng, "Hard QCD scatterings in diffractive reactions at HERA," Tech. Rep. CERN-TH-4949, CERN, 1988.

[64] P. Bruni and G. Ingelman, "Diffractive W and Z production at colliders and the pomeron parton content," *Phys. Lett.* **B311** (1993) .

[65] T. Sjöstrand, S. Mrenna, and P. Skands, "Pythia 6.4 physics and manual," *JHEP* **05** (2006) 026.

[66] T. Sjöstrand, S. Mrenna, and P. Skands, "Pythia version 8.135," *Comput. Phys. Commun.* **178** (2008) 852–867.

[67] B. Andersson, G. Gustafson, G. Ingelman, and T. Sjöstrand, "Parton fragmentation and string dynamics," *Physics Reports* **97** no. 2-3, (1983) 31 – 145.

[68] S. Navin, "Diffraction in Pythia." 2010. `arXiv:1004.0384 [hep-ph]`.

[69] V. Gribov, "A reggeon diagram techinque," *Sov. Phys. JETP* **26** (1968) .

[70] **ATLAS** Collaboration, "Charged-particle multiplicities in pp interactions measured with the ATLAS detector at the LHC," *New J. Phys.* (2010) , `arXiv:1012.5104 [hep-ex]`.

[71] **ATLAS** Collaboration, "ATLAS Monte Carlo Tunes for MC09.". ATLAS-PHYS-PUB-2010-002, http://cdsweb.cern.ch/record/1247375.

[72] P. Skands, "The Perugia Tunes." 2009. `arXiv:0905.3418 [hep-ph]`.

[73] R. D. Field, "Min-bias and the underlying event at the Tevatron and the LHC." 2002. Talk presented at the Fermilab MC Tuning Workshop.

[74] S. van der Meer Tech. Rep. CERN-ISR-PO-68-31, CERN, 1968.

[75] **ATLAS** Collaboration, "Updated Luminosity Determination in pp Collisions at $\sqrt{s} = 7$ TeV using the ATLAS Detector.". ATLAS-CONF-2011-011; http://cdsweb.cern.ch/record/1334563.

[76] L. Evans, (ed.), P. Bryant, (ed.), "LHC Machine," *JINST* **3** (2008) S08001.

[77] E. Eichten, I. Hinchliffe, K. Lane, and C. Quigg, "Supercollider physics," *Rev. Mod. Phys.* **56** no. 4, (Oct, 1984) 579–707.

[78] M. Bajko *et al.*, "Report of the task force on the incident of 19th september 2008 at the lhc.," Tech. Rep. LHC-PROJECT-Report-1168. CERN-LHC-PROJECT-Report-1168, CERN, 2009.

[79] "CERN-DI-0812015, http://cdsweb.cern.ch/record/1260465.".

[80] J. Blewett, "200 TeV Intersecting Storage Accelerators," in *8th Int. Conf. on High Energy Accel.* 1971.

[81] S. Myers and F. Zimmermann, "Chamonix 2010 summary report," in *Proceedings of Chamonix 2010 Workshop on LHC Performance*. 2010.

[82] S. Myers and F. Zimmermann, "Chamonix 2011 summary report," in *Proceedings of Chamonix 2011 Workshop on LHC Performance*. 2011.

[83] **ATLAS** Collaboration, "The ATLAS Experiment at the CERN Large Hadron Collider," *JINST* **3** (2008) S08003.

[84] G. Aad *et al.*, "ATLAS pixel detector electronics and sensors," *JINST* **3** (2008) .

[85] A. Abdesselam *et al.*, "The barrel modules of the ATLAS semiconductor tracker," *Nuc. Inst. Meth.* **568** (2006) .

[86] **The ATLAS TRT** Collaboration, "The atlas trt barrel detector," *Journal of Instrumentation* **3** no. 02, (2008) P02014.

[87] **The ATLAS TRT** Collaboration, "The atlas trt end-cap detectors," *Journal of Instrumentation* **3** no. 10, (2008) P10003.

[88] **ATLAS** Collaboration, "Liquid argon calorimeter technical design report.". CERN-LHCC-96-41.

[89] **ATLAS** Collaboration, "Readiness of the atlas liquid argon calorimeter for lhc collisions," *The European Physical Journal C - Particles and Fields* **70** (2010) .

[90] B. Aubert *et al.*, "Development and construction of large size signal electrodes for the atlas electromagnetic calorimeter," *Nuc. Inst. Meth.* **539** (2005) .

[91] **ATLAS** Collaboration, "Expected Performance of the ATLAS Experiment - Detector, Trigger and Physics," `arXiv:0901.0512 [hep-ex]`.

[92] **The Tile Calorimeter Subsystem of the ATLAS** Collaboration, "Design, construction and installation of the atlas hadronic barrel scintillator-tile calorimeter," Tech. Rep. ATL-TILECAL-PUB-2008-001. ATL-COM-TILECAL-2007-019, CERN, Geneva, Nov, 2007.

[93] K. Anderson *et al.*, "Design of the front-end analog electronics for the atlas tile calorimeter," *Nucl. Inst. Meth* **551** (2005) .

[94] T. Cornelissen *et al.*, "Concepts, Design and Implementation of the ATLAS New Tracking (NEWT)." 2007.

[95] R. Frühwirth *et al.*, "Application of Kalman Filtering to Track and Vertex Fitting," *Nucl. Instr. Meth.* **A262** (1987) .

[96] D. Wicke, "New Algorithm for Solving Track Ambiguities," Tech. Rep. DELPHI, 236:93-163, 1998.

[97] H. Gray, *The Charged Particle Multiplicity at Center of Mass Energies from 900 GeV to 7 TeV measured with the ATLAS Experiment at the Large Hadron Collider*. PhD thesis, California Institute of Technology, 2010.

[98] R. Duda and P. Hart, "Use of the Hough Transformation to Detect Lines and Curves in Pictures," *Comm. ACM* **15** (1972) .

[99] **ATLAS** Collaboration, "Performance of primary vertex reconstruction in proton-proton collisions at $\sqrt{s} = 7$ TeV in the ATLAS experiment.". ATLAS-CONF-2010-069, http://cdsweb.cern.ch/record/1281344.

[100] R. Frühwirth *et al.*, "Adaptive Vertex Fitting," *J. Phys.* **G34** (2007) .

[101] **ATLAS** Collaboration, "The atlas inner detector commissioning and calibration," *Eur. Phys. J. C* **70** no. arXiv:1004.5293. CERN-PH-EP-2010-043, (Jun, 2010) 787–821. 34 p.

[102] **ATLAS** Collaboration, "ATLAS Approved Inner detector Plots.". https://twiki.cern.ch/twiki/bin/view/AtlasPublic/ApprovedPlotsID.

[103] W. Cleland and E. Stern, "Signal processing considerations for liquid ionization calorimeters in a high rate environment," *Nuclear Instruments and Methods* **338** no. 2-3, (1994) .

[104] E. Fullana *et al.*, "Digital signal reconstruction in the ATLAS hadronic tile calorimeter," in *Real Time Conference, 2005. 14th IEEE-NPSS.* 2005.

[105] **ATLAS** Collaboration, "Performance of the Minimum Bias Trigger in p-p Collisions at $\sqrt{s} = 7$ TeV." 2010. ATLAS-CONF-2010-068; http://cdsweb.cern.ch/record/1281343.

[106] M. Tylmad *et al.*, "Pulse Shapes for Signal Reconstruction in the ATLS Tile Calorimeter," in *Real Time Conference, 2009. 16th IEEE-NPSS.* May, 2009.

[107] **ATLAS** Collaboration, "The ATLAS Simulation Infrastructure," *Eur. Phys. J.* **C70** (2010) 823–874, `arXiv:1005.4568 [physics.ins-det]`.

[108] **GEANT4** Collaboration, S. Agostinelli *et al.*, "GEANT4: A simulation toolkit," *Nucl. Instrum. Meth.* **A506** (2003) 250–303.

[109] **ATLAS** Collaboration, "Charged particle multiplicities in pp interactions at $\sqrt{s} = 7$ TeV measured with the ATLAS detector at the LHC.". ATLAS-CONF-2010-024; http://cdsweb.cern.ch/record/1277656.

[110] R. Veness *et al.*, "The ATLAS Beam Vacuum System," in *Proceedings of PAC09*. 2009.

[111] **ATLAS** Collaboration, "Luminosity Determination in pp Collisions at sqrt(s)=7 TeV Using the ATLAS Detector at the LHC," *Eur.Phys.J.* **C71** (2011) 1630, `arXiv:1101.2185 [hep-ex]`.

[112] W. Herr and B. Muratori, "Concept of Luminosity," in *Proceedings CAS2003, CERN-2006-002*, p. 361. 2006.

[113] H. Burkhardt and P. Grafstrom, "Absolute Luminosity From Machine Parameters," Tech. Rep. LHC-PROJECT-Report-1019, CERN, 2007.

[114] **ATLAS** Collaboration, "Luminosity Determination Using the ATLAS Detector.". ATLAS-CONF-2010-060, http://cdsweb.cern.ch/record/1281333.

[115] P.Darriulat and C. Rubbia Tech. Rep. CERN Internal Document 68/340/5 SIS/si., CERN, 1968.

[116] **ATLAS** Collaboration, "Charged particle multiplicities in pp interactions at $\sqrt{s} = 7$ TeV measured with the ATLAS detector at the LHC.". ATLAS-CONF-2010-024, http://cdsweb.cern.ch/record/1277665.

[117] G. D'Agostini, "A Multidimensional unfolding method based on Bayes' theorem," *Nucl. Instr. Meth.* **A362** (1995) 487–498.

[118] **ATLAS** Collaboration, "Charged-particle multiplicities in pp interactions at $\sqrt{s} = 900$ GeV measured with the ATLAS detector at the LHC," *Physics Letters B* **688** (2010) 21–42.

[119] G. Anders *et al.*, "LHC Bunch-Current Normalization for the April-May 2010 Luminosity-Calibration Measurements," tech. rep., CERN, 2011.

[120] J. J. Gras and M. Ludwig and P. Odier, "The 2010 lhc dc bct measurement system and its main sources of uncertainties," Tech. Rep. LHC-Project-Note-432 ; CERN-LHC-Project-Note-432, CERN, 2010.

[121] **ATLAS** Collaboration, "Studies of Diffractive Enhanced Minimum Bias Events in ATLAS." 2010. ATLAS-CONF-2010-048; http://cdsweb.cern.ch/record/1281302.

[122] **CMS** Collaboration, "Charged particle multiplicities in pp interactions at $\sqrt{s} = 0.9$, 2.36, and 7 tev. oai:cds.cern.ch:1309522," *J. High Energy Phys.* **01** no. arXiv:1011.5531. CERN-PH-EP-2010-048. CMS-QCD-10-004, (Nov, 2010) 079. 36 p.

[123] **ALICE** Collaboration, "First proton-proton collisions at the lhc as observed with the alice detector: measurement of the charged particle pseudorapidity density at $\sqrt{s}$ = 900 gev," *Eur. Phys. J. C* **65** no. arXiv:0911.5430. 1, (Dec, 2009) 111. 15 p.

[124] **ALICE** Collaboration, "Charged-particle multiplicity measurement in proton-proton collisions at $\sqrt{s}$ = 7 tev with alice at lhc," *Eur. Phys. J. C* **68** no. arXiv:1004.3514. 3-4, (Apr, 2010) 345–354. 11 p.

[125] **ATLAS** Collaboration, "Rapidity gap cross-sections in pp interactions $\sqrt{s} = 7$ TeV .". ATLAS-CONF-2011-059, http://cdsweb.cern.ch/record/1344487.

[126] **ATLAS** Collaboration, *ATLAS Forward Detectors for Measurement of Elastic Scattering and Luminosity*. Technical Design Report. CERN, Geneva, 2008.

[127] **TOTEM** Collaboration, "The totem experiment at the cern large hadron collider," *Journal of Instrumentation* **3** no. 08, (2008) S08007.

[128] M. M. Block and F. Halzen, "Forward hadronic scattering at 7 tev: An update on predictions for the lhc," *Phys. Rev. D* **83** no. 7, (2011) 077901.

[129] "LHC-PHO-1999-172.". http://cdsweb.cern.ch/record/842530.

[130] A. Martin *Phys. Rev.* **D80** (2009) .

[131] E. Gotsman, E. Levin, U. Maor, and J. S. Miller *Eur. Phys. J.* **C57** (2008) .

[132] E. Gotsman, E. Levin, and U. Maor `arXiv:hep-ph/10105323`.

[133] M. E. Peskin and D. V. Schroeder, *An Introduction To Quantum Field Theory (Frontiers in Physics)*. Westview Press, 1995.

APPENDIX A

Mandelstam Variables

The Mandelstam variables describe the kinematics of two-body scattering, as shown in Figure A.1. The four-vectors of the particles involved are given by $P_{1,..,4}$ and they can be combined into several lorentz invarient quantities:

$$s = (P_1 + P_2)^2 \tag{A.1}$$
$$t = (P_1 - P_3)^2 \tag{A.2}$$
$$u = (P_1 - P_4)^2 \tag{A.3}$$

with the relation

$$s + t + u = \sum_{i=1}^{4} m_i^2. \tag{A.4}$$

where m_i is the invariant mass of particle i. Due to energy and momentum conservation, only two out of the three mandelstam variables are independent. Most commonly s and t are used, with s corresponding the square of the center-of-mass-energy and t corresponding to the square of the momentum transfer between P_1 and P_3. Often t and q^2 are used interchangeably, where q^2 is the momentum transfer in a more complicated interaction than 2→2. In the case of hadron-hadron scattering s is the center-of-mass of the two particle, or equivalently, the two beams of particles in the case of colliding beams. In calculating partonic cross-sections $\hat{s}$ is used, where $\hat{s}$ is the center of mass in the parton scattering frame.
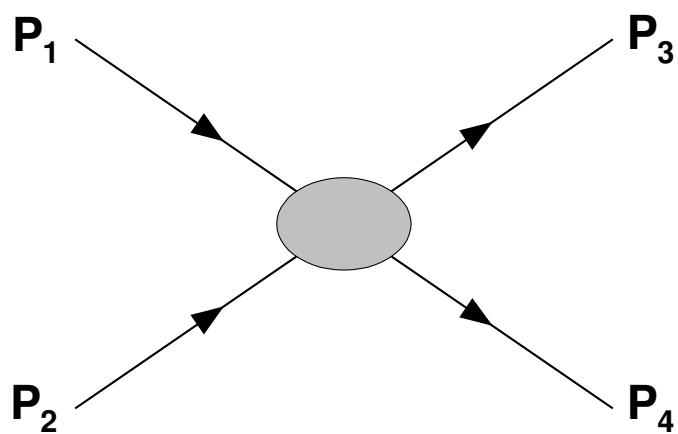
Figure A.1. Two-to-two scattering process. P_i denotes the four-momentum of particle i.

APPENDIX B

The Optical Theorem

The optical theorem is a useful property of the scattering matrix which relates the forward elastic scattering amplitude to the total cross-section. Let S be the scattering matrix, i be the initial state, and f be the final state. The probability to be in f given i is given by

$$P_{fi} = |\langle f|S|i\rangle|^2 \tag{B.1}$$

where f has the property

$$\sum_f |f\rangle\langle f| = 1 \tag{B.2}$$

which is simply the statement that f covers all possible final states. Additionally, the probability to end up is some final state must be unity, therefore

$$
\begin{aligned}
1 &= \sum_f |\langle f|S|i\rangle|^2 & \text{(B.3)}\\
&= \sum_f \langle i|S^\dagger|f\rangle\langle f|S|i\rangle & \text{(B.4)}\\
&= \langle i|S^\dagger S|i\rangle. & \text{(B.5)}
\end{aligned}
$$

which is to say that S is unitary. It follows that

$$
\begin{aligned}
\delta_{ij} &= \langle j|S\dagger S|i\rangle & \text{(B.6)}\\
&= \sum_f \langle j|S\dagger|f\rangle\langle f|S|i\rangle & \text{(B.7)}
\end{aligned}
$$

for orthonormal states i and j. Let's assume a two-body initial state i with particles with four-momenta k_1 and k_2 and a final state f with an arbitrary number of particles, n. Then we can define a transition matrix, T such that $S = 1 + iT$ and it follows that

$$
\begin{aligned}
\langle f|S|i\rangle &= \langle k_1'k_2'\cdots k_n'|S|k_1k_2\rangle & \text{(B.8)}\\
&= \delta_{if} + i(2\pi)^4\delta^4(P^f - P^i)\langle f|T|i\rangle & \text{(B.9)}
\end{aligned}
$$

where $P^i = k_1 + k_2$ and $P^f = k'_1 + k'_2 + \cdots + k'_n$. The transition rate, R_{fi}, is normalized such that

$$R_{fi} = (2\pi)^4 \delta^4(P^f - P^i)|\langle f|T|i\rangle|^2 \tag{B.10}$$

The total cross-section for $12 \to n$ particles is then given by

$$\sigma_{12 \to n} = \frac{1}{4|\mathbf{k}_1|\sqrt{s}} \sum_{fn} R_{fi} \tag{B.11}$$

where $\mathbf{k}_1$ is the three-momentum of particle 1 in the center-of-mass frame. In order to derive the optical theorem we note that $S^\dagger S = 1$, therefore $(1 - iT)^\dagger(1 - iT) = 1$ and if follows that

$$-i(T - T^\dagger) = T^\dagger T. \tag{B.12}$$

Considering two states i and j we then have

$$\langle j|T|i\rangle - \langle j|T^\dagger|i\rangle = \sum_f (2\pi)^4 \delta^4(P^f - P^i)\langle j|T^\dagger|f\rangle\langle f|T|i\rangle \tag{B.13}$$

which can alternately be obtained by inserting Equation B.9 into Equation B.7. If $j = i$ then

$$2\mathrm{Im}\langle i|T|i\rangle = \sum_f (2\pi)^4 \delta^4(P^f - P^i)|\langle f|T|i\rangle|^2. \tag{B.14}$$

Using Equation B.11 we find that

$$\sigma_{12}^{\mathrm{Tot}} = \frac{1}{2|\mathbf{k}_1|\sqrt{s}}\mathrm{Im}\langle i|T|i\rangle \tag{B.15}$$

$$= \frac{1}{2|\mathbf{k}_1|\sqrt{s}}\mathrm{Im}A(s, t = 0). \tag{B.16}$$

Equation B.16 is the statement of the optical theorem: the total cross-section is related to the imaginary part of the $2 \to 2$ scattering cross-section taken to the limit of no momentum transfer. Figure B.1 graphically illustrates this concept.
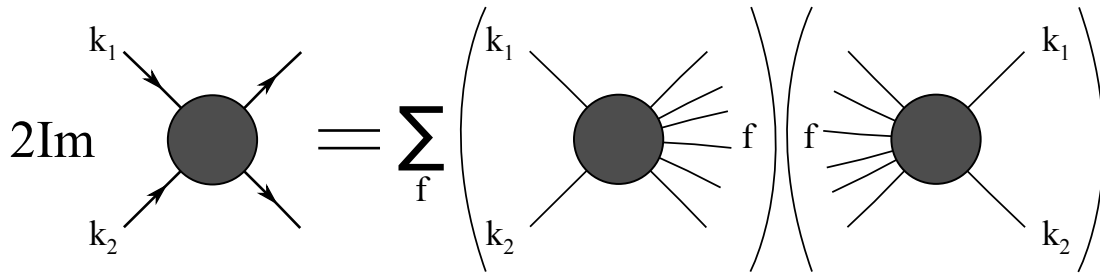
Figure B.1. An illustration of the optical theorem.

This derivation drew on References [11] and [133].